Dissertation
Submitted to the
Combined Faculties for Natural Sciences and for Mathematics
of the Ruperto-Carola University of Heidelberg, Germany
for the degree of
Doctor of Natural Sciences

Put forward by
Diplom-Physicist Leif Vogel
Born in Lübeck, Schleswig-Holstein, Germany

Oral examination: December 13th, 2011

Volcanic plumes:
Evaluation of spectroscopic measurements, early detection, and bromine chemistry

Referees: Prof. Dr. Ulrich Platt
Prof. Dr. Thomas Wagner

Vulkanfahnen: Auswertung spektroskopischer Messungen, Früherkennung und Bromchemie

Vulkane emittieren unter anderem hochreaktive chemische Verbindungen, welche die Atmosphäre lokal, regional und global beeinflussen können. Gegenstand dieser Studie sind Messungen von Vulkanfahnen mittels differentieller optischer Absorptionsspektroskopie (DOAS). Ein neues Werkzeug zur Analyse und Optimierung der Auswertung von Absorptionsspektren wurde entwickelt, welches auf jede DOAS Messung angewandt werden kann. Brommonoxid (BrO) und Schwefeldioxid (SO_2) wurden in der Vulkanfahne des Ätna (Italien) gemessen. Die hier vorgestellenten Messungen bei Fahnenaltern von 5 bis 100 Minuten stellen die ersten, simultanen Messungen von BrO in „älteren“ Vulkanfahnen dar. Es wurden BrO/SO_2 Verhältnisse zwischen $0.4 \cdot 10^{-4}$ und $1.2 \cdot 10^{-4}$ bestimmt. Die Messungen zeigen, dass die chemischen Modellrechnungen die gemessene Entwicklung nur unzureichend wiedergeben. Desweiteren wurde zum ersten Mal BrO in der Vulkanfahne des Pacaya Vulkans (Guatemala) nachgewiesen und die Entwicklung von BrO vom Kraterrand ($< 0.2 \cdot 10^{-4}$) bis 5 Minuten nach Emission ($1.25 \cdot 10^{-4}$) erstmalig in hoher zeitlicher Auflösung verfolgt. Eine Studie am Popocatépetl Vulkan (Mexiko) zeigte, dass die DOAS-Technik für flugzeuggestützte SO_2 Früherkennungssysteme für Wolken vulkanischen Ursprungs anwendbar ist. Eine für Flugzeuge gefährliche Vulkanwolke ist bis zu einer Entfernung von 80 km detektierbar.

Volcanic plumes: Evaluation of spectroscopic measurements, early detection, and bromine chemistry

Volcanos emit inter alia highly reactive chemical compounds, which influence the atmosphere on a local, regional and global scale. Subject of this study are measurements of volcanic plumes via differential optical absorption spectroscopy (DOAS). A new tool for analysis and optimisation of evaluation schemes was developed, which is applicable to any DOAS measurement. Measurements of bromine monoxide (BrO) and sulphur dioxide (SO_2) are presented, which were gathered at Mt. Etna (Italy) and Pacaya (Guatemala). For Mt. Etna, the measurements describe the evolution of BrO at plume ages of 5 min. - 100 min., which are the first simultaneously performed measurements in “aged” plumes. Measured BrO/SO_2 ratios range between $0.4 \cdot 10^{-4}$ and $1.2 \cdot 10^{-4}$. The measurements show, that chemical model calculations inadequately describe the evolution of BrO. Furthermore the first detection of BrO at Pacaya volcano (Guatemala) is presented, the evolution of BrO from the crater rim ($< 0.2 \cdot 10^{-4}$) to a plume age of 5 min. ($1.25 \cdot 10^{-4}$) at high time resolution was observed. At Popocatépetl volcano, the feasibility of the DOAS technique was explored to be a central component in an early in-flight warning system of volcanic SO_2 clouds for aviation. A maximum detection distance of 80 km is derived.

Contents

1 Introduction

Volcanic emissions were believed to be chemically relative inert and mainly affect the atmosphere by precipitation changes and radiative dimming via sulphate aerosols and emitted ash (e.g. Robock, 2007). This view changed by the discovery of bromine monoxide (BrO) in the plume of the Soufrière Hills Volcano, Montserrat (Bobrowski et al., 2003). Measured mixing ratios of BrO ranged up to 1 ppb, which constitutes the highest measured concentration of BrO in the atmosphere. Since BrO participates in auto-catalytic reactions of highly reactive halogen radicals destroying ozone (O_3) (Barrie et al., 1988; Barrie and Platt, 1997; Hebestreit et al., 1999; von Glasow and Crutzen, 2007, and references therein), it may lead to O_3 depletion in volcanic plumes (Bobrowski et al., 2003; Oppenheimer et al., 2006; Roberts et al., 2009; von Glasow, 2010), which was validated by Rose et al. (2006); Millard et al. (2006); Vance et al. (2010).
Besides the destruction of O_3, reactive halogens are involved in reactions of mercury (Hg), for which volcanic emissions are one of the important natural sources (e.g. Nriagu and Becker, 2003). Reactive halogens influence the speciation of Hg from gaseous elemental mercury (GEM, Hg^0) into reactive gaseous mercury (RGM, Hg(II)), which is harmful for animals and humans. See e.g. (Aiuppa et al., 2007; von Glasow, 2010) for the case of volcanic emissions.
Since BrO is not directly emitted by the volcano but rather its precursor HBr (Gerlach, 2004), an auto-catalytic reaction cycle similar to the "Bromine–explosion" in polar regions was proposed (Bobrowski et al., 2003; Oppenheimer et al., 2006; Bobrowski et al., 2007). The proposed increase of BrO concentrations with increasing distance to the volcano was validated in Bobrowski et al. (2007), and the photochemical nature of the proposed reaction cycle was proven by Kern et al. (2009).

Besides conclusions about the influence of volcanoes on the atmosphere, measurements of volcanic emissions also allow insights into volcanic processes at depth. The amount of released gases and their relative composition depends on the magma composition and degassing pressure of the respective gas species (e.g. Oppen-

heimer et al., 2003; Aiuppa and Federico, 2004; Aiuppa et al., 2009, and references therein). For example, changes in ratios of emitted halogen species may be used to gain information on the volcanic conduit system and derive whether new magma is ascending (Spilliaert et al., 2006; La Spina et al., 2010).

However, volcanic emissions may not only influence atmospheric processes and endanger life on the ground. A series of life threatening encounters of aircraft with ash-loaded volcanic clouds in the 1980s highlighted the risk of volcanic emissions to aviation. The main threat is posed by volcanic ash (Miller and Casadevall, 2000; ICAO, 2007; Prata and Tupper, 2009, and references therein), which may lead to engine failure via flame-outs when entering high temperature jet engines. The public was reminded of the vulnerability of modern society to volcanic clouds by the eruption of the Icelandic volcano Eyjafallajökull from March till May 2010. The eruption led to an unprecedented closure of European airspace. Fortunately, no lives where lost. However, the economic loss was estimated to reach up to 2.5 € billion for the airline industry alone (Zehner, 2010).
In the context of volcanic aviation hazards, SO_2 detection is used as a supplementary technique, because volcanic ash clouds are usually associated with SO_2 clouds of approximately equal size and location. SO_2 can be identified by its molecular absorption structures, both in the UV and IR spectral regions, the extent of a SO_2 cloud can serve as an indicator for areas affected by volcanic ash.

Remote sensing techniques of volcanic gases are a sensible choice when dealing with volcanoes. To be able to measure gases from the distance has many advantages. Volcanic gases can be determined at a safe distance during eruptions, or at otherwise inaccessible places, e.g., determining the composition of a volcanic plume several kilometres above the observer, or below in the case of satellites. Remote sensing of SO_2 in the ultraviolet (UV) range has been successfully applied since the early 1970's, when correlation spectroscopy was used to determine SO_2 fluxes from volcanoes (COSPEC and later TOMS, see for instance Moffat and Millan, 1971; Krueger, 1983). Today, most retrievals of SO_2 in the ultra violet wavelength range are based on Differential Optical Absorption Spectroscopy (DOAS) technique (e.g. Platt and Stutz, 2008). DOAS allows to monitor a large number of trace gases, including NO, NO_2, O_3, SO_2, BrO, ClO, OClO, HCHO amongst others. For monitoring volcanic emissions, ground based passive DOAS instruments using scattered sun light were first used to determine SO_2 fluxes (Edner et al., 1994; Galle et al., 2002; Edmonds et al., 2003). Since then, the DOAS technique has established itself as a pillar of ground based volcanic flux

SO_2 measurements. For example, in the frame of the "Network for Observation of Volcanic and Atmospheric Change" (NOVAC) project, more than 64 instruments were deployed worldwide at 24 volcanoes (Galle et al., 2010, 2011) by May 2011. However, not only SO_2 can be measured by DOAS but also other species in volcanic plumes. Of great interest are e.g. BrO, ClO and OClO due to their great impact on atmospheric chemistry and the possibility to draw conclusions on volcanic processes at depth as explained above.

Subject of this study are BrO and SO_2 DOAS measurements of volcanic plumes. (I) A novel tool was developed, which was used to obtain optimal retrieval parameters for the DOAS evaluation of both species. However, due to the general nature of the tool, it is applicable to any DOAS measurement. Measurements of BrO and SO_2 are presented, which were recorded at different plume ages. (II) New insights into the bromine chemistry of volcanic plumes are described, which show that our current understanding of the bromine chemistry in volcanic plumes may be quantitatively correct, but that current model studies do not capture all aspects and need to be improved. (III) The feasibility of the DOAS technique was explored to be a central component in an early in-flight warning system of volcanic SO_2 clouds for aviation.
A short introduction is given to the respective parts followed by the general structure of this thesis.

All trace gases detectable by the DOAS technique exhibit a characteristic, wavelength absorption structure. The wavelength dependent interval, in which the retrieval is performed, is one of the most important parameters to be set for a DOAS retrieval. It should include prominent absorption features of the trace gas of interest, in order to obtain optimum sensitivity, whilst excluding strong absorption features of other trace gases and possible instrumental artefacts. However, the proper balance has to be found between sensitivity and possible interferences. A novel tool was developed, which helps to obtain the optimal retrieval wavelength range. These so called retrieval-maps enable the easy visualization of results for a large set of evaluation wavelength ranges and thus offer an intuitive tool to show how certain key parameters influence the result. As application examples, measurement conditions are studied using synthetic spectra, focusing on retrievals of stratospheric BrO and BrO in volcanic plumes studied with passive DOAS measurements using scattered sunlight. Besides those more general examples, a

detailed study is performed using advanced synthetic spectra of volcanic BrO measurements, which are compared to the measurements of volcanic plumes presented in here. Optimal wavelength intervals are obtained for the retrievals of BrO and SO_2.

Based on the results of the data evaluation described above, spectra recorded during three measurement campaigns are evaluated. The first two extensive campaigns were conducted at Mt. Etna, Italy, during July 2008 and July 2009. During the third campaign, measurements were taken close to the crater of the Pacaya volcano, Guatemala on February 5^{th}, 2010. The aim of the extensive measurement campaigns at Mt. Etna was to study the evolution of BrO inside volcanic plumes by simultaneous measurements at different plume ages. So far, published measurements of volcanic BrO are relatively sparse. Published studies for Mt. Etna are Bobrowski et al. (2007); Bobrowski and Platt (2007); Louban et al. (2009), which discuss measurements in September/October 2003, August - October 2004, and May 2005. With the exception of Bobrowski et al. (2007) measurements were not performed simultaneously at different plume ages, which makes data interpretation difficult due to the possibility of changes in atmospheric and volcanic conditions. The focus of the new data sets presented here from Mt. Etna was to obtain simultaneous measurements at a variety of different plume ages. Especially, the first capture of the simultaneously measured evolution of BrO columns at different plume ages greater than 30 min is of great interest, since the evolution of BrO columns is not well known.
At the Pacaya volcano, spectra of volcanic plumes were recorded which capture BrO in a different plume age regime. They were collected not at older plume ages, but rather observed a very young plume (< 5 min plume age). These measurements fill a gap in the current knowledge, since the evolution of BrO columns from the crater rim (Kern et al., 2009) till several minutes plume age have not been captured, yet. The presented measurements in this study constitute the first detection of BrO in the plume of the Pacaya volcano and are the first measurements of the BrO evolution at early plume ages and at a high time resolution.

In the third part, the feasibility of the DOAS technique will be explored to be a central component of an early detection in-flight warning system of SO_2, able to detect volcanic plumes and clouds. Prototype systems were tested at the Popocatépetl volcano, Mexico in April 2010. Its plume was approached with a small aircraft with forward looking DOAS instruments on board. The gathered data is compared to theoretical radiative transfer studies, which allows to draw

conclusions on the response of such a system to different ash contents of volcanic clouds present. A maximum flight altitude of 10 km is studied, which is typical for commercial carriers.

The thesis is structured as follows: First, an introduction to the bromine chemistry of volcanic plumes is given in chap. 2, followed by an outline of DOAS in chap. 3. The application of the technique for volcanic plume measurements is explained in chap. 4, where common instruments and measurement geometries are presented. In chapters 5, 6 and 7, a novel tool to determine optimal DOAS evaluation wavelength intervals is introduced and applied to measured spectra of BrO and SO_2. Measurements of volcanic plumes at Mt. Etna and Pacaya are described in chap. 8, with the respective results given in chap. 9. In the latter, retrieved values are also compared to expected results according to previously published chemical models. The feasibility of DOAS as an in-flight early detection system for SO_2 is discussed in chap. 10. This study concludes with a summary of all results and an outlook.

2 Bromine chemistry of volcanic plumes

Reactive halogens are playing an important part in tropospheric and stratospheric chemistry. That these species are also present in volcanic plumes was, was unknown until the discovery of bromine monoxide (BrO) in the plume of the Soufrière Hills Volcano, Montserrat (Bobrowski et al., 2003). Measured mixing ratios of BrO ranged up to 1 ppb, which constitutes the highest measured concentration of BrO in the atmosphere. BrO is produced in reaction cycle similar to the "Bromine-explosion" in polar regions, which also has been observed over salt lakes (e.g. Barrie et al., 1988; Barrie and Platt, 1997; Hebestreit et al., 1999; Hönninger et al., 2004). Due to the non linear increase of BrO in volcanic plumes with increasing plume age, the same expression has been coined for the BrO production in volcanic plumes. The assumed reaction cycles for halogen reactions in volcanic plumes have been discussed extensively in Bobrowski et al. (e.g. 2003); Gerlach (e.g. 2004); Oppenheimer et al. (e.g. 2006); Bobrowski et al. (e.g. 2007); Roberts et al. (e.g. 2009); von Glasow et al. (e.g. 2009); von Glasow (e.g. 2010). Their efforts shall not be repeated here, thus only an overview is given in the following section. In the second section, model runs published by von Glasow (2010) are reviewed, since they are later used in the comparison with measured data.

2.1 Bromine chemistry in volcanic plumes

The reaction cycle of the bromine explosion in volcanic plumes has been depicted in fig. 2.1. In short, emitted HBr is oxidised in an auto-catalytic reaction cycle by destroying O_3 entrained in the plume from the ambient atmosphere. Gerlach (2004); Martin et al. (2006) showed that bromine is emitted primarily as HBr. The initial amount of other bromine species is highly dependent on the high temperature mixing (T$>$ 800°C) of atmospheric air and hot volcanic volatiles at the source.

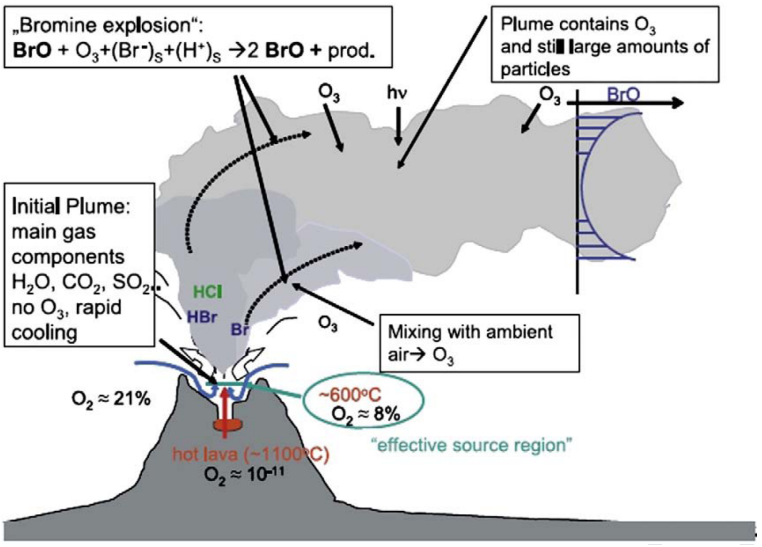

Figure 2.1. Atmospheric chemistry of volcanic plumes, figure from Bobrowski et al. (2007). Emitted halogen halides (mainly HCl, HBr) are oxidised to halogen oxides (BrO_x, ClO_x) by entrained O_3, which is present in the ambient atmosphere. BrO is produced via a fast, auto-catalytic reaction cycle.

For example, von Glasow (2010) calculated mixing ratios for Br of 15 ppm, Br_2 of 200 ppb and BrO of 3 ppb for a mixture of 15% atmospheric air and 85% magmatic gases. This corresponds to an increase in comparison to the pure magmatic gas of $\times 40$, $\times 1.5 \cdot 10^4$ and $\times 1.5 \cdot 10^5$, respectively. HOBr is calculated at 1.5 ppb if ambient air is present at above ratio. One has to be aware, that these high mixing ratios are diluted further by ambient air after the calculations of the high temperature mixture (see sec. 2.2). Also elevated values of OH and HO_2 are expected in the early plume-air mixture, which are key species in many chemical reactions in the atmosphere. BrO and HO_2 react to produce HOBr. HBr and HOBr can be uptaken by aerosols (R2, R3). In the aqueous phase, the Br^-_{aq} will react with $HOBr_{aq}$ to form $Br_{2,aq}$ (R4), which is released back into the gaseous phase.

$$BrO + HO_2 \rightarrow HOBr + O_2 \quad \text{(R1)}$$

$$HBr \rightarrow Br^-_{aq} + H^+_{aq} \quad \text{(R2)}$$

$$HOBr \rightarrow HOBr_{aq} \quad \text{(R3)}$$

$$HOBr_{aq} + Br^-_{aq} + H^+_{aq} \rightarrow Br_{2,aq} + H_2O \quad \text{(R4)}$$

$$Br_{2,aq} \rightarrow Br_2 \quad \text{(R5)}$$

The Br_2 is photolysed by sun light and produces two Br radicals (R6), which react with O_3 to produce BrO (R7). BrO can react with another BrO molecule to either from two Br radicals or a Br_2 molecule, leading back to reaction (R7, R8).

$$Br_2 + h\nu \rightarrow 2Br \quad \text{(R6)}$$

$$2\,(Br + O_3) \rightarrow 2\,(BrO + O_2) \quad \text{(R7)}$$

$$BrO + BrO \rightarrow 2Br + O_2 \quad \text{(R8)}$$

$$BrO + BrO \rightarrow Br_2 + O_2 \quad \text{(R9)}$$

$$BrO + HO_2 \rightarrow HOBr + O_2 \quad \text{(R10)}$$

If BrO reacts with HO_2, HOBr is formed, which can again enter the aqueous phase and lead to the release of two more Br radicals entering the cycle. The netto reaction can thus be described as a BrO production cycle, fuelled by O_3 and particle bromine (HBr_{aq}).

Further reactions involve chlorine, in which BrCl, ClO and OClO may be produced (Bobrowski et al., 2007).

$$HOBr_{aq} + Cl^-_{aq} + H^+_{aq} \rightarrow BrCl + H_2O \quad \text{(R11)}$$

$$BrO + ClO \rightarrow Cl + Br + O_2 \quad \text{(R12)}$$

$$BrO + ClO \rightarrow OClO + Br \quad \text{(R13)}$$

$$BrO + ClO \rightarrow BrCl + O_2 \quad \text{(R14)}$$

OClO and BrCl will be split by photolysis:

$$OClO + h\nu \rightarrow ClO + O \quad \text{(R15)}$$

$$BrCl + h\nu \rightarrow Br + Cl \quad \text{(R16)}$$

There is no ClO explosion, because Cl is ineffectively converted to HOCl, which is needed for a reaction cycle releasing Cl radicals from the aqueous phase (see R4). Furthermore, bromine shows a stronger surface segregation effect in the aqueous phase than chlorine, and is thus more likely to participate in a reaction with HOBr (R4 vs. R11), see also von Glasow and Crutzen (2007). Nevertheless, chlorine is an important species in e.g. methan (CH_4) destruction and thus may impact atmospheric chemistry in "aged" plumes (von Glasow, 2010).

Next to HBr, also Br radicals are emitted according to high temperature models (Gerlach, 2004; Martin et al., 2006). These Br radicals are quickly titrated by the predicted amounts of NO_x (von Glasow, 2010). This would lead to a diminished amount of Br and an enhanced build up of $BrNO_2$ already at the crater rim (plume age = 1 min), see fig. 2.2.

$$NO + O_3 \rightarrow NO_2 + O_2 \quad \text{(R17)}$$

$$Br + NO_2 \rightarrow BrNO_2 \quad \text{(R18)}$$

$$BrNO_2 + h\nu \rightarrow Br + NO_2 \quad \text{(R19)}$$

$$BrO + NO_2 + H_2O \rightarrow HOBr + HNO_3 \quad \text{(R20)}$$

The lifetime of $BrNO_2$ is on the order of 150 s before it is photolysed, making it a short time reservoir of bromine. Nevertheless, since Br radicals are abundant, $BrNO_2$ should be constantly produced and therefore contain a significant fraction of the total bromine (fig. 2.2). In the case of high NO_x concentrations, a possible reactions of BrO with NO_2 (R20) may lead to an increase in BrO production via an additional pathway to produce HOBr (von Glasow and Crutzen, 2007). Besides the destruction of O_3, reactive halogens are involved in reactions of mercury (Hg), for which volcanic emissions are one of the important natural sources (e.g. Nriagu and Becker, 2003). Reactive halogens influence the speciation of Hg from gaseous elemental mercury (GEM, Hg^0) into reactive gaseous mercury (RGM, Hg(II)), which is harmful for animals and humans. For the case of volcanic emissions, see e.g. Aiuppa et al. (2007); von Glasow (2010).

The key reactions of the bromine explosions have been validated by measurements. Next to the increase of the BrO ratio with increasing plume age, diminished O_3 concentrations inside volcanic plumes were measured by Rose et al. (2006); Millard et al. (2006); Vance et al. (2010). Furthermore, O_3 is not present in the initial plume but needs to be entrained with ambient air, it is expected that BrO concentrations are increased at the plume's edges. This has been validated by Bobrowski et al. (2007); Louban et al. (2009). The photochemical nature of the reaction cycle was shown by Long-Path DOAS measurements (Kern et al., 2009).

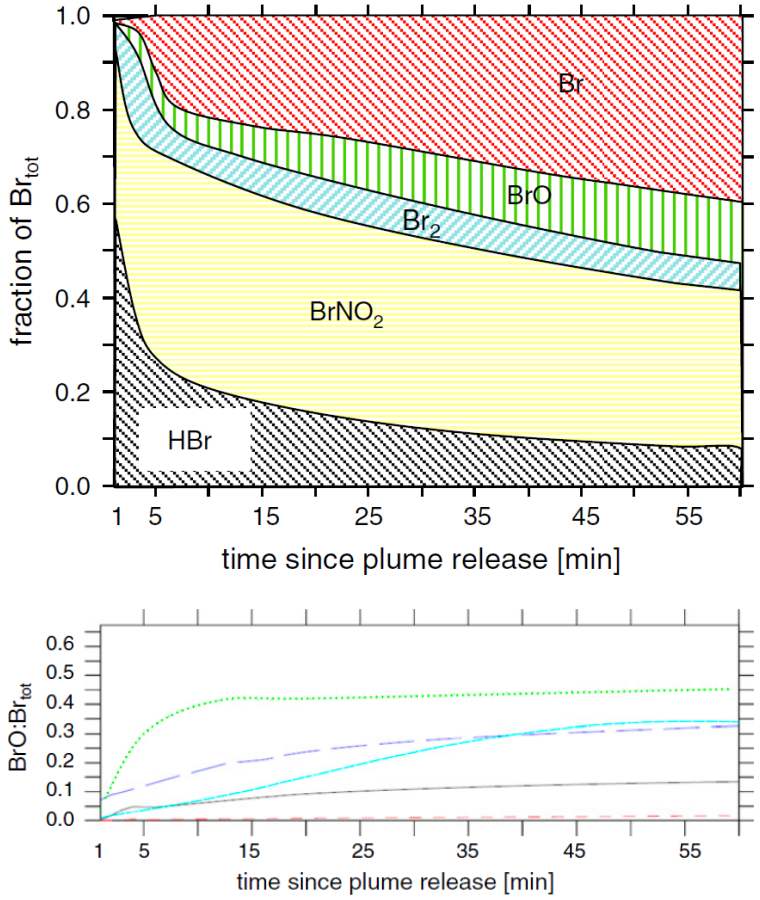

Figure 2.2. Top graph: Participation of bromine species predicted by model runs from von Glasow (2010). In this model run ("Base run" also called model run A in chap. 9), only a small fraction of the total amount of bromine (Br_{total}) is present as BrO. $BrNO_2$ is produced by titration of Br radicals with NO_2 and acts as a short-term reservoir species. Bottom graph: BrO/Br_{total} ratios for different model runs presented in von Glasow (2010). The black line corresponds to the base run shown in the top graph. The dotted green line shows results for model runs initialized with a $\times 10$ stronger plume dilution by ambient air than the base run, light blue corresponds to no dilution ("pure volcanic volatile"). Both graphs are adapted from (von Glasow, 2010).

Observing changes in BrO via the BrO/SO_2 ratio

Gaseous SO_2 is oxidised in the atmosphere mainly by OH forming H_2SO_4, this process is occurring at a time-scale of about two weeks in the gas phase (e.g. von Glasow and Crutzen, 2007). H_2SO_4 is subsequently deposited on cloud particles or aerosols, and may itself act as a cloud condensation nuclei. If SO_2 is deposited to particles or droplets, its lifetime is strongly reduced to days or even less (von Glasow, 2010).
However, it is relatively inert compared to BrO and is used as a tracer to capture ongoing BrO chemistry. By taking the BrO/SO_2 as a measure for the evolution of BrO in volcanic plumes, aspects cancel like plume dilution by ambient air, plume dispersion and varying emission strengths of the volcano.
Figure 2.3 depicts model runs published by von Glasow (2010). Vertical slant columns (VCD) are plotted versus plume age for BrO and SO_2. The bottom graph shows the derived BrO/SO_2 ratio. Although the SO_2 VCDs and BrO VCDs are diminishing due to dilution by ambient air and plume dispersion, an increase in the BrO/SO_2 is observed corresponding to production of BrO in the volcanic plume.

2.2 Previously published model runs

Three different model runs are present in (von Glasow, 2010), as depicted in fig. 2.3. The model uses an updated version of the one in Bobrowski et al. (2007), where the one dimensional atmospheric model MISTRA (von Glasow et al., 2002) was used to calculate the chemistry in volcanic plumes after leaving the vent. The composition of the volcanic gases at the vent was calculated in both cases with the software HSC, Outokumpu Tech., Finland. The region in the vent, where volcanic volatiles may be diluted with ambient air but are still at very high temperatures (>600°C) is called the “effective source region”. The gas composition of the effective source region is important for the further development of the plume chemistry, which can be seen in fig. 2.3. Three different model runs have been modelled for conditions at Mt. Etna in terms of emitted gas composition and meteorological conditions in von Glasow (2010). The model runs are described briefly in the following, since they are later compared to measurements from Mt. Etna (Italy) and from the Pacaya volcano (Guatemala), which are presented in chap. 8 and 9. For an in depth

discussion on initialisation, the reader is referred to the publications of Bobrowski et al. (2007); von Glasow (2010).

Model run A: This is the base run, which uses a mixture of 85% volcanic volcatiles and 15% ambient air for the effective source region. The gas mixture released from the effective source region is diluted with ambient air by a factor of $\times 10$, based on measured SO_2 mixing ratios at the crater rim. The model runs is denoted by a black line in fig. 2.2 and 2.3.

Model run B: Here, the volcanic volatiles are not diluted in the effective source region. The model run is consequently named "pure volcanic volatiles". Model run B is drawn in light blue in fig. 2.2 and as a dashed green line in fig. 2.3.

Model run C: This run is the same as model run A, except that it neglects aerosol chemistry, and thus key reactions in the auto-catalytic bromine cycle (R2-R5). The corresponding evolution of BrO is marked as red, dashed line in both figures (2.2, 2.3).

The different model runs show distinct features. Model run A yields a strong increase of the BrO/SO_2 ratio in the first minutes after release, followed by a slower increase due to the ongoing bromine explosion. Model run B (pure volcanic volcatiles) misses the strong, initial increase in ratio in the first 5 min.. However, after a delayed start of the bromine explosion, ratios of model run A and B reach a comparable level after 40 min. In case aerosol chemistry is neglected (model run C), BrO is only produced at a small amount during the first 15 min., afterwards the BrO/SO_2 ratios is constant. This last model run highlights the necessity of heterogeneous chemistry for the bromine explosion.
The main difference between model run A and B, the strong initial increase, points out the importance of entrained ambient air in the effective source region to fit the measurements, as will be shown in chap. 9. The effective source region leads to a greater partitioning of bromine species into compounds other than HBr. The fractions of Br_2, Br, BrO and BrCl are orders of magnitudes higher in model run A than in model run B at start of the atmospheric model (after modelling the effective source region). Furthermore, NO_x concentrations are increased, which in combination may "kick-start" the bromine explosion.

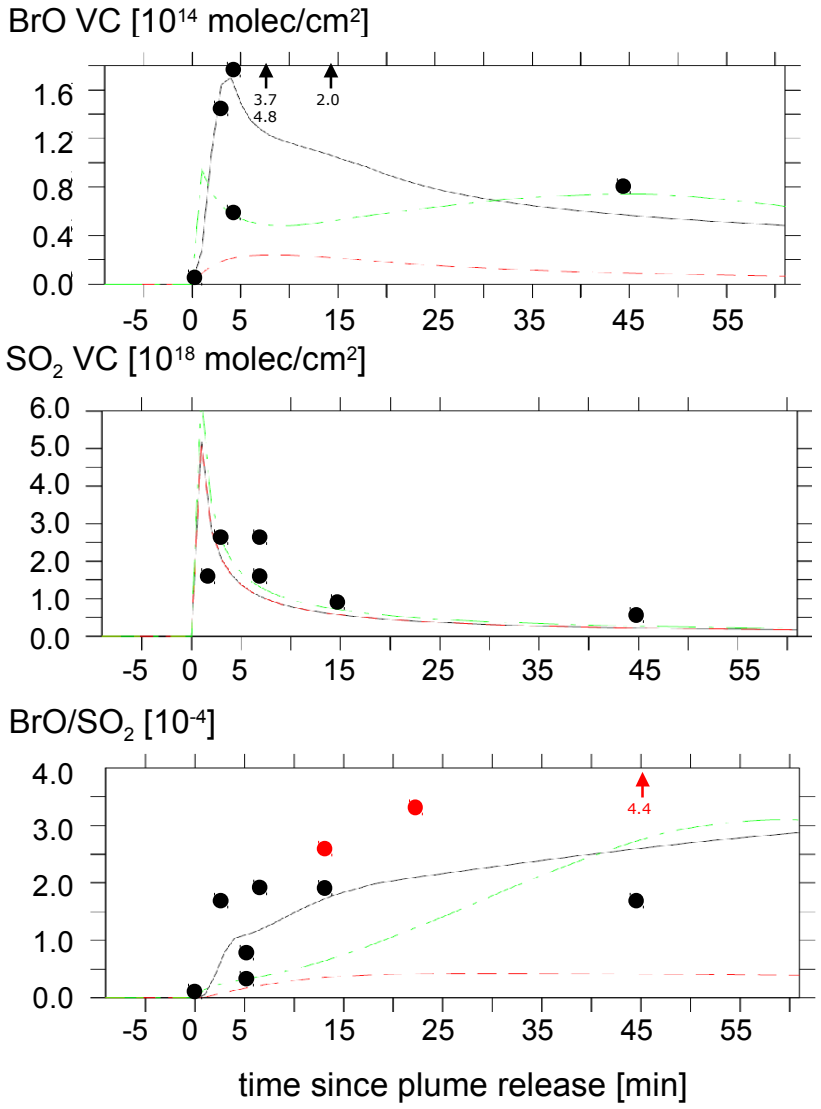

Figure 2.3. Model Runs as published in von Glasow (2010). The top graph depicts BrO vertical columns, in the middle vertical SO_2 columns are plotted and the bottom graphs shows their ratio. The solid black line denotes a model run where ambient air is entrained at the ratio 15:85 into the volcanic plume at the beginning (base run "Etna85:15", model run A); the dashed green line indicates a model run where no dilution with ambient air is present at the start ("pure volcanic volcatiles", model run B); a model run without aerosol chemistry is drawn in a red dashed line (model run C). The dots show previous measurements by Bobrowski et al. (2007) at Mt.Etna, von Glasow (2010) assumed a wind speed of 7 m/s. The red dots indicate simultaneously performed measurements. Figure from (von Glasow, 2010)

3 Differential Optical Absorption Spectroscopy (DOAS)

In this chapter, an introduction to Differential optical-absorption spectroscopy (DOAS, Platt and Stutz, 2008) is given. For a comprehensive overview over different DOAS systems and their technique see Platt and Stutz (2008).
DOAS is an established technique to quantify the concentration and distribution of a large number of atmospheric gases in the ultraviolet (UV), visible (VIS) and near-infrared (NIR) wavelength ranges. The technique is based on the Lambert-Beer-Law (also Bouguer-Lambert-Law), which states that the intensity of electromagnetic radiation with an initial intensity I_0 will decrease exponentially depending on the amount of absorber present and their respective absorption cross section.

$$I(\lambda) = I_0(\lambda) \cdot e^{-\int_L \sigma(\lambda) \cdot c(l)\ dl} \tag{1}$$

Here, λ denotes the wavelength, $\sigma(\lambda)$ the absorption cross section of an absorber, integrated along a light path L and concentration $c(l)$ at point l. Next to absorption process, also Rayleigh and Mie scattering occur in the atmosphere which can be described by there extinction coefficients ϵ_R and ϵ_M, respectively. The total extinction processes in the atmosphere can thus be described by

$$I(\lambda, L) = I_0(\lambda) \times exp\left(\int_0^L \sum_i (\sigma_i(p, T, \lambda, l) c_i(l)) - \epsilon_R(\lambda, l) - \epsilon_M(\lambda, l) dl\right) \tag{2}$$

with absorption cross sections also depending on pressure p and temperature T. In the following, the pressure and temperature dependencies will be ignored.

The idea behind DOAS is to split the absorption cross section $\sigma(\lambda)$ in its broad band and narrow band parts (absorption structures widths typically smaller than a few nm), also called the differential absorption. Thus it is possible to determine the amount of trace gases with sufficiently strong differential absorption features by splitting the total absorption into broad band extinction and narrow band absorption. A suitable filter, e.g. a polynomial can be applied to describe the

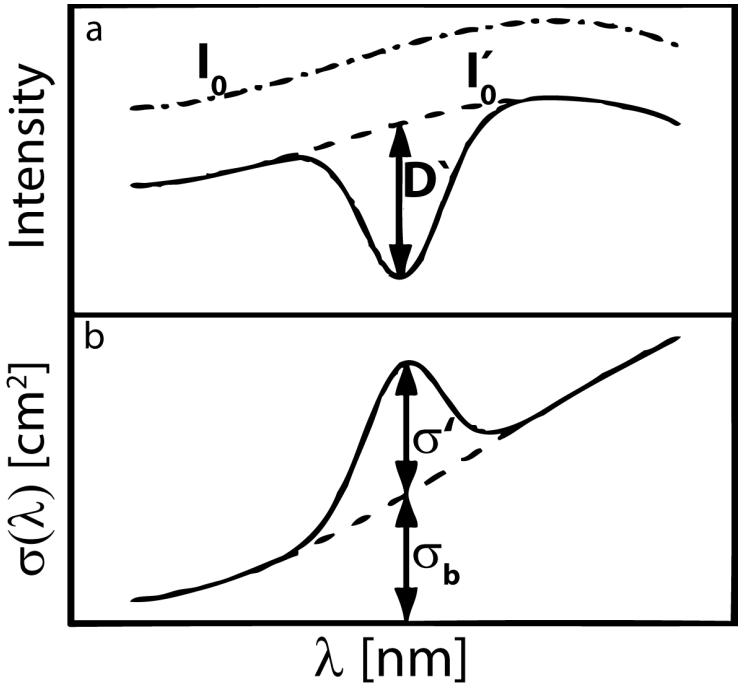

Figure 3.1. The idea behind DOAS is to split the intensity I_0 and absorption σ into broad band absorptions (σ_b and I_0') and narrow band absorptions (σ' and D') by a suitable filter, e.g. a polynomial. Figure adapted from Platt and Stutz (2008)

combined broad absorption structures together with Rayleigh and Mie extinction and broad band instrumental features, whereas the amount of trace gases of interest are derived from their narrow band absorption structures. DOAS measurements yield column densities (SCDs) S, which are the integrated concentration along the lightpath, $S = \int_L c(l)dl$. If the light path is known, mean concentrations can be calculated as $\bar{c} = S/L$. Eq. (2) can then be rewritten to

$$I(\lambda) = I_0(\lambda) \times exp\left(\sum_i (\sigma_i(\lambda)S_i) - P(\lambda)\right) \tag{3}$$

$$ln\left(\frac{I(\lambda)}{I_0(\lambda)}\right) = \sum_i (\sigma_i(\lambda)S_i) - P(\lambda) \tag{4}$$

where $P(\lambda)$ denotes the polynomial describing the combined broad band absorption processes and $ln\,(I(\lambda)/I_0(\lambda))$ is the optical density.
Because many trace gases have differential absorption structures typically due to vibrational transitions, a manifold of different trace gases can be determined by the same measurement.

3.1 Active and passive DOAS systems

Usually, DOAS systems can be classified into active and passive DOAS systems, which apply artificial light sources or natural ones (scattered sun light, direct sun, moon or star light), respectively.
Active DOAS instruments allow to compare spectra of light at the source with a beam that passes a certain distance through a volume of air containing the absorbing gas before being recorded due to their artificial light source. Instrumental designs including Cavity-Enhanced DOAS (CE-DOAS) or long-path instruments (LP-DOAS) are limited to measurements near the ground due to the necessity of stable deployment of light source, receiver as well additional reflectors (e.g. Merten et al., 2011, and references therein). Advantages of those measurements are that (1) the light path is known, which allows the direct calculation of mean concentrations along the light path from the measured SCDs, (2) the initial intensity $I_0(\lambda)$ can usually be easily determined, (3) the measured wavelength interval can be chosen with the respective artificial light source. This allows measurements e.g. below 300nm, where the low intensity of scattered sun light prohibits ground based, passive measurements due to the strong absorptions of atmospheric O_3. Applications range from measurements of urban pollution, marine and polar boundary layers till gases of volcanic plumes.
Passive instruments use scattered sun light or direct sun, moon or star light as a light source. This allows for the construction of versatile instruments which are compact and of low power consumption without necessities for an additional emitter and/or ray deflectors like mirrors or reflectors. Thus they are much less restricted in viewing directions and allow the probing of different atmospheric layers from the same location. Applications include satellite measurements, Multi-AXis DOAS (MAX-DOAS) from different platforms (ground based, aircraft, balloon and ships), car traverses, and measurements of volcanic plumes.
Because scattered sunlight is used instead of an artificial light source, recorded spectra are highly structured and contain strong Fraunhofer lines, in contrast to active light sources with usually more smooth broad band emissions (see sec. 3.5, I_0 effect). Also, radiative transfer studies are necessary to determine the light path and subsequently be able to calculate trace gas concentrations.
A passive technique with defined light path is Topographic Target Light scattering-Differential Optical Absorption Spectroscopy (ToTaL-DOAS), which uses scattered sunlight from artificial surfaces (e.g. walls) to determine SCDs between target and instrument (Frins et al., 2006).

Due to the differences in absorption structure, it is possible to retrieve different gases in the same measurement and spectral region. The intensities recorded usually have overlaying absorption structures of several trace gases, which need to be carefully separated in order to determine the SCD of the trace gas of interest. Because trace gas absorption spectra used in the retrieval process, also named reference cross sections (RCS), are usually recorded at much higher spectral resolution than common DOAS instruments, these laboratory absorption references are convoluted with the instrumental slit function (ISF) to calculate the absorption structures at instrumental resolution (sec. 3.4).

3.2 Ring-Effect

In order to completely remove the influence of Fraunhofer lines, the so called Ring-effect must be removed. It was first observed by Sefnov (1959) as well as Grainger and Ring (1962), and describes the "filling in" of Fraunhofer lines and can also result in the filling in of absorption structures. Today it is most commonly agreed that the effect is caused by inelastic rotational Raman scattering (e.g. Solomon et al., 1987; Chance and Spurr, 1997; Vountas et al., 1998; de Beek et al., 2001; Wagner et al., 2009a, and references therein). Since the Ring-effect can be on the order of several % optical density at typical measurement conditions of passive DOAS instruments, a correction scheme for this effect is mandatory to determine the SCDs of measured trace gases. Solomon et al. (1987) showed that one approach to correct the Ring effect is to treat it as an additional absorber by including a so called Ring-spectrum in the fitting process. Although this approach is not strictly correct, it yields sufficient results in most cases. The Ring spectrum at hand is commonly calculated by today's evaluation software packages by convolving the measured FRS with a calculated Raman scattering cross section.

3.3 Reference cross sections

Commonly, a certain set of RCSs and other properties like the DOAS polynomial and wavelength range is called a fit scenario, which is used to describe the measured spectrum in terms of the spectrum without absorptions. Fig. 3.2 depicts absorption structures of several trace gases which are detectable with DOAS. The choice

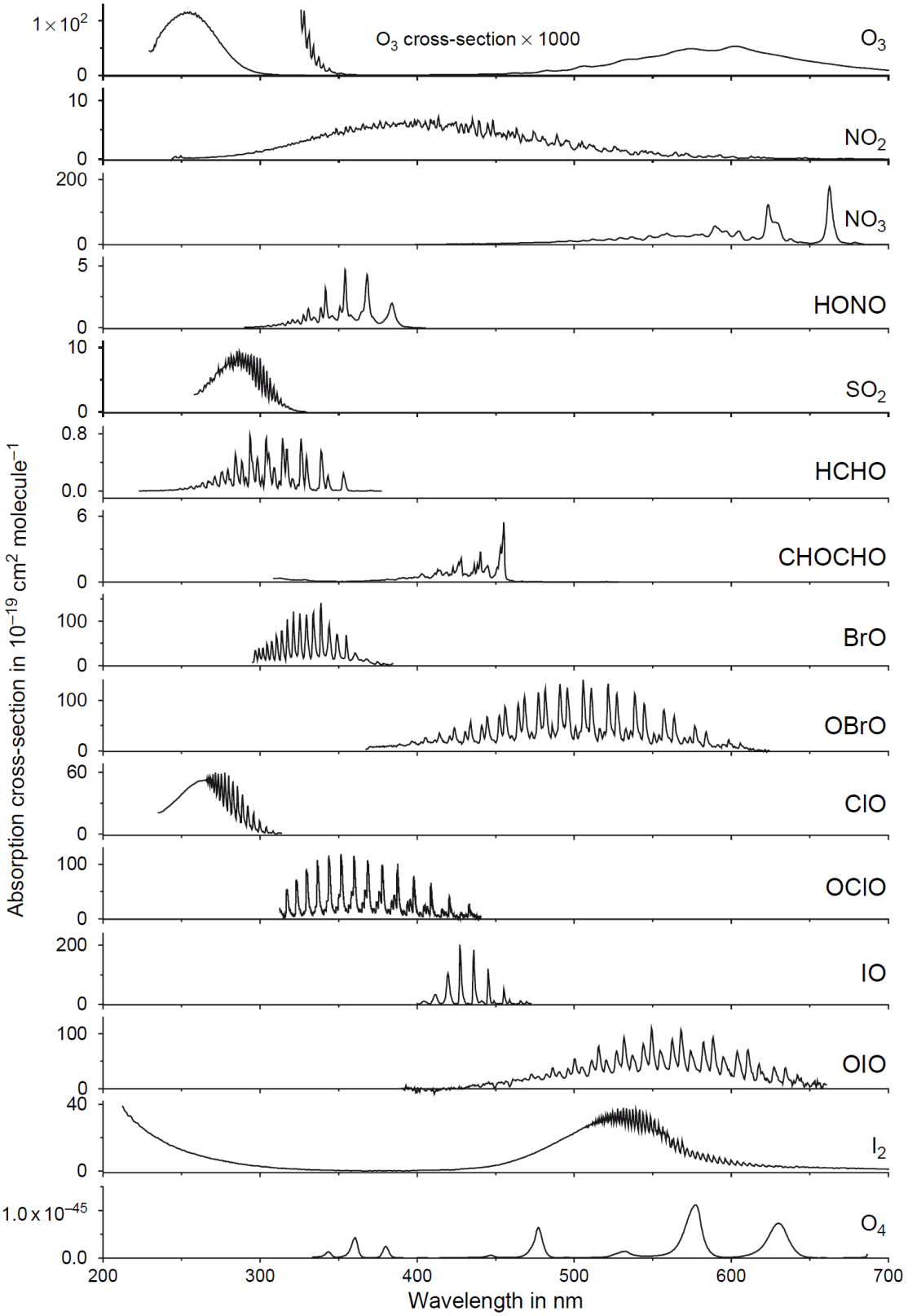

Figure 3.2. Absorption cross sections of several trace gases which are detectable with DOAS. Of special interest for evaluation of BrO and SO_2 are NO_2, O_3, O_4 and HCHO. Figure adapted from Platt and Stutz (2008).

of RCSs is limited by the actual conditions of the measurement (temperature, pressure) and wavelength range of the instrument. Often several cross sections were published for the same trace gas, indications which one to use can be found e.g. in (Sander et al., 2011).

If the absorptions of the target trace gas are much weaker than other absorbers in the respective wavelength range, these other absorbers may conceal the target trace gas and their absorption structures need to be determined most accurately. Small errors in absorption cross sections might lead to a small errors in determination of the strong absorber, but can heavily influence the retrieval of other much weaker absorbers. If not all cross sections are known precisely, it is not possible to uncover the weaker absorptions structures. Errors in used reference cross sections (RCSs) will lead to additional structures which in turn could be erroneously interpreted as absorptions. Another source of error are possible cross correlations between absorption cross sections. Although the differences in differential absorption structure of a set of RCSs should allow an exact solution of eq. (4) in principle, noise and systematic structures may induce cross correlations between absorption cross sections. These cross correlations must be studied and the retrieval optimized accordingly, because they may lead to systematic offsets of retrieved trace gas concentrations.

3.4 Instrumental slit function

Most DOAS instruments apply a spectrograph where a grating is used to disperse the spectral range of interest on typically 500 - 3600 pixels. Optical resolution depends on e.g. width of the instrumental slit and number of grates per mm of the grating. These instrumental features are described by the instrumental slit function W. The recorded intensity I'$_i$ at pixel i is given by convoluting the incident radiation I(λ) with the instrumental slit function W. The intensity I(λ) is recorded at discrete intervals, given by the spectral interval of width Δ_i recorded by each pixel i, centered around λ'_i.

$$I'(\lambda') = \int_{\lambda} I(\lambda - \lambda') \cdot W(\lambda - \lambda') d\lambda \tag{5}$$

$$I'_i = \int_{\lambda'_i - \Delta/2}^{\lambda'_i + \Delta/2} I'(\lambda') d\lambda' \tag{6}$$

Commonly, RCSs are used during an evaluation of measured spectra, which have

not been recorded with the instrument that performed the measurement. Instead, published RCSs are used which have been recorded in a laboratory at high resolution, and consequently need to be convoluted with the ISF to obtain RCSs at the resolution of the instrument. Thus the spectra with and without absorptions recorded by the instrument can be described by

$$\begin{aligned} I_0'(\lambda) =& (I_0 * W)(\lambda) \\ =& \int I_0(\lambda') W(\lambda - \lambda') d\lambda' \end{aligned} \tag{7}$$

$$\begin{aligned} I'(\lambda) =& (I * W)(\lambda) \\ =& \int I(\lambda') W(\lambda - \lambda') d\lambda' \\ =& \int I_0(\lambda') exp\left(-\sum_i \sigma_i(\lambda') \cdot S_i\right) W(\lambda - \lambda') d\lambda' \end{aligned} \tag{8}$$

3.5 I_0 effect

High resolution absorption cross sections are measured with artificial light sources, the spectra of which are in general smooth and unstructured. The Fraunhofer spectrum on the other hand is highly structured. In the case of passive measurements, this introduces errors when a high resolution RCS σ_i is convoluted with the instrumental slit function to calculate RCS at the instrument's resolution (I_0-effect, see e.g. Platt and Stutz, 2008).

As described by eq. (7) and (8), spectra with (I) and without (I_0) absorption structures are recorded by the instrument and consequently are convolved with the instrumental slit function. Since the convolution operation is not associative with the operations in Lambert-Beers-Law, the ratio I/I_0 does not exactly yield $exp\left(-\sum_i \sigma_i(\lambda) \cdot S_i\right)$:

$$\begin{aligned} \frac{I'(\lambda)}{I_0'(\lambda)} =& \frac{I(\lambda) * W}{I_0(\lambda) * W} \\ =& \frac{\left[I_0(\lambda) \cdot exp\left(-\sum_i \sigma_i(\lambda) \cdot S_i\right)\right] * W}{I_0(\lambda) * W} \\ \neq& exp\left(-\sum_i \sigma_i(\lambda) \cdot S_i\right) \cdot \frac{I_0(\lambda) * W}{I_0(\lambda) * W} \end{aligned}$$

In consequence, the SCDs trace gases have to be known in advance to calculate correct absorption cross sections. This dilemma can be solved by either assuming a certain column, or more accurately by using iterative approaches.

uncorrected RCS: In this work , RCSs will be denotes as uncorrected RCSs if they are not corrected for the above described I_0 effect. They are constructed by convolving laboratory RCSs with the instrumental slit function W to the instrumental resolution.

$$\sigma_i'(\lambda) = (\sigma_i * W)(\lambda) \tag{9}$$

Errors in uncorrected RCSs used in the fit may be small for the individual cross section. However, usually several gases are absorbing in the same wavelength range. If the optical density of the the trace gas of interest is much smaller than other absorptions present, small errors in the RCSs of the stronger absorbers can lead to highly erroneous results in the retrieval of the trace gas of interest.

First order corrected RCS are corrected for the I_0 effect by only taking into account the respective absorber. Corresponding to (Platt et al., 1997; Aliwell et al., 2002; Wagner et al., 2002a), I_0-corrected cross-sections can be estimated by

$$\sigma_i'(\lambda) = -\frac{1}{S_i} \ln \left(\frac{([I_{K,0} \exp(-\sigma_i S_i)] * W)(\lambda)}{(I_{K,0} * W)(\lambda)} \right) \tag{10}$$

$I_{K,0}$ denotes a high resolution solar spectrum (e.g. Kurucz, 2005; Chance and Kurucz, 2010), which does not exhibit any absorption structures of the earth's atmosphere. RCSs calculated in this way will be denoted as I_0 corrected in this work.

Second order I_0 correction: However, using a solar atlas for correcting the I_0 effect neglects that many absorbers are present at partly very high optical densities (e.g. O_3). Thus for a true correction of the I_0 effect, all absorbers in the respective wavelength range need to be considered. This can only be achieved if a spectrum $I_{K',0}$ is used in eq. 10, which consists of $I_{K,0}$ modified by all other absorptions present except the one to be corrected.
Although this can easily achieved for synthetic spectra with known SCDs of absorbers, it would require a very high amount of computational power in retrievals applied to measured spectra, which is not feasible for common DOAS retrievals.

3.6 Fitting algorithm

Most modern DOAS retrieval algorithms apply a combination of a non-linear Levenberg-Marquardt fit and a linear least squares fit, which is also incorporated in the evaluation software Doasis (Doasis, 2010; Kraus, 2006; Lehmann, 2011) used in this study. In the algorithm, the linear least squares fit determines the different slant column densities (SCDs) of absorbers and the nonlinear Levenberg-Marquardt algorithm correcting possible shifts in wavelength - pixel alignment of measured spectra. Details on the procedure can be found in e.g. Platt and Stutz (2008); Press et al. (1986). The algorithms find the best solution in the framework of the supplied spectra, RCSs and parameters supplied like polynomial order of broad band correction and evaluation wavelength interval. However, the user must take special care judging the error calculation of the parameters. Sources of errors can be attributed to photon shot noise, which can be regarded as the lower limit of possible errors, instrumental noise (electronic noise introduced by the different components, detector non-linearities and variations in pixel sensitivity) as well as retrieval specific errors. The later describes all errors introduced during the retrieval, e.g. temperature and pressure dependence of included RCSs, none or incomplete correction of the I_0 effect, errors in wavelength calibration of the spectrograph, missing RCSs and/or the Ring effect.

3.7 Error calculation

It is important to note that above described evaluation algorithms usually use an uncorrelated least squares fit. This assumes that the intensities detected by the different pixels of the detector are independent and that the residual left after the fitting process is random. This neglects systematic structures present from unknown or in the retrieval neglected absorbers, systematic errors by faulty RCS and correlations between the different pixels of the detector. In an extensive study, Stutz and Platt (1996) (see also Platt and Stutz (2008)) presented implementation and error analysis for such cases. They found that the calculated fitting error underestimates the true standard deviation of the measurements by up to 600%, depending on the width τ of residual structures left and the spectral width V of structures of the trace gas of interest. In order to determine the measurement error corresponding to the true standard devia-

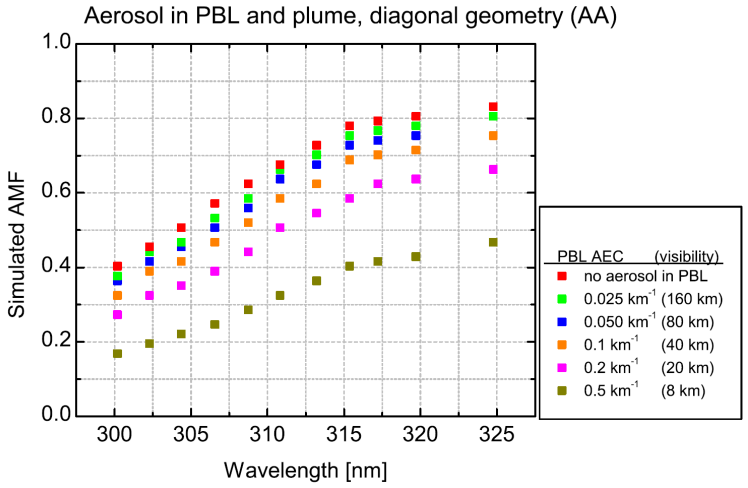

Figure 3.3. Figure from Kern et al. (2010a), showing air mass factors for measured SO_2 SCDs for different aerosol extinction coefficients (AECs) in the ambient air. The plume is located at 1 km - 1.5 km above the instrument in 3 km lateral distance. It is simulated with an AEC of 8 km^{-1}. The airmass factor increases from 305 nm to 315 nm by a factor ≈ 2, showing only minor a dependency on AEC in the planetary boundary layer.

tion of the retrieved SCDs, a correction factor $C(\tau, V)$ is multiplied to the fit error.

3.8 Radiative transfer effects when measuring volcanic plumes

Radiative transfer effects are one of the major source of error in determining correct SO_2 columns of a volcanic plume (Kern et al., 2010a). Next to multiple scattering enhancing the lighpath inside the plume and thus increasing the measured SO_2 SCD, also light dilution may decrease measured SO_2 SCDs, where light scattered into the field of view of the instrument between plume an and instrument reduces the absorption signal.

A common measurement geometry consists of a scanning instrument located not directly under the plume but in some lateral distance. This set-up is the most frequent in the measurements presented in this work (chap. 4). The plume is between 1km and 3km above the instrument, and centred up till 15km away (lateral distance). The instrument is located in the planetary boundary layer, and aerosols in the ambient air decrease the measured absorption signals depending on aerosol extinction coefficient (AEC) and wavelength. In Kern et al. (2010a) a similar case

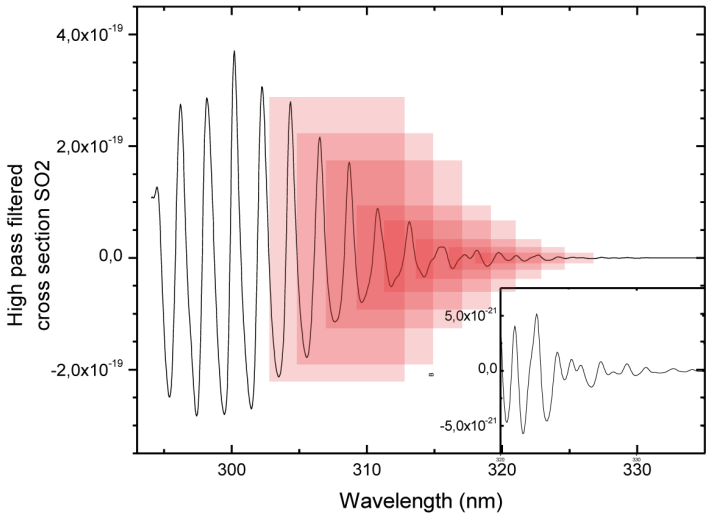

Figure 3.4. Differential absorption cross section of SO_2. The inlayed graph depicts the cross section magnified by a factor of 100. Red squares indicate different retrieval wavelength ranges. Although more sensitive to SO_2, ranges at smaller wavelengths are also more affected by radiative transfer effects.

has been studied with radiative transfer algorithms for the case of a SO_2 retrieval. The results are depicted in fig. 3.3. In the study, a plume was simulated which is located between 1-3 km above the instrument with the plume centre at a lateral distance of 3 km. A straight column density of 1,000 ppmm is assumed, corresponding to $\approx 2.5 \times 10^{18}$ molec/cm^2, and the plume contained scattering aerosol described by a single scattering albedo=1, Greenstein-Henyey coefficient g=0.8 and AEC of 8km^{-1}. A strong dependency of retrieved SO_2 SCDs on wavelengths is observed. For a certain wavelength, differing amounts of scattering aerosols in the ambient atmosphere can lead to differences by a factor of 2 in retrieved SO_2 SCDs due to light dilution (comparing 305 nm to 320 nm).

Radiative transfer effects in common SO_2 retrieval wavelength ranges

In order to retrieve correct SO_2, time consuming radiative transfer algorithms are necessary. An alternative approach has been laid out in (Kern, 2009), named weak absorption technique. It is based on shifting the retrieval wavelength interval to longer wavelengths until SO_2 is evaluated at optical densities $< 5\%$. However, this approach is only yields a good estimation if the distance between plume and instrument is shorter than 2 km, and as long as plume and ambient atmosphere have low aerosol content. Errors increase further if the distance between plume and instrument increases. Nevertheless, evaluating SO_2 at longest possible wavelengths

will yield the best approximation without applying radiative transfer algorithms if mutliple scattering inside the plume is low (low aerosol contents of the plume).

Radiative transfer effects in common BrO retrieval wavelength ranges

Common retrieval wavelength ranges of BrO can be found at longer wavelength ranges, since its strongest absorption band is centred around 338 nm (see chap. 5 and 6). Retrievals of BrO SCDs are not as prone to errors induced by radiative transfer effects as retrievals of SO_2, since optical densities encountered for BrO are typically more than one magnitude below optical densities of SO_2 at their respective retrieval wavelength range. Rayleigh scattering ($\propto \lambda^{-4}$) and to lesser extent Mie scattering ($\propto \lambda^{-1.3}$) also diminish with increasing wavelength, which further decreases the influence of multiple scattering inside the volcanic plume and light dilution between plume and instrument. Nevertheless, these effects are present and have to be taken into account.

Influence of radiative transfer on the retrieved BrO/SO_2 ratio

BrO/SO_2 ratios are commonly used to describe the evolution of BrO in volcanic plumes (see sec. 2.1). Besides eliminating changes absolute SCDs due to plume dilution and dispersion as well variations in emission strengths, radiative transfer effects will cancel in the ratio up to a certain amount. BrO and SO_2 are evaluated in different wavelength intervals as determined in the in chap. 6 and chap. 7. The strongest differential absorption band of SO_2 is located at ≈ 316 nm for BrO it is centred around 338 nm in their respective retrieval ranges. An upper bound for the induced error can be approximated under certain assumptions. (1) Multiple scattering inside the volcanic plume can be neglected. In consequence, this is only applicable to plume of low aerosol content. (2) The ambient atmosphere can be approximated by a purely Rayleigh scattering atmosphere. (3) Differences in retrieved SCDs can be approximated by the wavelengths 316 nm (SO_2) and 338 nm (BrO). (4) Distance between plume and instrument is below the mean optical pathlength of photons at both wavelengths. Since the Rayleigh scattering coefficient is $\propto \lambda^{-4}$, the relative difference of the Rayleigh scattering coefficient for 316 nm and 338 nm is

$$\left(\frac{338}{316}\right)^{-4} = 0.76 \quad . \tag{11}$$

Consequently, measured BrO/SO_2 ratios may be overestimated by 25%, since light dilution will lead to a stronger diminishing of measured SO_2 SCDs than for BrO SCDs. However, with an increasing amount of aerosols in the ambient atmosphere, the relative difference between retrieved SCDs and their true value will diminish for both absorbers together with the error induced in the ratio. Thus the calculated value can only be regarded as an upper bound.

4 Passive DOAS measurements of volcanic plumes

Three different types of measurements were performed during both campaigns. (1) Plume composition measurement are measurements where a stationary MaxDOAS instruments records a spectrum of the volcanic plume and a fraunhofer reference spectrum in turns. (2) During flux measurements of a stationary MaxDOAS instrument, the sky and the volcanic plume are scanned at varying elevation angles. A derive a plume cross section of SO_2 SCDs is derived in this way. Together with wind speed and wind direction, the SO_2 flux of the volcano can be determined. (3) Plume cross sections can also be determined by traverses. In this case, a zenith looking telescope is mounted on a car (or any moving platform) and measurements are performed while traversing under the plume. The obtained plume cross section is commonly used to calculate the SO_2 fluxes with a given wind direction and speed.
In the following, the different measurement configurations are described briefly together with the configuration of their specific evaluations of SO_2 and BrO.

4.1 Plume composition measurement with stationary MaxDOAS instruments

Plume composition measurements are used to determine trace gases other than SO_2 in volcanic plumes. Spectra are recorded longer measurement times increase the signal to noise ratio. Common measurement routines consists, e.g., of alternating measurements of plume spectra and FRS or a set of plume spectra (<10) at different elevation angles together with a FRS (see e.g. Bobrowski and Platt, 2007; Kern, 2009). Since only a small number of plume spectra are taken, recorded FRS and plume measurement are usually less than 20 min. apart and the influence of stratospheric absorbers due to changing solar zenith angle (SZA) is negligible.

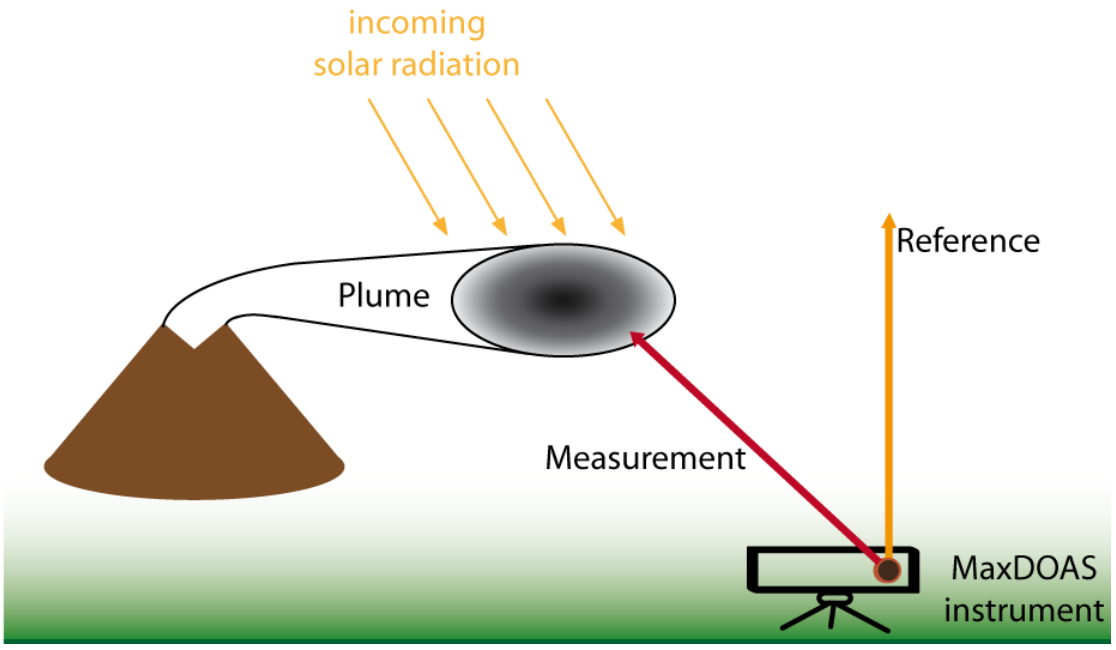

Figure 4.1. Plume composition measurements: Alternating measurements of plume and FRS are performed at longer measurement times to increase the signal to noise ratio.

Fig. 4.1 depicts the set-up schematically. The great advantage of this measurement mode is that no compromises in signal to noise have to be made as e.g. for SO_2 flux measurements. Thus the SO_2 and BrO retrieval is relatively simple. The measurement times are usually set so that the measured plume spectrum can be evaluated against the FRS without further modifications like summing up measured spectra and FRS to increase the signal to noise ratio.

4.2 Flux measurements with stationary MaxDOAS instruments

SO_2 flux measurements with stationary MaxDOAS instruments have become a routinely applied measurement technique in monitoring volcanic emissions (e.g. Galle et al., 2002; Edmonds et al., 2003; Galle et al., 2010). A plume cross section of SO_2 SCDs is determined by scanning the volcanic plume at various elevation angles and a fixed azimuth angle ("flat scan") (Edmonds et al., 2003). Another possibility is to scan along a cone encompassing the volcano (Galle, 2007; Galle et al., 2010). Together with wind speed and direction, the SO_2 emission strength is calculated. Since the aim of this measurements is an accurate assessment of SO_2 fluxes and not

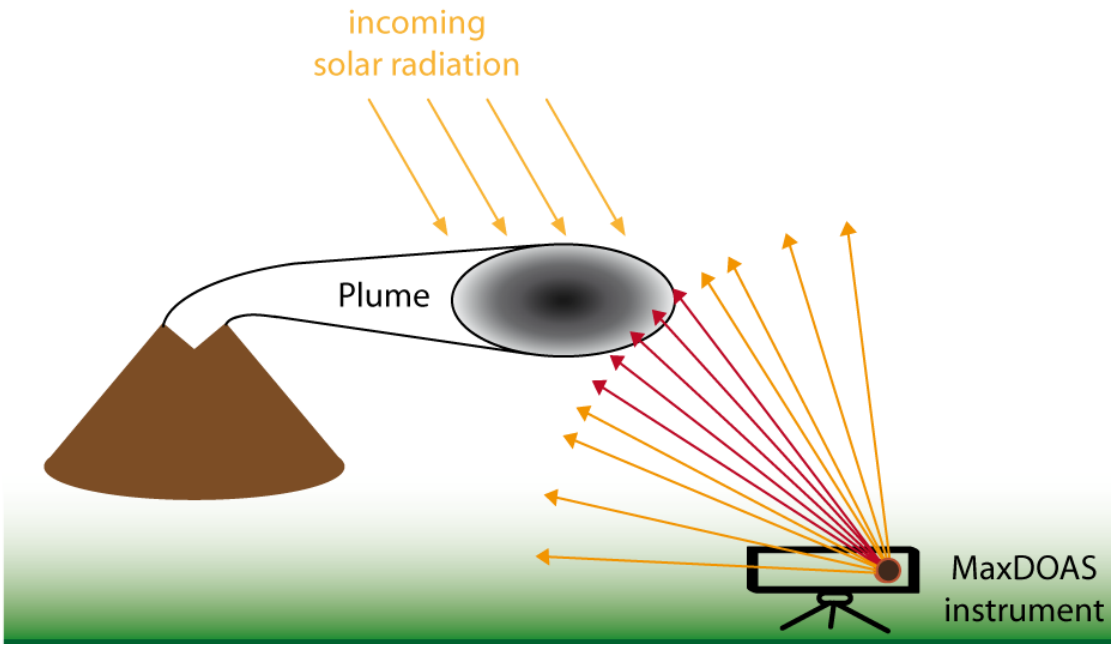

Figure 4.2. Depicted is a typical measurement set-up for measuring SO_2 fluxes with a MaxDOAS scanning instrument. The plume is scanned at varying elevation angles and short measurement times at respective elevation angle to obtain a SO_2 plume cross sections at time resolutions < 20 min. Pointing directions of the telescope are marked in red if the plume is measured. To achieve a sufficient signal to noise ratio for a BrO retrieval, spectra measuring the plume and spectra measuring clear sky have to be added to a plume spectrum and FRS, respectively.

primarily measurements of other trace gases, the measurement set-up is optimized accordingly. A SO_2 cross section of the plume is obtained by using a multitude of different elevation angles at short measurement times in order to capture short time fluctuations of the SO_2 emission strength (<20 min.). Scanning instruments used during the campaigns (chap. 8) were of type NOVAC Mark II and miniMax. Construction of instrument, operation and calculation of SO_2 emissions has been extensively discussed in Galle et al. (2002); Edmonds et al. (2003); Bobrowski and Platt (2007); Kern (2009); Galle et al. (2010).

BrO evaluations:

As mentioned before, scanning geometry of volcanic plumes is aimed at obtaining SO_2 cross sections of a volcanic plumes at high time resolution by using a fast scanning time with consequently low number of added spectra at each elevation angle. Adding of spectra observing the volcanic plume to a “plume spectrum” and of spectra of clear sky to a FRS is necessary to achieve a sufficient low signal to

noise ratio for the detection of BrO. In order to determine which spectra measured the volcanic plume, each scan is first evaluated for SO_2 (see fig. 4.2). Based on these results, the plume's center is identified by a running mean of 10 SO_2 SCDs versus elevation angle. The new plume spectrum is calculated by adding the 10 spectra yielding the highest running mean. Assuming a single plume centre (SO_2 SCDs), the so calculated plume spectrum usually covers the greatest part of a volcanic plume (10 spectra commonly correspond to a field of view of $\approx 30°$). The FRS is calculated by adding up the 10 measurements with lowest SO_2 absorptions, instead of using a running mean. In this way, the approach is also feasible for wider plumes which might be encountered directly above the instrument with clear sky only visible at lower elevation angles at both sides of the plume. Only spectra are used to calculate the FRS, which were recorded at elevation angles $> 15°$ above horizon in order to minimize possible cross correlations with trace gases present in the ambient lower planetary boundary layer.
This approach may yield a sufficient signal to noise ratio for the evaluation of BrO. However, one has to be aware of the errors that are introduced. The summed up individual spectra are taken at different elevation angles and exhibit different strengths of absorption structures for both, plume spectra and clear sky spectra. Since Lambert-Beers-Law is non-linear, the optical density obtained by adding the intensities of spectrum with low absorption structures and one with high absorption structures does not correspond to the average absorption from both. The approach is only truely correct for the hypothetical case, where all plume spectra and all spectra acting as FRS show the same absorption structures. The non-linearity does not cancel in calculated BrO/SO_2 ratios either, since both gases are measured at very different optical densities. Thus even if both gases show the same relative changes in concentration over the plume cross section measured, retrieved SO_2 SCDs will be more underestimated than BrO SCDs by this approach. Since radiative transfer effects lead to an underestimation of SO_2 SCDs as well for a plume of low aerosol content (light dilution effect > enhancement of SCD by multiple scattering), BrO/SO_2 ratios will always be overestimated by this approach and can only act as an upper limit.
The DOAS evaluation of spectra follows the approach as outlined in chap. 5 and for BrO and SO_2, respectively. The RCSs for both retrievals are I_0 corrected using an iterative approach, where the SCD retrieved in an evaluation applying uncorrected RCSs are used as an estimated to construct I_0 corrected RCS for each retrieval.

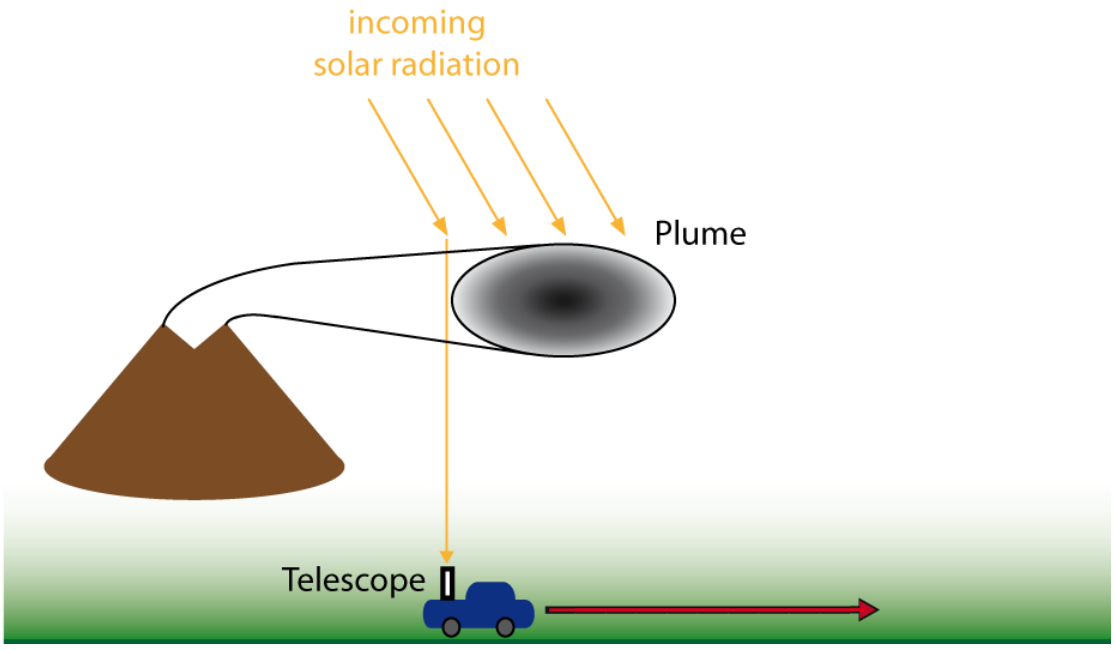

Figure 4.3. Traverse measurements are schematically depicted. A SO_2 plume cross section is obtained by traversing underneath with zenith pointing DOAS instrument. The measured centre of the plume yields an approximate wind direction. The SO_2 flux is calculated for a given wind speed.

4.3 Car based traverse measurements

A cross section of the volcanic SO_2 plume is obtained by crossing under it with a zenith looking telescope mounted on a car. It is a common measurement setup and has been used with COSPEC instruments for over four decades to determine SO_2 fluxes from volcanoes and industrial point sources (e.g. smoke stacks) (Stoiber and Jepsen, 1973). These measurements can also be performed with DOAS instruments (see e.g. McGonigle et al., 2002; Galle et al., 2002), which now has become a standard procedure. Together with a known wind speed, the emission strength is readily determined by multiplying the obtained SO_2 cross section along the measurement path perpendicular to the wind direction which is determined by assuming a linear travel path of the plume between traverse and source.

Wind directions used in this work have been approximated by first calculating the azimuth angle between each measurement point and the crater. The plume centre can be robustly identified by plotting azimuth angle against retrieved SO_2 SCDs for each measurement point and fitting a Gaussian curve. The assumption of a Gaussian distribution of SO_2 concentration leads to a correct identification

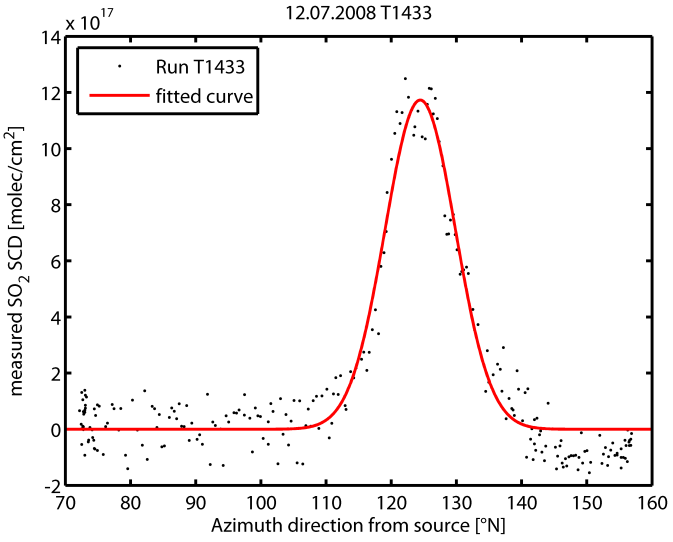

Figure 4.4. Depicted are measured SO_2 SCDs versus azimuth angle from source during a traverse on July 12^{th}, 2008, started at 14:33h UTC. The red line shows the fit of a Gaussian function, which is used to determine a wind direction of 304°.

of plume centre if the distribution of SO_2 SCDs vs. azimuth angle to source is symmetric, even if the the true distribution might not represent a Gaussian. All derived wind directions have also been checked manually to ensure that these assumptions hold and possible changes in wind direction during the traverse together with multiple plume captures do not lead to erroneous wind directions.

BrO evaluations

In order to achieve a better signal to noise ratio and detect BrO absorptions, it is necessary to add spectra. Taking the SO_2 evaluation as a basis, a running mean over SO_2 SCDs of 30 spectra has been calculated for each traverse. Subsequently, the spectra of the maximum running mean are added up and evaluated against the sum of spectra with the lowest running mean of SO_2 SCDs. In this way, the plumes centre and spectra gathered outside the plume are robustly identified. Also, it is ensured that spectra are evaluated against each other which exhibit the greatest difference in volcanic absorptions. Because each recorded spectrum is already the sum of 30-80 individual spectra added during traverse measurements, the total number of spectra in the newly constructed ones is on the order of 1500, which is sufficient for detection of BrO. By adding spectra, which exhibit different absorption structures for both, volcanic plume and FRS, an error is introduced as discussed in the previous section. However, the variations between

subsequently recorded spectra are much smaller for traverse measurements than for flux measurements with MaxDOAS instruments. Several hundred spectra may be collected when traversing a plume, especially if it is measured at greater distance to the crater and has significantly widened. Thus the error induced by adding spectra of different absorption structures can be disregarded in this case.

DOAS evaluation of spectra follows the approach as outlined in chap. 5 and for BrO and SO_2, respectively. The RCSs for both retrievals are I_0 corrected using an iterative approach, where the SCD retrieved in an evaluation applying uncorrected RCSs are used as an estimated to construct I_0 corrected RCS for each retrieval. Sensitivity tests have been performed on the number of iterations necessary, and changes in retrieved SCDs for higher number of iterations are usually less than 5%.
An additional Offset correction had to be applied for spectra gathered for traverses performed during 2008. Gathered with a USB2000 spectrograph (serial number USB2G25267), spectra showed strong straylight components with intensity on the order of 10% comparing mean itensities in the range of BrO retrieval and below 290nm. This was corrected for by subtracting the average number of counts measured below 290nm for each spectra.

5 Retrieval wavelength mapping

The wavelength interval in which the fit is performed is one of the most important parameters to be set for a DOAS retrieval. It should include prominent absorption features of the trace gas of interest, in order to obtain optimum sensitivity, whilst excluding strong absorption features of other trace gases and possible instrumental artefacts. However, balance has to be found between sensitivity and possible interference. A broader range increases the information available to the algorithm but also involves the danger of incorporating strong absorption structures of other gases present. In some cases, a broader wavelength range can increase errors, e.g. insufficient modelling of the wavelength dependency of the Ring effect at presence of higher aerosol loads or clouds (e.g. Wagner et al., 2002b; Langford et al., 2007; Wagner et al., 2009a). Also wavelength dependent radiative transfer effects must be considered, e.g. multiple scattering and light dilution effects for measurements of volcanic clouds (Kern et al., 2010a). A narrower evaluation wavelength range on the other hand can lead to an increase in cross correlation between the different RCS, moreover the retrieval might be distorted by the DOAS polynomial.

Several attempts to find an optimal evaluation range for a certain trace gas were made in the past. The most popular systematic study, at least for the bromine monoxide (BrO) retrieval, is the one by Aliwell et al. (2002), where DOAS retrievals were studied for measurements of stratospheric ozone (O_3) via ground based zenith-looking telescopes at mid-latitudes. In that case one faces low BrO SCDs combined with very high O_3 slant column densities (SCD), interfering with the evaluation. Aliwell et al. (2002) advised to use a wavelength range of 346 nm - 359 nm in the retrieval, limiting O_3 interferences via the set lower wavelength boundary and include two BrO absorption bands (upper wavelength boundary). Theys et al. (2007) validated the suggested wavelength range with an additional radiative transfer study. In other cases, the atmospheric or instrumental boundary conditions differ. Table 5.1 shows previously used wavelength ranges for different platforms and conditions. It is not complete but indicates the diversity of used

	Lower Limit [nm]	Upper Limit [nm]	Type of measurement	Reference
	346	358	Zenith sky	Otten et al. (1998)
	344.7	359.0	Zenith sky	Richter et al. (1999)
I	346	359	Zenith sky	Aliwell et al. (2002)
	346.5	359.2	MAX-DOAS, m.b.l.	Leser et al. (2003)
	346	359	MAX-DOAS, Arctic	Hönninger et al. (2004)
III	320	360	MAX-DOAS, Volcanic Plume	Bobrowski and Platt (2007)
IV	332	352	MAX-DOAS, Volcanic Plume	Bobrowski and Platt (2007)
	346	359	MAX-DOAS, Volcanic Plume	Bobrowski and Platt (2007)
	310.9	377.8	MAX-DOAS, Volcanic Plume	Boichu et al. (2011)
	335.3	358.9	MAX-DOAS, Antarctic	Wagner et al. (2007b)
	330.0	373.6	Airborne, Volcanic Plume	Bani et al. (2009)
	324	354	Airborne, Volcanic Plume	Heue et al. (2011)
	345	359.5	GOME	(Wagner and Platt, 1998)
	344.7	359.0	GOME	Richter et al. (1998)
I	346	359.0	GOME	Hegels et al. (1998)
	345	359	GOME	Richter et al. (2002)
I	346	359	GOME	Aliwell et al. (2002)
V	336.0	347.0	SCIAMACHY	Afe et al. (2004)
	336	351.5	SCIAMACHY	De Smedt et al. (2004)
	344.5	359.0	OMI	Chance (1998)
I	345	359	OMI	Chance (2002)
II	319	347.5	OMI	Salawitch et al. (2010)
	336	352	GOME-2	Theys et al. (2009)
VI	336.0	351.1	GOME-2	Valks et al. (2009)
V	336	347	GOME-2	Begoin et al. (2010)
	336	360	GOME-2	Heue et al. (2011)
	336	360	GOME-2	Sihler et al. (2011)

Table 5.1. Selection of previously published measurements of BrO by ground-based, airborne and satellite instruments and their wavelength ranges for the DOAS evaluation. This list indicates the broad range of wavelengths applied in the different retrievals. The roman numbers in the first column mark the respective wavelength range to be highlighted in several figures for orientation.

wavelength intervals.

In this work, 3-D maps of DOAS retrieval results are introduced. The lower and upper limits of the evaluation wavelength intervals are the coordinates, while the retrieved column density is colour-coded (sec. 5.1). These retrieval-maps enable the easy visualization of results for a large set of evaluation wavelength ranges and thus offer an intuitive tool to show how certain key parameters influence the results. As application examples, measurement conditions are studied using artificial spectra, focusing on retrievals of stratospheric BrO and BrO in volcanic plumes studied with passive DOAS measurements using scattered sunlight (sec. 5.2). Section 5.2.2 describes the tests performed on the synthetic spectra: (1) the influence of the I_0-effect, (2) cross correlations between trace gas absorption cross sections and variations in assumed trace gas SCDs corrected for the I_0 effect, and (3) the behaviour of retrieved results if noise is added to the synthetic spectra. The results are presented and discussed in sec. 5.3. A discussion on common features

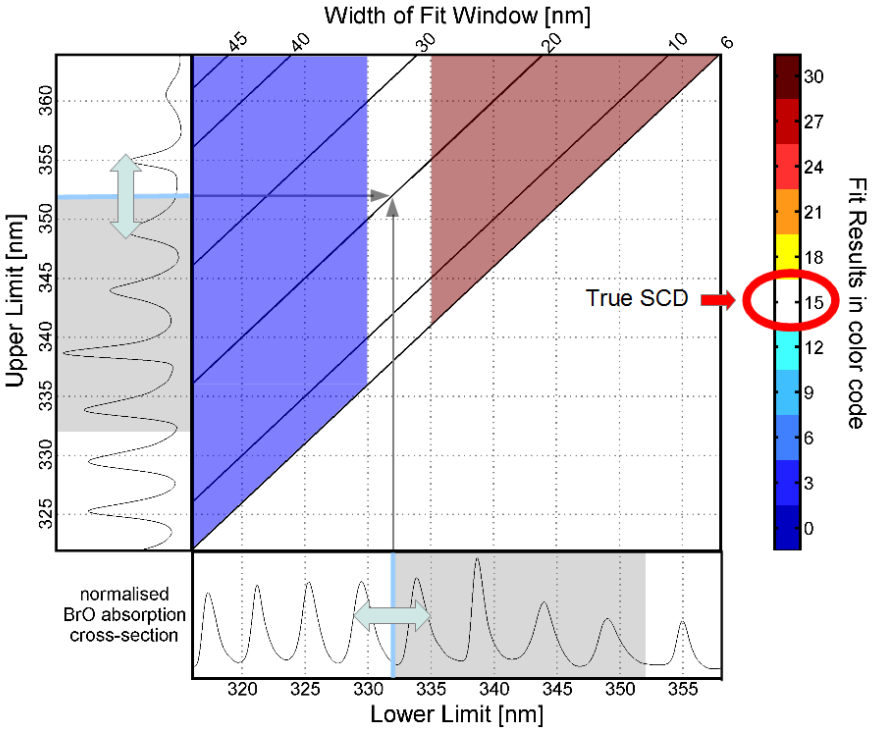

Figure 5.1. A retrieval wavelength map: The abscissa shows the lower wavelength end of the retrieval wavelength interval, the ordinate the upper wavelength end. The fit results i.e. the retrieved column densities are colour-coded (colour-scale on the right side). In this arbitrary example, only retrievals using a spectral range of lower wavelength limit 330 nm - 335 nm yield correct SCDs.

is given in the subsequent section 5.3.3, followed by concluding remarks.

5.1 Visualizing the parameter space - General approach

Considering only a single set of measurement and reference spectra, systematic spectral structures (instrumental, erroneous I_0 correction, cross correlations, etc.) influence the result of DOAS retrievals at different wavelength intervals. The presented mapping method is based on the fact that these errors change with wavelength. When varying the retrieval wavelength interval, the results of the DOAS retrieval will thus reflect systematic errors. Random noise on pixel bases might increase the general noisiness, but does not cause systematic variations of results as a function of the evaluation wavelength interval.

Thus a DOAS retrieval performed systematically over a wide range of different

wavelength ranges yields information, which is hidden if only results of retrievals at a few individual wavelength ranges are compared. The retrieval result for a trace gas of interest can then be visualized in a 3-dimensional plot, where the first and second dimension are the lower and upper limits of the evaluation wavelength interval, respectively. The results are plotted in the third dimension, e.g. with a colour code. Thus, each point in the plot corresponds to one particular wavelength interval. The resulting maps allow to spot wavelength evaluation intervals which are likely to lead to erroneous results due to strong absorbers present, systematic instrumental structures or correlation with other absorbers.

As an example of this novel tool, the above described retrieval mapping is performed on simulated spectra. These offer the advantage that the true SCDs used in the construction of these spectra are known and the results can be compared. Fig. 5.1 is an example to familiarise with the depiction. Retrieved SCDs are mapped to the evaluation wavelength range. It covers all evaluation wavelength intervals with lower limits of 316 nm - 358 nm, upper limits of 322 nm - 364 nm and all values in between at 0.1 nm steps, as long as the interval width ω is 6 nm$< \omega <$45 nm. The true SCD is marked in white, under and overestimated results in blue and red, respectively.

The advantage of the retrieval wavelength mapping is obvious: In a first assessment, certain retrieval wavelength intervals can be disregarded, others could be subject to further investigation. For instance, it can be immediately seen from Fig. 5.1 that an evaluation range including wavelengths below 330 nm yields erroneous SCDs. On the other hand, if an evaluation wavelength range is used with a lower wavelength limit above 335 nm, retrieved columns overestimate the true value. In this arbitrary example, only retrievals using a spectral range with a lower limit of 330 nm - 335 nm will yield correct SCDs.

Computational requirements to map the wavelength evaluation ranges are moderate. All shown individual maps were generated on a desktop PC within 30 minutes for given wavelength evaluation ranges at 0.1 nm steps. Thus, this novel tool can easily be used to give a quick overview of possible pitfalls in DOAS evaluations. It offers great potential in validation and optimization of fit ranges of any DOAS retrieval. In the following sections a few examples are given for the application of retrieval wavelength mapping, focussing on retrieved SCDs of artificially constructed spectra. Note that possibilities of the presented technique are not restricted to the retrieved column densities, but that many other important characteristics of a fit can be displayed in the same way, e.g., cross sensitivities between trace gases, retrieval errors, wavelength shifts and squeezes performed by

Spectral range [nm]	Number of channels	dispersion [nm/channel]	resolution FWHM [nm]
300 - 402.3	1024	0.1	0.65

Table 5.2. Spectral range and resolution of the instrument assumed for the study on artifical spectra. The instrumental function determining the resolution is assumed to be Gaussian.

the algorithm can be investigated by our method.

5.2 Application of the wavelength-interval-mapping technique to synthetic spectra

The tool described above was used to study synthetic spectra, which were constructed from a high resolution solar spectrum (Kurucz et al., 1984) and applying Lambert-Beer's law with a set of literature RCSs. This approach allows to model effects in the DOAS retrieval with or without limitations by noise or instrumental features. The results can be compared to the SCDs of all trace gases used in the construction of the synthetic measurement spectra. Given these simplifications, the results can be assumed to yield the lowest error possible and act as a "best case" scenario. Certain limits are posed on the application of studied synthetic measurement set-ups to measured spectra. For one, e.g., the Ring-effect and full radiative transfer needs to be accounted for in passive DOAS measurements. The Ring effect has only been considered for the advanced measurement scenario (sec. 5.2.3), in order to limit the scope of this work. The retrieval mapping technique highlights retrieval wavelength areas to be treated with caution, even in this "best case" and others to be studied in greater detail.
In the following, information will be given on how the synthetic spectra were constructed and subsequently the different measurement scenarios are introduced. The software package DOASIS was used for computation of all spectra and retrieval of results (Doasis, 2010; Kraus, 2006; Lehmann, 2011), but the same results can be expected for other software.

5.2.1 The generation of synthetic spectra and reference cross sections

For this theoretical study, a spectrometer with a detector of 1024 pixels was assumed with a spectral range of 300 nm - 402.3 nm. Pixel to wavelength mapping is linear, corresponding to 0.1 nm/pixel. The optical resolution is given by an instrumental slit function of Gaussian shape with 0.65 nm FWHM, allowing to disregard possible undersampling effects (Roscoe et al., 1996; Platt et al., 1997; Chance et al., 2005). The simulated instrument corresponds to the commonly used spectrometers in ground based Max-DOAS and satellite instruments.
The same approach was taken for all measurement scenarios in constructing synthetic spectra with and without absorption structures as well as RCSs. Since this study focuses on measurements using scattered sun light, a high resolution solar spectrum $I_{K,0}$ (Kurucz, 2005) is used as a spectrum without absorption structures. The absorption cross sections of the different trace gases ($\sigma(\lambda)$, see sec. 5.2.3) were first interpolated to the resolution of the solar atlas, $\sigma_K(\lambda)$ with $\approx 3 \cdot 10^5$ channels from 300 - 450nm. Subsequently, they were multiplied with the SCDs S assumed for each studied case and their absorption applied to the solar atlas according to Lambert-Beer's Law. The so obtained spectrum I_K with absorption structures and the spectrum $I_{K,0}$ without absorption structures are convolved with the assumed ISF W (Gaussian with FWHM = 0.65 nm) in order to simulate intensities measured at a typical DOAS instrument resolution (see sec. 3.4).

Reference cross sections and I_0 effect

RCSs $\sigma_{K,i}$ are used in the construction of synthetic spectra as described above. In order to obtain RCSs at the resolution of the instrument, these RCSs $\sigma_{K,i}$ need to be converted to RCSs σ_i corresponding to the resolution of the spectrograph. As described in sec. 3.5, the I_0 effect needs to be considered for passive DOAS measurements, since the incident solar spectrum I_0 is highly structured in comparison to laboratory light sources used to measure typical reference absorption cross sections.
Two different sets of RCSs are constructed for all tests. One consists of RCSs convoluted with the ISF without further modifications and are thus uncorrected for the I_0 effect. The second set of RCSs has been corrected for the I_0 be a first order correction and are denoted as I_0 corrected RCSs in the following. Tests with RCSs, which have been corrected for the I_0 effect by a second order correction are

neglected, since only deviations from true SCDs on a the scale of numerical errors can be expected for theoretical studies. Details of the calculations performed are given in sec. 3.5.

Raman scattering and Ring effect

For advanced tests on synthetic spectra, also the Ring effect (Grainger and Ring, 1962, see sec. 3.2) has to be taken into account. To study the effect of Raman scattering, the approach of constructing synthetic measurement spectra was modified to resemble usual practice in DOAS retrievals of real measurements. A Raman spectrum was calculated from the synthetic measurement spectrum at the high resolution of the solar atlas. The integrated intensity of the simulated spectra (synthetic spectra at high resolution and its corresponding Raman spectrum) is used as a measure to calculate fraction of Raman spectrum and spectrum without elastic scattering. Assuming a certain amount of Raman scattering (usually on the order of a few percent), the synthetic spectrum including Ring effect is the sum of the Raman spectrum and the spectrum it was calculated from. The calculated spectrum is normalised after integrating the Raman spectrum so that the integrated intensities before and after the operation remain the same. For a detailed description on amounts of Raman scattering used in FRS and simulated measurements, the reader is referred to sec. 5.2.2. The final synthetic measurement spectrum is constructed as usual by convolving it with the instrumental slit function in order to achieve a synthetic spectrum at instrumental resolution.
The Raman scattering is applied by calculating a Raman spectrum from a given spectrum using the software DOASIS (Doasis, 2010; Lehmann, 2011) according to (Bussemer, 1993). This Raman spectrum corresponds to the Raman scattered intensities of the given spectrum at respective channel wavelength mapping. The Ring spectrum included in the fit scenario is calculated using DOASIS from Fraunhofer reference spectra at instrument resolution, in order to keep the retrieval of the using simulated measurement spectrum as close to common praxis as possible.

5.2.2 Tests performed on synthetic spectra

Retrieval wavelength maps were constructed for several tests performed on both measurement scenarios. For simplicity, only two different sets of RCSs are used for

the respective measurement conditions and are not varied during the tests. One fit scenario uses RCSs, which are uncorrected for the I_0 effect, the other one applies I_0 corrected RCSs for the respective measurement scenario (sec. 5.2.3). The only exception is test IV (sec. 5.2.2) were additional Ring spectra are included in the fit scenarios. The tests are performed by varying the synthetic measurement spectra (e.g. the amount of absorbers included, adding of noise).

In both retrieval set-ups, the logarithm of the Fraunhofer reference spectrum I_0 was fitted together with the RCSs to the logarithm of the artificial measurement spectrum instead of fitting the RCSs to the logarithm of the ratio I/I_0. This is a common approach in order to account for small shifts in wavelength pixel mapping between Fraunhofer reference and measurement spectrum, which can occur e.g. by temperature drifts of the optical bench of the spectrograph. The fit coefficient of the Fraunhofer reference was kept fixed to 1. In order to mimic common evaluation practice the set of RCSs and the FRS (FRS and Ring spectrum in case of advanced modelling) were allowed to shift and squeeze in wavelength as a whole. In this way, changes in wavelength calibration are corrected without endangering the stability of the retrieval. Furthermore a DOAS polynomial of second order was included. This was sufficient because no broad band extinction is included during the construction of synthetic spectra.

Test I: Influence of the I_0 effect

As a first test, retrieval wavelength maps were constructed for all measurement scenarios using retrievals with uncorrected and I_0 corrected RCSs. This allows to study the influence of the I_0 effect and draw conclusions at which accuracy the SCDs of respective trace gases can be reproduced using only first order I_0 corrected RCSs. This test allows direct comparison to the study of Aliwell et al. (2002) for the Zenith-DOAS measurement scenario.

Test II: Cross-correlation of absorbers and influence of variations of absorber strength on the I_0-effect

This test is designed to yield information on the sensitivity of the retrieval to small variations of the amount of absorbers present and the sensitivity of the I_0

effect to these variations. Cross correlations between the differential absorption cross sections of the different absorbers affect the retrieved SCDs. Due to the wavelength dependency of the absorption cross sections, these cross correlations are depending on the evaluation wavelength range. For real measurement spectra, cross correlations can pose a problem, especially if additional residual structures and noise are present. A wrongly assumed amount of trace gas, while correcting the RCS for the I_0 effect, will lead to small additional structures. The SCDs of each absorber were varied in turn, while constructing the artificial measurement spectrum. A fit was subsequently performed on this spectrum using the original RCSs. Relative changes of retrieved values can be expressed as

$$\frac{\delta S_{BrO}}{\delta S_A} = \frac{S_{BrO,A+} - S_{BrO,A-}}{2\Delta S_A} \cdot \left(\frac{S_{BrO,0}}{S_{A,0}}\right)^{-1} \quad (1)$$

where S_A denotes the SCD of absorber A and $S_{BrO,A+}$ and $S_{BrO,A-}$ are the BrO SCDs retrieved after changing S_A^0 by $\pm\Delta S_A$. With the simplification that variations of S_A of absorber A do not influence variations of SCDs S_B of absorber B, the variations of BrO SCDs due to variations in other absorbers can be assessed by

$$\frac{dS_{BrO}}{dS_A} = \sum_A \frac{\delta S_{BrO}}{\delta S_A} \quad (2)$$

An additional error is introduced by varying the absorbers, since SCDs are varied during construction of the artificial measurement spectrum but are RCSs used in retrieval still are corrected for the I_0 effect with the original SCDs.
The variations of the trace gases were set to 1% in case of measurement scenario A (assessing stratospheric BrO by Zenith DOAS) and 10% in case of measurement scenario B (BrO in volcanic plumes) as oulined in sec. 5.2.3.

Test III: Effect of noise on retrieval and error calculation

Tests were performed on the synthetic spectra with additional noises, in order to bring the artificial study closer to reality. Typical residual structures are simulated by adding gauss-distributed noise to the logarithm of the measurement spectra. The standard deviation of the noise structure was normalized to $3 \cdot 10^{-4}$ optical density, corresponding to common residual amplitudes. Additional broad band features were introduced by binomial low pass filtering (e.g. Jähne, 2005) of the Gaussian noise with a [1 2 1] filter and 0, 10 and 50 iterations with subsequent

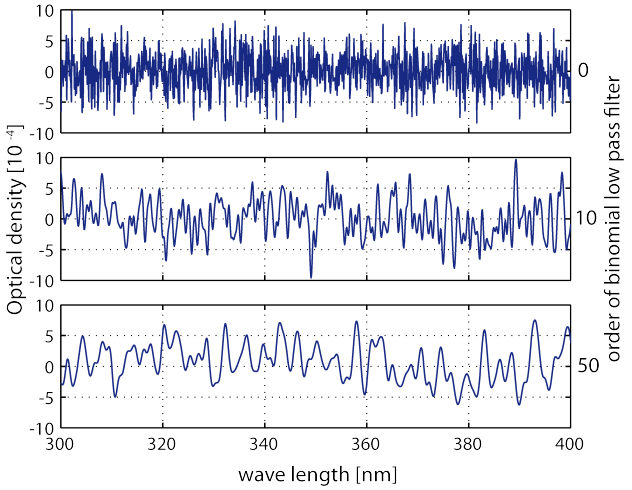

Figure 5.2. Examples of different noises added to the logarithm of the artificial spectrum. The noises in the simulation are produced with DOASIS and follow a Gaussian distribution. The broad band structures are constructed by a low pass binomial filter of [1 2 1] and 0 (top trace), 10 (center trace) and 50 (bottom trace) iterations, respectively. After low pass filtering, the noise was rescaled to the original standard deviation of amplitude $3 \cdot 10^{-4}$.

rescaling (see fig. 5.2). 10 and 50 iterations correspond to a filtering using a running mean of 6 and 15 pixels, respectively, allowing to compare the results to the error calculation by Stutz and Platt (1996). For an average FWHM of 1.5nm (15 pixels) of an BrO absorption band, the correction factor given by Stutz and Platt (1996) should be ≈1.5 for unfiltered noise, $\approx 2.5 - 3$ for noise filtered with 10 iterations and ≈ 4.5 for 50 iterations.
The influence of noise on retrievals with I_0 corrected and uncorrected RCSs was tested only for the case of unstructured noise. Broader residual structures are studied only for I_0 corrected RCS. 100 Maps were constructed with independent noise for every retrieval/point on the retrieval map in order to get reasonable statistics with independent retrieval results for every wavelength evaluation range.

Test on advanced modelled synthetic spectra

The test on advanced modelled synthetic spectra was designed to simulate true measurement conditions as close to reality as possible, without the use of additional radiative transfer algorithms. It is only applied to synthetic spectra of volcanic measurements (scenario B, sec. 5.2.3), in order not to exceed the scope of this work. The test resembles Test I, where uncorrected and I_0 corrected

RCSs are compared, with the exception that here it is repeated on an advanced measurement scenario under consideration of the Ring effect, as detailed below:
Test I on synthetic spectra was repeated on the modified measurement scenario for volcanic plumes, in order to study the influence of the Ring effect on DOAS measurements. In the simplified scenarios for measurements of BrO in the stratosphere and volcanic plumes (see sec. 5.2.3), the Ring effect is not considered. However, for a realistic approach, the Ring effect must be included due to its strong narrow band structures with strong influence on the DOAS retrieval.Furthermore, the optical density of the fitted Ring spectrum can be an order higher than optical densities of the trace gases of interest (e.g. BrO). Depending on were the Ring Effect takes place, it will not only lead to "filling in" of Fraunhofer lines but also to a "filling in" of absorption structures of the trace gas of interest. To reflect those possibilities, the original calculation of synthetic spectra as laid out in sec. 5.2.1 was modified. The construction of synthetic spectra is split into two parts: (1) Stratospheric absorbers to be included in the simulated FRS and the simulated measured spectrum. (2) Tropospheric absorbers as well as volcanic plume (SO_2 and BrO), applied only to the measurement spectrum. The strength of the Ring effect depends on the atmospheric aerosol load. An increased aerosol load leads to a diminished Ring effect compared to a purely Rayleigh scattering atmosphere (Wagner et al., 2009b). Assuming cloud free conditions and a low aerosol load, the Ring effect will be present stronger in the FRS, e.g. with a fraction of about 5% Raman scattered photons for a spectrum taken at 90° elevation angle (Wagner et al., 2009b). The spectrum taken of a volcanic plume is, in general, less affected by the Ring effect, due to its increased aerosol load (single scattering albedo ≈ 1, mostly sulfate aerosols). Commonly measured differential Ring effects are on the order of 3% optical density, where the spectrum of the volcanic plume shows lesser Ring structures than the FRS.
The construction of spectra is described in the following. If not stated otherwise, all calculations on spectra are performed at the high resolution of the solar atlas. Details of used absorbers are given in Table (5.4).

1. A realistic FRS is calculated by applying respective amounts of stratospheric absorbers to the solar atlas. This ensures a realistic FRS as measured by the (virtual) instrument.

2. The synthetic measurement spectrum is constructed by applying respective tropospheric absorbers to the Fraunhofer reference.

3. The final FRS is calculated by constructing a Raman spectrum and adding it to the FRS. Both spectra are normalized to a channel integrated intensity of 95% (FRS spectrum) and 5% (Raman spectrum) resulting in an fraction of 5% Raman scattered photons to the total intensity.

4. The measurement spectrum with Ring effect is simulated by calculating a Raman spectrum from the original measurement spectrum. Both are added at a share of 98% (channel integrated intensity) of the measured spectrum and 2% of the Raman spectrum.

5. High resolution Fraunhofer reference and measurement spectrum are convolved with the instrumental slit function to obtain the spectra perceived by the virtual instrument.

The Ring spectrum used in the retrievals with uncorrected and I_0 corrected RCSs is calculated from the FRS, which includes stratospheric absorbers and the Ring effect as well. The set of RCSs and FRS together with the Ring spectrum are allowed to shift and squeeze in wavelength, in order to model common fit routines as closely as possible.

This approach is repeated for different amounts of BrO SCDs in the synthetic spectra. The influence on retrieval results for different true SCDs is studied. It is important, because it can not be expected that observed relative deviations from true SCDs will remain the same for different amounts of BrO present. For example, if residual structures are present at constant strength, they may lead to a constant wavelength depending offset of retrieved BrO SCDs. Thus spectra which contain less BrO absorptions may be more affected than spectra with stronger BrO absorption structures.

5.2.3 Measurement scenarios

Scenario A: Zenith-DOAS

Measurement scenario A employs trace gas column densities typical for zenith sky DOAS measurements at the example of a BrO retrieval. Commonly, spectra are recorded with a zenith looking telescope at high solar zenith angles (SZA). Evaluation of spectra at higher SZA against reference spectra at e.g. 70° SZA

yield information about stratospheric trace gases. The main problem for retrievals of stratospheric BrO SCDs are the encountered strong O_3 absorption structures at lower wavelengths. The findings can be transferred to other measurement scenarios of similar conditions. Information on the assumed RCS and SCDs are given in tab. 5.3. The assumed values are the same as the ones used in a previous study by Aliwell et al. (2002), where an inter-comparison of stratospheric BrO retrievals is presented with data measured with several different zenith-DOAS instruments and additional theoretical considerations on the I_0-effect. However, instead of the BrO cross-section by Wahner et al. (1988) at 223K, the cross section by Fleischmann et al. (2004) at 298K was used, because the latter is available at higher resolution and BrO cross-sections recorded at the same temperature can be used for both scenario A and B. Sensitivity tests were performed for cross sections at different temperatures and by different authors (Wahner et al., 1988; Wilmouth et al., 1999; Fleischmann et al., 2004). Although they can differ significantly in amplitude, differences in shape are small at least for RCSs by Wilmouth et al. (1999) and Fleischmann et al. (2004). For this reason and because of the small BrO optical density compared to the other absorbers, it can be assumed that the relative changes in retrieved SCDs are independent for all tests performed. Only negligible differences in retrieved SCDs can be observed in the results presented later between this study and (Aliwell et al., 2002), section 5.3.1.

Scenario B: BrO in volcanic plumes

The SCDs assumed for respective trace gases (tab. 5.4) simulate measurements of a volcanic plume observed at 30° elevation above horizon against a Fraunhofer reference spectrum taken at zero solar zenith angle (SZA), with consequently

Set-up A

Trace gas	Temperature [K]	Reference cross-section	SCDs [molec · cm^{-2}]
BrO	298	Fleischmann et al. (2004)	1.5×10^{14}
O_3	221	Burrows et al. (1999)	8×10^{19}
O_3	241	Burrows et al. (1999)	2×10^{19}
NO_2	220	Vandaele et al. (1998)	5×10^{16}

Table 5.3. SCDs used to construct the synthetic measurement spectrum of scenario A. It corresponds to slant column densities typical for zenith-DOAS measurements, reproducing the settings in Aliwell et al. (2002).

increased sensitivity to ambient tropospheric trace gases. Atmospheric conditions are different to the zenith-DOAS Scenario, where BrO is studied in the stratosphere. Although measured SCDs of tropospheric O_3 are smaller by two orders of magnitude, the volcanic plume includes SO_2 at high concentrations, which absorbs in a similar wavelength range. Possible cross correlation of BrO with ambient HCHO must be taken into account due to a similar shape of absorption structures and encountered optical density. Assumed tropospheric SCDs of NO_2, O_3 and HCHO correspond to a slightly polluted troposphere, as found e.g. at Mt. Etna, Italy, during the summer months (Huijnen et al., 2010; Curci et al., 2010; Heckel et al., 2005). BrO and SO_2 SCDs are typical for a diluted plume, released several minutes before the measurement (e.g. Bobrowski and Platt, 2007; von Glasow, 2010, and this work).
Two different approaches are taken to simulate measured spectra of volcanic plumes. First, the same simplified approach is taken as for scenario A. Although this approach can be used to gain insights into possible pitfalls of the DOAS retrieval, additional efforts were made to better simulate measured spectra. This allows for a better comparison between measured and synthetic spectra, improving the understanding of the sources of error in this kind of DOAS retrievals and to find an optimal retrieval wavelength range.

Simplified approach:
Several simplifications are made for the assumed measurement conditions. For one, stratospheric absorbers are neglected. Both spectra, Fraunhofer reference and artificial measurement spectrum with absorbers, are assumed to be recorded in close proximity in time. Thus they include the same absorption structures of stratospheric gases which cancel out in the retrieval. Consequently the I_0 effect for tropospheric trace gases is simulated only for tropospheric trace gases (see also 5.2.1). This assumption can be regarded valid at low solar zenith angles, but should be treated with care for measurements at early and late times of the day. As mentioned earlier, also the Ring-effect is disregarded in this approach. The SCDs of all absorbers used to construct the synthetic measurement spectra are given in tab. (5.4).

Advanced modelling of the retrieval of BrO in volcanic plumes
As an attempt to simulate reality more closely, tests were performed using an advanced scenario set-up of synthetic spectra including all absorbers in a com-

mon evaluation. Specifically, a realistic FRS is created by applying stratospheric absorbers to the high-resolution solar reference, O_4 absorptions are included in the synthetic measurement spectrum and the Ring effect is modelled. This is especially important, since the Ring spectrum is commonly one of the strongest (pseudo-)absorber encountered, with optical densities on the order of a few percent.

In this advanced scenario the stratospheric absorbers are applied to the solar reference to construct a realistic Fraunhofer reference. This modified Fraunhofer reference is then used to model the synthetic measurement spectrum by applying the given absorbers. A detailed description on how the synthetic spectrum is constructed is given in sec. 5.2.2 accounting also for Raman scattering as the source of the Ring effect.

Since the effect of systematic wavelength depending residual structures on the retrieval may differ for different BrO columns, three different BrO SCDs are modelled. For example, if systematic residual structures are present at constant strength, they may lead to a constant wavelength depending offset of retrieved BrO SCDs. Thus spectra containing less BrO SCD are more affected than spectra with stronger BrO absorption structures.

Set-up B

Trace gas	Temperature [K]	Reference cross-section	Simplified × [molec · cm^{-2}]	Advanced Fraunhofer Reference [molec · cm^{-2}]	Advanced Measurement [molec · cm^{-2}]
O_3	221	Burrows et al. (1999)	–	8×10^{18}	–
O_3	241	Burrows et al. (1999)	–	2×10^{18}	–
NO_2	220	Vandaele et al. (1998)	–	5×10^{15}	–
BrO	298	Fleischmann et al. (2004)	1.5×10^{14}	–	0.5×10^{14} *
			–	–	1×10^{14} *
			–	–	1.5×10^{14} *
O_3	273	Burrows et al. (1999)	1×10^{18}	–	1×10^{18}
NO_2	294	Vandaele et al. (1998)	5×10^{16}	–	5×10^{16}
SO_2	298	Vandaele et al. (2009)	1×10^{18}	–	1×10^{18}
CH_2O	298	Meller and Moortgat (2000)	3×10^{16}	–	3×10^{16}
O_4		Hermans et al. (2003)	–	–	1×10^{42}
Ring Effect			–	5%	2%

Table 5.4. Absorber SCD used in the construction of synthetic spectra in order to simulate BrO measurements in volcanic plumes as described in sec. 5.2.1 and 5.2.2. *) Spectra are simulated for three different BrO SCDs.

5.3 Results for simplified measurement scenarios

5.3.1 Scenario A, Zenith-Sky stratospheric BrO retrievals

Test I, influence of the I_0 effect

Figure 5.3 and 5.4 depict the results for I_0 corrected and uncorrected RCSs used in the retrieval algorithm, respectively. Because fig. 5.3 is the first example of retrieval wavelength mapping, the BrO cross section is depicted at abscissae and ordinate for better orientation and interpretation of results. A column of $1.5 \times 10^{14}\text{molec} \cdot \text{cm}^{-2}$ was used in the construction of the synthetic measurement spectrum (see also sec. 5.2.3). Evaluation wavelength intervals including wavelengths below $\approx$ 330nm and 340nm, respectively, yield erroneous results for both types of RCSs, because this scenario applies very high O_3 SCDs. Using uncorrected RCSs in the retrieval results in deviations greater than 100%, and even the results in white marked areas 5.4 can differ by $< 20\%$ from the true BrO SCD. The retrieval applying I_0 corrected RCSs shows much smaller variations of results, which are on the order of $\pm 3\%$ if the fit includes wavelengths below 330nm. Results colour-coded in white deviate only by less then 0.7% from the true BrO SCD. The variations in fig. 5.3 can be explained by the residual structures induced in the retrieval by insufficient correction of the I_0 effect. In the first order correction of the I_0 effect applied to the RCSs, changes in the Fraunhofer solar spectrum due to the strong O_3 absorptions are not accounted for.

For both sets of RCSs, one of the major features visible in the retrieval maps is that the results are depending mostly on the lower wavelength limit of the fit. This is again an indication for the influence of the strong O_3 absorptions, because their absorption structures are decreasing with increasing wavelength. Preferences to under- or overestimate the true BrO SCD are changing with the in the evaluation wavelength range included BrO absorption peaks.
If uncorrected RCS are used in the fitting algorithm, the retrieval map indicates the difficulty to find a suitable evaluation wavelength range at all.
Figure 5.5 depicts retrieval results and residuals at the example of three different wavelength ranges as well as uncorrected and I_0 corrected RCSs used in the fit. The evaluation wavelength intervals chosen correspond to the ones marked by IV (319-347.5nm), II (332-352nm) and I (346-359nm) in tab. 5.1 and fig. 5.3, 5.4. Greater residual structures of retrievals at 319-347.5nm confirm that retrievals at lower wavelength ranges and use of uncorrected RCSs must be avoided if higher

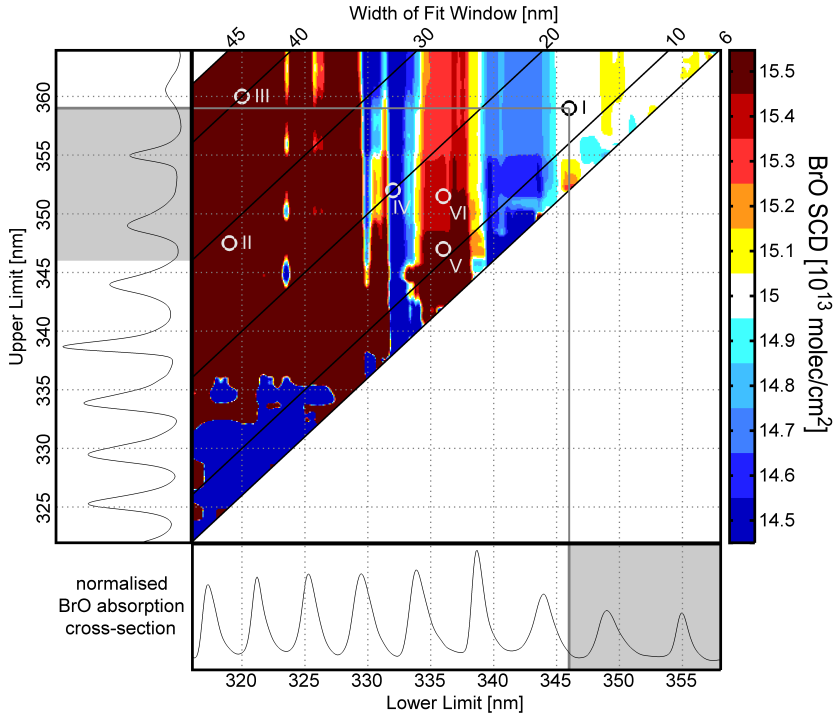

Figure 5.3. Retrieval results from a wavelength mapping of a synthetic spectrum constructed according to scenario A (tab. 5.3) with a BrO SCD of $15 \cdot 10^{13}$ molec/cm^2. The retrieval applies I_0 corrected RCS. The abscissa shows the lower wavelength end of the retrieval wavelength interval, the ordinate the upper wavelength end. The retrieved column densities are colour-coded. Retrieval results in the interval [14.95 to 15.05]$\cdot 10^{13}$ molec/cm^2 are marked in white, under- and overestimated results in blue and red, respectively. The circles with roman numbers mark previously applied wavelength retrieval ranges (see tab. 5.1).

O_3 absorptions are present in the measurement spectra, even in this "best case" using synthetic spectra without noise. If I_0 corrected RCSs are applied in the fitting process, the residuals of the retrievals using another wavelength range than 346-359nm still show induced structures. The residual structures of the retrieval using uncorrected RCSs at 346-359nm reproduce well the results of test A2 and B3 described in (Aliwell et al., 2002).

The previous study by Aliwell et al. (2002) advised to use an evaluation wavelength range 346-359nm (marked by circle and roman number I in both figures 5.3 and 5.4) due to lesser variations in retrieved SCDs from measured spectra. These evaluation wavelength range is well studied and validated (e.g. Theys et al., 2007). Using the same approach as Aliwell et al. (2002), it is not surprising that the retrieval maps show that evaluations at longer wavelengths are to be advised. Evaluations of BrO

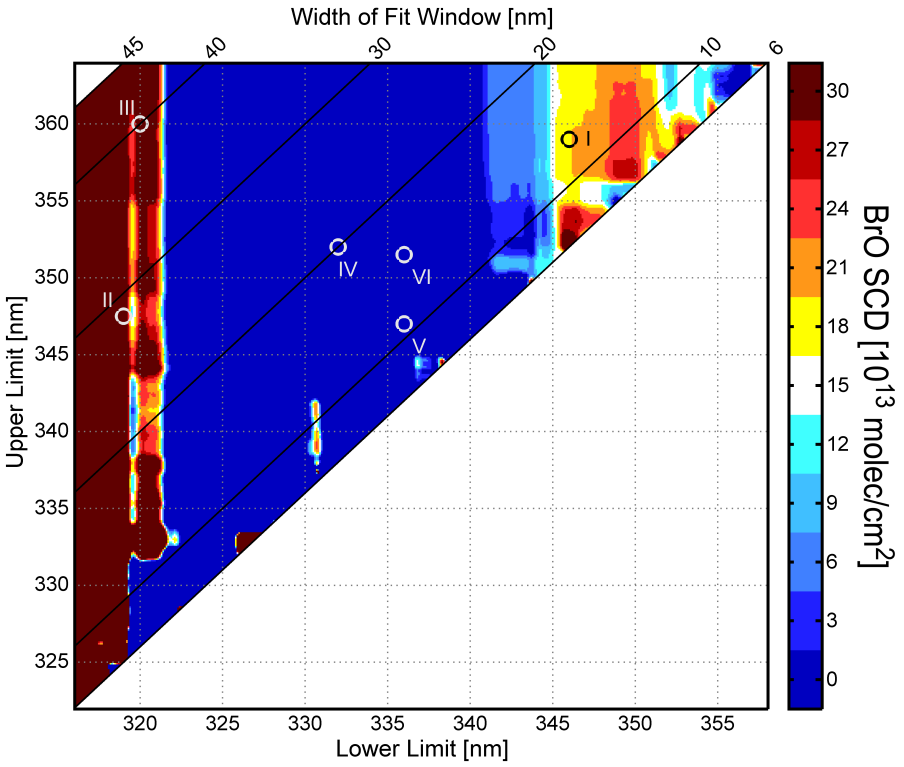

Figure 5.4. Scenario A, retrieved SCDs with uncorrected RCSs. The artificial spectrum contains true stratospheric BrO SCD of $15 \cdot 10^{13}$ molec/cm^2 (tab. 5.3). Note that the color-code scale covers a 30 times larger SCD-interval compared to the I_0 corrected retrieval shown in fig. 5.3. The roman numbers denote certain wavelength ranges (tab. 5.1) for orientation.

at shorter wavelengths are to be treated with caution if strong O_3 absorptions are present. In this sense, it is shown how the introduced retrieval wavelength maps can be used to help visualize and interpret retrieval results. Aliwell et al. (2002) advised to move from 345-359nm to 346-359nm due to greater stability of retrieved values from measured spectra. The retrieval maps indicate that the greater variabilities at 345-359nm could have their source at stronger dependency on the lower evaluation wavelength limit. Assuming a constant upper evaluation wavelength limit of 359nm and moving along a lower wavelength limit from 344 to 347nm on the retrieval maps, the gradient of retrieved BrO SCDs show a steep slope at 345nm but has reached a plateau at 346nm. It can only be speculated that the retrieval from 346-359nm might lead to less deviations of results but slightly overestimating the true value without further comparison with measured data.

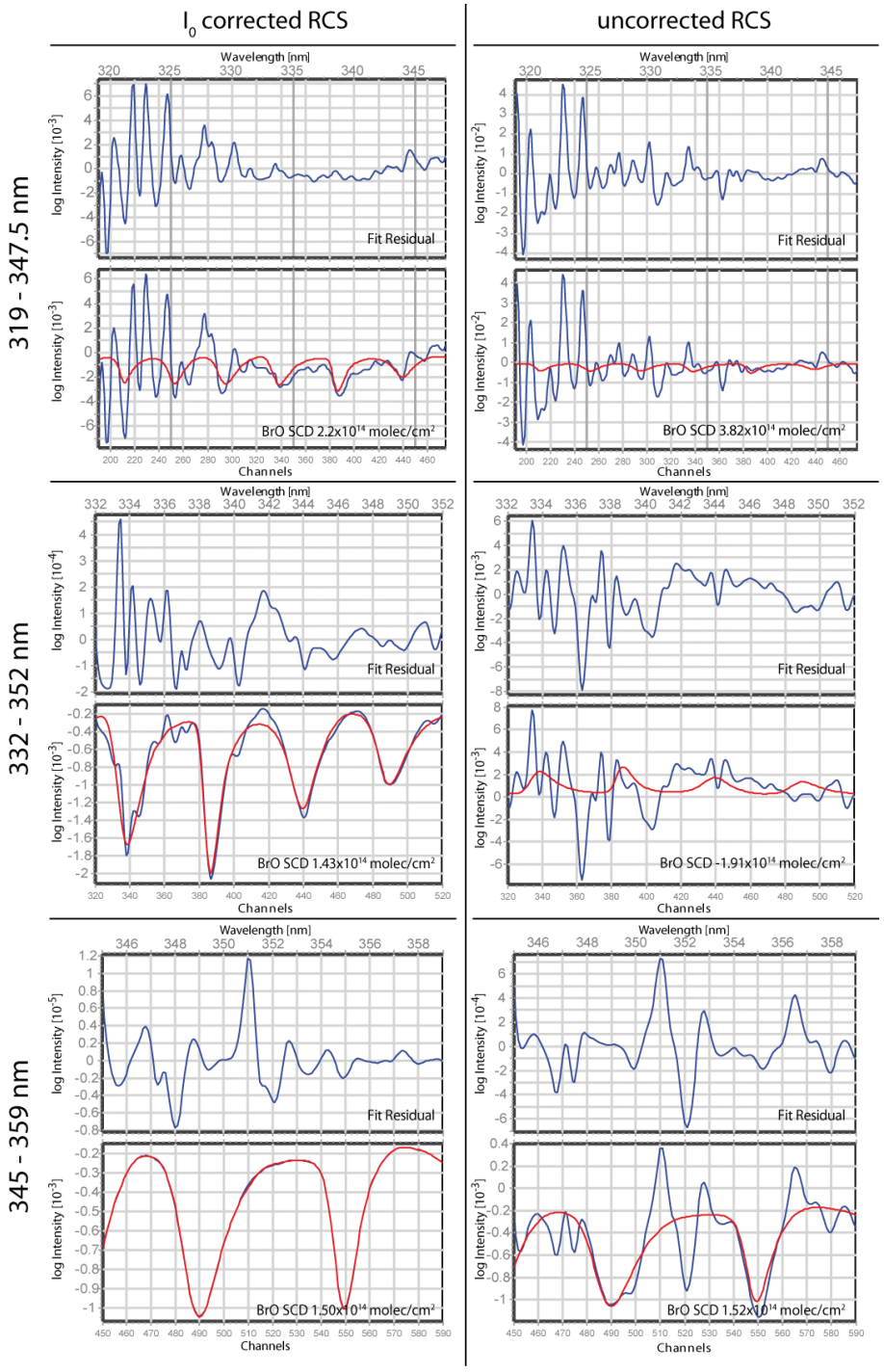

Figure 5.5. Scenario A, stratospheric BrO: Shown are fit results for certain wavelength ranges. Regardless of uncorrected or I_0 corrected RCSs, a fit at the longest wavelength range yields best results. For uncorrected RCSs, this is mandatory to achieve a reasonable result with a still highly structured residual. At 346-359nm, tests A2 and B2 on synthetic spectra in Aliwell et al. (2002) are reproduced.

Test II, Variation of absorber strengths

Beyond the behaviour of retrieved trace gas SCDs with changing evaluation wavelength intervals, many other properties of a fit can be investigated. As an example we show the dependencies of the retrieval result on wavelength evaluation range and assumed SCDs for I_0 corrected RCSs, which are depicted in fig. 5.6. If any of the O_3 RCSs are varied by 1%, a relative change of BrO of more than 10% occurs for wavelength ranges of a lower limit between 316nm - 330nm. Even above a lower wavelength interval limit of 330nm changes greater than 10% are present for O_3 at 221K, the stronger of the two O_3 RCSs used. Relative changes of BrO SCD due to O_3 at 241K remain mostly below 5% above a lower limit of ≈335nm and become negligible above 345nm. The variations of SCDs for scenario A show a clear imprint of the strong O_3 absorptions. They generally lead to an overestimation of BrO SCDs if wavelengths <330nm are included in the retrieval. Strong absorptions also affect the results at longer wavelengths, although not as severe. It must be noted that the shown differences are resulting from a combination of slightly erroneous I_0 correction and possible cross correlation of absorption cross section.

Compared to O_3, the influence of NO_2 is only a minor effect which can be disregarded above a lower limit of 345nm. Variations in NO_2 have only minor effects on the retrieval. The depicted dependency of NO_2 on the shorter wavelength end of the evaluation range is surprising. Other than O_3, the differential optical absorption bands of NO_2 increase in strength at longer wavelengths in the ranges studied here. Thus a dependency on the upper wavelength end of the evaluation retrieval would be expected. The seen feature is most likely an effect of the insufficient I_0 corrections of RCSs due to neglecting the strong O_3 absorptions in the correction process (see sec. 5.2.1). Indications are the structures observed already in the plots for varying O_3 strengths.

Test III, effect of noise on retrieval and error calculation

Figure 5.7 depicts the results of the retrieval with additional noise structures. For each of the points a different gausian distributed noise was created and low pass filtered with a binomial of low pass filter ([1 2 1]) of 0, 10 or 50 iterations (see fig. 5.2). The noise was normalized to a standard deviation of $3 \cdot 10^{-4}$ optical density. The columns show the results from left to right for a fit using uncorrected RCSs

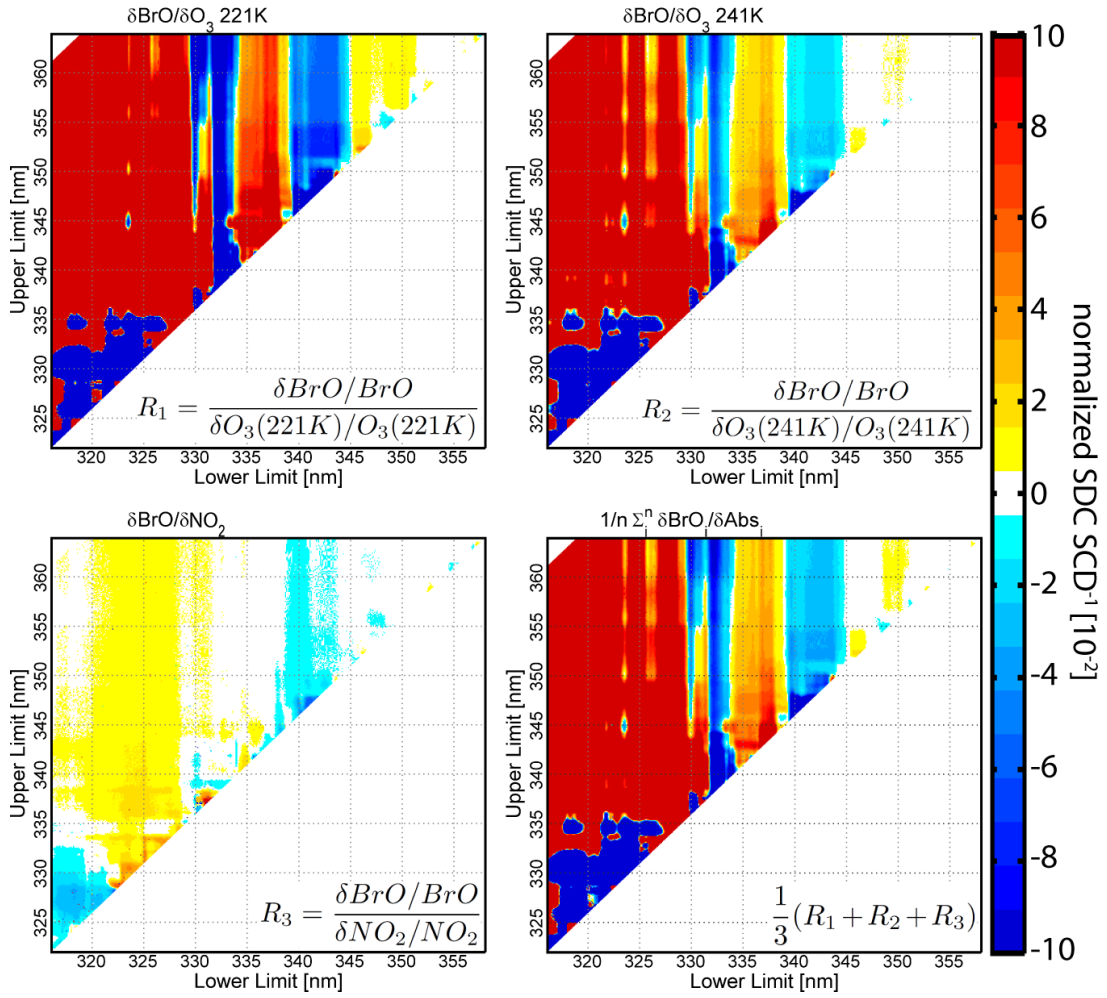

Figure 5.6. Zenith-Sky DOAS scenario: Shown are the resulting changes in BrO SCDs if respective absorbers are varied by 1%. The color-code depicts relative changes of BrO per relative change of absorber. At lower wavelengths, clearly the strong O_3 absorptions are dominating (upper row), whereas the influence of NO_2 is negligible in comparison (lower left). The average of all relative changes is depicted at the lower right graph.

and unstructured gaussian noise, fits applying I_0 corrected RCS with unstructured gaussian noise, followed by low pass filtered gaussian noise with a binomial filter of 10 and 50 iterations (see fig. 5.2). The top row gives the resulting BrO SCDs, the middle row shows the standard deviation for the respective wavelength retrieval range and the bottom row gives the correction factor defined by Stutz and Platt (1996), which is the ratio of standard deviation of results by mean error of fit.
Comparing the retrieved BrO SCDs from synthetic spectra without noise (test I) and with the different structured noise types, it is apparent that the mean BrO SCDs of the noisy spectra in general do not differ from the ones without noise, regardless if RCS are corrected or not for the I_0 effect (fig. 5.3, 5.4). The noise only leads to an increased spread of results, which can clearly be observed for the I_0 corrected RCS, column 2 till 4. This agrees with the intuitive expectation that the average should remain the same for the case of a distribution of noise structures without systematic features depending on wavelength. An increase in standard deviation of results is observed, but also the variations observed in fig. 5.3 and 5.4 are more apparent with increasingly structured noise. Whereas the average BrO SCDs around a lower retrieval wavelength limit of 332.5nm for all upper limits (thus following a vertical line) do not deviate from the results of synthetic spectra without noise, the average of the retrieval starts to systematically underestimate the results with increasing noise structure. The same is true for an overestimation of values between lower limits of 334-338nm. These results are already observed at the spectrum without noise, but at a lower scale. This indicates that underlying systematic errors are not concealed by noise but actually become more pronounced. The standard deviation shows a clear change at ≈338, 345 and 350nm for the different noises studied and RCS used due to the strengths of BrO absorption bands included in the fitting process. Comparing standard deviations of uncorrected and I_0 corrected RCS, no major difference can be observed. Thus the unstructured noise does not influence the distribution of retrieved values even if systematic structures are present. On the other hand, the systematic structures are having a great influence on the error of the fit. This is best studied by looking at the correction factor, the ratio between standard deviation and fit error (see sec. 5.2.2), which is shown in the bottom row of fig. 5.7. Looking at the maps of unstructured noise, a correction factor below 1 is calculated for evaluations of lower limit $< 330nm$ for I_0 corrected RCS, and even a factor below 1 for all evaluations of lower limit $< 345nm$ for uncorrected RCS. A possible reason for this is discussed in the section about general findings from both measurement scenarios (sec. 5.3.3).

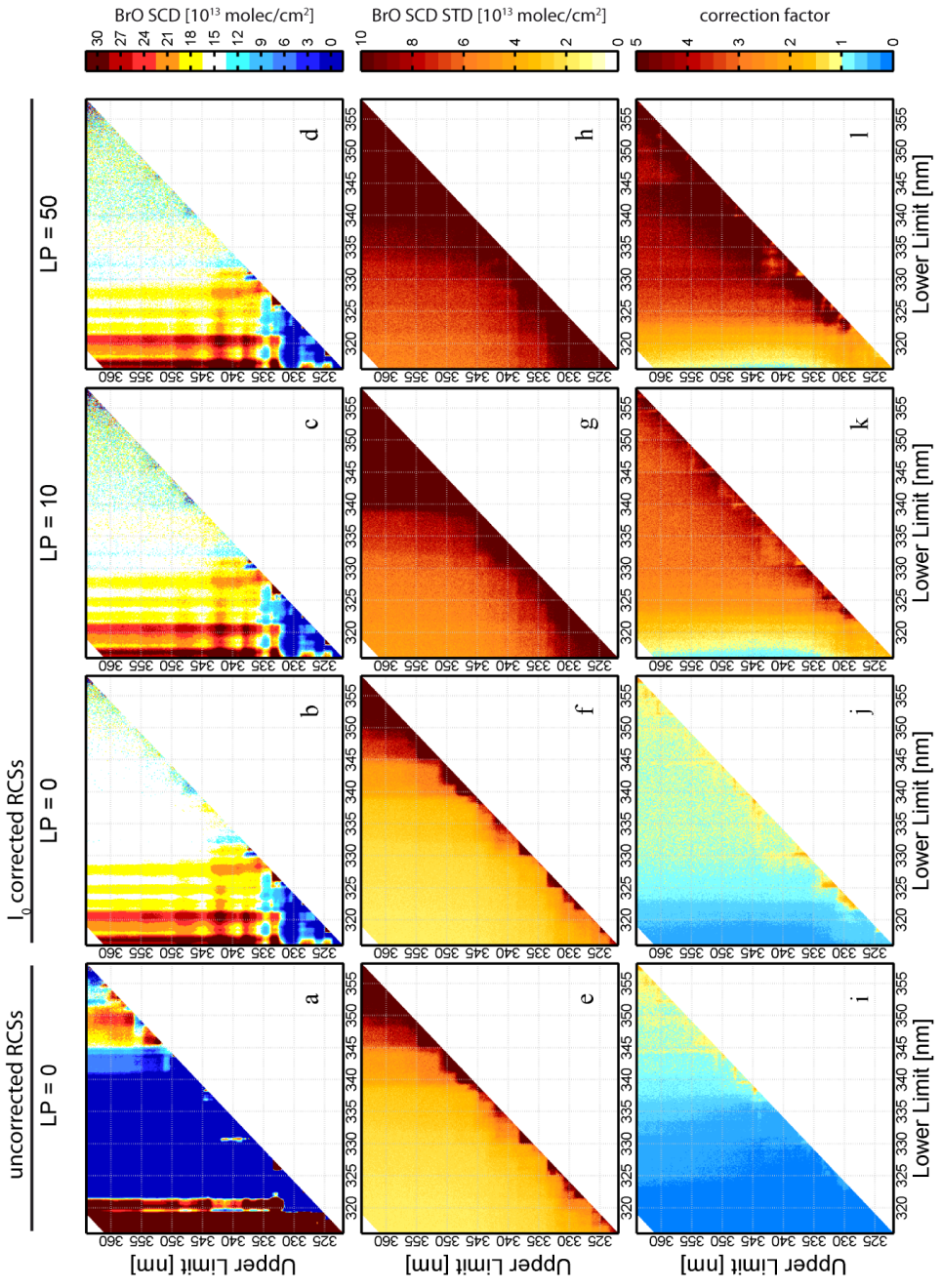

Figure 5.7. Results from the statistical study on scenario A. The first column gives the mean of retrieved BrO SCDs for an uncorrected set of reference spectra together with unstructured noise. Second till fourth column depict results for I_0 corrected reference spectra and different structured noises. The rows (upper to lower) correspond to retrieved SCDs, standard deviation of results, and calculated correction factor to retrieve the standard deviation from the fitting error (top to bottom row). See text for interpretation of results and details about noise.

5.3.2 Scenario B: BrO in volcanic plumes

Test I, influence of the I_0 effect

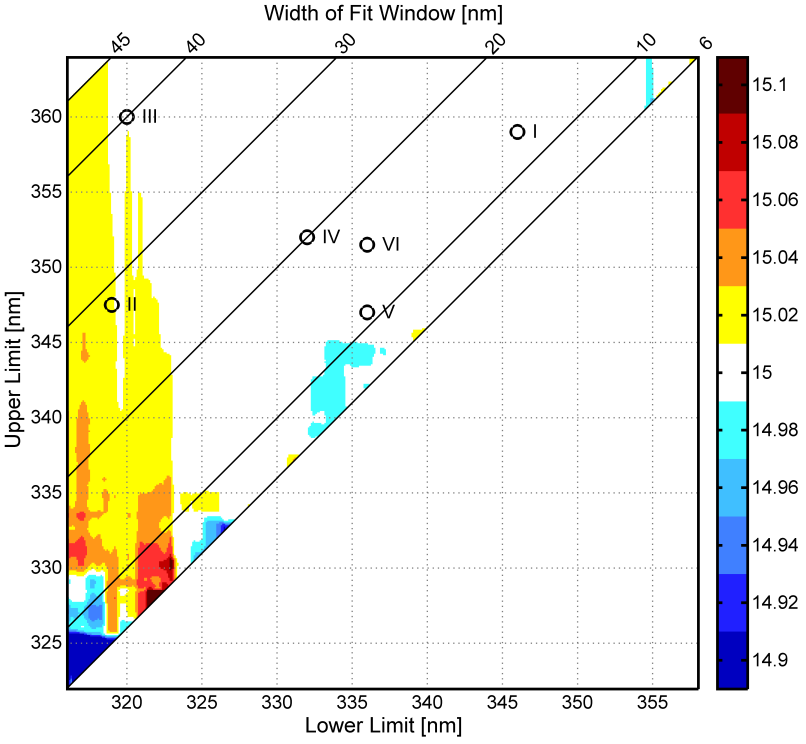

Figure 5.8. Retrieved BrO SCDs for scenario B (BrO in volcanic plumes) using I_0 corrected RCS. The synthetic spectrum was constructed using $15 \cdot 10^{13}$ molec/cm^2. Compared to fig. 5.3, the wavelength retrieval map only shows minor structures if lower wavelengths are included in the fit. These can be attributed to SO_2 and O_3 absorptions. The roman numbers indicate the different fit ranges in tab. 5.1.

Figure 5.8 shows the results for a wavelength-retrieval mapping of scenario B for I_0 corrected RCSs. It is apparent that the I_0 corrected retrieval yields correct results at most evaluation wavelength intervals. Negligible variations of retrieved BrO SCDs are on the order of up to 1% if the fit is performed with a retrieval interval starting below ≈323nm. The features can be attributed to the stronger SO_2 and O_3 absorptions at lower wavelengths. Compared to scenario A, retrievals with I_0 corrected RCSs fig. 5.3, the variations in retrieved values are much smaller. This can be explained by the much smaller absorptions of all trace gases, which reduces the errors induced by only aplying a first order correction of the I_0 effect as discussed in section 5.2.1. Also residual structures shown for three different evaluation wavelength ranges are negligible (fig. 5.11).

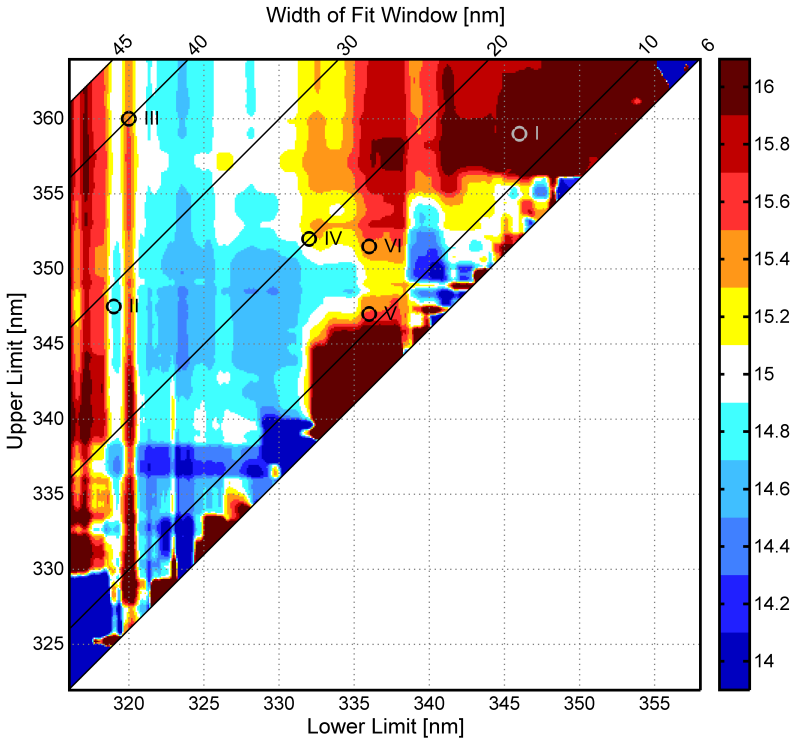

Figure 5.9. Scenario B, retrieval with uncorrected RCS. Over- or underestimation of the target BrO SCD of $15 \cdot 10^{13}$ molec/cm^2 is increased, compared to the I_0 corrected RCS (fig. 5.8). The roman numbers denote certain wavelength ranges (tab. 5.1) for orientation. For a detailed analysis see text.

If uncorrected RCSs are used, the retrieved BrO SCDs show greater variability (fig. 5.9), however far less than observed in scenario A (fig. 5.4) due to the generally lower strength of absorptions. Deviations from the target BrO SCD range up to 10 % for most retrieval ranges. Assigning deviations at a specific wavelength evaluation range to a certain trace gas is difficult in general due to possible cross correlations between all trace gases. Also, changes in retrieved SCDs of absorbers do not directly translate to the same changes in optical density of the differential optical absorption structure, because of its varying strength with wavelength. As an example, optical densities are given in table 5.5 for scenario B at three different wavelengths. With these values as indications for the influence of the respective trace gas, the individual retrieval results are depicted in fig. 5.10. Deviations from the true value given by the white color code can in this way be assigned to the influence of the respective trace to the erroneous fits.

It is safe to assume that SO_2 and O_3 absorptions influence the fit if BrO bands at lower wavelengths (<325 nm) are included, although by far not as strong as in

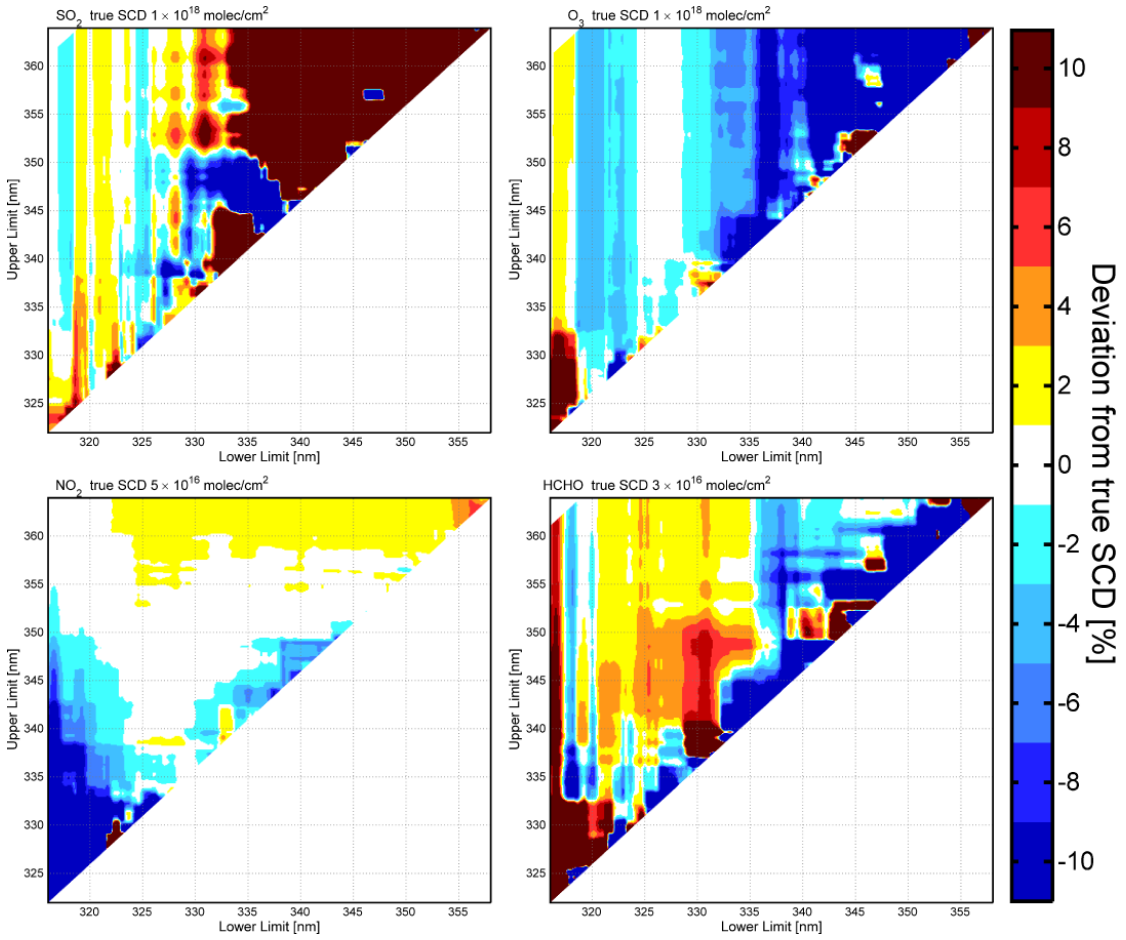

Figure 5.10. Deviations from the true SCDs of other trace gases than BrO for scenario B using uncorrected RCSs. The respective true SCD is indicated in white (0% deviation), over- and underestimation in red and blue colours.

the case of scenario A. Due to the increasingly smaller absorption cross sections at longer wavelength ranges for both species, their influence is reduced at longer wavelengths, although the optical density of O_3 is still comparable to the one of BrO at 338 nm. Strongly deviating SCDs are retrieved for SO_2 above 335 nm (fig. 5.10), but its optical density at these wavelengths is negligible compared to other absorbers.

If the fit is including longer wavelengths (>≈350nm), it can be assumed that errors due NO_2 are becoming more pronounced as its absorption structures are increasing as well as an overestimation of SCDs occurs (see fig. 5.10). The absorption bands of HCHO on the other hand have a structure very similar to BrO and can lead to an anti-correlation of both trace gases. The overestimation of HCHO SCDs for evaluation ranges starting at a lower limit (approximately between 320 nm and 335 nm) thus might decrease retrieved BrO SCDs in that area. On the other hand,

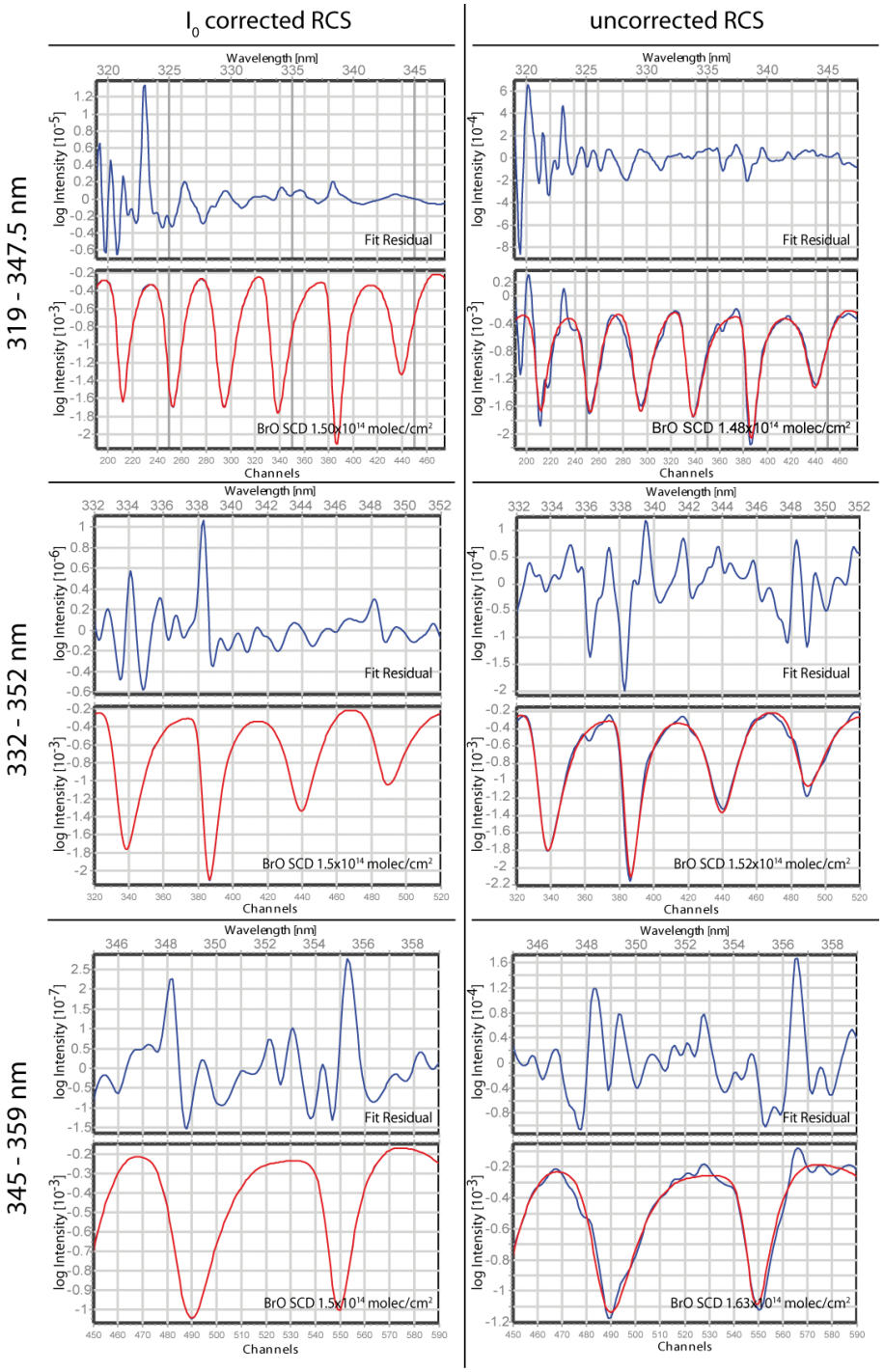

Figure 5.11. Scenario B, BrO in volcanic plumes: At the simulated measurement conditions, all wavelength ranges yield results with negligible residual structures for I_0 corrected RCSs. For fits applying uncorrected RCSs, greatest deviation is seen for 346 nm - 359 nm in contrast to scenario A.

underestimation of HCHO SCDs at lower limits >335 nm can increase BrO SCDs. These findings are reflected in fig. 5.8, where a BrO SCDs are generally lower in evaluation regions of a lower limit range between 320 nm to 335 nm and higher if the lower limit above. Because the deviations of BrO SCDs resulting from cross correlations between all trace gases, it is not unambiguously possible to single out a single other absorber as a source.

Figure 5.11 displays fit examples for uncorrected and I_0 corrected RCSs. As expected from the previously shown figures 5.8 and 5.9, only small residual structures and deviations from the true BrO SCD are observed. For the retrievals applying I_0 corrected RCSs, all three different evaluation wavelength ranges yield negligible residual structures. In contrast to the fit examples of scenario A (fig. 5.5), the evaluation wavelength range of 332 nm - 352 nm gives the best result and the wavelength range of 346 nm - 359 nm the greatest deviations to the true BrO SCD are observed. The differences may be explained by the presence of the additional absorber HCHO in scenario B with an anti-correlation to the BrO cross section, but as mentioned above, from the performed studies it is not possible to assign deviations to true SCDs to a single trace gas alone.

A correct retrieval of BrO SCDs should go hand in hand with correct retrievals of the other absorber, otherwise the retrieval might depend on other trace gas concentrations. Because this study is performed only with synthetic spectra, it is difficult to advice for a specific wavelength evaluation range. Further studies on measured spectra are needed before a clear suggestion can be made.

Wavelength range center [nm]	BrO	SO_2	O_3	NO_2	HCHO
	Optical Density [10^{-3}]				
325	0.7	6.2	5.0	0.7	1.0
338	1.2	0.1	1.2	2.0	0.7
350	0.3	0.1	0.1	3.5	0.2

Table 5.5. Differential optical densities of trace gases at SCDs of set-up B. It has been calculated by taking the peak to peak value of a high pass filtered absorption cross sections multiplied with the respective SCD in a 5 nm wavelength range. The 325 nm and 350 nm wavelengths have been chosen to indicate roughly optical densities in the lower and higher wavelength ranges. The strongest absorption band of BrO is situated at ≈338 nm.

Test II, Variation of absorber strengths

As described in the previous paragraph, I_0 corrected RCSs yield accurate results with only slight deviation from the theoretical BrO SCDs when lower wavelengths are included (<325 nm, fig. 5.8) due to the generally low absorber strenghts. These results are also confirmed when varying the different absorber strengths of measurement scenario B. Their influence on the retrieval results of BrO are visible for I_0 corrected RCSs in fig. 5.13. The increased absorptions of O_3 and SO_2 below 325nm lead to a slight overestimation of BrO SCDs if included in the fit wavelength range. In the case of NO_2, almost all wavelength intervals show a slight anti-correlation with BrO. The absorption structure of NO_2 is rather complex and does not show clearly overlapping absorption bands with BrO, nevertheless NO_2 interacts unfavourably with BrO due to its comparably high optical density (tab. 5.5). This can lead to unexpected effects if NO_2 is not I_0 corrected. In contrast to the HCHO dependencies of the BrO retrieval using uncorrected and I_0 corrected RCSs as discussed in the previous section, varying the HCHO SCDs while constructing the synthetic spectra barely effects retrieved BrO SCDs. The changes induced by an erroneous I_0 correction (difference of 10 % to the true HCHO value) leads to an anti-correlation of BrO and HCHO absorption structures of less then 0.1 % of the true BrO column. Disregarding widths of wavelength ranges smaller than 15nm, only intervals with lower limits between 335nm and 340 nm yield slight dependencies. This can be attributed to the strongest absorption bands of similar features for both trace gases at ≈338 nm. It must be noted that these findings are in contrast to the correlations of both species when evaluating real spectra (see also sec. 5.4 and sec. 6.4).
For the average of all dependencies in fig. 5.12, an area least affected by varying absorber strengths is observed between lower limits of 326 nm - 333 nm. In order to avoid possible influences of stronger NO_2 absorptions on the retrieval, an area least affected by varying absorber strengths lies between lower limits of 326 nm - 333 nm and upper limits between 346 nm - 350 nm or around a lower limit of 327.5 nm and upper limit above 355 nm. But dependencies in total remain negligible as long as the stronger absorption structures of SO_2 and O_3 are avoided.

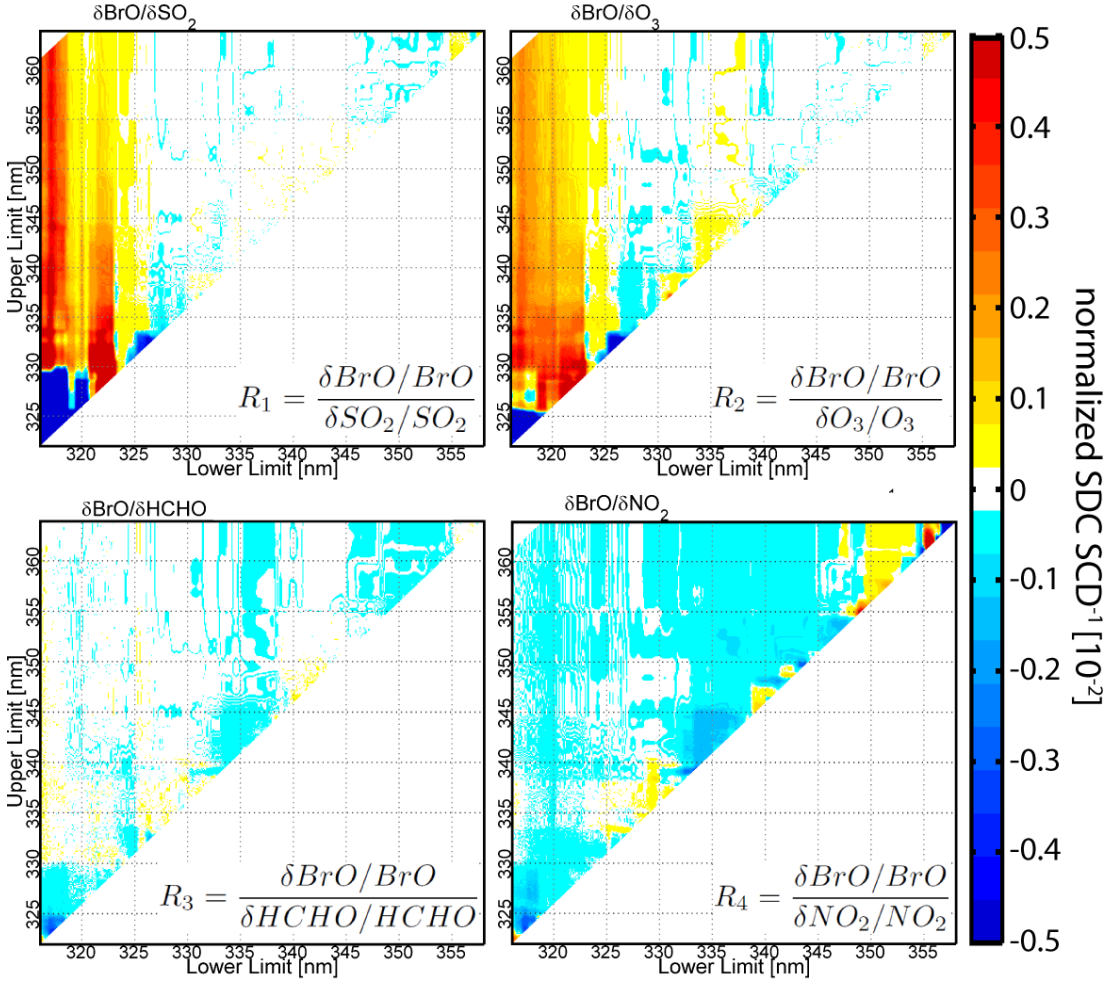

Figure 5.12. Interferences in BrO restrieval for Scenario B: Wavelength retrieval maps constructed with synthetic spectra and absorber strengths varied by 10 %. The original I_0 corrected set of RCSs was used. Greatest changes in retrieved BrO SCDs occur where strong absorption features of SO_2 or O_3 are included (e.g. at evaluation ranges including wavelengths <323 nm). While these effects correlated to the BrO SCDs, NO_2 and HCHO mostly anti-correlate with BrO, where NO_2 absorptions show greatest influence. Overall, cross correlations of absorption cross sections are very small.

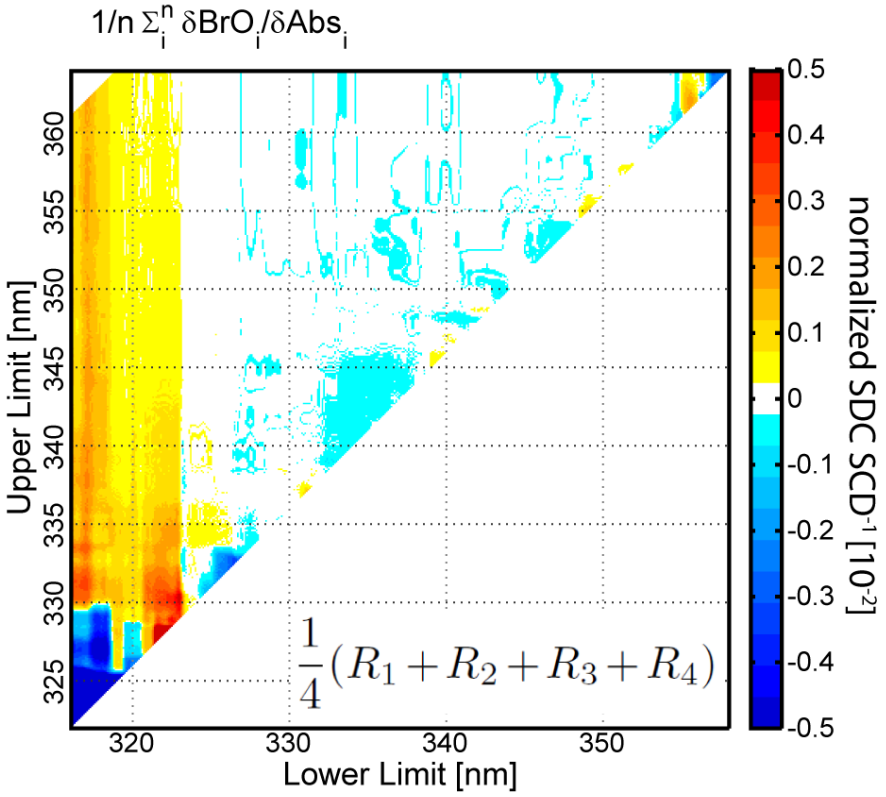

Figure 5.13. Average of respective dependencies of the BrO SCDs to the strength of other absorbers present and their I_0 correction of RCSs as shown in fig. 5.8. Wavelength evaluation ranges with a lower limit < 325 nm are dominated by O_3 and SO_2 features, where as the other wavelength ranges may be influenced mainly by NO_2 and HCHO, although derivations from the true BrO SCD are negligible. A region which appears to be most stable against variations is located between lower limits 326 nm - 333 nm to upper limits 346 nm - 350 nm (see also fig. 5.12).

Test III, effect of noise on retrieval and error calculation

The results of differently structured noises on the retrieval of BrO in volcanic plumes are depicted in fig. 5.14. As already observed for scenario A, certain weak variations of BrO SCDs are becoming more pronounced by the induced noise, comparing fig. 5.9 with fig. 5.14a for the case of an evaluation using uncorrected RCSs. Possible minor deviations from the theoretical BrO SCDs for evaluations applying I_0 corrected RCSs are still concealed by the noise.
Comparing the standard deviations for retrievals using uncorrected and I_0 corrected RCSs (fig. 5.14e,f), no major differences can be distinguished, although results for both types of evaluations differ. In the case for the I_0 corrected RCSs, the average values remain the same. With increasingly structured noise due to the stronger low pass filter, e.g. going from 0 iterations (LP0) to 50 iterations (LP50), a general increase in standard deviation is visible. For all noise structures a sudden increase in standard deviation occurs at a lower evaluation wavelength limit of 338 nm and 345 nm corresponding to a decrease in amplitude of the differential optical absorption bands of BrO.
The calculated correction factor shows a clear transition at 320 nm lower limit for the uncorrected RCSs changing from below 1 to an average value of 1 for all other retrieval wavelength intervals. For evaluation wavelength intervals incorporating wavelengths <320 nm, strong SO_2 and O_3 induce residual structures increasing the fit error. As the standard deviation is not affected, consequently the correction factor is scaled down. If the fit is performed at longer wavelength ranges, also larger deviations from the true BrO SCD occur. These are not reflected in the correction factor because of the better fit, although the BrO SCDs show a larger offset.
For I_0 corrected RCSs, the correction factor only shows a small wavelength dependency. For unfiltered noise, standard deviation and measurement error do not differ significantly, for low pass filtered noise (10 and 50 iterations of the binomial filter), correction factors of $\approx$3 and $\approx$4.5 need to be applied to calculate the true standard deviation from the fit error. This is to be expected, since low-pass filtered noise has a larger pixel to pixel correlation and agrees well with previous studies (Stutz and Platt, 1996).

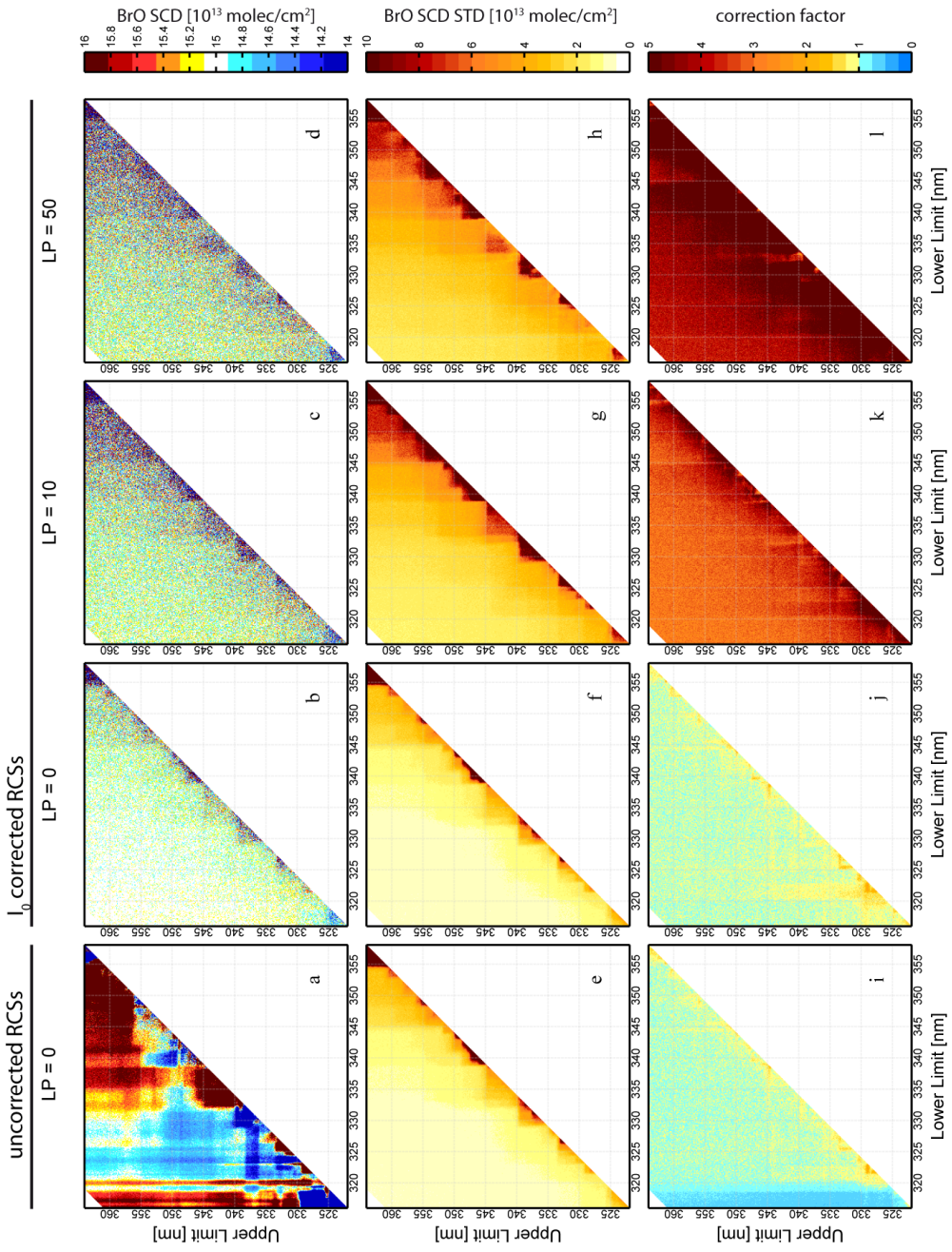

Figure 5.14. Results from the study with noise on scenario B. The first column gives the mean of retrieved BrO SCDs for an uncorrected set of RCSs together with unstructured noise. Second till fourth column depict results for I_0 RCSs and different structured noises using low pass filtered gaussian noise with a binomial filter of 0, 10 and 50 iterations. See text for interpretation of results.

5.3.3 Discussion of general findings

Next to the results for the specific measurement set-ups, several features can be observed which are common to both scenarios. Even if generalisation can not be made without a thorough mathematical description, these features offer insights and reveal pitfalls in common DOAS evaluations.

I_0 corrected and uncorrected reference cross sections

Although the two measurement scenarios incorporated absorptions of differing strengths, retrieved SCDs showed that an I_0 correction should be applied. This is especially true if very strong absorbers are present (e.g. O_3 in scenario A). In this case, an evaluation of BrO at lower wavelengths and comparable O_3 absorptions should only be performed when the I_0 effect can be truly corrected. For scenario B, optical densities of the different absorbers are not exceeding the optical density of BrO by orders of magnitude. Thus deviations of the retrieved SCDs are less then for scenario A, but I_0 correction of RCSs remains mandatory to achieve correct results. It must be noted that sensitivity tests were performed with second order I_0 corrected RCSs as outlined in Sec. (5.2.1). Retrieved SCDs differed from the true SCDs only in the range of numerical errors introduced during the performed calculations for all absorbers and both scenarios.

Sensitivity of the I_0 effect to variability in absorber strength

In order to successfully correct for the I_0 effect, a priori knowledge of the trace gas SCD is necessary. This is only possible if additional information on the trace gas concentrations is available or by taking an iterative approach. Still, minor errors may remain in the assumed SCDs and affect the retrieval. Thus even when using I_0 corrected RCSs, retrieval wavelength ranges should be avoided where strong absorptions occur of trace gases other then the one of interest.

In the case of scenario A, the errors introduced by erroneous I_0 correction are more severe due to the stronger O_3 than for scenario B with relatively small O_3 and SO_2 absorptions in comparison. Another interesting feature is the negligible BrO and HCHO cross correlation when evaluating the synthetic spectra. Although low cross correlations can be expected in this ideal case, cross correlations on the order of more than 25 % can be observed when falsely evaluating measured spectra of volcanic plumes. Because these differences are not observed for the synthetic spectra, they must originate from noise present in the spectra and structures

introduced in the fit by strong absorbers. It can be speculated that the Ring effect is a likely source of error because it shows in general optical densities on the order of 1 % or more if treated as an additional absorber (Ring spectrum) in the fitting process. Retrieval mapping of such measured spectra may thus act as an indicator of the goodness of the fit, helping to obtain a parameter set at which lowest variations of retrieved columns occur when varying the evaluation wavelength.

Influence of noise on the retrieval

By adding noise of different structures to the studied spectrum, several interesting features become visible. The results presented in sec. 5.3.1 and 5.3.2 show that (1) noise induces small systematic deviations in the average retrieved SCDs compared to the retrieval without noise. (2) The standard deviation of the results does not depend on the systematic wavelength depending deviations present due to incorrect I_0 correction. (3) The fit error on the other hand is greatly increased by these systematic structures, leading to a discrepancy between standard deviation of results, fit error and correction factor by Stutz and Platt (1996).

The first result can be understood by the nature of the added noise spectra. This is to be expected, because they are generated from random noise and no wavelength dependent systematic structures are induced. The average chi-square minimum is still obtained for the same columns if the chi-square space is symmetric in proximity to the global minimum chi-square for synthetic spectra without noise. Otherwise changes are observed in the retrieved average SCDs. Thus the observed changes between the mean result of wavelength retrieval maps with noise and the corresponding map without noise do not necessarily lead to a greater discrepancy to the true column.

Results regarding the relationship between standard deviation and the correction factor to calculate the measurement error from the fit error need to be addressed together. In cases where the residual structure is small, the correction factor calculated corresponds to the previously published ones, namely ≈1.5 for unfiltered noise, $\approx 2.5 - 3$ for noise filtered with 10 iterations and ≈ 4.5 for 50 iterations. If larger residual structures are present, correction factors with values below 1 are observed. Retrieved BrO SCDs differ greatly from the true value of $1.5 \cdot 10^{14}$ molec/cm^2 at these wavelength ranges (see also fig. 5.5, 5.11). For both scenarios A and B, residual structures due to the I_0 effect do not influence the standard deviation, even if the amplitude of systematic residual structures can be one order

of magnitude higher than the amplitude of induced noise and can also differ on the same order of magnitude between the different sets of RCSs. This can best be seen by comparing the average results for retrievals using uncorrected and I_0 corrected RCS (fig. 5.7). But larger residual structures lead to an increase in fit error, which results in the low correction factor equal to the ratio of standard deviation to fit error.
Two differences to the error calculation by Stutz and Platt (1996) must be noted: First, they assumed residual structures of purely statistical noise without systematic wavelength depending structures. This is violated by the residual structures. Secondly, the boundary condition in the retrieval differ from the previous study in that a shift and squeeze in wavelength is only allowed for all RCSs together and not individually. The combined wavelength shift and squeeze of the RCSs is dominated by the stronger absorber in the fit. It can be assumed that the shift of the whole set of RCSs is less erroneous as if individual shifts for each RCS would be allowed. Both differences will decrease the correction factor, the first by increasing the fit error, the second by decreasing the standard deviation.
To perform an extensive error analysis on a theoretical basis is beyond the of the scope of this work. But it appears to be advisable to use correction factors for the case of no systematic residual structures also if residual structures are present, because all effects leading to reduced correction factors are accompanied with a systematic offset of the average retrieved BrO SCDs.

5.4 Results of the advanced modelling of the BrO retrieval in volcanic plumes

Retrieval wavelength maps were calculated for advanced modelled synthetic spectra of measurements of volcanic plumes, in order to better understand the influence of the Ring effect and the I_0 effect on the retrieval results. Three different synthetic spectra with true BrO SCDs of 5, 10 and 15 $\times 10^{13}$ molec/cm^2 are used. Retrievals are performed using uncorrected and I_0 corrected RCSs.
Results of the performed study are given in Fig. 5.15, where retrieved BrO SCDs are mapped for different true SCDs and retrievals, using both together, uncorrected and I_0 corrected RCSs for better comparison. Fig. 5.16 (I_0 corrected RCSs) and 5.17 (uncorrected RCSs) depict retrieved SCDs of all absorbers to highlight possible cross correlations.

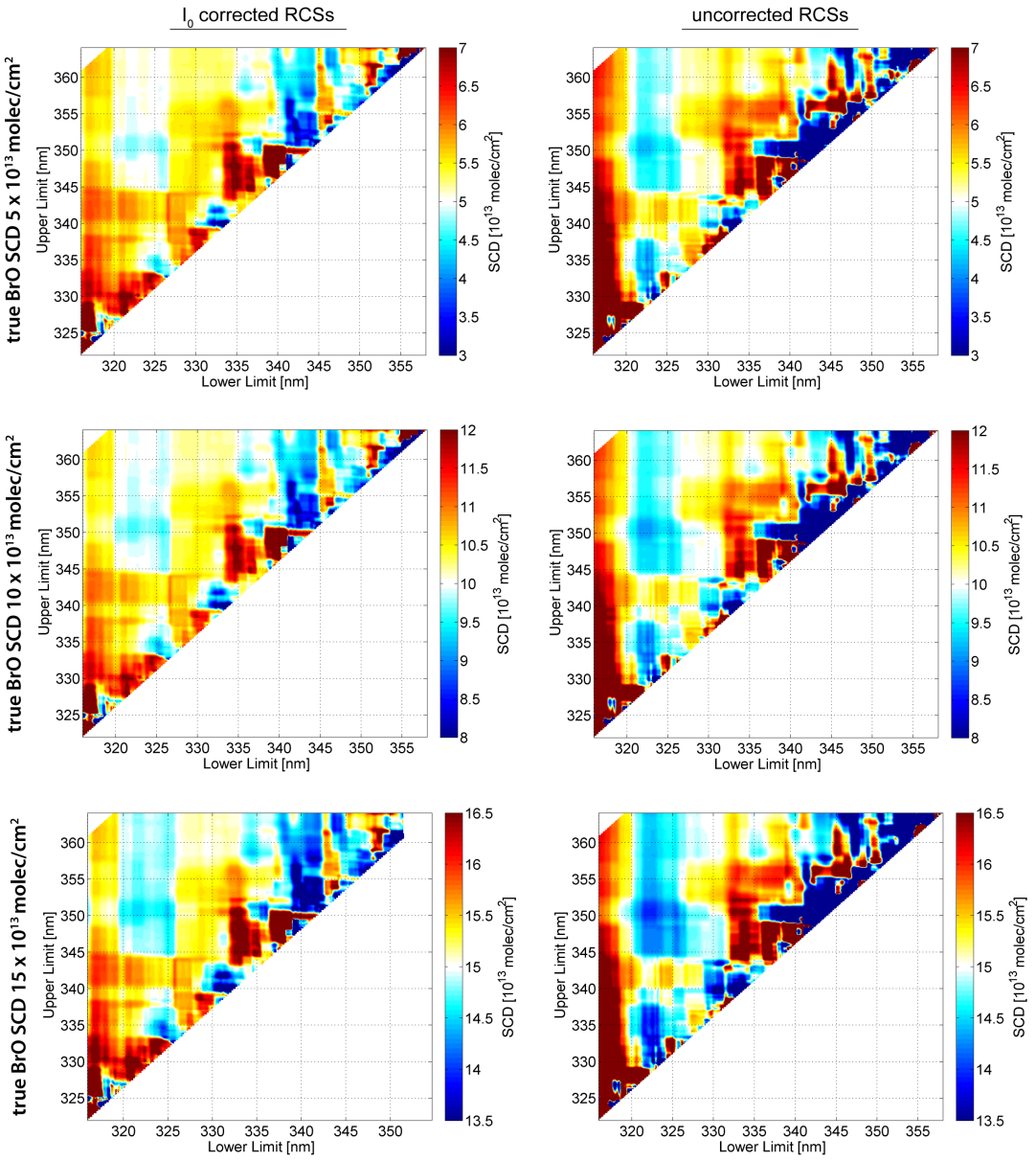

Figure 5.15. Retrievals of advanced modelled spectra of volcanic plumes. BrO SCDs are depicted for different true SCDs (5, 10 and 15 $\times 10^{13}$ molec/cm^2, top, middle and bottom row) and retrievals using I_0 corrected RCSs (left column) and uncorrected RCSs (right column). Note that the range of the colour scale is decreasing from true SCD $\pm 40\,\%$ (top row) true SCD $\pm 20\,\%$ (middle row) to true SCD $\pm 10\%$ (bottom row).

5.4.1 Varying BrO SCDs

From Fig. 5.15, it is immediately obvious that higher deviations from the true BrO SCD are retrieved compared to the simplified measurement scenario (see sec. 5.3.2). This is the case for both sets of RCSs, uncorrected and I_0 corrected. Note also that for both sets of RCSs the range of the colour scale is decreasing from true SCD $\pm 40\,\%$ (top row) true SCD $\pm 20\,\%$ (middle row) to true SCD $\pm 10\,\%$ (bottom row). The most striking observation is that wavelength depending deviations from true BrO SCDs do not change qualitatively with changing true BrO SCD. Relative deviations are approximately inversely proportional to the change of true BrO SCDs. Ranging from $\pm 40\,\%$ for a true BrO SCD of $5 \times 10^{13}\,\mathrm{molec/cm^2}$, deviations deminish to approximately $\pm 10\,\%$ for $1.5 \times 10^{14}\,\mathrm{molec/cm^2}$. These observations can be explained under the assumption that residual structures, which are induced in the retrieval by erroneous correction of the Ring effect and I_0 correction of RCSs, are not affected by changes of the BrO SCDs due to the small optical densities of the absorptions involved. The offset in retrieved BrO SCDs would be independent of the true BrO SCD and a similar dependence of relative deviations to the true BrO SCD would be observed. This shows, that relative deviations from a model run can not be simply compared to measured spectra with a different SCD of the trace gas of interest. Rather the general dependency of SCDs on the retrieval wavelength range may be used in a comparison of retrieval of modelled and measured spectra.

Compared to Test I on the simple measurement scenario, certain observations remain the same. In case of the simple scenario, uncorrected RCSs showed compared to I_0 corrected RCSs, (1) an overestimation of BrO SCDs if smaller wavelengths ($< 320\,\mathrm{nm}$) are included in the evaluation wavelength range. (2) BrO SCDs are in general underestimated for a lower wavelength limit between approximately 320 nm - 332.5 nm. (3) For a lower wavelength limit $> 332.5\,\mathrm{nm}$, BrO SCDs are overestimated. These three findings can also be observed in Fig. 5.15, when comparing relative differences of retrieved BrO SCDs using uncorrected and I_0 corrected RCSs in the fit. This reflects the previously observed dependency on the I_0 effect. Influences of the Ring effect and its correction on the retrieval dominate (or are at least comparable) to the I_0 effect for both sets of RCSs. The Ring effect seems to show similar general characteristics as the I_0 effect in terms of dependency of the retrieved BrO SCDs on the lower evaluation wavelength

limit. Retrieval wavelength ranges which are relatively stable with changes in wavelength are found in the range of 320 nm - 332.5 nm (lower limit) and > 345 nm (upper limit).
In the following, only details of the retrieval of the synthetic spectra with a true BrO SCD of 10×10^{13} molec/cm^2 are discussed. These results can be transferred with only minor deviations to the other spectra.

5.4.2 Cross-correlations between absorbers

Figure 5.16 shows all retrieved SCDs for the case of I_0 corrected RCSs. The dependency of BrO SCDs on retrieval wavelength range observed on the retrieval map may not be attributed to correlations with another single absorber in all cases. By comparing retrieval maps of BrO and HCHO, a clear anti-correlation of SCDs can be observed over greater areas of the evaluation wavelength intervals. E.g. a general anti-correlation can be seen for spectral retrieval intervals at upper limits < 345 nm, at 320 nm - 325 nm lower limit and upper limit > 345 nm, and also for a lower limit of 330 nm - 338 nm. Retrieval wavelength intervals at longer wavelengths > 338 nm exclude the strongest BrO absorption band centred at ≈ 338 nm and also show highly erroneous SCDs for most other absorber.
O_3 SCDs show a dependency to the lower limit, reflecting the monotonic falling differential optical density of O_3 with increasing wavelength. Remarkable is the general underestimation of O_3 SCDs, especially at lower wavelengths, where O_3 absorption bands should be strong enough to allow correct retrievals. This may result from a "filling in" of absorption structures by Raman scattering.
Stronger deviations are visible for retrieved SO_2 SCDs at a lower wavelength limit > 330 nm. The optical density of differential SO_2 absorptions is on the order of 10^{-4} at these wavelength ranges. Consequently, the retrieval may not be influenced much. Observed is an overestimation of SO_2 SCDs in retrieval wavelength ranges with a lower limit < 330 nm and an upper limit > 345 nm.
NO_2 SCDs show a relatively low spread over all retrieval wavelength ranges. Nevertheless, at all retrieval wavelength ranges a systematic underestimation of NO_2 SCDs occurs. Retrieval wavelength ranges yielding NO_2 closest to the true SCD may be found for upper limits < 347.5 nm. A possible explanation for the systematic underestimation is the fact that the NO_2 absorption cross sections exhibits many narrow band differential absorption structures. They are comparable in width to structures of the Ring spectrum, indicating possible cross

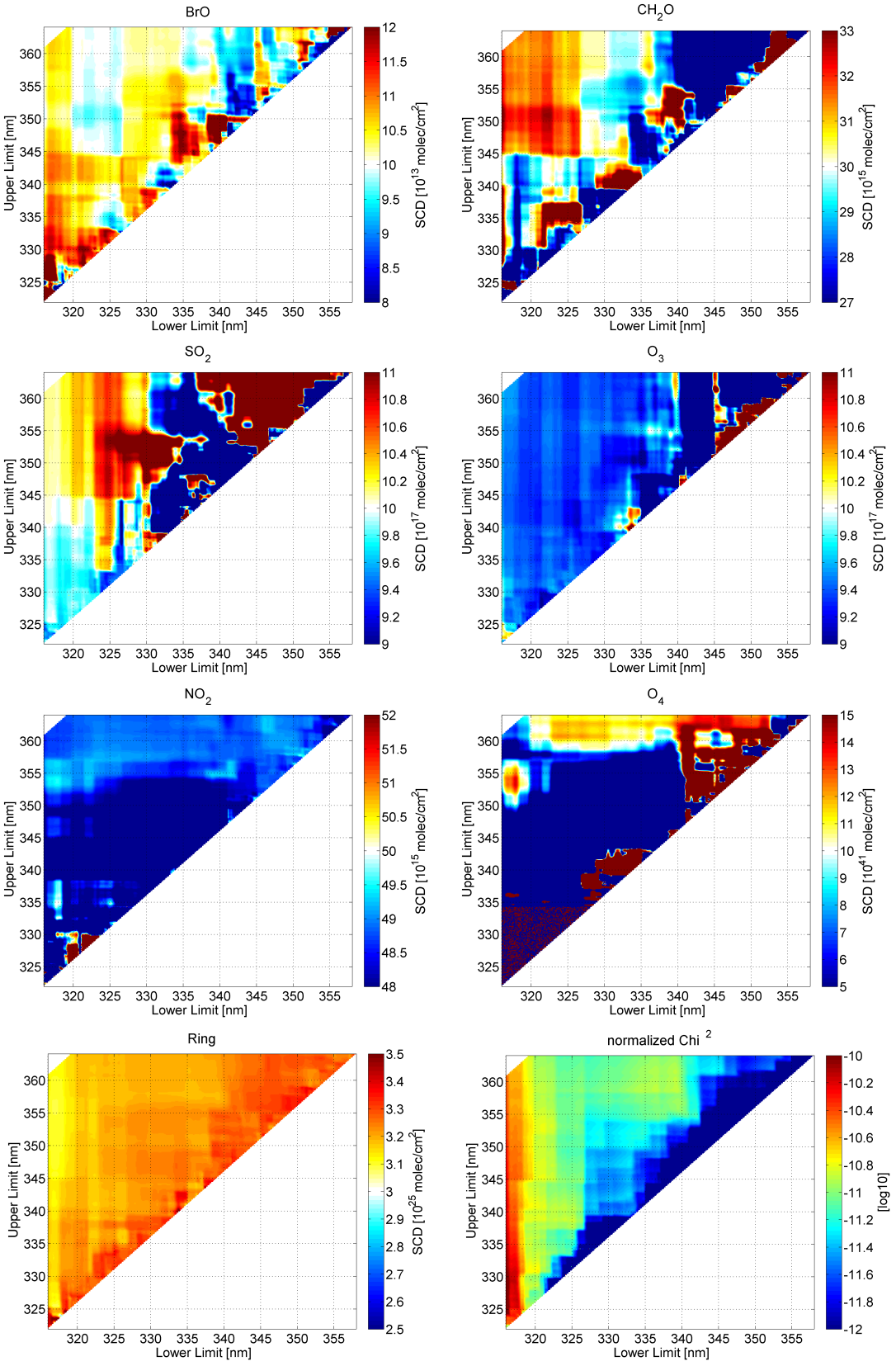

Figure 5.16. Advanced modelling of volcanic plume spectra, with a true BrO SCD $= 10 \times 10^{13}$ molec/cm^2: Depicted are retrieved SCDs of all trace gases included in the fit applying I_0 corrected RCSs.

correlations.
In the case of O_4, it must be noted that the absorption cross section of O_4 only extends to a lower limit of $\approx$ 335 nm. The first absorption band is situated between 340 nm - 347 nm. Meaningful retrievals of O_4 SCDs can only be expected for an upper limit $>$ 347 nm. Retrieval wavelength ranges yielding SCDs differing less than 50 % from the true value are only observed at lower limits of 320 nm - 337.5 nm and an upper limit $>\approx$ 357 nm.
The Ring spectrum should be retrieved at a SCD of $\approx 3 \times 10^{25}$ molec/cm^2, corresponding to $\approx$ 3% optical density. An overestimation occurs over all wavelength ranges. A possible source of cross correlation may lie in the absorption structures of NO_2 and partly of O_4. The Ring effect as modelled in construction and evaluation of synthetic spectra shows an effect on a similar or greater scale than the I_0 effect. Both simulated spectra, measurement and FRS, are subject to a Ring effect of different strength, affecting both, Fraunhofer lines and absorption lines in each spectrum differently. Thus it is expected that a Ring spectrum calculated from the FRS can not totally compensate the difference in Ring effect of both spectra.

The complexity of the retrieval can best be observed by comparing wavelength depending SCDs of all absorbers, using the changing of O_3 and SO_2 SCDs with lower limit as a guideline. Most of the features visible for O_3 and SO_2 can be encountered at retrieval maps of all other absorbers! It can not be determined, whether its source is an erroneous fit of these two absorbers or introduced by an error in Ring effect compensation.

As expected, results from the retrieval using uncorrected RCSs mostly show a greater deviation from the true SCD of respective absorbers (fig. 5.17). Correlations between different absorber SCDs are observed as already described for the case of I_0 corrected RCSs. The additional errors introduced by the I_0 effect increase these correlations in some cases. One example are retrieved BrO and HCHO SCDs for a lower limit of 320 nm - 325 nm and an upper limit of $<$ 345 nm. On the other hand it can be observed that cross correlations between absorbers are not as prominent if uncorrected RCSs are used (BrO and HCHO, lower limit of 325 nm - 332.5 nm, upper limit $<$ 345 nm). Whereas for SO_2 and O_3 greater deviations are observed over all wavelength ranges, NO_2 results are closer to the true SCD for upper limits $<$ 355 nm. It can be seen that this is not a result of a

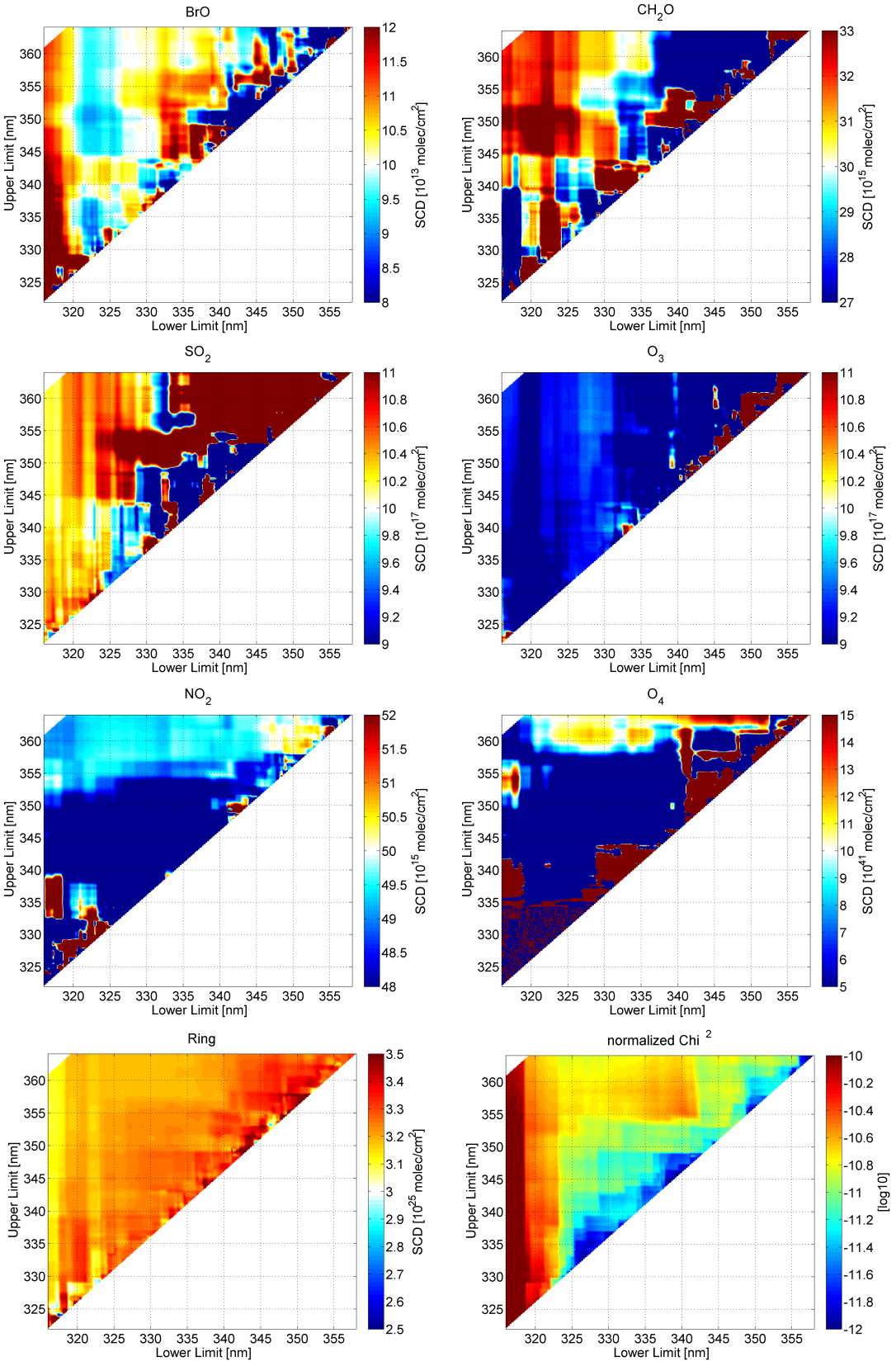

Figure 5.17. Advanced modelling of volcanic plume spectra with a true BrO SCD $= 10 \times 10^{13}$ molec/cm^2: Depicted are retrieved SCDs of all trace gases included in the fit applying uncorrected RCSs.

better fit at the respective wavelength ranges by comparing the normalized Chi^2 values for both sets of RCSs: In general, using I_0 corrected RCSs results in Chi^2 values one order of magnitude smaller than for the case of uncorrected RCSs.

5.5 Conclusions: Simplified artificial spectra

In this study, a novel technique is presented, which varies systematically the evaluation wavelength range of DOAS retrievals in order uncover systematic deviations of retrieved SCD. Examples are given on how it may be used to find optimal evaluation wavelength ranges and/or to highlight pitfalls in any DOAS retrieval. It is based on the fact that wavelength dependent residual structures (e.g. instrumental features, cross correlations between RCSs, erroneous I_0 correction, Ring effect, errors in RCSs) will lead to evaluation wavelength range depending results in contrast to unstructured noise of e.g. photonic origin.
Several tests were performed on two different measurement scenarios of passive BrO DOAS measurements to prove the concept. Scenario A reproduced Zenith-DOAS conditions of stratospheric BrO measurements in the tropics. For better comparison, it largely follows the scenarios of Aliwell et al. (2002) using synthetic and measured spectra. Scenario B is an attempt to capture typical conditions for evaluations of BrO in volcanic plumes. For these measurement conditions, this work constitutes the first systematic study of the dependency of retrieved BrO SCD on the evaluation wavelength range. Studied were the effect of uncorrected and I_0 corrected RCSs on the retrieval and their dependency on the a priori assumed SCD for the I_0 correction. Furthermore, a statistical study was performed where different structured noise was added to the synthetic measurement spectra. This allowed to draw conclusions of the effect of noise on the measurement error in the presence of systematic residual structures.
For scenario A, the tests showed that the evaluation wavelength range 346 nm - 359 nm as suggested by Aliwell et al. (2002) for respective measurements is located in the area of the wavelength parameter space, which offers least dependency on the I_0 effect and that nevertheless an I_0 correction of RCSs is mandatory. The dependency of the results on the lower end of the evaluation wavelength range results from an insufficient I_0 correction of the strong O_3 absorptions. As the absorptions are decreasing with increasing wavelength, so does the induced error and wavelength dependency of the BrO SCD. The suggested wavelength range is also confirmed by Test II, in order to minimize systematic errors.
BrO retrievals for Scenario B show a much lower I_0 dependency of the BrO SCDs on the evaluation spectral range, mostly due to an about 100-times weaker total O_3 SCD. Whereas the fit applying I_0 corrected RCSs shows a good agreement with the true BrO SCD at most wavelengths, misleading values are produced for uncorrected RCSs. An evaluation wavelength range with a lower wavelength limit

between 320-335nm is found to be optimal because here the differences are smallest between retrievals applying uncorrected and I_0 corrected RCSs. In practice, the absorber strength at short wavelengths is most variable because of the great variability of volcanic SO_2 emissions and O_3 absorptions in early and late hours of the day. To ensure a comparable evaluation of data, measurements should be performed at the upper range of the suggested interval. A final conclusion of an optimal retrieval wavelength interval can not be made without additional tests on measured data. Small variations in the assumed SCDs to be applied in the I_0 correction of RCSs only lead to minor effects on the retrieved BrO SCDs.
The test of different noise structures showed the qualitatively same results for both scenarios. In general, the random noise did not lead to changes of the average SCDs compared to retrievals without noise. The standard deviation of results and thus the correction factor to calculate measurement errors from fit errors followed the error calculation of Stutz and Platt (1996) at evaluation wavelength intervals, at which the fit did not result in larger residual structures. If the assumptions in Stutz and Platt (1996) are not met as in the case of systematic residual structures, it was shown that an overestimation of the fit error occurs if correction factors are applied to calculate measurement error from fit error. The nature of a residual structure can not be deduced from a single measured spectrum. Keeping in mind that systematic residual structures (for which the correction factor is overestimated) most likely go hand in hand with a systematic offset of the retrieved values, error calculation by correction factor still offers the best estimate.
Some examples of application of retrieval wavelength mapping as a novel tool are given with these two scenarios. They may serve as guidelines on how optimal evaluation wavelength ranges can be identified for other scenarios. Furthermore, the potential of the technique lies in the combined study of synthetic and measured spectra. By studying synthetic spectra, interpretation of results is aided by knowledge of the SCDs used to construct the spectra. Measured spectra usually lack this a priori knowledge and thus an interpretation is not possible whether results at certain evaluation wavelength ranges are correct. These disadvantages of measured spectra might be circumvented by designing certain tests, where boundary conditions can be set to at least some of the parameters. For example, "zero" samples can be devised where only negligible SCDs should occur. In the case of Max-DOAS measurements, different FRS can be compared, whereas night-time measurements of LP-DOAS systems should not yield BrO or other photochemically produced species.

The application examples of retrieval wavelength mapping only displayed retrieved SCDs. The possibilities of the presented technique are not restricted to the retrieved column densities, but many other important characteristics of a fit can be displayed in the same way. For example, cross sensitivities between trace gases, retrieval errors, wavelength shifts and squeezes performed by the algorithm can be investigated by this method.

6 BrO: Retrieval wavelength mapping of measured spectra

When interpreting evaluation wavelength maps of measured spectra, one of the major difficulties is that the true SCDs of absorbers are usually unknown. In order to approximate the true SCDs measured, it is necessary to use additional information, or or to make additional assumptions on the correct state of the atmosphere. Without additional information, the "Zero Test" can be applied to measured spectra. In this test, reference spectra are evaluated against each other, taken outside the plume at the same measurement geometries and in close proximity in time. Evaluation procedures are given for the "Zero-Test" (Fraunhofer Reference vs. Fraunhofer Reference) in sec. 6.1 and for spectra of volcanic plumes in sec. 6.3. The different data sets are described briefly in sec. 6.3.1 and 6.4.2. For a complete description of both measurement campaigns, the reader is referred to the chapters 8 and 8, respectively.

6.1 Zero-test

One test which does not require any additional information is the construction of retrieval wavelength maps by evaluating different FRS recorded in close proximity in time. The state of the atmosphere does not change significantly, and changes in measurement geometry are only present in small changes in the solar zenith and azimuth angle. During common measurement routines, FRS are recorded at least every 10-20 minutes. Their close proximity in time justifies this approach. For both data sets used (sec. 6.3.1, 6.4.2), pairs of consecutive recorded FRS are evaluated against each other. The one recorded earlier is used as reference spectrum and the later as measurement spectrum. Since both data sets are recorded before midday, the SZA decreases. Thus retrieved SCDs should reflect minor changes in stratospheric absorbers (O_3, NO_2) and the strength of the Ring

effect. Whereas for the stratospheric absorbers retrieved SCDs are expected to be negative, the Ring spectrum may be retrieved at positive fit coefficients, e.g. in the case of white, condensed plume. Larger and systematic deviations from zero of each absorber's SCD are an indication for wavelength depending systematic structures, which may be due to cross correlation of absorbers, of instrumental or other origin (e.g. improper fit of the Ring spectrum). It can not be ruled out that evaluation wavelength ranges other than the ones that yield negligible SCDs will lead to correct results if absorbers are present. Nevertheless, with this test evaluation wavelength ranges are found, which result in a correct zero baseline of retrieved SCDs.

6.2 Plume measurements

Wavelength evaluation maps are created for plume measurements for each data set. In contrast to the "Zero-Test" and artificial spectra, different plume measurements will always yield different SCDs, because a different plume is observed. This is especially true, if strong variations of volcanic emissions are present on short time scales. If retrieval maps of different measurement spectra are compared, it is necessary to only use spectra, which were recorded under similar measurement conditions and volcanic emission strength.
Plume measurements of both data sets were evaluated against Fraunhofer reference spectra taken during the same respective measurement routine, thus spectra which are evaluated against each other were recorded within 15 min. The used cross-sections and SCDs applied in the I_0 correction are given in table 6.1. SCDs for the I_0 correction had to be assumed a priori. For BrO, NO_2, CH_2O and O_4, this was based on test evaluations at the wavelength range 332 nm - 352 nm Bobrowski and Platt (2007). SO_2 and O_3 were estimated by a retrieval in a wavelength range of 315 nm - 325 nm due to the increased sensitivity of both trace gases at that wavelength range and lesser successibility of SO_2 to radiative trasnfer effects. In the case of the measurements taken at Pacaya volcano, Guatemala, lower SCDs of NO_2 are expected due to low local pollution and the absence of greater highways or cities in close vicinity to the volcano. Also, possible air pollution is released in atmospheric layers below the volcanic plume and instrument. In comparison, higher NO_2 and O_3 SCDs are expected from measurements at Mt. Etna. Since the instrument was situated at an altitude 2.5 km below the crater, a prolonged light path

inside the planetary boundary layer can be assumed together with higher local air pollution due to relative high traffic, population density and frequent wild fires.

6.3 BrO retrieval of measured spectra

As already described above, two different kinds of evaluation wavelength maps are constructed for the different data sets. One evaluation scenario, where no absorption structures should be present (zero-sample) and evaluation scenario to be applied to plume spectra. The DOAS fitting process included a 3^{rd} order polynomial to account for broad band scattering effects and a 0^{th} order polynomial fitted in intensity space to correct for stray light in the spectrometers.
For the Zero-Test and evaluation of plume spectra, the same RCSs are used. In case of the evaluations of the zero-samples, the RCSs were not corrected for the I_0 effect, because only negligible absorber structures are expected. For retrieval of trace gases in volcanic plumes, the RCSs were I_0 corrected with a fixed column for each trace gas (tab. 6.1). An iterative retrieval approach is not feasible, where SCDs for an I_0 correction are determined by a previous retrieval with uncorrected RCSs, because the computational needs are too high. They result from the high amount of convolutions to be performed in the correction process rather then the additional retrievals necessary.
The evaluation wavelengths intervals were varied on the same range as for the theoretical studies. The retrieval was varied in the lower wavelength limit between 316 nm - 356 nm and in the upper wavelength limit between 322 nm - 364 nm. Again the range of the interval was limited to 6 nm - 45 nm. Each measurement or Fraunhofer spectrum was calibrated against a solar spectrum (Kurucz, 2005) prior to the fitting process to ensure correct wavelength to pixel alignment. The evaluation wavelength maps created are interpolated to a wavelength grid in these wavelength boundaries with a step width of 0.1nm. This is the same grid as used in the theoretical studies and the approach ensures that slight shifts in wavelength pixel mapping due to temperature induced shifts of the calibration in the spectrograph are compensated.

6.3.1 Spectra used in sensitivity tests from Pacaya volcano

The first data set was recorded at volcano Pacaya, Guatemala in February 2010, located about 20 km south of Guatemala city. The volcano has a summit height of 2550 m at which the measured gases were emitted. The instruments were operated 1.5 km away from the vent at an altitude of 2250 m. The measurements were performed between 9:30 am and 10:30 am local time with an QE65000 spectrometer from OceanOptics with an optical resolution of 0.75 nm. Two different sets of spectra of the volcanic plume were taken, one at different azimuth and one at different elevation angles. For the study on evaluation wavelength ranges, only the set measuring the plume at different elevation angles is used. It resembles the most common measurement set-up and allows comparison to retrieval wavelength maps constructed from the data gathered at Mt. Etna. Seven scans in vertical direction were performed with Fraunhofer reference spectrum taken at 0° SZA. The volcanic plume is detected at elevation angles between 8° - 20° above the horizon, with maximum BrO and SO_2 SCDs at 12° and 16°. From this data set, the FRS are used for the "Zero-Test", using consecutive recorded FRS. The FRS recorded earlier is used as reference, against which the later one is evaluated as measurement spectrum. Measurements taken at 12° elevation angle vs. FRS at are evaluated for the retrieval maps of plume spectra, since the retrieval is more sensitive at 12° elevation angle to other (tropospheric) absorbers in the ambient atmosphere than at 16°.

Trace gas	Temperature [K]	Reference cross-section	Pacaya [molec · cm^{-2}]	Etna [molec · cm^{-2}]
BrO	298	Fleischmann et al. (2004)	7.5×10^{13}	1×10^{14}
O_3	273	Burrows et al. (1999)	3×10^{17}	7.5×10^{17}
NO_2	294	Vandaele et al. (1998)	5×10^{14}	5×10^{15}
O_4		Hermans et al. (2003)	2×10^{42}	2×10^{42}
SO_2	298	Vandaele et al. (2009)	10×10^{17}	15×10^{17}
CH_2O	298	Meller and Moortgat (2000)	1.5×10^{16}	1.5×10^{16}

Table 6.1. Reference cross sections and their respective SCDs used for the I_0 correction. For each data set slightly different values are assumed due to the different atmospheric conditions and emission strength of the volcano. For the Zero-Test, the same reference cross sections are used but without I_0 correction.

6.3.2 Spectra used in sensitivity tests from Mt. Etna

The data set used in this study was obtained at Mt Etna, Italy on July 12^{th}, 2008. Mt. Etna's summit is at an altitude of 3330 m, at which the main vents emit. The instrument incorporating a HR2000 spectrometer (OceanOptics) was located in the village Milo (780 m a.s.l.) at a distance of 10 km to the crater. Its optical resolution is 0.4 nm. The plume was not blown directly over Milo, but was measured approximately at its centre with an elevation angle of 26° above the horizon and the reference taken at 72° elevation at the opposite azimuth direction. A total of 16 consecutive measurement scans are used for this study, recorded between 9 am and 1 pm UTC. Each scan consists of two FRS and plume measurements taken alternately. For the Zero-Test, the two FRS of each scan are evaluated against each other. The time difference between recording the two FRS is on the order of 10min. Thus the spectra acting as references in the test are all recorded at a lower SZA than the corresponding measurement spectra. For the plume measurements all pairs of plume measurement and FRS spectra are evaluated, resulting in a total of 32 different measurements.

6.4 Results

6.4.1 Pacaya volcano

Zero-Test: Comparing Fraunhofer references

The Zero-Test for spectra gathered at Pacaya volcano, Guatemala, is depicted in Fig. 6.1. The retrieval wavelength maps correspond to the average of seven reference spectra pairs evaluated against each other. Zero SCDs are expected for absorbers which columns are independent on the solar zenith angle (HCHO, SO_2, O_4). O_3, NO_2 should show slightly negative columns because of the decreasing SZA between FRS evaluated against each other. The presence of BrO in the stratosphere and consequent dependence of retrieved values on SZA are negligible, due to its relative low column and small changes in SZA. The fit coefficient of the Ring spectrum is expected to have slightly positive values, since the Ring effect should diminish with decreasing SZA. The reason for the switch of sign when comparing absorber and Ring spectrum is, that one is actually an absorber and

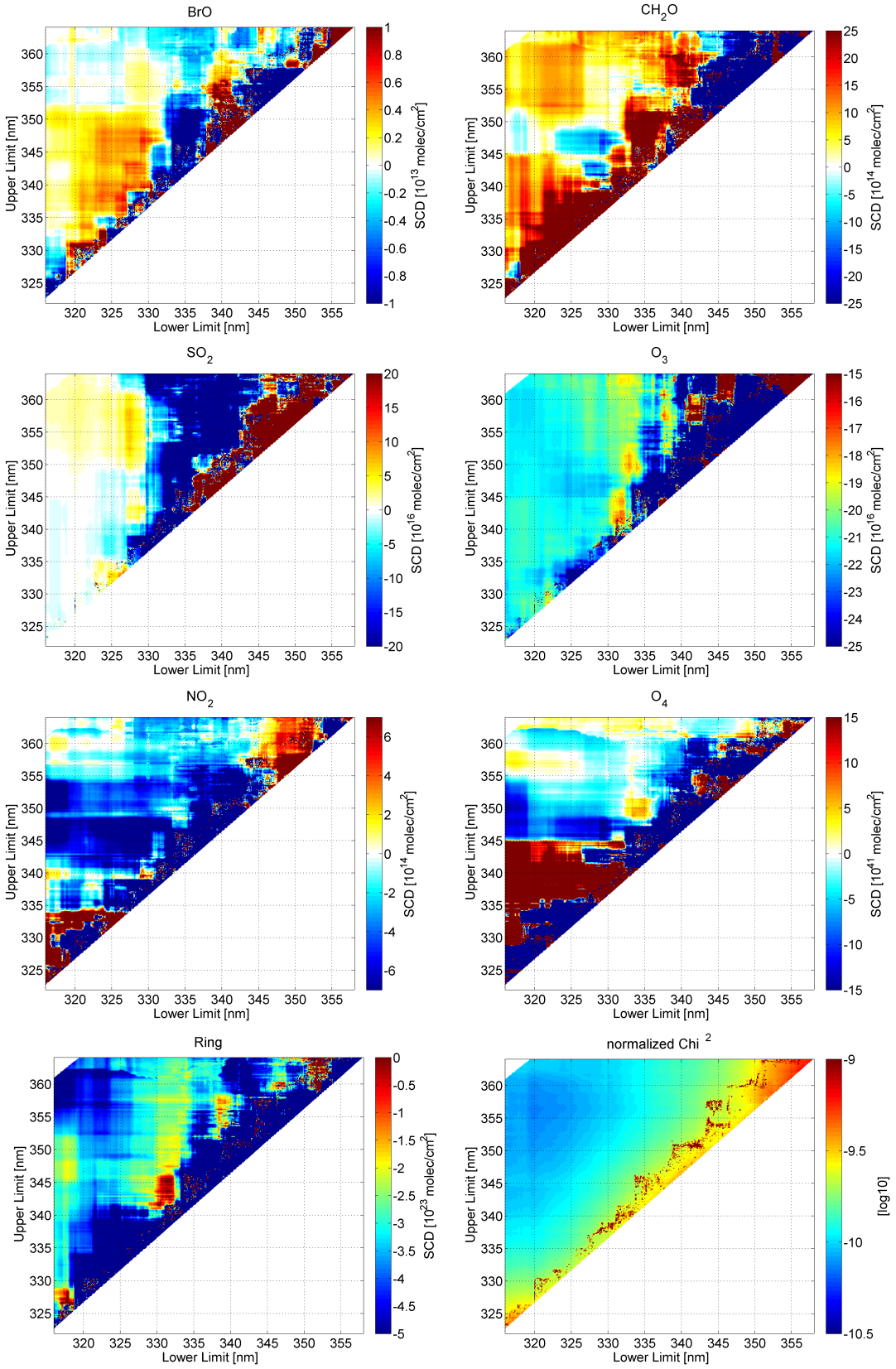

Figure 6.1. Zero-Test of seven consecutively taken FRSs at Pacaya volcano, Guatemala. Depicted are average retrieved SCDs. Note that for the O_3 and Ring spectrum a different colour code is used. Due to the decreasing SZA with time, SCDs < 0 molec/cm^2 are expected for those absorbers.

the other causes a "filling-in" of absorption lines.
In the case of BrO, it is surprising that all retrievals applying a lower wavelength limit $< 330\,\text{nm}$ and an upper wavelength limit $< 352.5\,\text{nm}$ yield positive BrO SCDs. Although these columns are not higher than $\approx 0.75 \cdot 10^{13}\,\text{molec/cm}^2$, they are on the order of 10 % of average BrO SCDs measured (see sec. 6.4.1).
When comparing BrO with HCHO SCDs, possible anti-correlations are observed at almost all wavelength retrieval intervals with an upper limit $> 345\,\text{nm}$. Both absorbers are retrieved with SCDs close to zero for a lower limit of 330 nm - 332.5 nm and an upper limit of 350 nm - 357.5 nm. Even for these retrieval wavelength intervals BrO SCDs are slightly elevated. Other retrieval wavelength intervals with low BrO SCDs must be treated with care, since HCHO SCDs are overestimated, e.g. at lower wavelength limits $< 330\,\text{nm}$.
SO_2 SCDs are retrieved close to zero mostly at smaller wavelengths, corresponding to the higher differential absorption structures and thus greater sensitivity at those wavelengths. Deviations from zero SCDs at lower limits $< 332\text{nm}$ are still acceptable due to the corresponding small optical densities of SO_2.
O_3 and NO_2 show slightly negative values as expected (see above). A true SCDs cannot be assigned to these gases because of possible absorption structures of stratospheric origin. Nevertheless, evaluations at a lower limit 332 nm - 335 nm and upper limit of 347.5 nm - 353 nm yield elevated values, which should easily be detectable at wavelength ranges with greater sensitivity to O_3 (lower limit $< 330\,\text{nm}$).
Average fit coefficients of the Ring spectrum are very close to 0, but at negative values. It must be noted that differential structures at these values only correspond to optical densities of less than 5×10^{-4}. Thus retrieved coefficients do not indicate erroneous fits, but rather a very low aerosol load in the atmosphere above the instrument, leading to the undetectable change of the Ring effect between two spectra taken at 90° elevation angle.

Judging from this test, the above described intervals (lower limit 330 nm - 332.5 nm, upper limit 350 nm - 357 nm) are advised for BrO retrievals, for the following reasons:

1. These intervals show the smallest cross correlation of BrO and HCHO with retrieved SCDs close to zero
2. Retrieval wavelength ranges including smaller wavelengths are avoided with possible strong O_3 and SO_2 absorptions during plume measurements

3. Retrieved O_3 and SO_2 SCDs correspond closely to SCDs evaluated at wavelength intervals more sensitive to those absorbers (starting at lower limits).

4. Fit coefficients of the Ring spectrum correspond best to the expectations

Retrieval maps of plume measurements, Pacaya

The retrieval maps shown in fig. 6.2 are the average of seven retrieval maps, constructed for measurements taken at 12° elevation angle and evaluated against FRSs at 90° elevation angle. A great diversity of retrieved BrO SCDs depending on wavelength ranges is observed. BrO SCDs range from $1 \cdot 10^{13}$ molec/cm^2 to more than $10 \cdot 10^{13}$ molec/cm^2. Disregarding results of retrieval wavelength ranges prone to retrieval errors (lower limit < 320 nm and > 332.5 nm, upper limit < 345 nm, see also sections 5.3.2 and 5.4), variations are still observed between approximately $3{\cdot}10^{13}$ molec/cm^2 and $6.5{\cdot}10^{13}$ molec/cm^2. These variations of BrO SCDs are mirrored by anti-correlating HCHO SCDs ($(10 - 30) \cdot 10^{15}$ molec/cm^2). Whereas for the advanced modelled spectra not all retrieval wavelengths showed this strong anti-correlation of BrO and HCHO, in this set of spectra from volcanic plumes these anti-correlations are observed at all retrieval wavelengths with a lower limit < 340 nm.
SO_2 and O_3 SCDs are varying only on the order of 25 % if retrieved SCDs above lower limit of 332.5 nm are disregarded. The true average SCD for both absorbers can be estimated to be in the range of (8 - 10)$\cdot 10^{17}$ molec/cm^2 for SO_2 and $\approx 2.5 \times 10^{17}$ molec/cm^2 for O_3, judging from SCDs retrieved at smaller wavelengths (lower limit < 320 nm), where both absorber exhibit strong differential absorption features. Since BrO and HCHO do not have such dominating absorptions, their true SCDs cannot be estimated in the same manner.
NO_2 can not be detected at significant columns, although for retrieval ranges with a lower limit < 334 nm and an upper limit > 354.5 nm a sudden increase in NO_2 SCDs is apparent. This increase on the order of $2 \cdot 10^{15}$ molec/cm^2 can be regarded as an artefact, corresponding to optical densities of the differential cross-section of less than $5 \cdot 10^{-4}$. Nevertheless, retrieval ranges in this intervals should be avoided because unexpected influences on the retrieval can not be ruled out. These slightly enhanced NO_2 SCDs go hand in hand with a slight increase in retrieved O_4 SCDs and a decrease in the Ring effect. Both absorber strengths are in the commonly expected range. The positive values of the fit of the Ring spectrum agree with the visual observations of a condensed, white plume and thus a decrease in the Ring

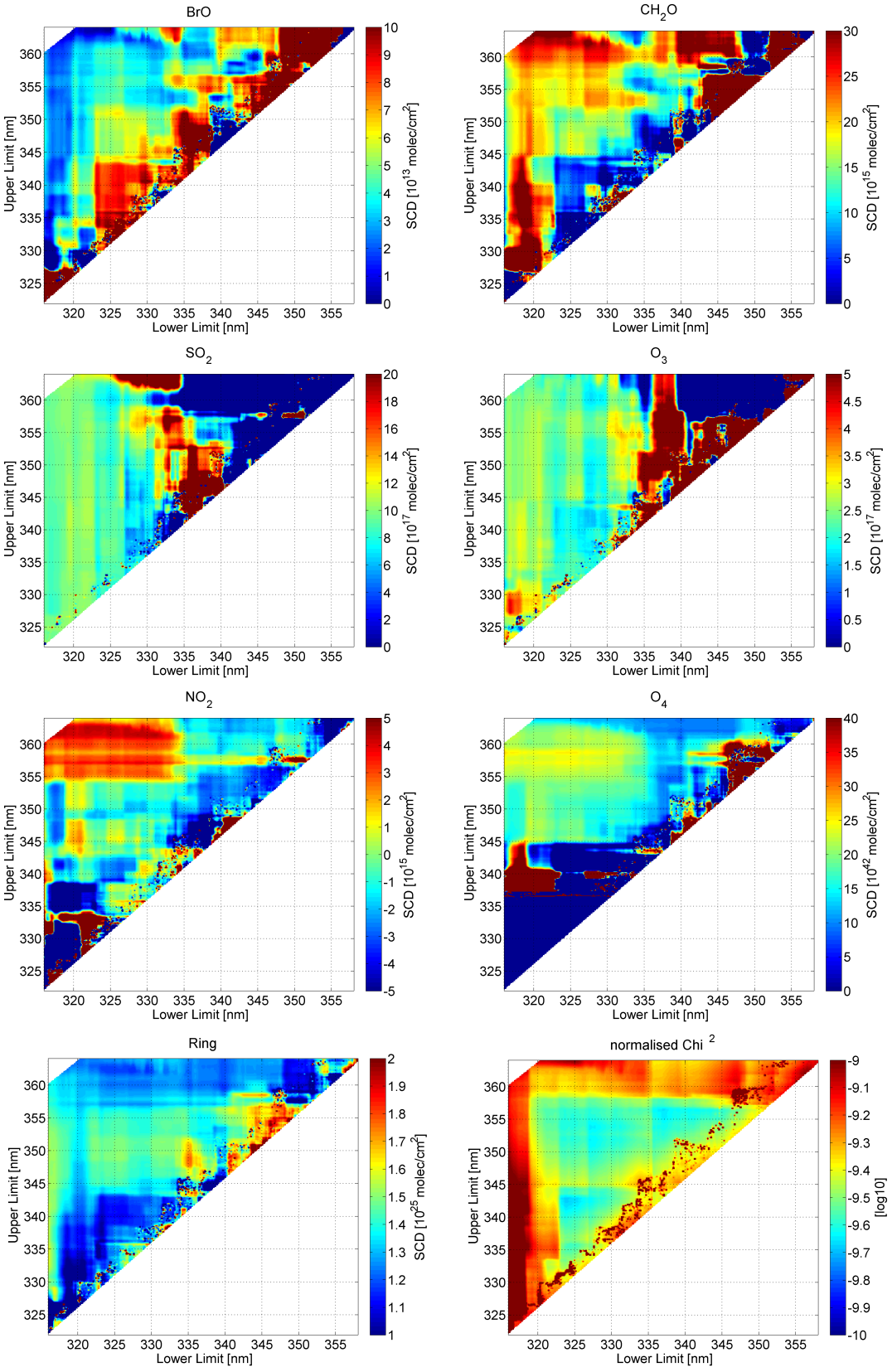

Figure 6.2. Average of seven retrieval wavelength maps constructed for spectra taken of the plume of Pacaya volcano, Guatemala. Plume spectra are recorded at 12° elevation angle and the FRS at 90°.

effect compared to the FRS at 90° elevation angle.
Without additional knowledge of the state of the atmosphere, it is not possible to judge which retrieval range yields SCDs closest to the true ones. Results from the plume measurement are compared to the Zero-Test and results of the advanced modelled spectra in sec. 6.5.

6.4.2 Etna

Zero-Test, Mt.Etna

For the Zero-Test of spectra gathered at Mt. Etna, 16 pairs of FRS spectra are evaluated. The averaged retrieval maps are depicted in fig.6.3. BrO SCDs do not show greater deviations from zero, except for an upper limit between 350 nm - 352 nm, disregarding retrieval wavelength ranges with a lower limit > 338 nm and an upper limit < 345 nm.
Anti-correlation of HCHO SCDs to BrO SCDs are visible, but not as pronounced as in the Zero-Test of spectra taken at Pacaya (fig. 6.1). The slightly enhanced BrO SCDs (upper limit 350 nm - 352 nm) may result from cross-correlation with the HCHO SCDs, which are diminished in the same retrieval wavelength ranges.
SO_2 is not detected at wavelength ranges starting at lower limits < 325.5 nm, following expectations. If evaluated at longer wavelength ranges (lower limit 325.5 nm - 332.5 nm), retrieved columns are increased, but impact on the retrieval of other trace gases may not be severe due to the very small optical densities of SO_2 at these SCDs and wavelengths.
O_3 is detected at elevated SCDs at $\approx 1 - 4 \cdot 10^{16}$ molec/cm^2, although slightly negative O_3 SCDs are expected with a decreasing SZA between reference and measurement spectrum. The observed O_3 SCDs and corresponding optical densities of differential absorptions are very small ($< 10^{-4}$ optical density) at all retrieval wavelength ranges.
NO_2 SCDs are also corresponding to negligible optical densities (upper limit > 342.5 nm).
O_4 SCDs are in the range of (-15 - 5)$\cdot 10^{41}$ molec/cm^2. Lower SCDs are retrieved as long as the greater absorption features are excluded from the retrieval wavelength range (absorption band centred around 360nm), but again the SCDs are corresponding to only negligible optical densities.
The Ring spectrum exhibits higher fit coefficients in comparison to the Zero-Test of measurements at Pacaya volcano (sec. 6.4.1). Their positive value agrees with

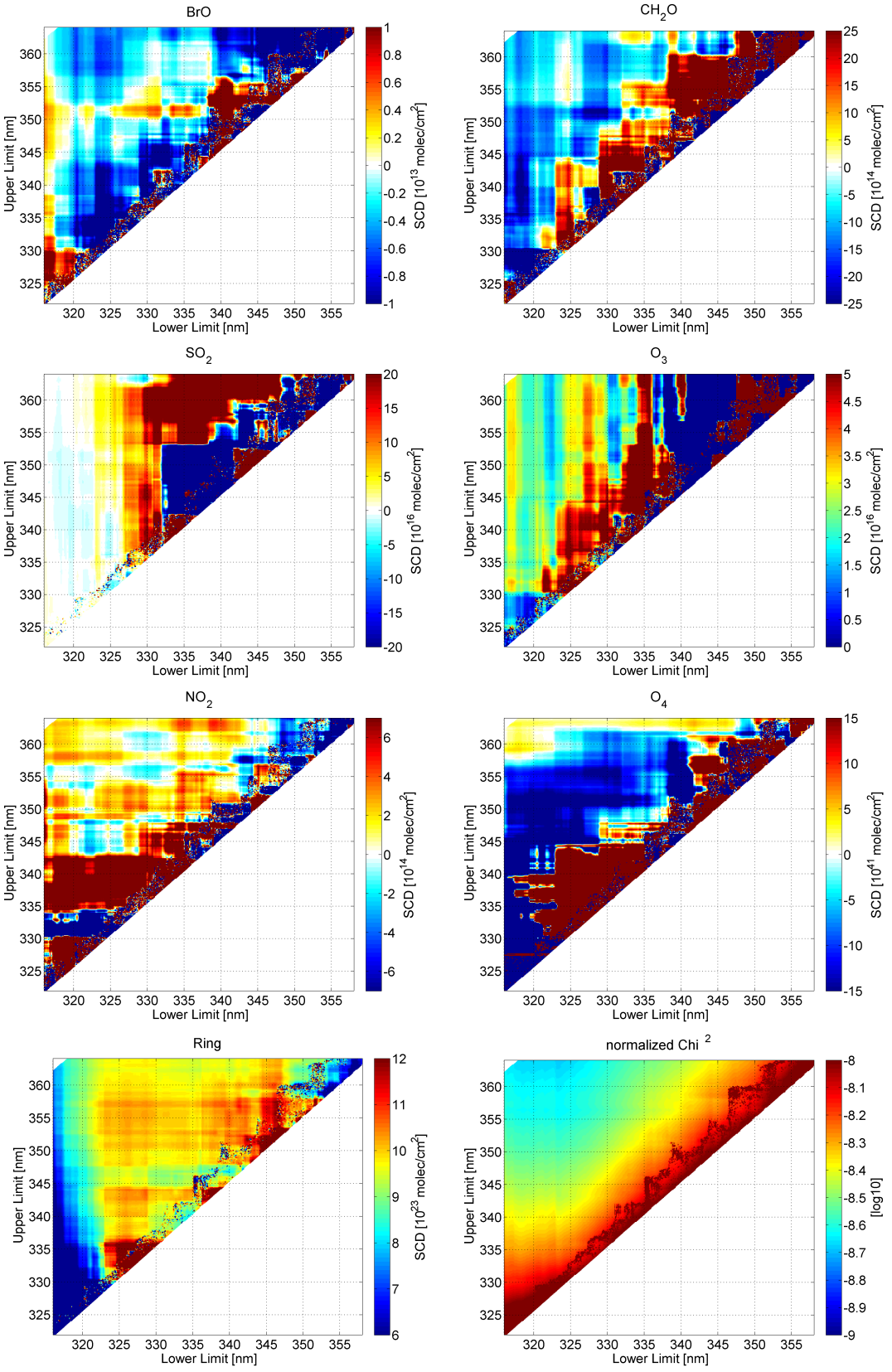

Figure 6.3. Zero-Test of 16 consecutively taken FRSs at Etna, Sicily. Depicted are average retrieved SCDs. Note that for O_3 and the Ring spectrum a different colorbar is used.

expectations as already described in sec. 6.1.

Based on the results of this test, several optimal retrieval wavelength ranges are investigated further. Priority is given to negligible BrO and HCHO SCDs, since their cross correlation is one of the biggest source of variations when evaluating plume spectra. To avoid possible strong O_3 and SO_2 absorptions, retrievals at wavelengths > 325 nm are strongly advised. Thus possible retrieval wavelength ranges might be found at a lower limit of 325 nm - 327.5 nm till an upper limit of 352.5 nm - 357.5 nm, where both BrO and HCHO show small deviations from zero. Also retrieval ranges at a lower limit 330 nm - 332.5 nm till an upper limit 352.5 nm - 357.5 nm show similar characteristics.
Differences at both interval ranges are observed for SO_2 and O_3 SCDs. Whereas the interval range at small wavelengths exhibits SO_2 SCDs at $\approx 5 \cdot 10^{16}$ molec/cm^2 and O_3 at $\approx 3 \cdot 10^{16}$ molec/cm^2, the interval range at the lower limit of 330 nm - 332.5 nm yields average SCDs of $\approx$(10 - 15)$\cdot 10^{16}$ molec/cm^2 (SO_2) and $\approx 1.5 \cdot 10^{16}$ molec/cm^2 (O_3). Variations of SO_2 SCDs between both interval regions can be neglected due to diminishing SO_2 cross section at longer wavelengths. O_3 on the other hand follows theoretical expectations better at the retrieval wavelength regions 330 nm - 332.5 nm (lower limit).

Plume measurements, Etna

In order to study cross correlations of absorber cross sections depending on the retrieval wavelength range, 32 spectra of the plume of Mt. Etna are used to construct retrieval wavelength maps. The average SCDs for all absorbers included in the retrieval are plotted in fig. 6.4. Focusing on retrieval ranges with a lower limit of 320 nm - 338 nm and an upper limit of > 345 nm, it is obvious that BrO and HCHO SCDs anti-correlate. BrO SCDs vary between (3 - 10)$\cdot 10^{13}$ molec/cm^2, HCHO SCDs between (10 - 40)$\cdot 10^{15}$ molec/cm^2. Certain features are visible in the retrieval of plume spectra, which were already observed for the Zero-Test. A possible underestimation of HCHO occurred at lower limits of 327.5 nm - 330 nm and upper limits of > 345 nm, which is also reflected in fig. 6.4. For BrO some joint features for both type of measurements are present (e.g. dependence of retrieved SCDs to lower limit at < 325 nm). SO_2 SCDs are not varying extensively at lower limits < 328 nm, although the amplitude of the differential SO_2 cross section is steadily decreasing with increasing wavelength. A gap of retrieved SCDs

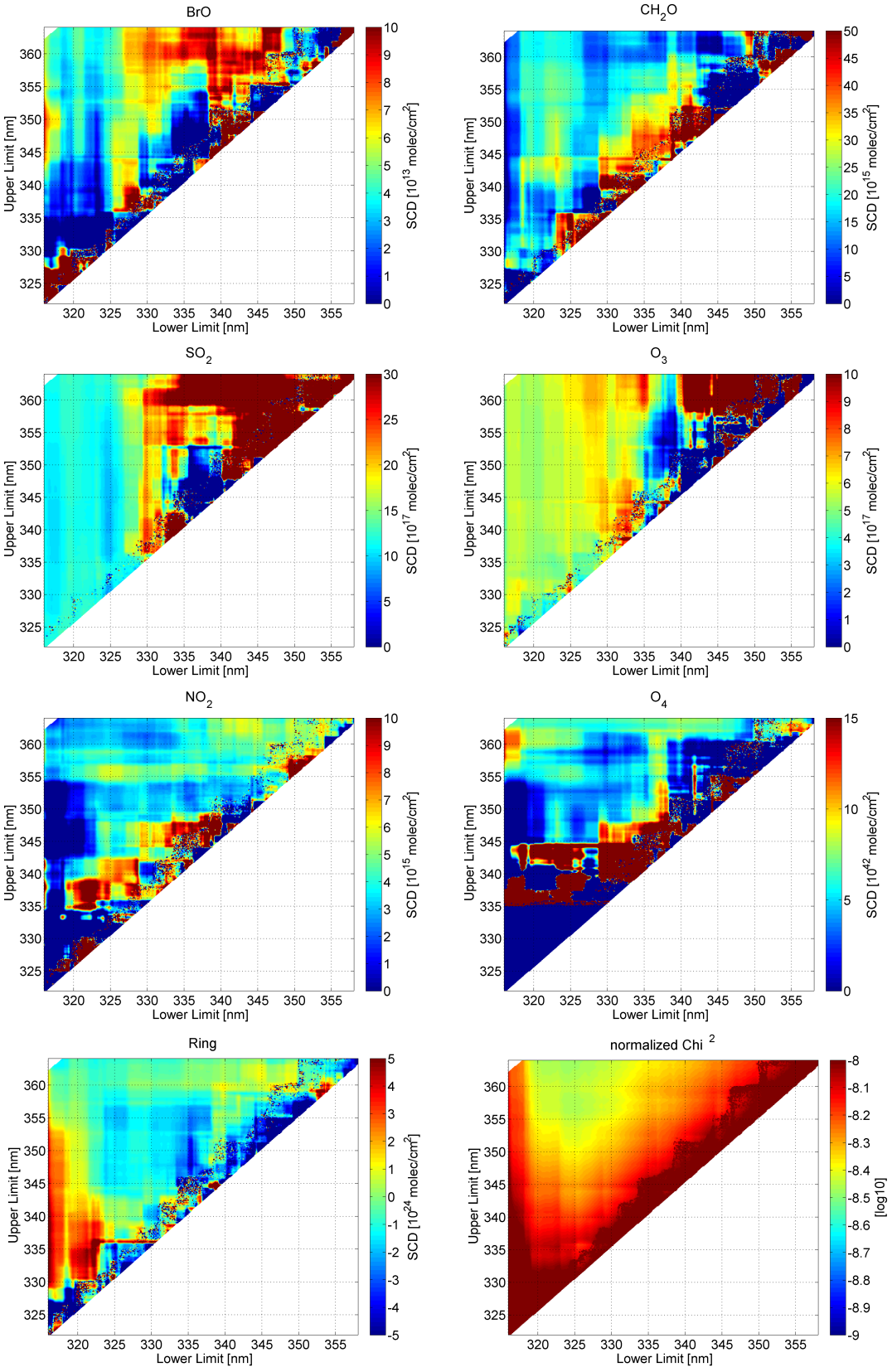

Figure 6.4. Retrieval using plume spectra recorded at Mt. Etna. Shown is the average of 32 retrieval wavelength maps, constructed for spectra taken between 9:00 and 13:00h UTC on July 12^{th}, 2008.

occurs at 330 nm lower limit, corresponding to a minimum of the differential SO_2 cross section. In contrast, O_3 SCDs do not exhibit strong variations in SCDs for retrievals $<$ 335 nm, ranging from (4.5 - 6.5)$\cdot 10^{17}$ molec/cm^2. NO_2 shows an increase in retrieved SCDs for an upper limit of 355 nm - 357.5 nm. This can be regarded as an artefact. If longer wavelengths are included in the fit range, retrieved SCDs are diminished again although the differential cross-section of NO_2 is increasing with increasing wavelengths. The Ring spectrum is measured mostly at negative values or close to zero at wavelengths $>$ 325 nm (upper limit).
Results from the plume measurement are compared to the Zero-Test and results of the advanced modelled spectra in sec. 6.5.

6.5 Comparison of measurements and advanced modelled spectra

In order to find an optimal BrO retrieval wavelength range, results from the advanced modelled spectra and from measured spectra (Zero-Test and plume measurements) need to be compared. In this section, first results from the simulated spectra are compared against results from measured spectra recorded at both volcanoes. Secondly, results from the Zero-Test and plume spectra are discussed together, followed by a conclusion and advise on optimal retrieval wavelength range of BrO based on these tests.

6.5.1 Modelled vs measured spectra

Fig. 6.5 and 6.6 attempt to display all results in a comprehensive, if somewhat condensed way. In both figures, results of the plume measurements of Pacaya and Etna are colour coded. The overlayed contour plot in dashed lines depicts results from the advanced modelled spectra with a true BrO SCD of $10 \cdot 10^{13}$ molec/cm^2. the white dashed line marks deviations from the true BrO SCD by $\pm 1\,\%$, the black dashed line by $\pm 1.5\,\%$ (to aid in orientation), whereas grey dashed lines denote variations of $\geq 2\%$ in steps of $1\,\%$. Retrieval results for both sets of RCSs are given. In the top row, the contour plot depicts results with I_0 corrected RCSs, the bottom row with uncorrected RCSs.
Changes in BrO SCDs with retrieval wavelength intervals should occur at the same wavelength coordinates, if the model reflects real measurement conditions. The measured spectra show far greater deviations in SCDs than the simulated measurement predicts. This might be a result of smaller BrO SCDs measured in the spectra (see sec. 5.4). The comparison has a quantitative character since many changes in measured spectra are not found in the modelled ones. It is apparent that the retrieval of the synthetic spectrum using I_0 corrected RCSs predicts changes in BrO SCDs much better than a synthetic spectra evaluated with uncorrected RCSs. This can be observed, e.g., for the erroneous fits at a lower limit $> 333\,$nm and an upper limit $< 352.5\,$nm in the magnified maps in the right columns of fig. 6.5 and 6.6. The strong variations are well simulated with synthetic spectra applying I_0 corrected RCSs, whereas retrievals using uncorrected RCSs predict similar strong changes at $\approx 332\,$nm lower limit. Also other dependencies on the lower limit are better captured by the I_0 corrected RCSs.

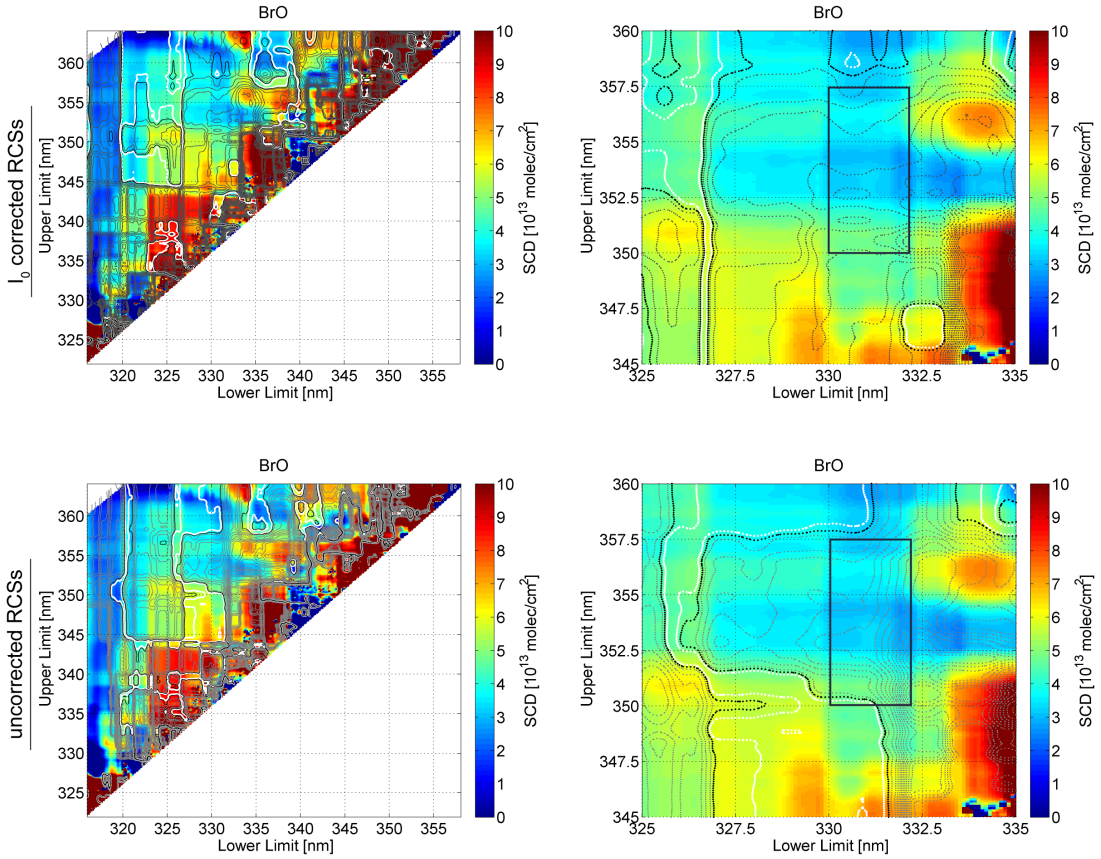

Figure 6.5. Comparison of retrievel wavelength maps of plume measurements at Pacaya volcano to advanced modelled synthetic spectra. Results of measured spectra are overlayed with a contour plot (dashed lines) of retrieval maps from modelled spectra applying I_0 corrected RCSs (top row) and uncorrected RCSs (bottom row). The white dashed lines indicate the ±1% deviation from the true BrO SCDs in the simulated retrieval, black dashed lines ±1.5%. The grey dashed lines mark deviations in the retreived SCDs in steps of 1% to highlight areas of rapid changes in modelled results. The black rectangle in the magnified graph denotes optimal retrieval wavelength ranges as derived from the Zero-Test.

This is especially visible in the magnified retrieval map of measurements at Mt. Etna (fig. 6.6).

Surprisingly, the simulated spectra reflect these changes quite well, although they are constructed without advanced radiative transfer algorithms and only with a rough approximation on the state of the atmosphere. However, it is also apparent, that the modelled spectra only give a quantitative guideline and do not show many features of greater deviations, especially in the range of lower limits 320 nm - 327.5 nm and upper limits > 345 nm. In general, the dependencies on the lower limit with changes in retrieved BrO SCDs at approximately 320 nm, 322.5 nm, 326 nm, 330 nm and 332 nm are only indicated (especially at 326 nm) but fail to

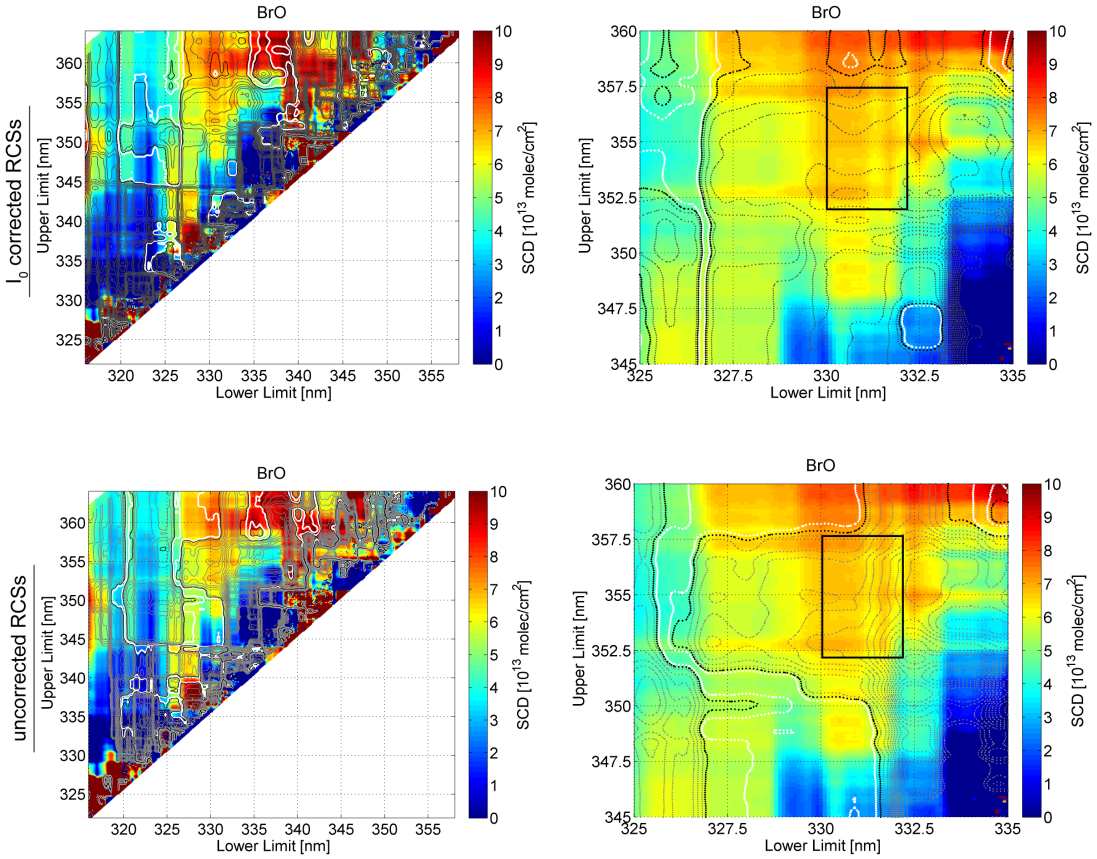

Figure 6.6. Comparison of retrieval wavelength maps of plume measurements at Mt. Etna to advanced simulated synthetic spectra. Results are overlayed with a contour plot (dashed lines) of retrieval maps from modelled spectra applying I_0 corrected RCSs (top row) and uncorrected RCSs (bottom row). The white dashed lines indicate the $\pm 1\%$ deviation from the true BrO SCDs in the model, black dashed lines $\pm 1.5\%$. The grey dashed lines mark deviations in the model in steps of 1% to highlight areas of rapid changes in the simulated retrieval. The black rectangle in the magnified graph denotes optimal retrieval wavelength ranges as derived from the Zero-Test.

simulate measurements in the strength of variations. Sources of these deviations are most likely O_3 and SO_2, since retrieval of these gases depends strongly on the lower limit of the retrieval wavelength range due to their absorption structure. However, the modelled spectra predict retrieval wavelength ranges, which yield correct SCDs and are subject to greater variations in the measurements and/or have to be treated with care due to possible erroneous retrievals in case of stronger O_3 or SO_2 absorptions. Thus, they should only be used as guideline of second order with priority given to the Zero-Test of measured tests.

6.5.2 Zero-Test vs Plume spectra

Possible retrieval wavelength intervals are indicated with black rectangles in the magnified maps on the right side of fig. 6.5 and 6.6, based on the Zero-Test of respective measurements. These ranges of retrieval wavelengths were chosen based on correct retrievals of BrO and HCHO SCDs as described in sec. 6.4.1 and 6.4.2. With this window as a basis, a possible retrieval wavelength range can be further narrowed down by taking into account retrieved SCDs from the other absorbers, both, in the Zero-Test and Plume measurements. Table 6.2 lists all wavelength ranges in the respective interval. Retrieval wavelength maps zoomed into this region are found in fig. 6.7, 6.8 for Zero-Test and plume measurements of Pacaya and for spectra gathered at Etna in fig. 6.9, 6.10.

Based on these findings, the optimal BrO retrieval wavelength range can be estimated to be in the range of 330.3-330.8nm lower limit and 352.5-353nm upper limit.

6.6 Conclusion: Optimal retrieval wavelength range of volcanic BrO

Two comparisons were presented in the previous sections, retrievals of measured spectra vs. simulated spectra of known SCDs and retrievals of spectra of volcanic plumes together with a Zero-Test of their respective FRS.
Modelled spectra reflected the observations on measured spectra well, keeping in mind that the simulated spectra are calculated within a minute without the necessity of more time consuming radiative transfer calculations. However, the modelled spectra failed to describe measured spectra quantitatively, but were able to simulate qualitatively many variations observed in the measured spectra. In this frame it could be shown that the evaluations applying I_0 corrected RCSs agree with the retrieval maps constructed from measurements.
Many variations of SCDs with retrieval wavelengths could not be simulated satisfyingly. Retrieval wavelength ranges showing the least deviations with synthetic spectra (lower limits of 320 nm - 327.5 nm and upper limits $>$ 345 nm) have to be treated with great caution, since changing cross correlations with changing O_3 absorptions can be expected at early and late times of the day. This prohibits

Absorber	Zero-Test		Plume measurements	
	lower limit [nm]	upper limit [nm]	lower limit [nm]	upper limit [nm]
Pacaya				
BrO	330-332.5	350-357	to be determined	to be determined
HCHO	330-332.5	350-357	to be determined	to be determined
O_3	–	–	330-331.5	350-354
SO_2	330-330.8	351-357	330-331	352.5-356
NO_2	–	–	332.5	350-354
O_4	–	> 351.2	330-332.5	350-354
Ring	–	–	–	< 356
Etna				
BrO	330-332.5	352-357	to be determined	to be determined
HCHO	330-332.5	352-357	to be determined	to be determined
O_3	330-332	–	330-331	350-357
SO_2	330-330.8	< 353	330.3-331.8	< 353
NO_2	–	–	330-332.5	–
O_4	–	352.2-354.2	330-332	–
Ring	–	–	–	–
Best estimate	330-330.8	352.2-353	330.3-331	352.5-353

Table 6.2. Measurements at Pacaya and Mt. Etna. Possible retrieval wavelength ranges are given, which best estimate the SCD of respective absorber. Only retrieval wavelength ranges of lower limits of 330 nm - 332.5 nm and upper limits of 350 nm - 357 nm are considered, based on the Zero-Test of BrO and HCHO SCDs. Retrieval ranges of plume measurements were chosen based on most probable SCDs, i.e. for SO_2 and O_3 determined at more sensitive retrieval wavelength intervals, artefacts in the retrieval of NO_2. "–" marks not conclusive data. No estimation of retrieval wavelength ranges for BrO and HCHO are given, because retrieved SCDs of these species are too closely correlated.

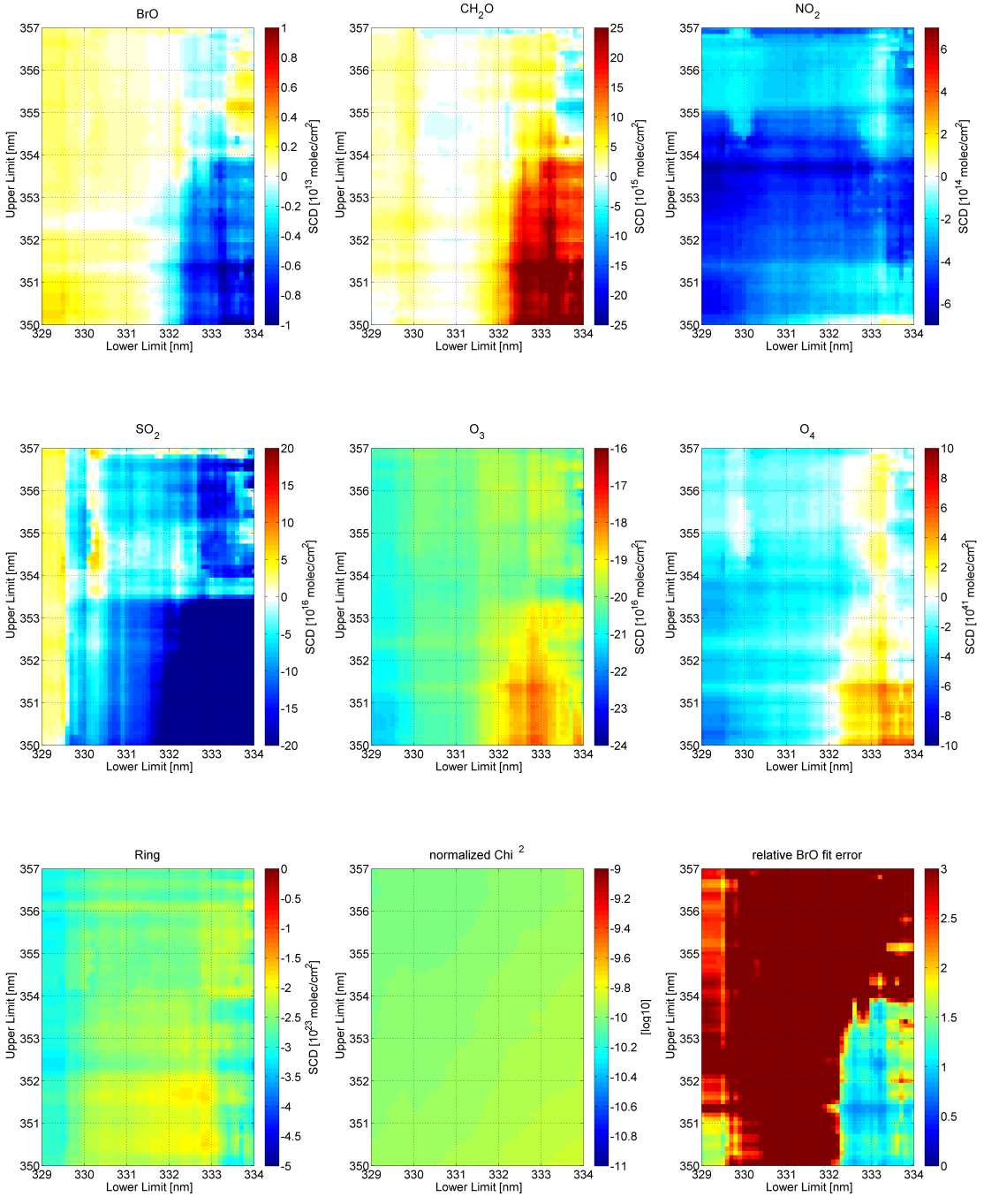

Figure 6.7. Zero-Test of spectra gathered at Pacaya, magnified to the region of retrieval wavelength ranges of interest. See also tab 6.2.

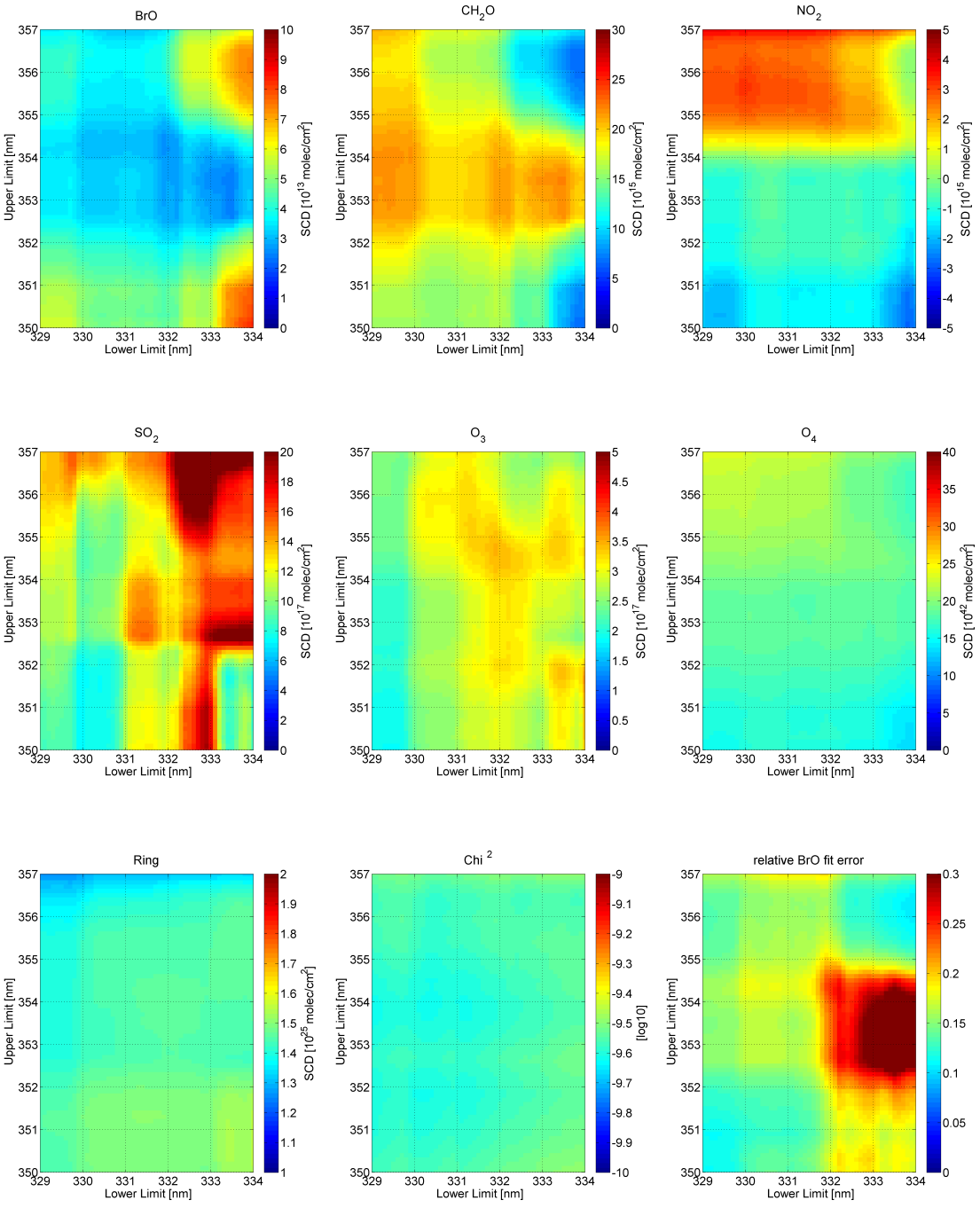

Figure 6.8. Retrieval wavelength maps of spectra gathered at Pacaya, magnified to the region of retrieval wavelength ranges of interest as determined by the Zero-Test. See also tab 6.2.

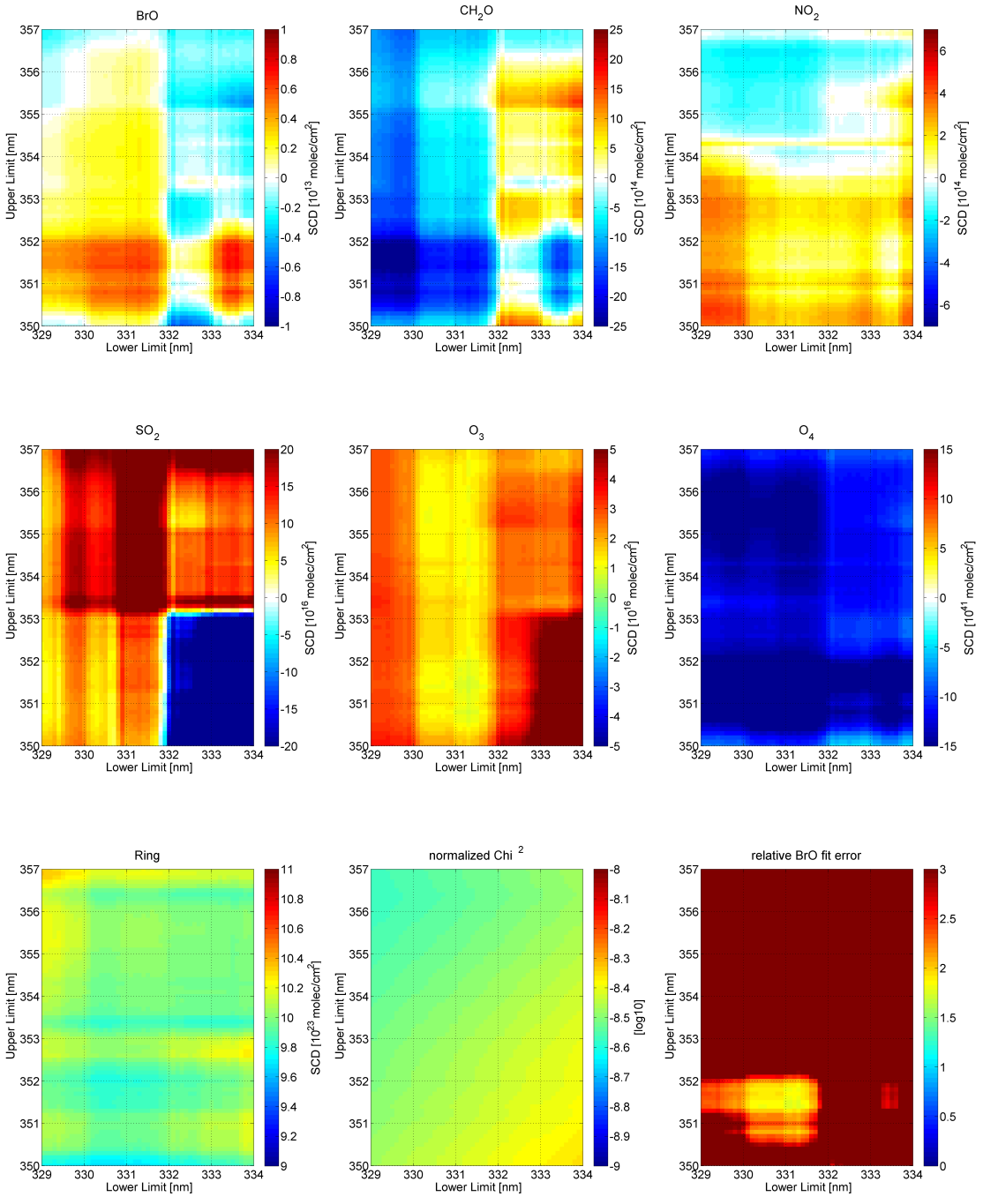

Figure 6.9. Zero-Test of spectra gathered at Etna, magnified to the region of retrieval wavelength ranges of interest. See also tab 6.2.

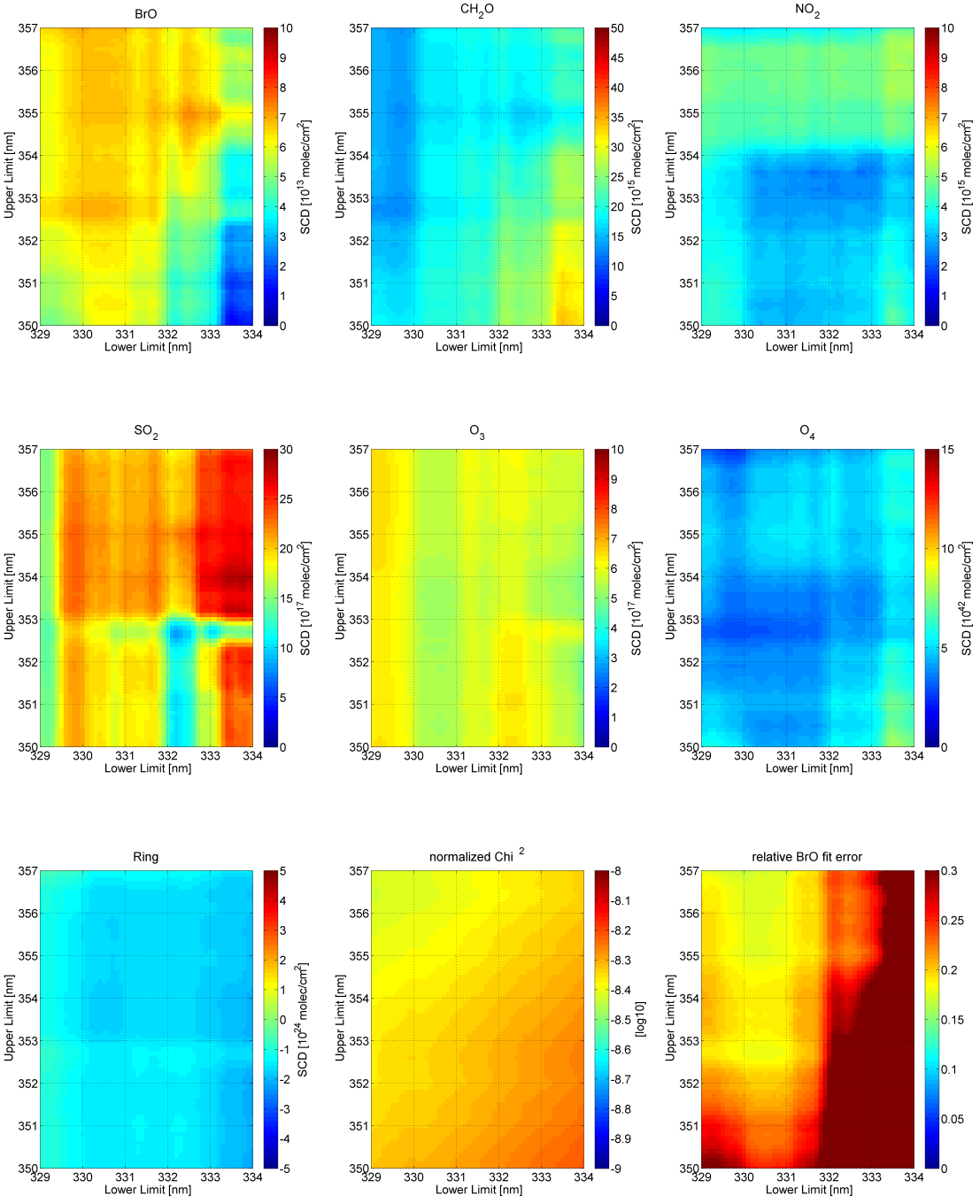

Figure 6.10. Retrieval wavelength maps of spectra gathered at Etna, magnified to the region of retrieval wavelength ranges of interest as determined by the Zero-Test. See also tab 6.2.

the use of these retrieval wavelength intervals to in the evaluation of greater data sets including spectra gathered at variable conditions. The variations in retrieved SCDs from measured spectra indicate strong residual structures, which may be due to insufficiently modelled Ring effect and/or the inability to correct for the Ring effect in measured spectra. Other sources of error are certainly radiative transfer effects like multiple scattering inside, and light dilution effects outside the plume. This may lead to modifications in SO_2 and/or O_3 absorptions which are not well reproduced absorption cross sections recorded in the laboratory. An indication are the dependencies observed on the lower limit for retrieved SCDs. Since it cannot be concluded that the results from the simulated atmospheric conditions can be transferred to the atmospheric conditions of the measurement, it is not unambiguously to draw conclusions which retrieval wavelength range is optimal based on the simulations. However, the simulated results allow to give a better approximation on the measurement error. Regardless of the fit error (see also results of test III, sec. 5.5), BrO SCDs retrieved at a wavelength range of a lower limit of 330.3 nm - 330.8 nm and an upper limit of 352.5 nm - 353 nm may differ from true SCDs by more than 10%, assuming a true BrO SCD of 5×10^{13} molec/cm^2 (sec. 5.4).

The Zero-Test of measured FRS together with retrieval maps of plume measurements yields best results based on the fact that when evaluating two reference spectra against each other, no volcanic absorbers should be detected. It is independent on the state of the atmosphere, excluding rapid changing weather conditions, and should hold regardless of differences between model and measured spectra. This may not necessarily result in the retrieval of true SCDs using plume spectra at the same retrieval wavelength range, but is the best estimate that can be given and approximates a linear relationship of retrieved SCDs with amounts of absorbers present. Thus the optimal BrO retrieval wavelength interval derived from comparing plume measurements and Zero-Test is

330.6 nm - 352.75 nm.

Based on this study, BrO is evaluated for all measurements presented in this thesis by calibrating the FRS against a solar spectrum (Chance and Kurucz, 2010) and copying this calibration to the respective measurement spectrum. The logarithm of the FRS is included in the fit together with a Ring spectrum, calculated using

DOASIS, and both spectra are linked in wavelength pixel mapping. RCSs as given in tab. 6.1 are I_0 corrected by an iterative approach, where the SCDs used in the correction are approximated by a first retrieval using uncorrected RCSs. They are linked in shift and squeeze as a separate set. A polynomial of third order is used to account for broad band absorptions, an offset polynomial of 0^{th} order corrects for possible stray light in the spectrograph. All shifts and squeezes in wavelength pixel mapping are restricted to -0.1 nm - 0.1 nm and 0.99 - 1.01, respectively.

7 SO_2: Retrieval wavelength maps of measured spectra

In chap. 5 retrieval wavelength mapping was introduced as a novel tool. Next to BrO, SO_2 SCDs need to be retrieved in order to calculate BrO/SO_2 ratios and draw conclusions about the atmospheric chemistry of volcanic plumes. Different challenges are faced when retrieving BrO and SO_2. Whereas in case of the BrO retrieval, one has to cope with in general small absorption structures and cross correlations with other absorbers,e.g. HCHO, sources of error in the retrieval of SO_2 SCDs include the at times very high optical densities encountered and possible cross correlations with O_3. The SO_2 retrieval is more sensitive to radiative transfer effects than the BrO retrieval, due to high optical densities encountered and absorption features at smaller wavelengths $<$ 320nm. Radiative transfer effects are enhanced, e.g. Rayleigh scattering by more than 25% comparing 320nm to 340nm. If the BrO/SO_2 ratio is determined by evaluating BrO and SO_2 in the same wavelength range, these dependencies approximately cancle. Unfortunately, this is not possible under most conditions. Common BrO retrieval wavelength ranges are at located at longer wavelengths, where SO_2 cannot be retrieved without great errors. BrO retrievals at shorter wavelengths are not feasible due to strong residual structures most likely induced by SO_2, O_3 and Ring effect, which cannot be easily corrected for.
In principle, it is not necessary to perform enhanced radiative transfer modelling in order to calculate correct SO_2 and BrO SCDs, but rather to calculate a correction factor accounting for the difference in radiative transfer effects between the evaluation wavelength range of BrO and SO_2. However, the great variability in measurement conditions encountered, e.g. aerosol content of ambient air and volcanic plume, different solar zenith angles, elevation and azimuth angle of observation, etc. .

In the following, the DOAS retrieval of SO_2 is introduced, which has been applied

to all data presented in this thesis. The general approach and two different retrieval set-ups are given in sec. 7.1. Resulting retrieval wavelength maps are given in sec. 7.3 and discussed. Finally in sec. 7.4, the results are compared to know strengths of radiative transfer effects.

7.1 DOAS evaluation of SO_2

Common SO_2 evaluations are performed without the use of complex sets of RCSs, because usually only O_3 exhibits differential absorption structures of similar strength in retrieval wavelength ranges below 320nm. Furthermore, SO_2 columns of several 10^{18} molec/cm^2 can easily be observed at volcanoes, corresponding to optical densities of more than 10% below 320nm. Thus usually only O_3 absorption cross sections are included in the retrieval next to a Ring spectrum calculated from the actual FRS. If a measurement setup is chosen, where the FRS can be recorded closely in time to the spectrum of the volcanic plume, the use of several O_3 cross sections accounting for stratospheric absorptions may be neglected. Since the SZA exhibits minor changes between measurements, stratospheric O_3 absorptions are neglectable. Consequently, SO_2 SCDs can be retrieved with a set of RCSs containing next to SO_2 only one O_3 cross section and a Ring spectrum.
If SO_2 is evaluated at longer wavelength retrieval ranges (< 320nm) on the other hand, it might be necessary to include other absorbers as well. Table 7.1 gives an overview of two different sets of RCS. Retrieval set-up A corresponds to a simple set of RCSs based on above described considerations. Retrieval set-up B contains the same RCSs as already used in the retrieval study of BrO, which includes all expected absorbers possibly carrying any weight in the retrieval process.

7.2 Retrieval wavelength maps of SO_2

Retrieval wavelength maps are created for both data sets (Pacaya, 6.3.1 and Etna, 6.4.2). The retrieval maps are calculated at a resolution of $\approx 0.1 - 0.15$nm. All maps are interpolated on a 0.1nm grid to account for possible changes in wavelength pixel calibration during the measurement periods and for easier comparison of retrieval wavelength maps. For both sets of RCSs (set-up A and B) and data sets (Pacaya and Mt.Etna), retrievals are performed in the range from a lower limit

305-328nm till an upper limit 315-342nm for retrieval wavelength ranges between 10 nm - 14 nm, encompassing 5 - 8 absorption bands of SO_2. Since the strength of SO_2 absorption bands decrease with increasing wavelengths, retrieval of SO_2 SCDs is strongly dependent on the lower limit of the retrieval wavelength range. Thus, it is not necessary to perform evaluations over greater wavelength ranges by varying the upper limit of the wavelength range extensively. This is also validated in sec. 6.4, were retrieved SO_2 show only a dependency on the lower limit at reasonable wavelength ranges.

In both fit scenarios, all FRS used are calibrated against a solar reference spectrum Chance and Kurucz (2010). A Ring spectrum is calculated from the calibrated FRS using the software Doasis. A polynomial of third order is used to correct for broad band absorptions, and an offset polynomial of 0^{th} order to correct for straylight in the spectrograph.

trace gas	temperature [K]	RCS	Pacaya A	Pacaya B	Etna A	Etna B	Quantity [molec · cm^{-2}]
BrO	298	Fleischmann et al. 2004	–	7.5	–	10	$\times 10^{13}$
O_3	273	Burrows et al. 1999	3	3	7.5	7.5	$\times 10^{17}$
NO_2	294	Vandaele et al. 1998	–	5	–	50	$\times 10^{14}$
O_4		Hermans et al. 2003	–	2	–	2	$\times 10^{42}$
SO_2	298	Vandaele et al. 2009	1	1	1	1	$\times 10^{18}$
CH_2O	298	Meller and Moortgat 2000	–	1.5	–	1.5	$\times 10^{16}$

Table 7.1. Different sets of RCSs used in the evaluation of SO_2. Set-up A uses a only one SO_2 and O_3 absorption cross section, whereas set-up B uses all absorbers considered in the retrieval of BrO. Given SCDs are used in the I_0 correction of RCSs.

7.3 Results

Figure 7.1 depicts results for retrieval set-up A and B for both measurement scenarios, Pacaya and Etna. The strong SO_2 absorptions $< 315\,nm$ dominate retrievals and lead to a good agreement between both sets of RCSs. However, set-up B can become unstable at upper limits $< 322\,nm$. For a lower limit of 315 nm - 320 nm, possible cross correlations with O_3 lead to lower retrieved SO_2 SCDs. This effect is comparable for both set-up A and B. With a further increase of the lower limit, the retrieval yields increasingly varying SO_2 SCDs. For lower limits $> 323\,nm$ the results vary greatly and retrievals in this wavelength range can be disregarded as erroneous.
The simple set of RCSs (set-up A) is sufficient to retrieve SO_2 for lower limits $< 315\,nm$. This is no surprise and similar set of RCSs are used nowadays in common DOAS retrievals of volcanic SO_2. It is remarkable, that also set-up B fails to achieve a stable SO_2 retrieval for lower limits $> 316\,nm$ at the absorption strength of SO_2 present. Thus it is sufficient to use set-up A to retrieve SO_2 SCDs at lower limits $< 315\,nm$. Fig. 7.2 depicts average retrieval results from Mt Etna and acts also as an example for average results from Pacaya, showing similar wavelength dependent SCD variations. It can be observed, that all variations in SO_2 SCD are accompanied by anti-correlating variations in O_3 SCD.
In the following, only SO_2 SCDs retrieved with set-up A are discussed further, since at lower limits of $< 415\,nm$ it is comparable to set-up B, and at upper limits $> 315nm$ both set-ups show strong variations in retrieved SCDs.

7.4 Comparison of results with radiative transfer effects and conclusion

Fig. 7.3 depicts average SO_2 SCDs retrieved for both test data sets from Pacaya and Etna. The abscissae shows only the lower limit of the retrieval wavelength range, since it has a constant width of 12nm. Next to SO_2 also O_3 SCDs are plotted to show their correlation. The red dashed line is polynomial of second order fitted to SO_2 SCDs retrieved for lower limits 305 nm - 316 nm and 320 nm - 322.5 nm. This polynomial indicates expected gradients of SO_2 SCDs with retrieval wavelength. A qualitative agreement with the radiative transfer study by Kern et al. (2010a) can be observed (see also fig. 3.3). However, the model

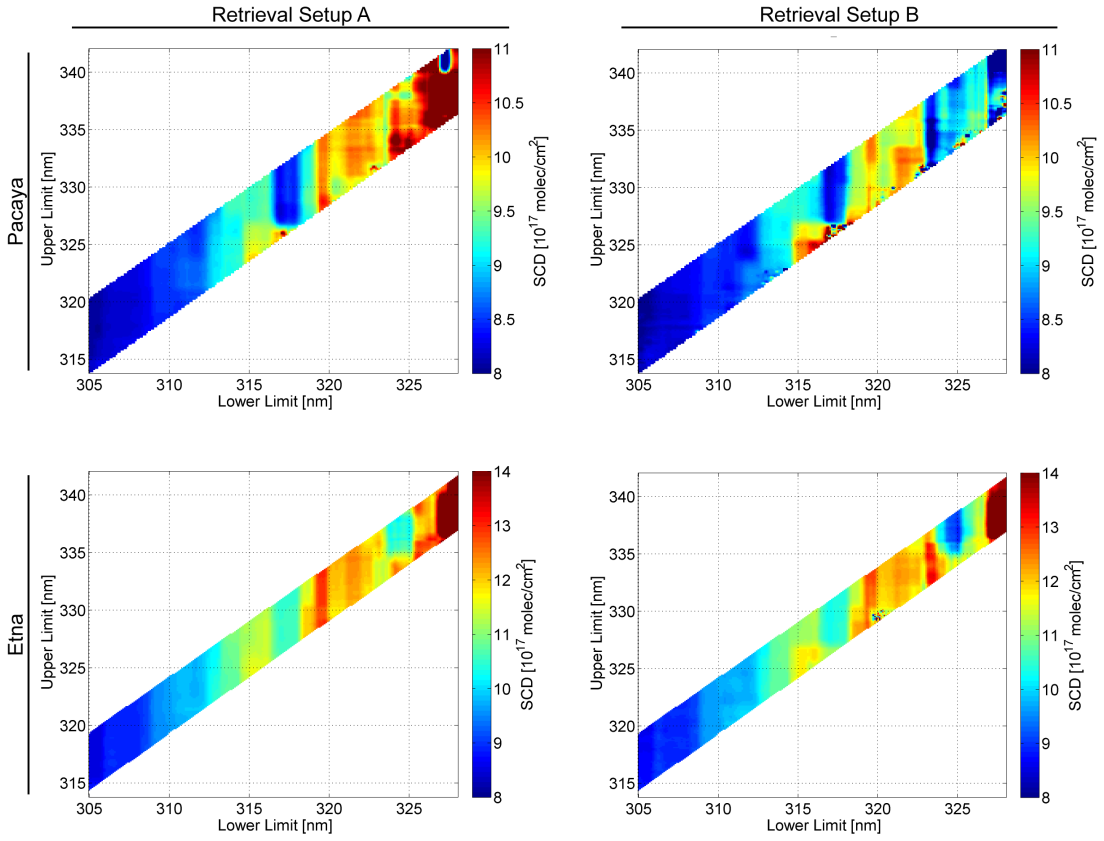

Figure 7.1. Comparison of SO_2 SCDs using retrieval set-up A (only SO_2 and O_3) and set-up B (the same set of RCSs as in the BrO retrieval). For lower limits < 315 nm both retrievals yield comparable SCDs. At retrieval wavelength intervals of lower limits > 315 nm, set-up A and set-up B fail to evaluate spectra in a robust manner.

study was performed at discrete wavelengths, whereas the here presented retrieval of measured data was performed over an interval of 12 nm, which diminishes the wavelength dependency of SO_2 SCDs since longer wavelengths are included which are less affected by radiative transfer effects.

As already mentioned at the beginning of this chapter, exact knowledge of the occurring radiative transfer effects is not necessary in order to determine correct BrO/SO_2 ratios. It is rather necessary to ensure that both gases are subject to the same radiative transfer effects in their respective retrieval wavelength range, thus these effects cancel when taking the ratio of SCDs from both gases. If the shown dependency of the SO_2 SCDs on retrieval wavelength could be extrapolated to the BrO retrieval wavelength interval derived in chap. 5, it would be possible to derive a best estimate on BrO/SO_2 without the use of radiative transfer calculations, based on the data itself. The retrieved SO_2 SCD dependency on wavelength shows

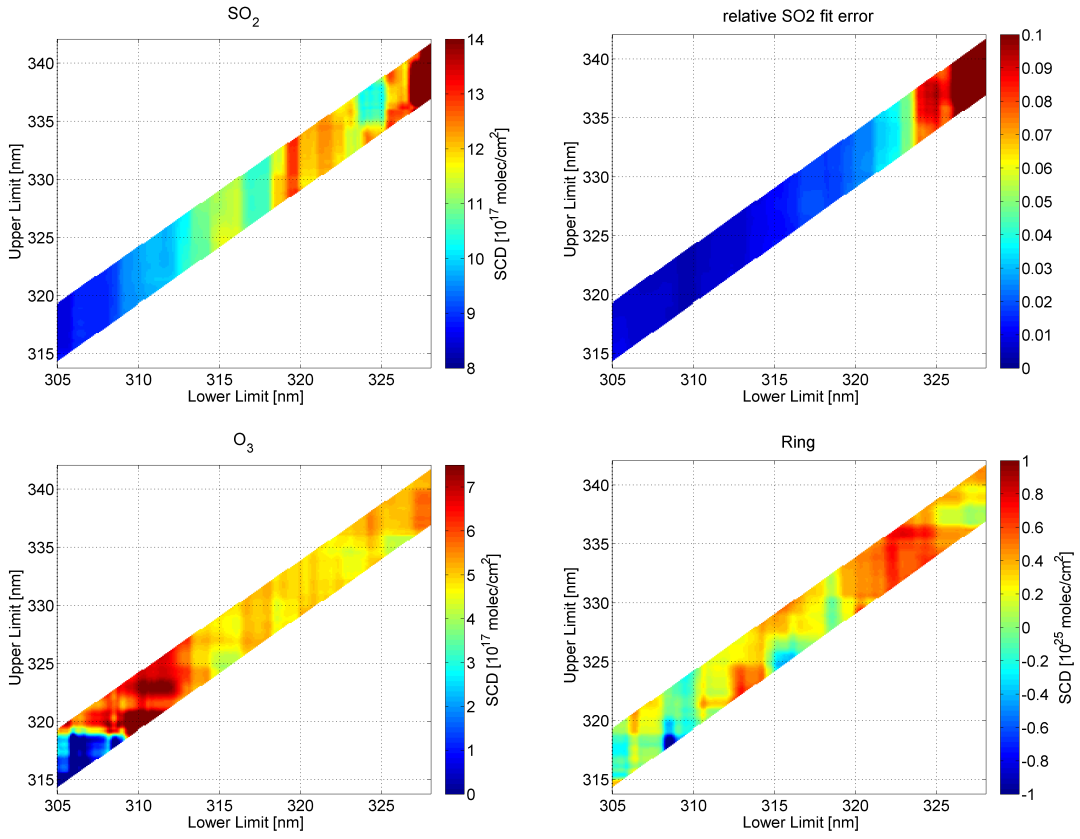

Figure 7.2. Depicted are average SCDs from all absorbers. Spectra have been recorded at Mt. Etna and evaluated with RCSs from set-up A.

a smooth gradient (fig.3.3) and can be approximated by a polynomial of second or third order. Fig. 3.3 also shows the difficulties: The gradient of air mass factor versus wavelength of retrieved SO_2 SCD may decrease for fit intervals $> 315\,nm$. Thus fitting a wavelength depending polynomial to retrieved SO_2 SCDs may be erroneous if only wavelength intervals are used in the fiting process with a lower limit $< 315nm$. However, retrievals of SO_2 for lower limits of 316 nm - 320 nm are clearly not following the expected dependencies in fig.7.3. Since sudden changes occur in retrieved SO_2 and O_3 SCDs, these retrieval ranges may suffer from cross correlations between absorber cross sections and have to be disregarded. Only retrieval wavelength intervals of lower limits of 320 nm - 322.5 nm may be used to retrieve SO_2 SCDs, where results follow the expected columns based on the radiative transfer calculations. At these wavelengths however, the amplitude of the differential SO_2 structure is on the order of 1×10^{-20} (see fig. 3.4), making it unfavourable for the detection of smaller SO_2 SCDs.

In general, air mass factors of SO_2 columns will be always lower at smaller

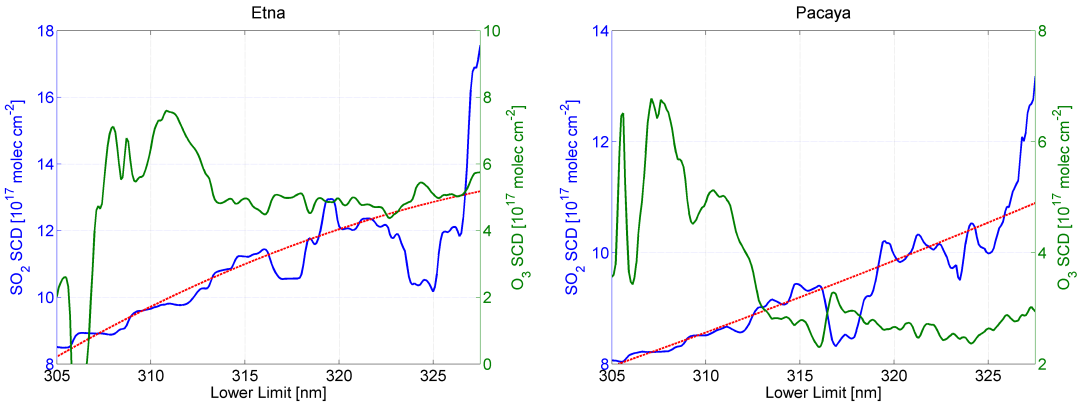

Figure 7.3. Average retrieved SO_2 and O_3 SCDs from measurements at Pacaya and Etna using RCS according to set-up A. All retrieval intervals have a range of 12 nm, the abscissae only denotes the lower limit. Next to SCDs, also a polynomial of second order is plotted in a red dashed line. It has been fitted to SCDs retrieved at lower limits 305 nm - 316 nm and 320 nm - 322.5 nm. The polynomial reflects estimated dependency of retrieved SO_2 SCDs on evaluation wavelength range due to radiative transfer effects.

wavelengths. This effect may be negligible at times, but may also lead to a severe underestimation of SO_2 columns which would be detected at BrO retrieval ranges with consequently overestimation of BrO/SO_2 ratios. As observed in fig. 7.3, retrievals of SO_2 at lower wavelength limits > 315 nm may either be affected by possible cross correlations with O_3, or are exhibit only small differential absorption structures which in turn makes them unfavourable for lower SO_2 SCDs measured. Thus as a first order estimate, evaluation of SO_2 should be performed at a range of

314.8 nm - 326.8 nm,

since this wavelength range yields the best compromise of a robust fit and low influence of radiative transfer effects. Resulting SO_2 SCDs are used to calculate BrO/SO_2 ratios.

The estimation of a correction factor to calculate (virtual) SO_2 SCDs at the wavelength range corresponding to the retrieval of BrO from the evaluation range of 314.8-326.8nm can not replace more accurate radiative transfer studies. But allows to give a first order lower limit of of BrO/SO_2, which can otherwise only be regarded as an upper limit.

Based on this, SO_2 is evaluated for all measurements presented in this thesis by calibrating the FRS against a solar spectrum (Chance and Kurucz, 2010) and copying this calibration to the respective measurement spectrum. The logarithm

of the FRS is included in the fit together with a Ring spectrum, calculated using DOASIS, and both spectra are linked in wavelength pixel mapping. RCSs corresponding set-up A are I_0 corrected by an iterative approach, where the SCDs used in the correction are approximated by a first retrieval using uncorrected RCSs. They are linked in shift and squeeze as a separate set. A polynomial of third order is used to account for broad band absorptions, an offset polynomial of 0^{th} order corrects for possible stray light in the spectrograph. All shifts and squeezes in wavelength pixel mapping are restricted to -0.1 nm - 0.1 nm and 0.99 - 1.01, respectively.

8 Measurements of BrO and SO_2 in volcanic plumes

In this chapter, the different measurement campaigns are presented. Besides two extensive measurement campaigns at Mt. Etna, Italy, during July 2008 and 2009, measurements were performed during several days at the Pacaya volcano, Guatemala. However, only on one day (February 5^{th}, 2010) efforts succeeded.

Mt Etna is located on the island of Sicily in southern Italy (37.734 °N, 15.004 °E). It is Europe's most active volcano and showed activity over the last 500,000 years. The summit raises to about 3300 m above sea level and consists of four main craters, the North-East crater, the South-East crater, Voragine and Bocca Nuova, where the last thwo are also sometimes referred to together as the Central crater. Eruptive activity consists mostly of persistent quite degassing interrupted by explosive eruptions together with minor lava flows. Strombolian eruptions may occur as well from flank vents together with lava flows, which was the case during the first campaign at Mt. Etna in July, 2008. Fig. 8.1 displays a map of Mt. Etna together with most common measurement sites during both campaigns.

Pacaya volcano is located at 14.381 °N, 90.601 °W, approximately 20 km south of the Guatemalan capital Guatemala City. The volcano consists of several cones and domes, of which only the McKenney cone is currently active. The summit of the McKenney cone is situated at 2550 m altitude. Pacaya volcano showed almost constant activity since 1961 after a dormant phase that lasted a century. Eruptions are mostly strombolian with sporadic lava flows, diffusive degassing and fumerolic activity. Recent major eruptive events occurred in 1998 and May 2010 with debris and ash ejected up to 5000m and subsequent ash fall on nearby cities, including the capital Guatemala City and its international airport La Aurora. The volcano and the measurement side are depicted in fig. 8.1.

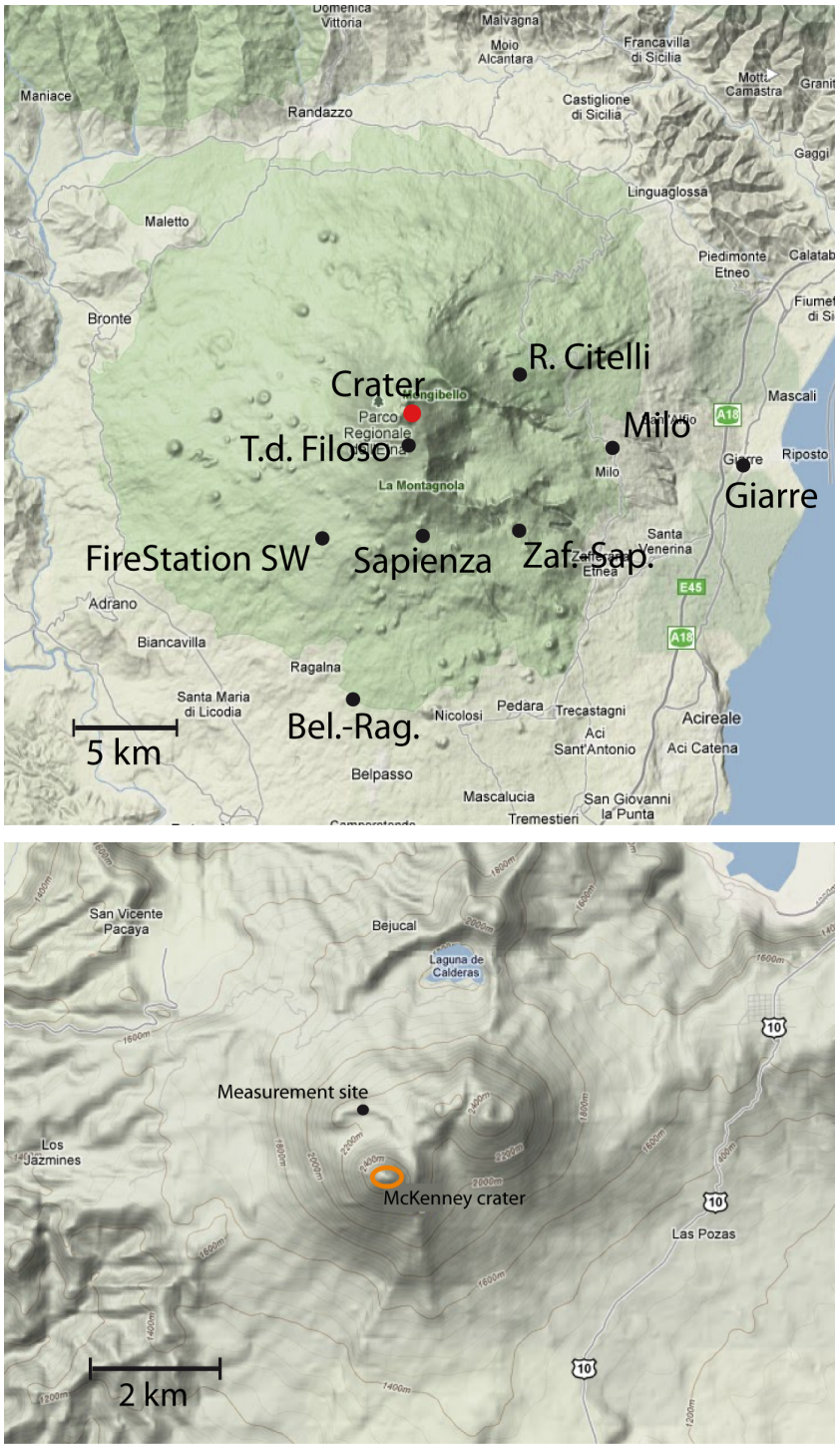

Figure 8.1. Depicted are maps of Mt. Etna, Italy (top), and Pacaya, Guatemala (bottom). On the map of Mt. Etna, the most common measurement sites of both campaigns are marked by black dots. Distances to the crater range from 1.5 km till Torre del Filosofo to 18 km till Giarre. On the map of Pacaya volcano, the McKenney crater is encircled in orange, and the measurement site indicated by a black dot. Maps adapted from GoogleMaps.

8.1 Etna, Italy, measurement campaign July 2008

During the first three weeks of July 2008, an extensive measurement campaign was performed at Mt. Etna with several goals: Determining SO_2 fluxes, testing of wind speed measurement algorithms of the NOVAC instrument mark II, testing of a novel UV-camera system able to image 2D SO_2 distributions and last but not least, capturing plume chemistry at different plume ages. The interested reader is referred to (Fickel, 2008) for results on SO_2 fluxes and wind speed algorithm and to (Wöhrbach, 2008) for campaign results regarding the UV-Camera. (Kern, 2009) also discusses performed Long-Path measurements next to giving a general overview of the campaign. Measurements of the campaign are compared to radiative transfer studies in a publication on radiative transfers effects in spectroscopy of volcanic plumes (Kern et al., 2010a). Here, measurements are presented of bromine chemistry in volcanic plumes at different plume ages via BrO/SO_2 ratios.

8.1.1 Volcanic activity

During the time of the campaign, Mt. Etna showed increased activity with occasional explosive eruptions, strombolian activity and diffusive ash emissions. This was accompanied with elevated SO_2 emissions and lava flows travelling into the Valle del Bove, originating from a newly opened flank eruption. A strong variability in activity was reported, changing on a day to day basis. On July 7^{th} and 8^{th}, weak ash emissions and gas emissions were observed by webcams (note that this does not allow conclusions about SO_2 emissions). A sudden increase of seismic tremor by 50% was reported on July $09th$ with a shift in assumed region (INGV, 2008). New strombolian activity could be seen at the flank on July 10^{th} with ongoing lava flows and lasting for several days. Also an increase in SO_2 emissions was reported, with fluxes on the order of 700 tons/day on July 10^{th} and 11^{th} (Coltelli, 2008). This increase in emissions is also clearly visible in our own observations (fig. 8.3, Fickel, 2008), although measured strength differs by a factor of 2 or more. 8.2 shows two pictures of the volcano taking during the day and at dusk. Visible is the higher ash content of the volcanic plume after an explosive event and the lava flows into Valle del Bove.

Figure 8.2. Increased activity of Mt. Etna during July 2008. On the top, higher ash content of the volcanic plume is visible shortly after an explosive event. The bottom picture shows lava flows into Vale del Bove. Both pictures are taken from the house in Milo which was used as frequent measurement location.

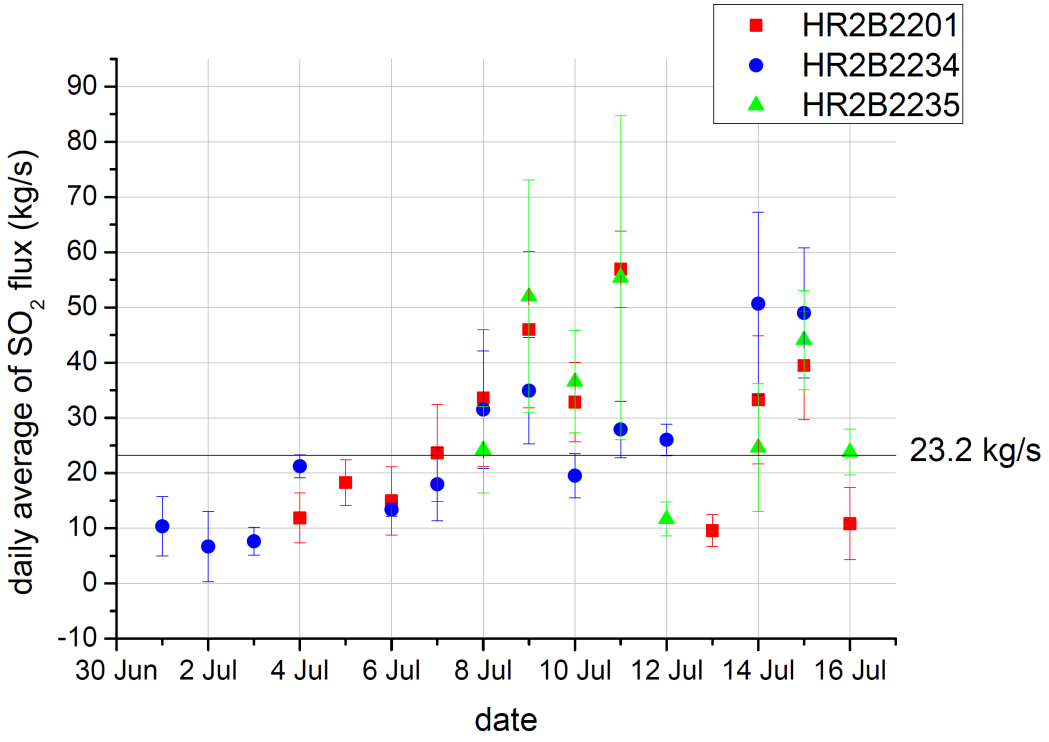

Figure 8.3. Measured SO_2 fluxes during the campaign, graph from (Fickel, 2008). The different colors correspond to the different NOVAC Mark II instruments used. At most times, HR2B2235 was placed in R.Citelli, HR2B2201 in Milo and HR2B2234 in Giarre. Measured mean SO_2 flux of 23.2 kg/s corresponds to $\approx$ 2000 tons/day. See also tab. 8.2.

8.1.2 Performed measurements

As described at the beginning of this section, a multitude of different measurements were performed during July 2008. Not all of them were primarily aimed at detecting BrO, but to supply information on SO_2 fluxes, test new equipment and algorithms. Measurements dedicated to capture halogen compounds in volcanic plumes are summarized in tab. 8.1. Other measurements which are also used to extract information on BrO/SO_2 ratios are SO_2 flux measurements and car traverses (tab. 8.2, tab. 8.3). In order to perform simultaneous measurements of the volcanic plume at different plume ages, the different instruments need to observe the volcanic plume at different distances to the volcano. Especially on July 12^{th}, 14^{th} and 16^{th}, efforts were made to achieve this and observe the volcanic plume at equally spaced distance to the crater.

Plume composition measurements

Three NOVAC instruments Mark II were used to perform the plume composition measurements. These stationary instrument incorporate a scanning mechanism,

Composition measurments

Date	Time of day	Measurement side	Instrument	No. of measurements
04.07.	11:30-12:30	R.Citelli	HR2B2201	4
	10:50-12:45	Milo	HR2B2234	8
05.07.	10:30-12:30	Milo	HR2B2201	14
09.07.	13:30-14:45	Milo	HR2B2201	6
10.07.	08:45-15:10	Milo	HR2B2201	15
11.07.	11:15-14:15	R.Citelli	HR2B2235	10
12.07.	09:50-14:30	R.Citelli	HR2B2235	14
	09:10-15:15	Milo	HR2B2201	46
	09:40-14:00	Giarre	HR2B2234	42
14.07.	10:00-14:45	R.Citelli	HR2B2235	18
	12:20-17:30	Milo	HR2B2201	18
	10:20-13:00	Giarre	HR2B2234	20
16.07.	11:45-14:15	Zaf.-Sap.	HR2B2235	18
	10:15-15:00	Milo	HR2B2201	30
	09:45-13:20	Giarre	HR2B2234	39

Table 8.1. Measurements performed during the campaign at Mt. Etna 2008 with a setup dedicated to detect BrO. All measurement spectra of volcanic plume consist of 300 individual spectra, which have been added to increase the signal to noise ratio.

allowing to point their telescope at any direction in the sky and perform advanced measurement geometries. Incorporated in these instrument is an HR2000 spectrograph by OceanOptics (OceanOptics, 2008), which is temperature stabilized. For a detailed description of the NOVAC Mark II system see (Kern, 2009; Galle et al., 2010).

The optical resolution of used spectrograph is 0.4 nm, 0.31 nm and 0.33 nm for HR2B2201, HR2B234 and HR2B2235, respectively. In order to achieve a sufficient signal to noise ratio, recorded spectra consisted of 300 individual spectra measured subsequently. Common exposure times are in the range of 300 ms till 800 ms, depending on the time of day. The measurement geometry consisted of alternating measurements of volcanic plume and FRSs, assuring a minimized influence of stratospheric absorbers on the retrieval. Because this type of measurement was commonly performed shortly after a scan of the volcanic plume to determine SO_2 fluxes, the elevation angle of the telescope pointing at the centre of the plume was known and the measurement routine could be adjusted accordingly. Table 8.1 shows performed plume composition measurements during July 2008.

SO_2 flux measurements

For SO_2 measurements, also the NOVAC instruments Mark II have been used. A

common plume scan was performed by scanning from horizon to horizon in steps of 5° elevation angle without changing the azimuth angle. This is referred to as a flat scan geometry in contrast to conical scanning (see Galle et al., 2010). In order to capture a plume cross section at higher time resolution, these measurements consisted of only 15 added measured spectra per recorded spectrum at one elevation angle. In order to retrieve typical BrO SCDs, it is thus necessary to add spectra gathered inside the volcanic plume to be evaluated against added spectra which have been recorded outside the plume, as described in chap. 4.2. Because of the other objectives of the measurement campaign, this was the most common measurement geometry used (see tab. 8.2).

Car traverses of volcanic plumes

Car traverses were performed by mounting a zenith looking telescope to a car, connected with an optical fibre to an USB2000 OceanOptics spectrograph (SN USB2G25267) with an optical resolution of 0.7 nm. In contrast to the spectrograph used in the NOVAC Mark II instruments, this spectrograph was not temperature stabilized, but kept at approximately 15 °C by being placed in the foot compartment of the co-driver at coldest air conditioning possible. Although a filter was incorporated into the telescope admitting only light in the spectral range 290-400 nm, the recorded spectra show stray light inside the spectrograph. An additional Offset correction had to be applied by subtracting the average number of counts measured below 290nm for each spectra.

As already described in 4.3, traverse measurements are aimed primarily at detecting SO_2 with a sufficient high spatial resolution to calculate a SO_2 column cross section of the volcanic plume. In order to evaluate spectra for BrO, a of sufficient high signal to noise ratio was achieved by adding 30 spectra gathered at the plume centre against the spectra taking outside of the plume. Each recorded spectrum is already the sum of 30-80 individual spectra, a total number of spectra of 900 - 2400 are added for a plume spectrum and corresponding FRS. An overview of conducted traverses is given in tab. 8.3.

From these traverses, the mean daily wind speed was calculated whenever possible. Otherwise, the READY (READY, 2008) was used for the mean wind direction. The wind direction was taken from the READY model for all days. The combined error of wind speed and wind direction in the calculation of the plume age is estimated to be 25%. This can be justified by the disturbance a topographic obstruction like Mt. Etna places on model wind direction and speed of the rather coarse resolution of the model (0.3°).

SO_2 flux measurements

Date	Time of day	Measurement side	Instrument	No. of measurements
01.07.	12:00-19:15	Milo	HR2B2234	12
02.07.	04:00-14:15	Milo	HR2B2234	14
	12:30-17:15	Giarre	HR2B2235	12
03.07.	04:30-17:45	Giarre	HR2B2235	34
	04:40-17:45	Milo	HR2B2234	21
04.07.	10:15-13:45	R.Citelli	HR2B2201	12
	04:00-10:45	Milo	HR2B2234	20
05.07.	09:45-18:30	Milo	HR2B2201	23
	5:00-09:15	Giarre	HR2B2234	10
06.07.	03:00-18:45	Milo	HR2B2201	74
	05:00-16:45	Giarre	HR2B2234	29
07.07.	03:00-18:45	Milo	HR2B2201	59
	05:00-16:40	Giarre	HR2B2234	29
08.07.	03:00-18:00	Milo	HR2B2201	44
	08:50-18:00	Milo	HR2B2235	35
	05:00-16:30	Giarre	HR2B2234	29
09.07.	04:00-17:30	Milo	HR2B2201	37
	06:30-17:30	Milo	HR2B2235	30
	05:00-16:30	Giarre	HR2B2234	28
10.07.	04:00-17:45	Milo	HR2B2201	45
	04:00-20:00	Milo	HR2B2235	35
	05:00-16:35	Giarre	HR2B2235	28
11.07.	10:50-14:00	R.Citelli	HR2B2235	8
	04:45-07:00	Milo	HR2B2201	10
	06:15-09:10	Milo	HR2B2235	10
	05:00-14:15	Giarre	HR2B2234	24
12.07.	08:45-15:00	R.Citelli	HR2B2235	6
	12:20-12:40	Milo	HR2B2201	1
	04:00-17:00	Giarre	HR2B2234	18
13.07.	12:45-17:40	Milo	HR2B2201	18
14.07.	10:30-14:30	R.Citelli	HR2B2235	4
	04:30-12:00	Milo	HR2B2201	29
	04:00-09:30	Giarre	HR2B2234	13
15.07.	06:00-11:30	Milo	HR2B2201	19
	05:30-11:30	Milo	HR2B2235	12
	04:00-17:30	Giarre	HR2B2234	33
16.07.	10:45-14:45	Zaf.-Sap.	HR2B2235	6
	09:30-16:30	Milo	HR2B2201	10
	04:00-09:10	Giarre	HR2B2234	10

Table 8.2. SO_2 flux measurements performed during the campaign at Mt. Etna 2008. These measurements also have been used to extract information on BrO/SO_2 ratios.

Traverse measurements

Date	Run	Time of day	Azimuth from source [°]	r^2	used
5 Jul 08	T1450	12:50-13:22	3142	0.202	FALSE
7 Jul 08	T1451	13:03-13:27	271	0.682	TRUE
	T1529	13:29-13:45	267	0.732	TRUE
	T1547	13:47-14:07	260	0.879	TRUE
	T1610	14:10-14:55	242	0	FALSE
	T1659	14:59-15:35	294	0.897	TRUE
8 Jul 08	T1347	11:47-12:05	232	0.608	FALSE
	T1407	12:08-12:33	273	0.569	FALSE
	T1439	12:40-13:17	274	0.805	TRUE
	T1520	13:20-14:02	274	0.832	TRUE
	T1605	14:06-14:47	271	0.842	TRUE
	T1649	14:49-15:11	270	0.836	TRUE
9 Jul 08	T1024	08:24-08:57	323	0.518	FALSE
	T1103	09:03-10:49	299	0.526	FALSE
	T1500	13:00-13:05	283	0	FALSE
	T1507	13:08-13:35	307	0.636	TRUE
	T1538	13:38-14:08	311	0.645	TRUE
	T1615	14:19-14:57	318	0.284	FALSE
	T1701	15:01-15:34	317	0.816	TRUE
11 Jul 08	T1242	10:44-11:11	326	0.526	FALSE
	T1358	12:04-12:39	319	0.124	FALSE
	T1439	12:42-13:21	317	0.885	TRUE
12 Jul 08	T1201	10:05-10:56	327	0.49	FALSE
	T1256	11:02-11:17	304	0.694	TRUE
	T1317	11:21-11:46	308	0.9	TRUE
	T1346	11:49-12:10	306	0.926	TRUE
	T1411	12:15-12:33	304	0.76	TRUE
	T1433	12:36-13:00	304	0.941	TRUE
	T1500	13:06-13:30	303	0.895	TRUE
	T1529	13:32-14:12	306	0.866	TRUE
14 Jul 08	T1036	08:39-08:48	256	0.895	FALSE
	T1050	08:51-09:24	272	0.574	FALSE
	T1203	10:04-10:21	267	0.807	TRUE
	T1227	10:28-10:56	255	0.272	FALSE
	T1258	11:00-11:13	255	0.837	TRUE
	T1328	11:31-12:17	252	0.75	TRUE
	T1422	12:25-12:50	254	0.851	TRUE
	T1549	13:49-14:36	263	0.437	FALSE
	T1639	14:41-14:55	268	0.853	TRUE
16 Jul 08	T1210	10:13-10:53	319	0.858	TRUE
	T1253	10:56-11:32	323	0.901	TRUE
	T1332	11:35-11:52	324	0.933	TRUE
	T1352	11:54-12:19	325	0.96	TRUE
	T1424	12:29-12:51	332	0.637	TRUE
	T1451	12:54-13:21	329	0.784	TRUE
	T1559	14:01-14:41	336	0.924	TRUE
	T1643	14:52-14:59	333	0.822	TRUE

Table 8.3. List of performed traverses during the campaign of July 2008 at Mt. Etna. Included are the azimuth angle from the crater to the measured centre of the plume, derived as described in sec. 4.3. Goodness of fit is indicated by given r^2, column "used" marks whether or not the traverse was used (true) or not(false) in the calculation of mean wind direction.

Date	Wind direction [°]	Wind speed [m/s]	Source
1 Jul 08	319	5	Ready
2 Jul 08	313	2	Ready
3 Jul 08	224	4	Ready
4 Jul 08	289	10	Ready
5 Jul 08	314	10	Ready
6 Jul 08	328	10	Ready
7 Jul 08	273	8	Traverses
8 Jul 08	273	20	Traverses
9 Jul 08	312	20	Traverses
10 Jul 08	313	20	Traverses
11 Jul 08	317	10	Ready
12 Jul 08	305	10	Traverses
13 Jul 08	263	5	Ready
14 Jul 08	259	9	Traverses
15 Jul 08	297	20	Ready
16 Jul 08	321	9	Traverses

Table 8.4. Table with wind directions and wind speeds used in the calculation of plume ages during July 2008. Due to mostly stable conditions, these parameters are used for all measurements during respective days. Wind directions are estimated from performed traverses when possible, otherwise meteorological data from the READY modell (READY, 2008) is used. All wind speeds are taken from the model calculations.

8.2 Etna, Italy, measurement campaign July 2009

A second measurement campaign at Mt. took place from July 13^{th} till July 30^{th}, dedicated to measuring halogen chemistry in volcanic plumes. To capture plume chemistry at different plume ages, care was taken to perform measurements simultaneously with stationary instruments close to the crater, at medium distances ($\approx 5 - 10$ km and perform car traverses at longer distances (> 20 km), which also is the maximum distance achievable with the car for westerly winds with the Mediterranean sea as boundary.

8.2.1 Volcanic activity

Started in May 2008, the eruption at the eastern flank of Mt. Etna ceased at the beginning of July 2009. Although no further strombolian eruptions occurred and the lava flow stopped, SO_2 emissions were still high, ranging up to 5000 tons/day at July 10^{th} and 12^{th} (Giammanco, 2009). SO_2 flux ranged between 1200 tons/day till 3200 tons/day between July 13^{th} and 21^{th} according to (Lodato, 2009). The amount of ash in the plume is greatly reduced compared to the campaign a year earlier due to the lower activity of the volcano, which can also be seen from visual observations (fig. 8.4).

8.2.2 Measurements

As in 2008, stationary instruments were used together with car traverses. Used was a NOVAC instrument Mark II, a miniMax DOAS instrument and car traverses employing a higher grade temperature controlled spectrograph (QE65000). A focus was set to capture BrO/SO_2 at plume ages as old as possible to gain insights on plume chemistry on larger time scales (>60min) then studied before. For the stationary instruments, plume composition measurements were the most common measurement set-up during the campaign, with a reduced number of scanning the volcanic plume to determine the SO_2 flux and determine the location of the plume in the sky. Car traverses with the most sensitive spectrograph were used to measure the plume at its greatest distance to the crater, where the signal is weakest due to dispersion of the plume.

Plume composition measurements

Table 8.5 gives an overview over performed plume composition measurements with

Figure 8.4. Volcanic activity of Mt. Etna during July 2009. The picture at the top shows Mt. Etna from Milo on the July 15^{th}. The volcanic plume is almost invisible, being blown to the south (left) at the altitude of the crater. Pictured on the bottom is the crater as seen from measurement site "Firestation South-West" on July 24^{th}. A slightly condensed plume is visible moving towards the observer. In the front, the NOVAC instrument Mark II is waiting to be set to work.

Composition measurments

Date	Measurement site	Instrument	Serial No.	No. of measurement
16.07.	Sapienza	NOVAC MKII	HR2B2285	16
	Torre de Filosofo	miniMax	USB2G10785	139
18.07.	Milo	NOVAC MKII	HR2B2285	39
	R.Citelli	miniMax	USB2G10785	123
	R.Citelli	miniMax	USB2G10785	58
19.07.	Milo	NOVAC MKII	HR2B2285	183
	bocche2008	miniMax	USB2G10785	163
22.07.	Nic-Rag	NOVAC MKII	HR2B2285	24
	Sapienza	miniMax	USB2G10785	144
24.07.	FireStation SW	NOVAC MKII	HR2B2285	44
	sottoCrateri	miniMax	USB2G10785	88
27.07.	Sapienza	NOVAC MKII	HR2B2285	52
	Bel.-Rag.	miniMax	USB2G10785	164
28.07.	North of Rag.	NOVAC MKII	HR2B2285	44
	Ragalna	miniMax	USB2G10785	144
	Torre de Filosofo	miniMax type	QEA0121	42

Table 8.5. Composite measurements performed during July 2009

SO_2 flux measurements

Date	Measurement site	Instrument	Serial No.	No. of measurement
16.07.	Sapienza	NOVAC MKII	HR2B2285	2
18.07.	Milo	NOVAC MKII	HR2B2285	22
20.07.	Milo	NOVAC MKII	HR2B2285	2
27.07.	Sapienza	NOVAC MKII	HR2B2285	2

Table 8.6. SO_2 flux measurements performed in July 2009

dedicated measurement geometry. These measurements were performed a NOVAC instrument Mark II with a HR2000 OceanOptics spectrograph (HR2B2285) and a mini-MAX-DOAS system incorporating an OceanOptics USB2000 (USB2G10785). Additionally, the QE65000 (QEA0121) spectrograph used for traverses was fitted with a scanning telescope for the last measurement day July 28^{th}. All three systems are temperature controlled. Optical resolution is 0.58 nm for the HR2B2285, the instrument recorded 300 spectra per measurement angle with an exposure time between 300-800ms. The miniMax DOAS instruments spectrograph had an optical resolution of 0.5 nm. Number of scans added for each measurement was 1000, but with a much lower exposure time ($\approx$ 100 ms). The QE65000 offers the best signal to noise ratio and was used with an exposure time of ca. 900 ms, adding 18 scans per measurement.

Traverse measurements

Date	Run	Time of day	Azimuth from source [°]	r^2	used
16.07.	run0005	12:01-13:00	189	0.741	TRUE
	run0006	13:10-14:05	185	0.833	TRUE
	run0008	14:30-15:25	188	0.557	TRUE
	run0009	15:34-15:44	187	0.598	FALSE
	run0010	15:47-17:23	-2888	0.665	FALSE
18.07.	run0002	14:00-14:45	87	0.966	TRUE
	run0003	14:48-15:51	90	0.955	TRUE
	run0004	15:55-16:50	93	0.887	TRUE
19.07.	run0001	10:05-10:27	0	NaN	FALSE
	run0002	10:31-11:31	127	0.956	TRUE
	run0005	11:50-12:30	130	0.969	TRUE
	run0006	12:36-13:14	130	0.903	TRUE
	run0007	13:19-14:27	137	0.65	TRUE
	run0008	14:34-17:13	159	0.515	FALSE
20.07.	run0001	10:27-11:47	128	0.862	TRUE
	run0002	11:52-12:46	125	0.968	TRUE
	run0003	12:51-13:59	126	0.936	TRUE
	run0004	14:03-16:06	138	0.745	TRUE
22.07.	run0002	10:39-11:06	170	0.208	FALSE
	run0003	11:10-11:45	1	NaN	FALSE
	run0004	11:48-12:26	1	NaN	FALSE
	run0005	12:30-13:24	158	0.793	TRUE
	run0006	13:28-14:12	160	0.925	TRUE
	run0007	14:17-15:26	162	0.732	TRUE
	run0009	15:37-18:12	177	0.728	TRUE
24.07.	run0001	09:39-10:59	210	0.889	TRUE
	run0002	11:04-11:59	204	0.866	TRUE
	run0003	12:02-12:36	202	0.948	TRUE
	run0004	12:39-13:09	202	0.932	TRUE
	run0005	13:16-14:09	202	0.951	TRUE
	run0006	14:11-15:05	203	0.916	TRUE
	run0007	15:10-16:14	198	0.837	TRUE
	run0009	16:36-17:07	190	0.965	TRUE
27.07.	run0002	10:40-11:53	183	0.219	FALSE
	run0003	11:58-12:38	171	0.976	TRUE
	run0004	12:42-14:06	168	0.915	TRUE
	run0005	14:17-15:13	156	0.444	TRUE
	run0006	15:16-15:59	154	0.972	TRUE
	run0008	16:30-16:56	179	0.267	FALSE

Table 8.7. Traverses performed during July 2009 at Mt. Etna. For each run, the azimuth direction is given from crater to measured centre of the traverse. Column "used" indicates whether or not the traverse could be used to calculate wind direction and plume ages.

Figure 8.5. Measurement setup of car traverses: The telescopes (arrows) pointing towards zenith are mounted at the driver side of the car in order to reduce obstruction of view by vegetation at the side of the road. Optical fibres lead to the spectrograph inside the cooling box in the car. View through the window is blocked in order to reduce heating of the cooling box by the sun.

SO_2 flux measurements Scans of the volcanic plume were only performed with a the NOVAC Mark II instrument described above. Typical measurement geometry consisted of a flat scan, e.g. of 23 measurements, which scanned the sky at steps of 5° elevation angle from 15° elevation above horizon at 180° azimuth from north to 70° elevation at 0° azimuth angle. Also scans with lower resolution of elevation angles were performed, aimed at identifying the volcanic plume for plume composition measurements and not to determine SO_2 fluxes. Due to the low number of spectra per scan, these are disregarded in the calculation of BrO/SO_2 ratio because number of scans to be added is too low to increase the signal to noise ratio above a reasonable detection limit for BrO. SO_2 fluxes are mainly calculated by performed traverse measurements.

Car traverses Car traverses were performed with a QE65000 Oceanoptics spectrograph, which offerers a back-thinned detector with high quantum efficiency in the the near ultra violet region. The detector was cooled at -5° C and the whole spectrograph kept in a temperature controlled box at 15° C. Measurement times per recorded spectrum were on the order of 2 s, corresponding to 3 single spectra added together with $\approx$ 700 ms exposure time each. The range of spectra measuring the plume and to be used for FRS were selected manually from SO_2 evaluations. In this range, every 10 subsequently taken spectra were added in order to evaluate these spectra for BrO. Sensitivity tests were performed which number of spectra

to add yields best results, and it was found that the signal to noise ratio did not significantly increase if more then 10 spectra are added. This may be explained by the greater time difference between measurement of the FRS outside the plume and measurements of the plume centre itself. Also the roads taken often were narrow with overhanging vegetation, which obscured the telescope at times.

8.3 Pacaya, Guatemala, measurements February 2010

On February 5^{th}, 2010, gas emission studies were carried out of the plume of Pacaya volcano, Guatemala. Although several attempts were made to measure the volcanic plume in the previous days, heavy traffic on the journey to the volcano combined with weather changes prevented successful measurements.

8.3.1 Volcanic activity

The volcanic activity of Pacaya in January 2010 was marked by occasional, weak strombolian eruptions together with quite degassing. Multiple lava flows were reported on the South, South-West and West flank of the McKenney cone, which travelled 25-200 m (Smithsonian, 2011). At least on of these lava flows was still present during the measurement period, together with quite degassing of ≈ 125 tons/day SO_2. The Instituto Nacional de Sismologia, Vulcanologia, Meteorologia, e Hidrologia (INSIVUMEH) also reported strombolian explosions on February 5^{th}, 2010, which ejected ash and material 30 m high and a lava flow moving down the flank. The last strong eruption started on May 28^{th}, 2010, with ash ejected to an altitude of 1.5 kilometres above the crater. Ash falls occurred downwind, including Guatemala city and Aurora International Airport. Increased activity continued till the beginning of August 2010. The volcano and the measurement side are depicted in fig. 8.1.

8.3.2 Measurements

Measurements were performed with two stationary ground based Multi-Axis Differential Optical Absorption Spectroscopy (MaxDOAS) systems and a zenith looking DOAS system mounted on a car. The MaxDOAS instruments were placed side

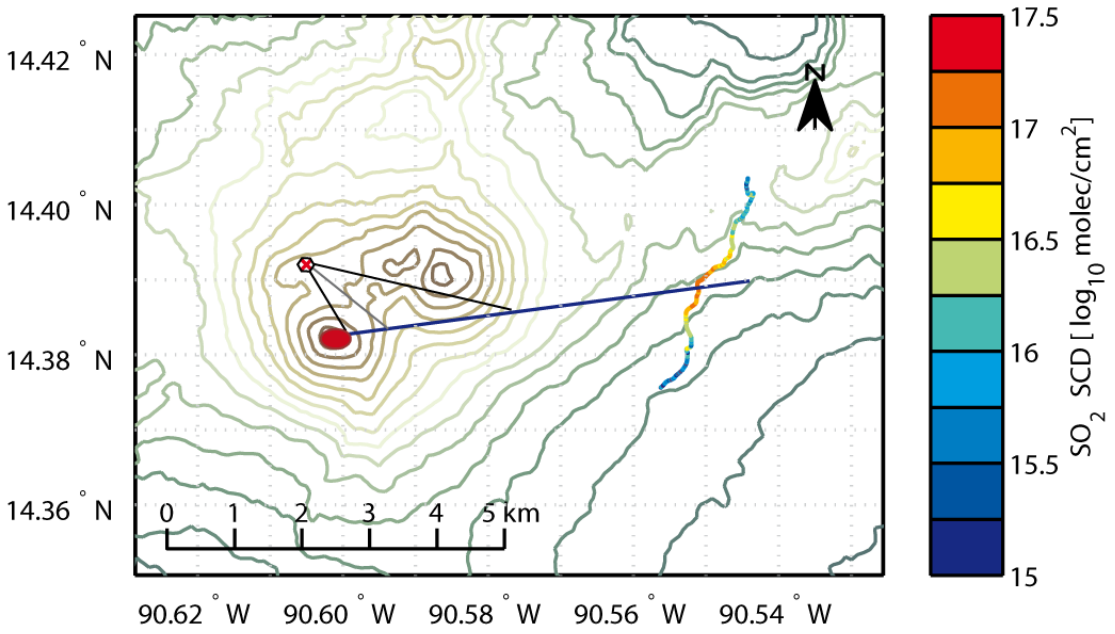

Figure 8.6. Map of Pacaya including performed traverse measurements. The red dot denotes the crater with the mean wind direction indicated by the blue line. Ground based measurement were situated north from the crater. The azimuth angles, at which the horizontal measurements were performed, are approximated by the black lines leading from measurement site to the travel path of the plume.

by side on the north-north-eastern flank of Pacaya at a distance of 1km from the crater. The traverse measurements were used to determine the wind direction obtain an estimate of volcanic SO_2 emissions. On the map (fig. 8.6), the crater of Pacaya is indicated by a red ellipse with the plume travelling direction indicated by the blue line. The measurement site is marked by a red x, and the field of view observing the plume from the measurement site is indicated by the black lines. They also mark the plume section observed by the horizontal plume measurements.

The two MaxDOAS instrument consisted of a standard miniMax DOAS instrument incorporating a USB2000 spectrograph, and an instrument which used a higher grade QE65000 spectrograph (OceanOptics, 2008). The QE65000 MaxDOAS used is very similar to the instrument described already in sec. 8.2, with the difference that the fixed telescope was exchanged against a scanning telescope, which allowed to perform measurements at different elevation angles. A cooling box is used to stabilize the spectrograph at 15° C, the detector of the spectrograph itself is cooled down to 5° C.
The miniMAX DOAS instrument was used to measure a plume cross section by recording spectra at various elevation angles with a fixed azimuth direction (tab.

Figure 8.7. Pictures of Pacaya, its plume and the instruments measuring it. The picture at the top gives a general impression off the measurements conditions. At the bottom left, miniMax DOAS instrument is visible as well as the scanning telescope belonging to the MaxDOAS instrument with incorporated QE65000 spectrograph (from left to right). The bottom picture shows the scanning telescope of the QE65000 instrument, with lines indicating both measurement set-ups used, horizontal and vertical plume scan.

Plume Composition measurements

Instrument	scanning direction	Fixed angle	Start time [UTC]	End time [UTC]	No. of measurements
MiniMax	Vertical	132° Azim.	16:00	18:03	11
MiniMax	Vertical	≈ 142° Azim.	18:13	19:15	4
QE65000	Vertical	132° Azim.	15:30	16:25	7
QE65000	Horizontal	19° Elev.	17:10	18:30	7

Table 8.8. Measurements performed during February 5^{th}, 2010, by stationary scanning instruments. Scanning direction indicates whether the scan was performed perpendicular to (vertical), or along the plumes travelling direction (horizontal), together with the angle that was kept fixed during respective measurement mode.

Traverses

Run	Start time [UTC]	End time [UTC]	Azimuth from source [°]	r^2
Run 1	16:58	17:08	82	0.8956
Run 2	17:09	17:18	87	0.7443
Run 4	17:25	17:35	91	0.9564

Table 8.9. On February 5^{th}, three traverses could be successfully performed at Pacaya. Next to the beginning and end of each traverse, also the direction of the plume's centre from the source is given, as well as the r^2 value for the goodness of respective fit.

8.8), whereas the MaxDOAS instrument with the QE65000 operated at two different modes:

1. Vertical scanning, where a measurement geometry was used with fixed azimuth angle (132°) and varying elevation angles (8° - 28°), similar to the one used with the miniMAX DOAS instrument.

2. Horizontal scanning, where the scanning telescope was mounted on a tripod to measure at varying azimuth angles instead of measuring at different elevation angles. The volcanic plume could be observed at various plume ages by varying the azimuth angle (104° - 145°) of the telescope at a fixed elevation angle of ≈ 17°, scanning the upper part of the plume.

The FRS were obtained at an elevation angle of 90° for both instruments scanning vertically. For the QE65000 MaxDOAS scanning horizontally, FRS were recorded at an elevation angle of 17° and azimuth angle of 175° upwind of the volcano. Table 8.8 gives an overview of performed measurement directions.
The photos depicted in fig. 8.7 show typical measurement conditions with the

plume of Pacaya propagating nearly horizontal. In the photo on top, both instruments are visible (miniMax and scanning telescope of the QE65000 spectrograph, from left to right). The bottom photo gives shows the two different measurement set-ups used with the QE65000 scanner. Red lines indicating the measurement direction along and perpendicular to the plume.

The car conducted plume traverses are shown to the east with their respective SO_2 column densities (fig. 8.6), giving the wind direction from the crater. They were conducted at about 5.5 km downwind of the volcano. Three traverses were successfully conducted (tab. 8.9). An SO_2 flux of 125 tons/day was measured by the traverses.

A portable weather station provided information on relative humidity and temperature. Relative humidity at the instrument site was measured to be 34% at 9:45h local time (15:45h UTC). The temperature was given as 30° C, but this value might be overestimated by several degrees. The wind speed could be well estimated by visual observations. "Puffs" of volcanic emissions could be tracked over the field off view, yielding observations during the first 5 min of plume age for the measurements in horizontal direction. This maximum plume age observed,measured was approximated to be 5 min. The wind direction showed slight changes during the last hour of measurements with the stationary instruments (tab. 8.8 and 8.9). An error is introduced by assuming a maximum observed plume age of 5 min for horizontal measurements, which is on the order of 20%. Since additional measurements of the wind speed are lacking, this is still the best estimate.

9 Results of SO_2 and BrO measurements in volcanic plumes

9.1 Mt. Etna, Italy, July 2008

As described in sec. 8.1, only July 12^{th}, 14^{th} and 16^{th} were exclusively dedicated to simultaneously measure the volcanic plume at different plume ages. Although at most other days also BrO/SO_2 ratios were retrieved, special focus is given to these three days. Results for all days are presented at the end of this chapter.

9.1.1 Retrieved BrO/SO_2 ratios on July 12^{th} 2008

On July 12^{th}, the three stationary NOVAC Mark II instruments were placed at R.Citelli, Milo and Giarre. Wind direction was stable during the times of measurement, which can be seen from tab. 8.7 and fig. 9.1.

BrO could only be detected without greater error by plume composition measurements, whereas as SO_2 flux scans and traverses failed to do so because of their higher detection limit of BrO. The volcanic plume was measured at an approximate plume age of 5min, 12.5min and 20min from Rifugio Citelli, Milo and Giarre respectively. Figure 9.2 gives an overview of all successful retrieved BrO/SO_2 ratios over the day, calculated from each individual measurement. Simultaneous measurements could be achieved between approximately 9:30h and 13:00h UTC. In contrast to the expected steady increase of BrO/SO_2 ratio with increasing plume age, the highest ratios are observed in the youngest plume. This is followed by a decrease in measured ratios at the plume measured from Milo ($\approx$12:30 min plume age), which is in the range of errors from both measurements. Afterwards, further increase of the BrO/SO_2 ratio is observed. Also visible are slightly diminished

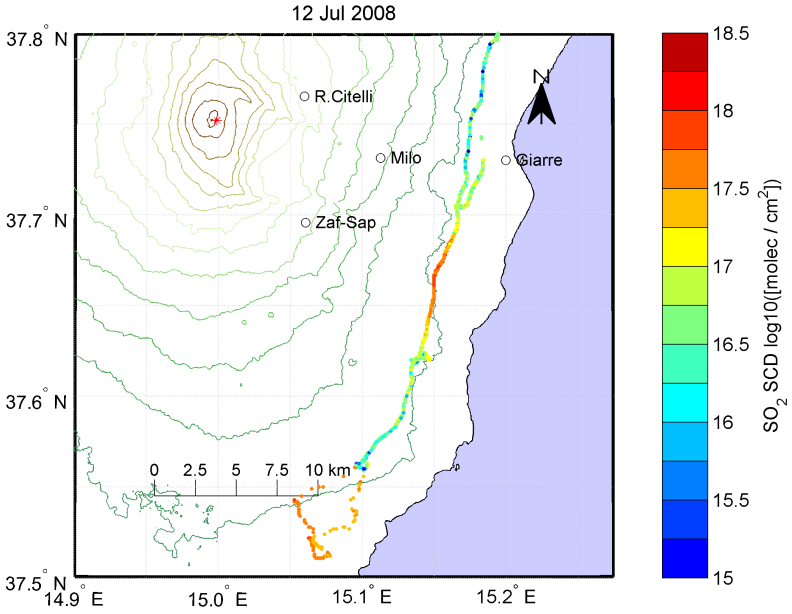

Figure 9.1. Traverses performed on July 12^{th} 2008. Wind direction was stable from West during all measurement times. During the first early traverse, an old plume was detected to the south west of Mt. Etna, which can be disregarded.

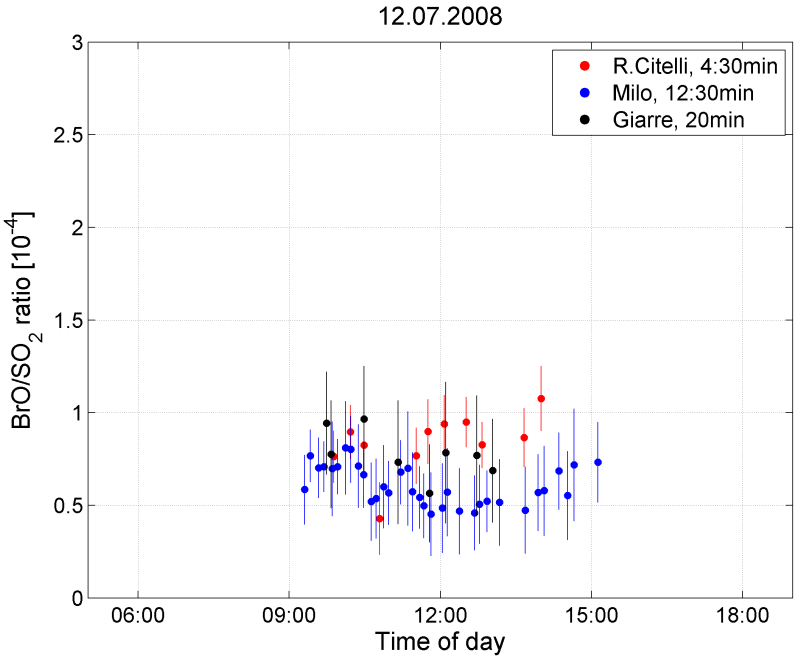

Figure 9.2. Depicted are successfully retrieved BrO/SO_2 ratios for July 12^{th} vs time of day [UTC]. Ratios at youngest plume age of ≈4:30 min are given in red, whereas measurements at ≈12:30 min are colored blue and ≈20 min black. A so far not predicted development of BrO/SO_2 ratios is the apparent temporal decrease seen for the measurements at 12:30 min.

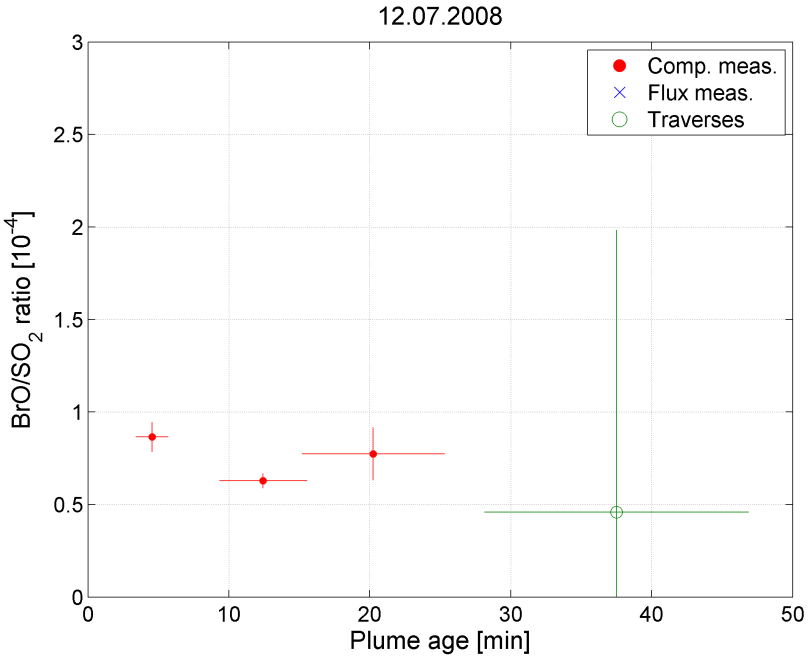

Figure 9.3. Depicted are mean BrO/SO_2 ratios for July 12^{th} during the first 50 minutes of plume age. BrO could only be detected successfully by plume composition measurements, traverses yield a ratio with greater error. A general error in wind speed of 25% is assumed.

ratios for the mid-aged plume during midday, which has not been described for BrO chemistry in volcanic plumes previously.

Mean ratios for the day (measured between 9:30 h - 15:00 h) are shown in Figure 9.3. It depicts ratios vs. plume age, where the ratios have been determined by correlating measured SO_2 and BrO values for each measurement site. For the fit, a polynomial of type $y = a \cdot x$ was used and each data pair weighted by their respective error of the ratio. A decrease in the BrO/SO_2 ratio at 12:30 min plume age is clearly visible in this average.

9.1.2 Retrieved BrO/SO_2 ratios on July 14^{th} 2008

On July 14^{th}, the wind was blowing the volcanic plume almost directly over the three measurement sites R.Citelli, Milo and Giarre. Only slight changes in wind directions were encountered during the day, which can be observed in fig. 9.4 were the plume was detected between Milo and Giarre during the first traverse.

Fig. 9.5 shows measured $BrOSO_2$ ratios over the day. Ratios determined by SO_2 flux measurements are depicted with "x" whereas composition measurements are marked by dots in order to differentiate between the different measurement

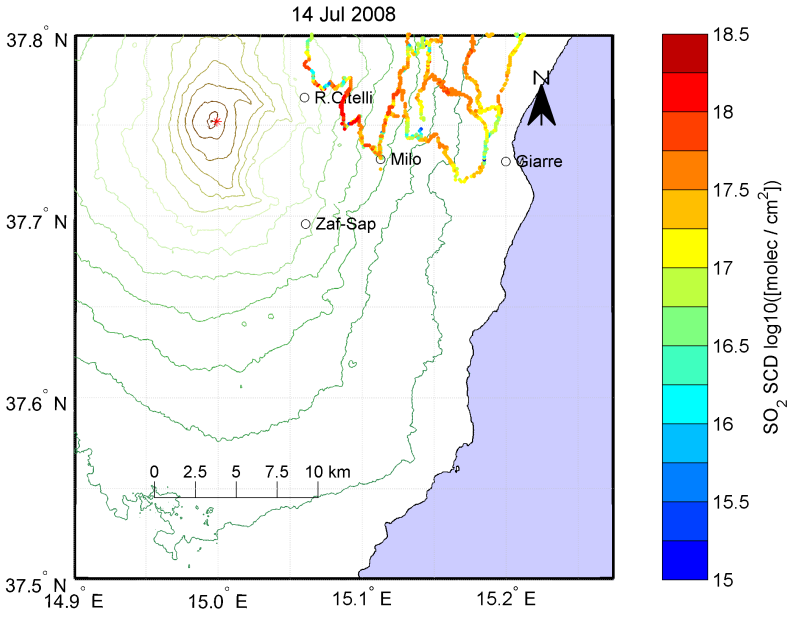

Figure 9.4. Traverses performed on July 14^{th} 2008. The wind was coming out of western direction. Difficulties to fully traverse the plume were encountered due to routeing and configuration of streets and roads. Nevertheless, the plume could be clearly identified and BrO detected (see also fig. 9.5 and 9.6).

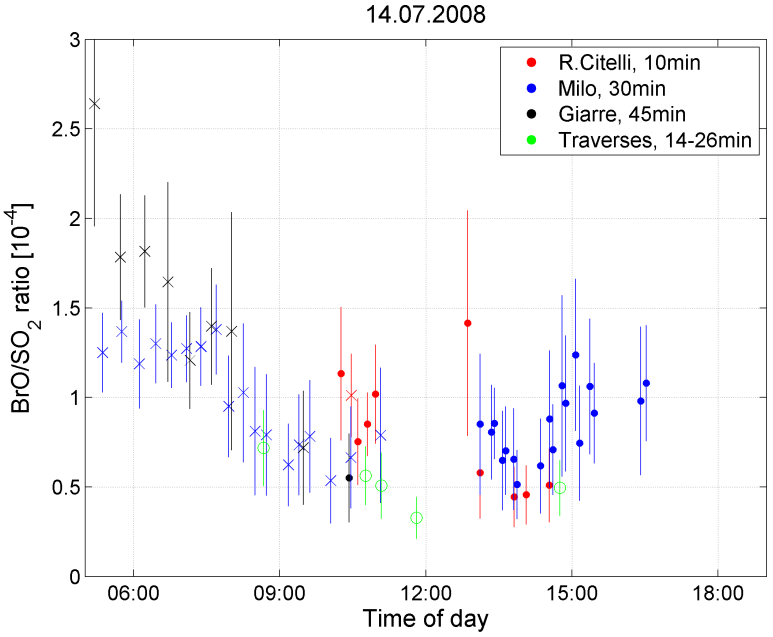

Figure 9.5. Depicted are BrO/SO_2 ratios measured at July 14^{th} at different times of day. BrO could not be simultaneously detected at all times. To differentiate between the different measurement geometries, BrO/SO_2 ratios determined by SO_2 flux measurements are marked by "x", whereas ratios determined by plume composition measurements are indicated by dots. For further details see text.

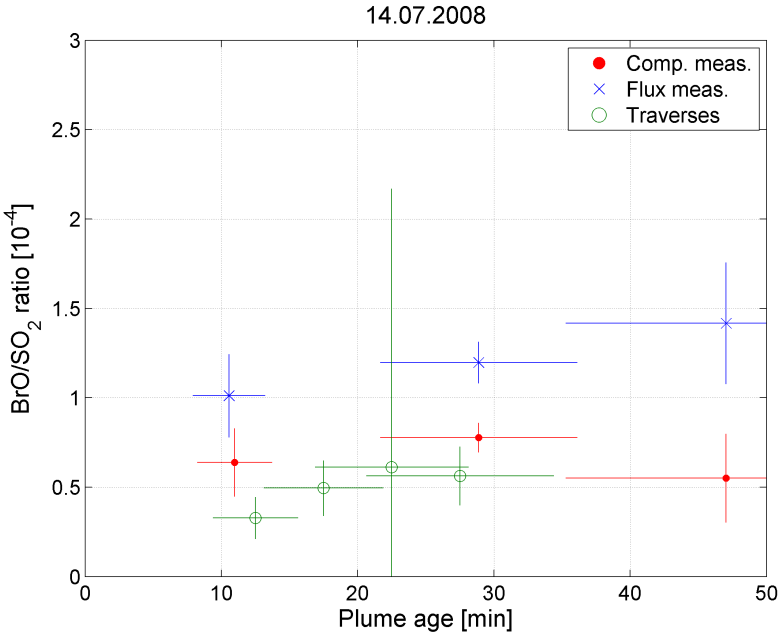

Figure 9.6. Depicted are mean BrO/SO_2 ratios for July 14^{th} during the first 50 minutes of plume age. A general error in wind speed of 25% is assumed. Observed is a strong dependence of retrieved ratios on the measurement setup, which may be attributed to falsely assigned plume ages for flux measurements above 25 min and possible radiative transfer effects. For details see text.

geometries. Unfortunately, BrO could not be simultaneous detected at all times of the day. Only between approximately 10:00h and 11:00h UTC, all three stationary instruments successfully determined BrO/SO_2 ratios. For these measurements, a steady decrease of ratios with increasing plume age may be indicated by the data, but within the measurement error, also a constant ratio is possible. During later times of day ($>$ 13h UTC), measured data suggests an increase of ratios with plume age. It must be noted though, that the plume was travelling slightly more in a northern direction with increasing time of the day. This increased the distance between the instrument in Milo and the plume, possibly resulting in a minor overestimation of the BrO/SO_2 ratio due to a stronger light dilution effect for the retrieval range of SO_2.

At plume ages of 30min and older for measurements performed from Milo and Giarre, only small changes in ratio are visible in the morning. Next to this, also elevated values at the earlier morning before 8:00h UTC are observed. The READY model predicted wind changes from 245° to 265° from 6:00h and 12:00h UTC, corresponding well to the wind direction measured by traverses at a mean of 259° N. This indicates that the plume might have been measured at older plume ages in the early mornings.

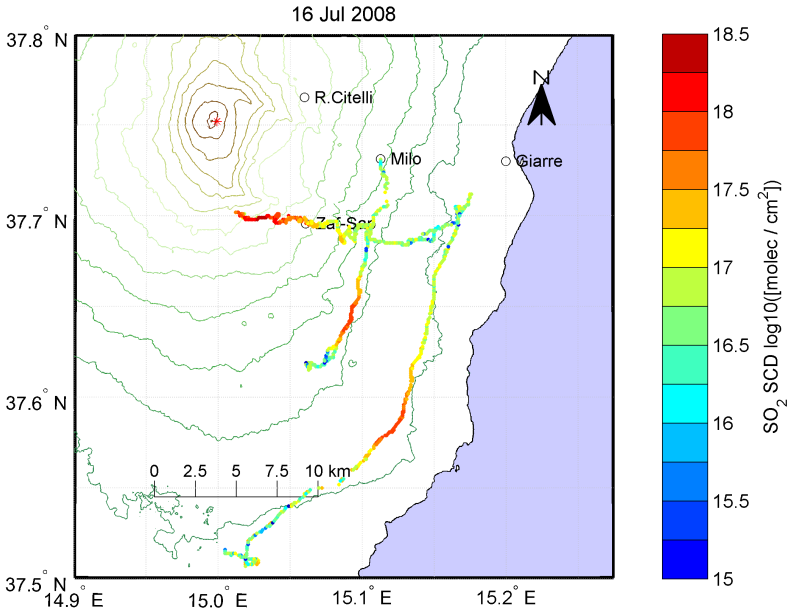

Figure 9.7. During July 16^{th}, the volcanic plume was blowing to the South-East at constant wind direction. Traverses closest to the crater could not reach the end of the plume because of the layout of the roads. At $\approx$ 15 km and $\approx$ 20 km distance to the crater, the plume had widened to 7.5 km and 10 km, respectively. The plume centre was well defined even at greatest distance with peak SO_2 SCDs on the order of $1 \cdot 10^{18}$ molec/cm^2.

Fig. 9.6 depicts the mean ratios for each measurement setup, which are determined via correlation plots. A discrepancy between the different measurement scenarios is apparent with highest BrO/SO_2 ratios measured with SO_2 flux measurements, intermediate ratios for plume composition measurements and lowest ratios retrieved from traverses. Although the ratios can differ by 100% on first sight, their measurement times must be considered as seen in fig. 9.5. Ratios determined by SO_2 flux measurements were obtained exclusively at early times of day. It is probable that these ratios were measured at older plume ages and are not directly comparable to the others. If ratios are measured in close proximity in time by both measurement geometries, they exhibit similar values (e.g. R.Citelli, $\approx$10:30 min, fig. 9.5).

9.1.3 Retrieved BrO/SO_2 ratios on July 16^{th} 2008

Traverses performed during July 16^{th} show constant wind directions with the volcanic plume being blown towards South-East. Observed is an almost linear

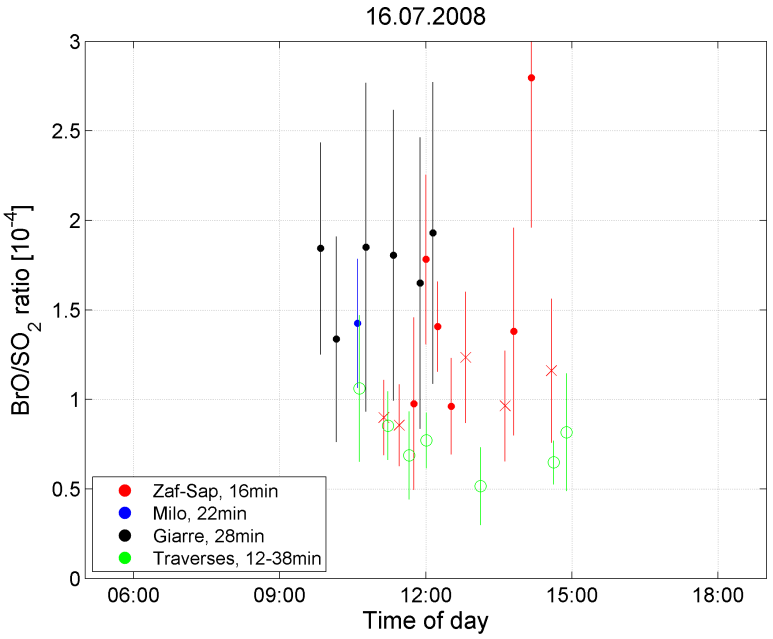

Figure 9.8. Measured BrO/SO_2 ratios during July 16^{th}. Because the wind was coming from the North-West, the instrument measuring usually at R.Citelli was placed along the road between Zaferana and Sapienza (Zaf-Sap). Although errors of ratios are high, an increase of ratios with increasing plume age is indicated from measurements before 12:00h UTC.

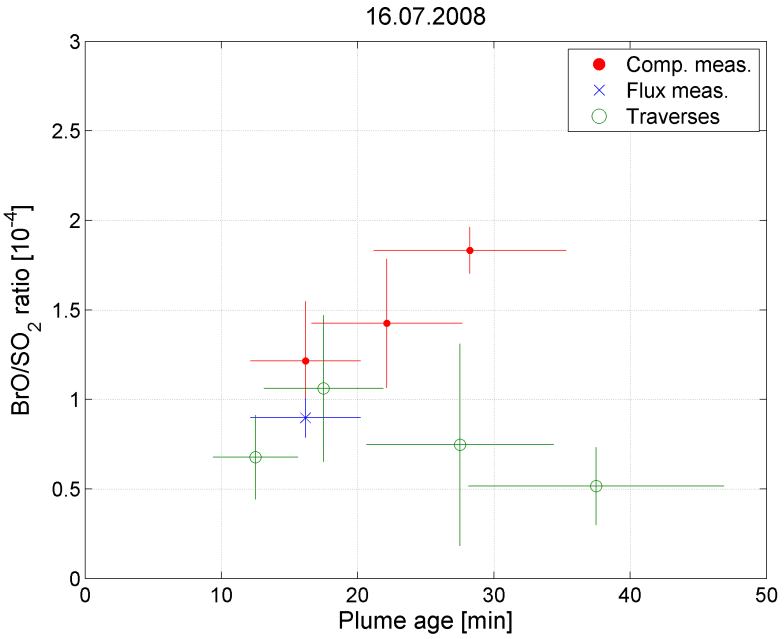

Figure 9.9. Depicted are mean BrO/SO_2 ratios for July 16^{th} during the first 50 minutes of plume age. Results of plume composition measurements and traverses differ after the first 25 min. This may be a result of radiative transfer effects due to the large distance ($\approx$ 25 km) between stationary instrument (Giarre) and plume. A general error in wind speed of 25% is assumed.

plume dispersion with increasing distance to the crater, with a maximum width of ≈ 10 km at 20 km distance. The NOVAC instrument measuring the youngest plume could be placed along the road (Zaf-Sap) directly under the plume.
Simultaneous measurements of BrO/SO_2 ratios could not be achieved from all three stationary instruments, because the instrument in Milo failed to detect BrO except for one measurement around 10:00 h UTC in the morning. Nevertheless, an increase of ratio with plume age is indicated by concurrent measurements from Zaf-Sap and Giarre. It must be noted, that due to the wind direction present during measurements, distance between instrument in Giarre and volcanic plume was on the order of 25 km, which is greater than the mean optical path length by more than a factor of 2. Due to the different strengths of radiative transfer effects for the retrieval wavelength ranges of BrO and SO_2, it can be assumed that the later is underestimated and thus their measured ratio can only be regarded as an upper limit.
If these values are used to calculate daily means via linear correlation for each respective data set (fig. 9.9), it is apparent that ratios determined by plume composition measurements and traverses differ after the first 25 min. The measurements of the oldest plume by composition measurements are done from Giarre and should be regarded only as an upper limit as discussed above. Measurements of BrO/SO_2 ratios at other plume ages agree within the respective measurement error. If the measurements from Giarre are ignored (red dot of $\approx 1.9 \cdot 10^{-4}$ molec/cm^2 at 28 min plume age), an evolution of the ratio is observed with a maximum value of $1.5 \cdot 10^{-4}$ molec/cm^2 is observed at 22 min with a subsequent decrease in BrO/SO_2 ratio.

9.1.4 BrO/SO_2 for all measurement days, July 2008

Figure 9.10 depicts combined BrO/SO_2 ratios retrieved during the Etna campaign in July 2008. They have been calculated by taking the mean and standard deviation of the average ratios of each day, binned to plume ages on a 5 min grid (0-5 min, 5-10 min, ...). The variability of retrieved ratios is due to day to day variations in ratios, as well as possibly changes in wind direction affecting the calculated plume age and overestimation of ratios due to radiative transfer effects (compare sec. 9.1.1 - 9.1.3). A strong increase in BrO/SO_2 ratios is observed in the during the first 5 min after emission. After this initial "BrO explosion", ratios increase only slowly or even remain on a comparable level within given errors (ignoring the outlier at 47.5 min plume age). The calculated means of BrO/SO_2 ratio increase

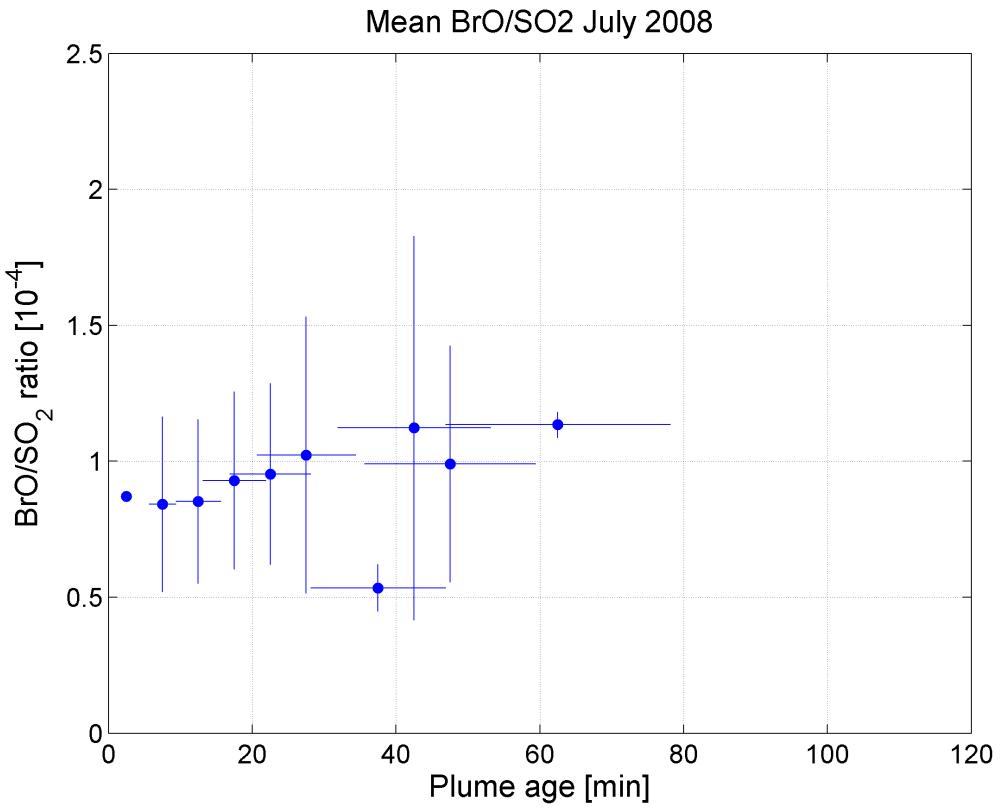

Figure 9.10. Combined BrO/SO_2 ratios for July 2008. Depicted values correspond to the mean and standard deviation of average retrieved values during each day, binned onto a 5 min plume age grid. If only one measurement exists during the respective plume age range, the measurement error is given instead of the stadndard deviation. A general error in wind speed of 25% is assumed. The errors observed results from the great variability of results, changing on a day to day basis.

from $0.84 \cdot 10^{-4}$ at 7.5 min till $1.15 \cdot 10^{-4}$ at 62.5 min. Disregarding any loss of SO_2, this corresponds to a build up of 75% of the number of BrO molecules measured in the first 5 min after emission of the plume.

9.2 Mt. Etna, Italy July 2009

During the campaign at Mt. Etna, July 2009, BrO/SO_2 ratios were measured by two stationary instruments and by car traverses. The later employed a high grade spectrograph (QE65000, OceanoOptics) in order to achieve an optical signal to noise ratio. Unfortuntately, the campaign was marked by an unusual variability of wind direction for the season, with the most prominent wind direction from North-West-North. Thus instrument placement and performed traverses suffered

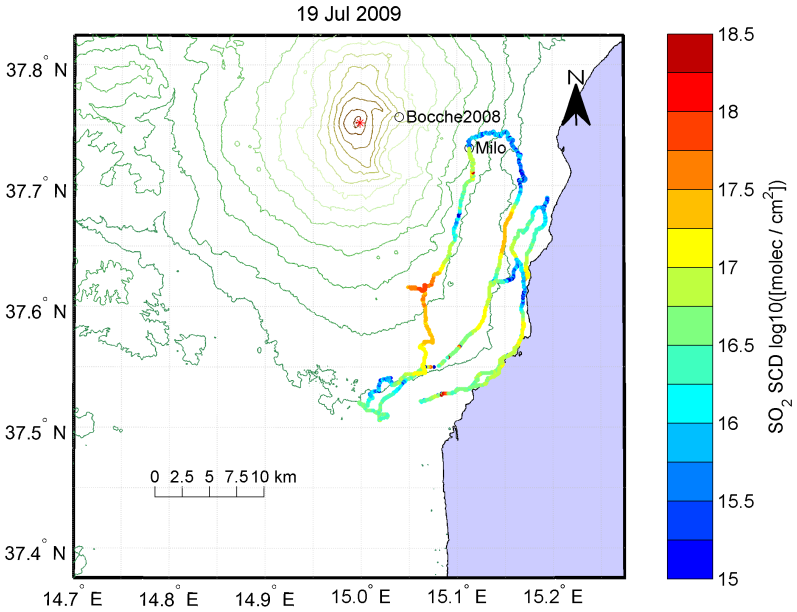

Figure 9.11. Traverses performed on July 19^{th} show that a change of wind speed occurred during the day, shifting the plume's main travel direction from WSW (127° at approx. 11:00h UTC) to SW (137° at approx. 13:45h UTC), see also tab. 8.7.

longer journeys to respective sites and times when the plume had to be searched tediously. Simultaneous measurements with successful detection of BrO could not be achieved by all three instruments most of the time. In the following, results from July 19^{th} and 24^{th} are presented in greater detail (sec. 9.2.1 and 9.2.2), representing typical measurement results. BrO could be observed in the volcanic plume simultaneously on July 19^{th}. General results of the campaign are presented in sec. 9.2.3.

9.2.1 Retrieved BrO/SO_2 ratios on July 19^{th} 2009

The already mentioned variability of wind direction during the Etna campaign 2009 is observed in fig. 9.11 for the July 19^{th}. During the course of the day, the plume was blown more to the south. The stationary instruments measured different plume ages during the day because the operated at a constant azimuth viewing angle. miniMax DOAS measurements at site Bocche2008 were not greatly affected due to close proximity to the crater and an azimuth viewing direction of 220°, changing from 8:30 min to 11:30 min plume age. The instrument stationed at Milo on the other hand was pointed at 180° on the other hand and observed plume

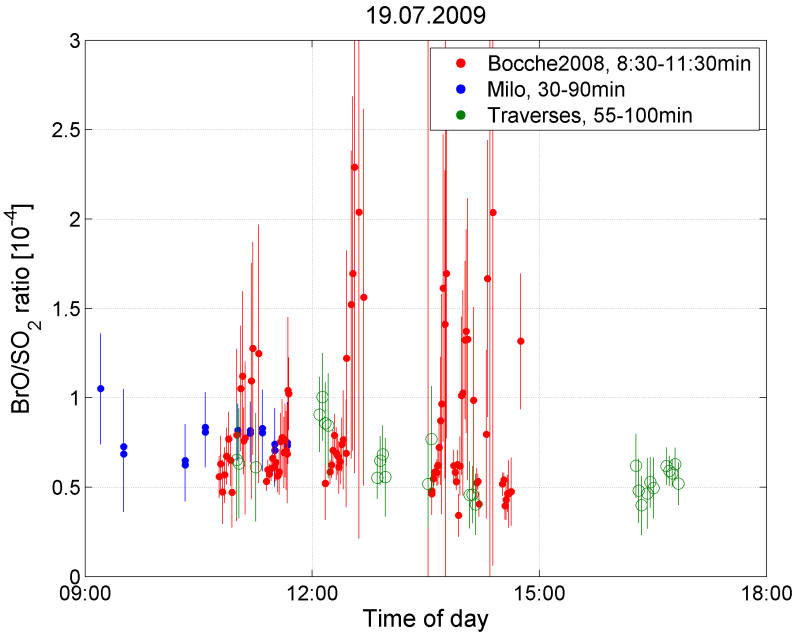

Figure 9.12. BrO/SO_2 ratios observed during July 19^{th}. Changing wind directions are responsible for the great diversity of plume ages observed from the stationary instruments. Although Milo measures $BrOSO_2$ ratios over a greater difference in plume age, ratios vary much more for measurements from Bocche2008. Details see text.

ages ranged from 30 min for the first measurements till approx. 85-90 min after 11:00h UTC. Retrieved BrO/SO_2 ratios measured over the day are depicted in fig.9.12. Although the variability of plume ages is much smaller for measurements performed from Bocche2008 than from Milo, the observed ratios differ much more for the site closer to the volcano. Ratios higher than $2.5 \cdot 10^{-4}$ are observed at times. An explanation for this greater variability may be that the plume is not well mixed with ambient air so close to the crater. Variations of emission strengths are more prominent and also different plumes from the different main craters of Mt. Etna may be observed, which are known to emit different amounts halogens (Pennisi and Le Cloarec, 1998; Bobrowski et al., 2007). BrO/SO_2 ratios measured from Milo on the other hand are comparatively stable with a mean value of $\approx 0.75 \cdot 10^{-4}$. Only the ratio measured earliest during the day at a plume age of 30 min surpasses 10^{-4}. Also at the plume ages observed, the volcanic plume has been well mixed with ambient air. If the velocity of the chemical reactions leading to BrO are comparable to the ones measured during July 2008 (sec. 9.1.4), an increase in BrO/SO_2 ratio can be expected to be slow at these plume ages - or in this case even steady.

In order to discuss the traverse measurements, it is instructive to look at fig.

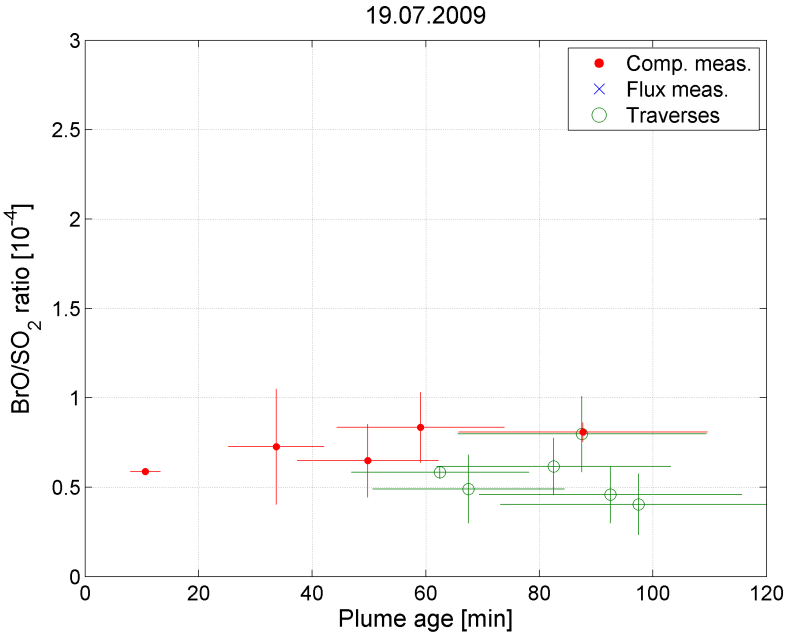

Figure 9.13. Depicted are daily means of BrO/SO_2 ratios for July 19^{th} 2009. Because of changing wind directions, plume ages measured from Milo differed greatly. To account for this, depicted composition measurements at 33 min, 49 min and 59 min are plotted separately from measurements 86 min. The later should be regarded as an upper limit due to the great distance ($\approx$ 26 km) between instrument and plume. Evolution of BrO/SO_2 ratio with plume age is resolved in the first 100 min after release.

9.13. It shows the average ratios during the day for mean plume ages measured at respective sites, except for measurements taken from Milo. Due to changing wind directions, these measurements are plotted individually for the first 60 min of plume age and the average is depicted for the plume ages $>$ 85 min. The latter should only be regarded as an upper limit because distance between measurement site and plume was approximately 26 km. The evolution of BrO/SO_2 ratio has been captured well if somewhat qualitatively for the first 100 min of plume age.

9.2.2 Retrieved BrO/SO_2 ratios on July 24^{th} 2009

During July 24^{th} more stable wind directions were encountered then on July 19^{th} for most of the measurements. Coming from 30° at about 10:30h UTC, wind direction changed to 23° between 11:00h and 15:00h UTC (see fig. 9.14). BrO could not be detected after 12:30h UTC, meaning that the stationary instrument might have probed plume cross sections of different plume ages. Possible errors in

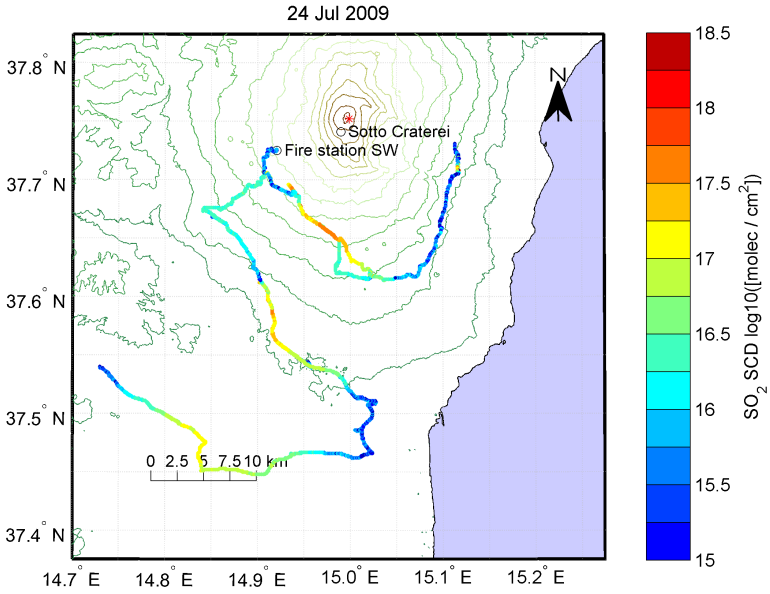

Figure 9.14. Traverses during July 24^{th} 2009 show a relatively constant wind direction ($\approx 23°$ N) during most times of the day.

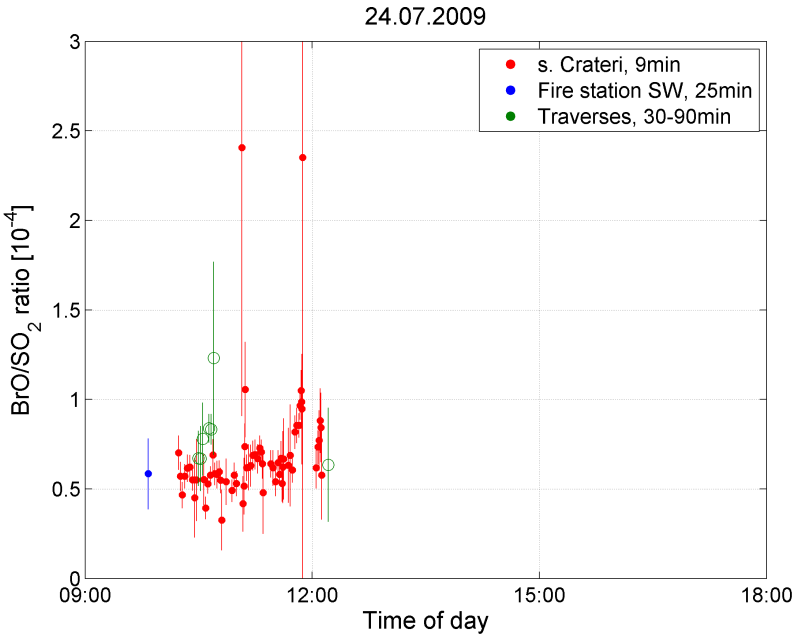

Figure 9.15. Ratios during July 24^{th} 2009 could not be detected simultaneously from both stationary instruments. However, ratios at older plume ages are observed by traverses measurements, indicating an increase in BrO/SO_2 ratio with increasing plume age.

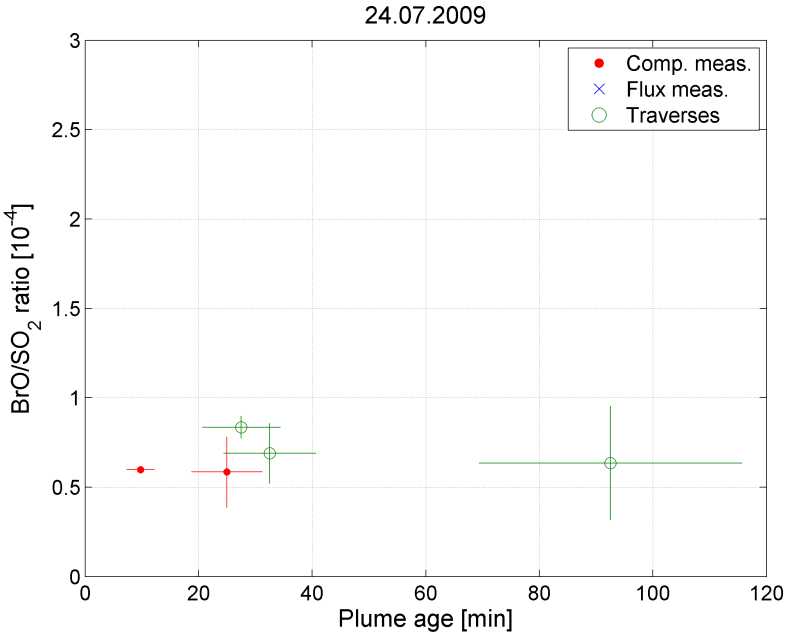

Figure 9.16. Mean BrO/SO_2 ratios measured on July 24^{th}2009. Composition measurements at 27.5 min were measured from site "fire statio SW" approximately 30 min before the other measurements. After the initial strong increase of ratios at 9 min plume age, further increase is observed by traverse measurements at 30 min followed by a possible decrease as indicated by traverse measurements at 90 min.

plume age calculation due not increase, because all wind directions are interpolated to the respective time of day and stationary instruments were located quite close to the crater (fig. 9.14) and close to the travel direction of the plume.

July 24^{th} represents typical results for measurement during the campaign 2009, because usually only two instruments (stationary and/or traverses) could detect BrO successfully. Nevertheless, simultaneous measurements are performed and conclusions on evolution of the BrO/SO_2 ratios can be drawn. Figure 9.15 depicts results vs. time of day. The early plume could be measured by the miniMax DOAS instrument at site "sotto Crateri", whereas traverses observed the older plume at a variety of plume ages. From the site "Fire station SW" only one successful detecion of BrO could be achieved right after deployment of the instrument, which does not coincide with other measurements.

Plotting obtained ratios against plume age in fig. 9.16, an increase in ratio is visible from about $6 \cdot 10^{-5}$ at 10 min to $\approx 7.5 \cdot 10^{-5}$ at 30 min plume age ignoring the composition measurement from "Fire station SW". This is remarkably similar to the evolution observed during July 19^{th} (fig. 9.13). If equal measurement conditions are assumed during all times of day thus including "Fire Station SW", the same development can still be observed within respective errors. Traverses

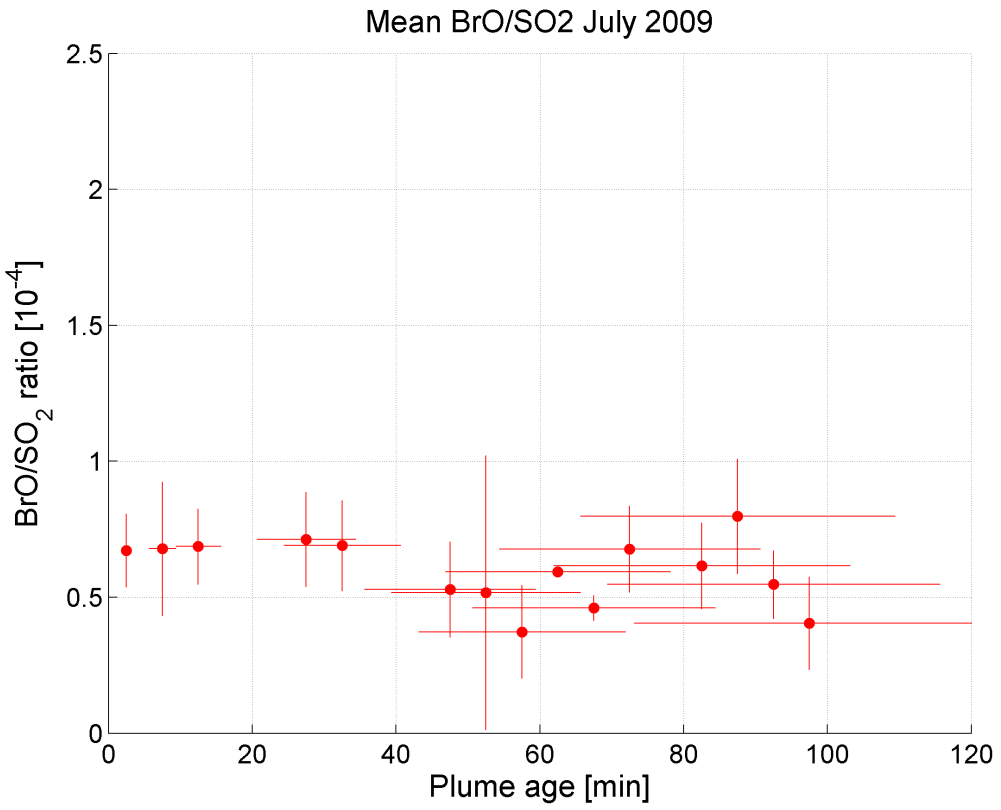

Figure 9.17. Combined BrO/SO_2 ratios for July 2009. Depicted values correspond to the mean and standard deviation of average retrieved values during each day, binned onto a 5 min plume age grid. A general error in wind speed of 25% is assumed. After an initial strong increase from 0 to $6.5{\cdot}10^{-5}$ during the first 5 min, BrO/SO_2, only minor increase can be seen, peaking at 30 min, if at all present. Afterwards ratios may decrease.

at greatest distance to the plume corresponding to 90 min plume age could also measure BrO/SO_2 ratio, although only with a relative error of 50%. Again, as already discussed for the earlier day (sec. 9.2.1), further increase of the BrO/SO_2 ratio cannot be reported. As a maximum, the ratio may have stayed at the same level between 30 min and 90 min, but the data indicates rather a decrease in ratio.

9.2.3 BrO/SO_2 for all measurement days, July 2009

The in the previous sections described evolution of BrO/SO_2 is generalised by combining all BrO/SO_2 ratios obtained between July 16^{th} and 28^{th}. Fig. 9.22 shows the daily means from stationary measurement sites and individual traverses at their respective plume age. An initial "bromine explosion" is apparent in the first 5 min after emission, reaching a ratio of $6.5{\cdot}10^{-5}$. Afterwards the ratio is

maintained but does not significantly increase further, which is differs from the results obtained a year earlier (sec. 9.1). Ratios at older plume ages (> 50 min) have been measured mostly by traverse measurements. The greater variability for this data points may be due to day to day changes in emitted volcanic gases and/or changes of atmospheric conditions and trace gas concentrations in the ambient air affecting the chemical reactions involved. Radiative transfer effect cannot be ruled either, but can be expected to be less severe for traverses than for other measurements due to relative close distance between car and overlaying cloud (max. 4km). E.g. ratios during July 19^{th} do not show such a large range at older plume ages (fig. 9.13). Nevertheless, in fig. 9.22 not only proof is given for the lack of increase of ratio but a decrease is indicated after the first 45 min.

9.3 Pacaya, Guatemala, Febr. 2010

In the following, results are presented from measurements on February 5^{th}, 2010, at Pacaya, Guatemala. Although two co-located instruments observed the volcanic plume, only the measurements performed incorporating the higher grade QE65000 spectrograph are discussed in detail in sec. 9.3.1 and 9.3.2, since some inconsistencies are present in the results from both spectrograph. They are discussed in sec. 9.3.3. For conclusions and comparison to modelled results, the reader is referred to sec. 9.4.1.

9.3.1 Vertical plume scans

The retrieved SCDs obtained during the vertical scan by the MaxDOAS instrument (QE65000 spectrograph) are depicted in fig. 9.18. Next to SO_2 and BrO (top), also NO_2 and HCHO SCDs are given (bottom). Obtained at an azimuth direction of 132° ($\approx$ 2 : 30 min plume age), the vertical scan clearly identifies the plume between 8° and 20° elevation. The exclusive detection of BrO at 12° and 16° shows its volcanic origin. The mean BrO/SO_2 ratios are comparable, with $4.4 \cdot 10^{-5}$ at 12° and $4.5 \cdot 10^{-5}$ at 16°, yielding a total mean of BrO/SO_2 of $4.42 \cdot 10^{-5}$ obtained during the vertical scans.
Included in the retrieval of BrO, HCHO and NO_2 were measured in the lower atmosphere. Their respective SCDs are depicted in the bottom graph of fig. 9.18. A decrease of SCDs with increasing elevation angles is expected due to the prolonged optical path length in the lower atmospheric layers at lower elevation

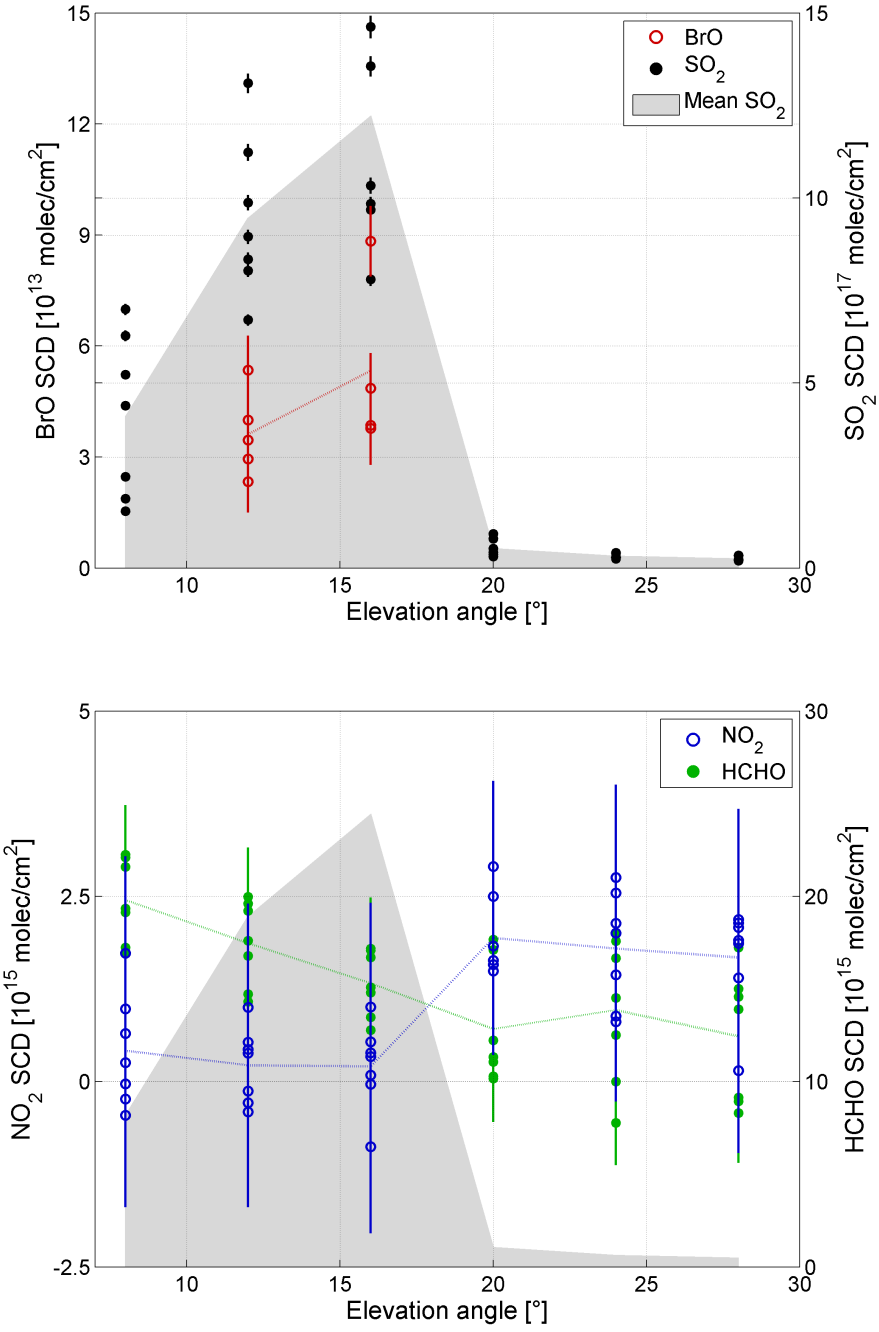

Figure 9.18. The graph at the top depicts BrO and SO_2 SCDs above the detection limit, measured with the QE65000 scanning instrument at 132° Azimuth. The plume is indicated by mean values of SO_2 SCDs at respective elevation angles. BrO can only be measured above the detection limit when the volcanic plume is measured. The graph at the bottom shows NO_2 and HCHO SCDs obtained in the retrieval of BrO. The respective mean is plotted by the dotted line. The plume is indicated by the grey shaded area (mean SO_2 SCDs).

angels, when the concentration of these trace gases is enhanced in the lower atmospheric layers. Measured HCHO SCDs are above the detection limit, with an apparent decrease in SCDs with increasing elevation angle, without dependence on the volcanic plume. Although estimation of HCHO concentration in the ambient atmosphere is not unambiguously possible, the measurements show an elevated HCHO abundance in the lower atmospheric layers. NO_2 SCDs are close to zero and usually below a detection limit of $2 \times \sigma$. However, their average values per elevation angles are depend on the volcanic plume. Instead of a further increase of NO_2 SCDs with lower elevation angles, a decrease in the volcanic plume is detected. This is remarkable in such, that NO_x species are suspected to influence the BrO production in volcanic plumes (see chap. 2). However, since retrieved NO_2 SCDs are below or close to the detection limit, conclusions on atmospheric chemistry in volcanic plumes are not possible. The low NO_2 SCDs can be regarded as an indicator for low air pollution in the vicinity of the volcano Pacaya.

Retrieved BrO SCDs from the miniMax DOAS instrument incorporating an USB2000 spectrograph showed some discrepancy, which is discussed further in sec. 9.3.3.

9.3.2 Horizontal plume scans

The horizontal plume scans were performed at a constant elevation angle of 17° and azimuth angles between 104° and 142° corresponding to plume ages between 1:30 min and 5 min. The calculation of BrO/SO_2 ratios are depicted in fig. 9.19. A clear increase of the BrO/SO_2 ratio is visible. The red triangles depict ratios, where BrO could not detected. An upper boundary of the respective BrO/SO_2 ratios was calculated by dividing the detection limit of BrO ($2 \times \sigma$) by the respective SO_2 SCD. For plume ages below 2 min, the BrO/SO_2 ratio is $< 0.1 \cdot 10^{-4}$, raising to $1.2 \cdot 10^{-4}$ in the following three minutes. This constitutes the hitherto first capture of volcanic BrO chemistry at early plume ages (< 5 min) and high temporal resolution.
In the following, results from the horizontal scan are discussed in detail. The depicted evolution of BrO/SO_2 ratios is compared with previously published model runs in sec. 9.4.1.

Fig. 9.20 shows BrO and SO_2 SCDs above the respective detection limit (top

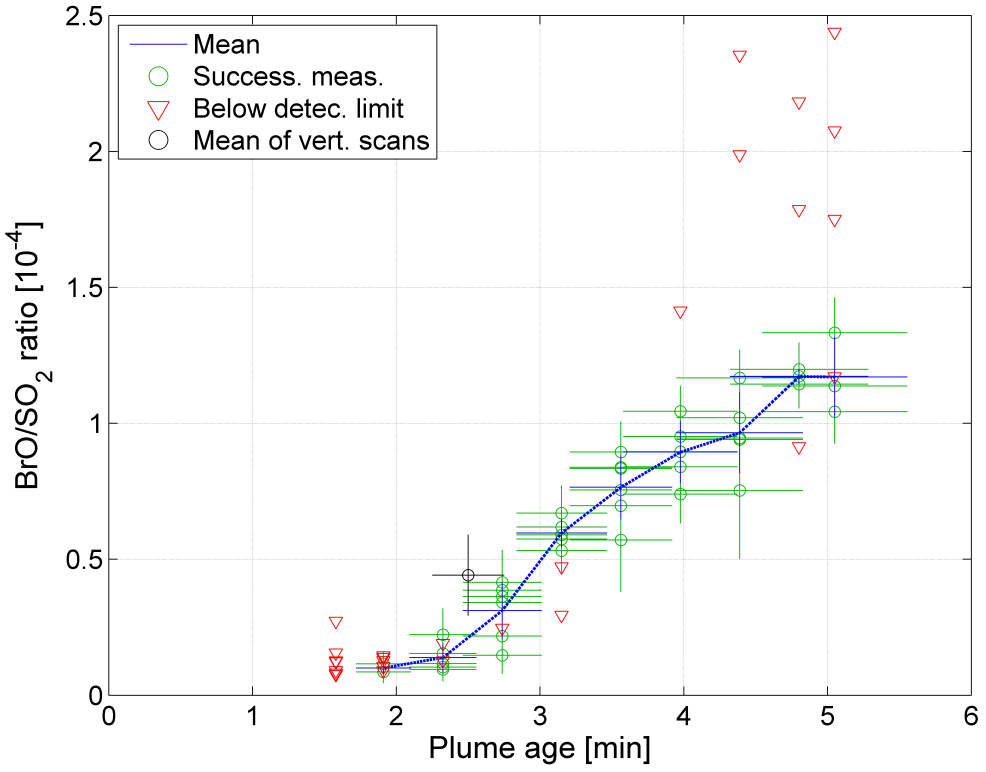

Figure 9.19. BrO and SO_2 SCDs measured with the QE65000 scanning instrument at 132° Azimuth. The plume is indicated by mean values of SO_2 SCDs at respective elevation angles. BrO can only be measured above the detection limit when the volcanic plume is measured.

graph). Note that the plume age is increasing from right to left. A clear increase of BrO SCD is measured with increasing plume age, whereas the SO_2 SCDs are decreasing. The increase in BrO can be assigned to an ongoing, auto-catalytic reaction inside the volcanic plume. For SO_2, a strong decrease in SCDs with increasing plume age (decreasing azimuth angle) is observed. This is remarkable, because only a small decrease in SO_2 SCDs due to light dilution or even an increase due to the prolonged light path inside the plume at smaller elevation angles may be expected (compare fig.8.6).

A constant SO_2 SCD would be expected in a thought experiment in which the following criteria are met: (1) transparent plume without radiative transfer effects like multiple scattering inside, and light dilution outside the plume; (2) the observer is located at the same altitude as the plume; (3) measurements are taken perpendicular to the plume's direction of travel at 0° elevation angle; (4) Vertical plume dispersion and chemical conversion and deposition of SO_2 are neglected.

In our case, light dilution as the main source of the decrease in SO_2 can be dis-

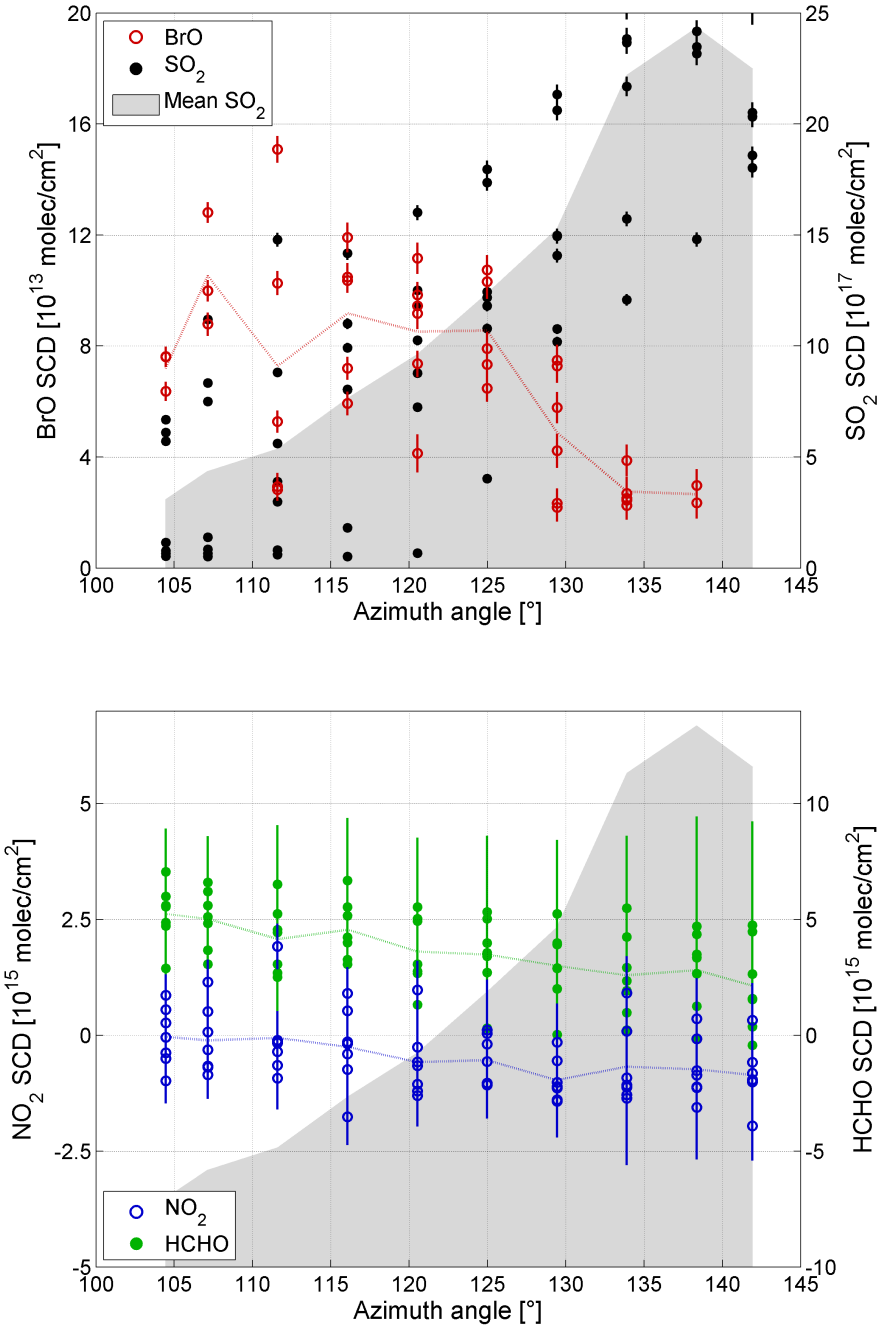

Figure 9.20. The top graph shows BrO and SO_2 SCDs measured with the QE65000 scanning instrument at in the horizontal scanning mode (varying azimuth angle, fixed elevation angle of 17°). Depicted are BrO and SO_2 SCDs above the detection limit. The plume age is decreasing from 5 min at 104° azimuth angle to 1:30 min at 142° azimuth angle. The graph at the bottom depicts NO_2 and HCHO SCDs, included in the BrO retrieval process.

regarded. Distance between instrument varies between $\approx$ 1 km at 142° azimuth angle and $\approx$ 3.5 km at 104° azimuth angle. Although light dilution does occur, the effect for these lateral distances will only lead to a relative change in observed SO_2 SCD of 10%, as approximated from studies by Kern et al. (2010a). Furthermore, the plume showed a greater AEC at early plume ages (visible observation, see fig. 8.7), which may have the opposite effect because less SO_2 is measured at early plume ages (see sec. 10.4, fig. 10.15).
The most probable and simple explanation is a change in the relative fraction of plume observed. Since the plume is moving away from the instrument measuring at a constant elevation angle, smaller fractions of the plume are observed with increasing plume age (decreasing azimuth angle).
Since the O_3 present in the ambient atmosphere is a key species in the production of BrO in volcanic plumes, enhanced BrO/SO_2 are expected at the plumes edges as compared to the centre. Measurements by Bobrowski et al. (2007); Louban et al. (2009) showed that the BrO/SO_2 ratio may be greater by up to 30% at the plume's edge. The observed "BrO-explosion" in fig. 9.19 shows an increase which is on the order of a factor $\times$10. Part of this increase might have been caused by measuring different plume positions. However, care was taken to scan only the upper part of the plume at each azimuth angle. Thus the main increase in BrO/SO_2 can clearly be attributed to the auto-catalytic production of BrO.

NO_2 and HCHO SCDs as measured during the BrO retrieval process are depicted in the bottom graph of fig. 9.20. Since only the azimuth but not the elevation angle was varied in this measurement geometry, the FRS was recorded at the same elevation angle. Thus variations in SCDs for both absorbers are not expected, if they are equally distributed in atmospheric layers of equal altitude. A small increase can be observed for both trace gas SCDs with decreasing azimuth angle. NO_2 SCDs are below the detection limit at all times and in their range close to zero. Negative mean NO_2 SCDs are on the order of $-2{\cdot}10^{15}$ molec/cm^2 in the very early plume (approx. 130° - 144° azimuth), which agrees with the decrease of NO_2 SCDs indicated from results of the vertical scan. However, observed SCDs correspond to optical densities on the order of $0.1{\cdot}10^{-3}$, which strongly indicates that the variations are artefacts of the retrieval process and do not reflect NO_2 depletion in the plume. HCHO is slightly increasing with decreasing plume age as well, but all retrieved SCDs are below the detection limit and correspond to optical densities $< 0.2 \cdot 10^{-3}$. Thus, it is not possible to draw conclusions from retrieved HCHO SCDs either.

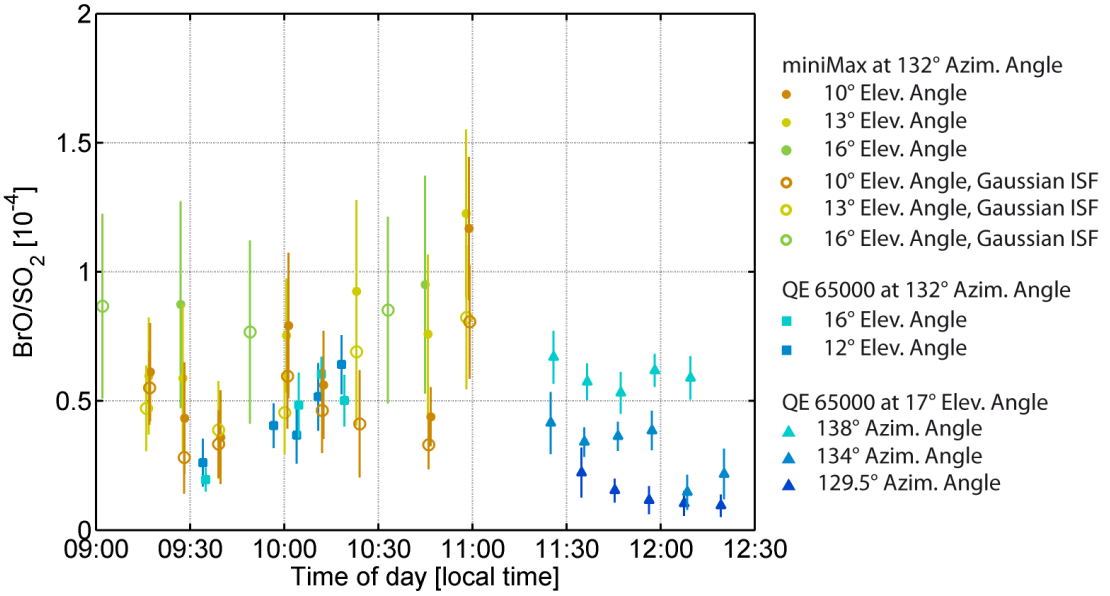

Figure 9.21. Shown are BrO/SO_2 ratios, retrieved with a miniMAX DOAS instrument and a MaxDOAS instrument incorporating a QE65000 spectrograph. Between 9:30h and 10:30h local time, both instrument observed the plume at a fixed azimuth angle and comparable elevation angles. Retrievals of the miniMax DOAS spectra were performed with two different sets of ISF, one with measured Hg lines at 302 nm (SO_2 retrieval) and at 334 nm (BrO retrieval), one with Gaussian ISFs calculated for the respective retrieval wavelength ranges with the software package QDOAS (QDOAS, 2011). Also plume measurements performed with the QE65000 MaxDOAS instrument are depicted, which scanned the plume in a similar direction between 11:30h and 12:30h local time.

9.3.3 Inconsistencies between MaxDOAS instruments

Only the results from the MaxDOAS instrument with the incorporated QE65000 spectrograph were presented as results in the previous sections, since the spectra gathered with the miniMax DOAS instrument and the QE65000 MaxDOAS showed inconsistencies. A direct comparison of spectra gathered by both instruments is difficult, since they are only approximately observing the same plume section, and the emission strength of the volcano is varying over short time scales.

Fig. 9.21 depicts all successful retrievals of BrO/SO_2 ratios from both instruments versus time of day. For the miniMax DOAS, the same spectra are evaluated with two different instrumental slit functions. The spectrograph exhibits a highly wavelength depending instrumental slit function. Measured Hg lines are commonly

used to approximate the instrumental slit functions (see sec. 3.4). However, only the Hg lines at 302 nm and 334 nm are feasible, since they are individual lines which can be resolved and in spectral proximity to the respective SO_2 and BrO evaluation wavelength ranges. BrO/SO_2 ratios are depicted as filled circles, which have been calculated using these Hg lines to convolute RCSs for the respective evaluations. The second evaluation of spectra was performed with an theoretical ISF, with results depicted as open circles in fig. 9.21. It was calculated for the respective wavelength range with the software package QDOAS (QDOAS, 2011). The ISF is approximated by non-linear least square fit, where the difference between measured FRS and a high resolution solar spectrum convoluted with the ISF is minimized. The advantage is, that an ISF can be calculated for the respective wavelength range. However, the true shape of the ISF has to be approximated by an analytical function, which in this case was Gaussian.
BrO/SO_2 ratios retrieved with the QE65000 MaxDOAS instrument are depicted in light and dark blue. Ratios shown from 9:30h - 10:30h are obtained by vertically scanning the plume (filled squares), whereas ratios measured by the horizontal plume scan are recorded between 11:30h and 12:30h local time (filled triangles). For the sake of clarity, only the BrO/SO_2 ratios are drawn from the horizontal scan of the QE65000 MaxDOAS, which have been recorded approximately at comparable viewing directions to the vertical scans.

It is apparent, that ratios calculated from spectra gathered with the miniMax DOAS instrument are by a factor of $\times(1.5 - 2)$ higher than the ones from the QE65000 MaxDOAS, if the used RCSs were convoluted with Hg lines. If the ISF is calculated for the evaluation wavelength ranges of SO_2 and BrO, ratios of the miniMax DOAS instrument are mostly comparable to the ones retrieved with the QE65000 MaxDOAS in the range of errors.

Retrievals from both instruments are affected by errors in their assumed ISF. However, the error induced by the miniMax DOAS ISF can be assumed to be greater due to its stronger wavelength dependency. Since the QE65000 MaxDOAS also offers a better signal to noise ratio, measurements gathered by the QE65000 MaxDOAS instrument are assumed to best reflect reality, and spectra from the miniMax DOAS instrument are ignored in this study of BrO/SO_2 ratios.

9.4 Comparison of Results with model data

9.4.1 BrO/SO_2 ratios at Etna

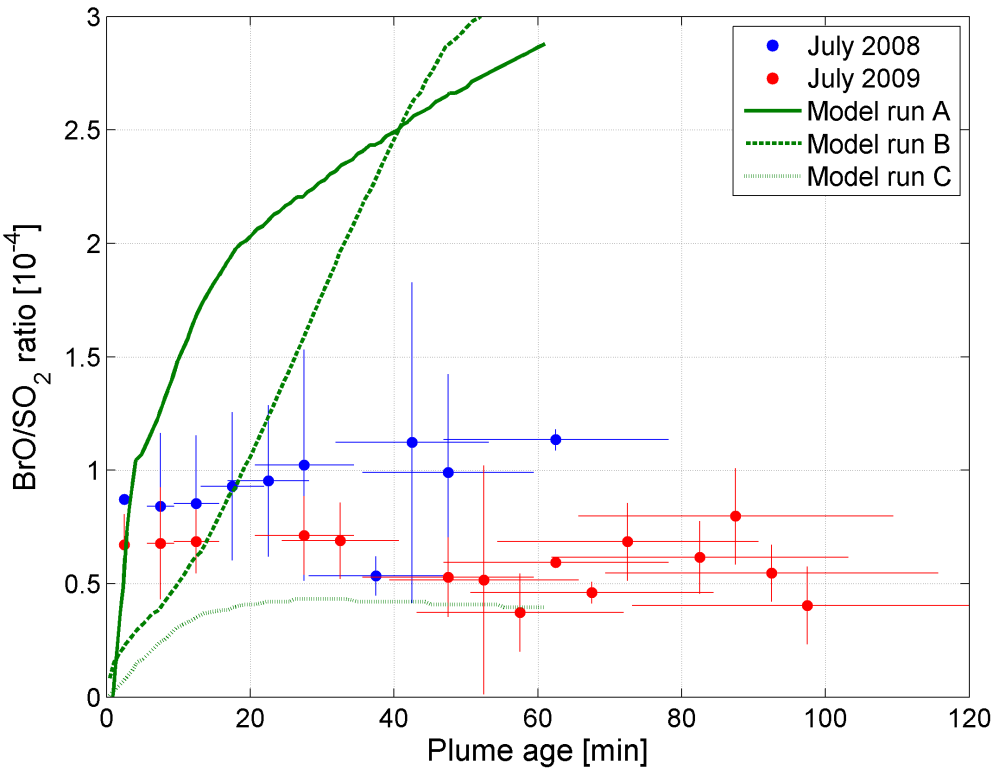

Figure 9.22. Combined BrO/SO_2 ratios from campaigns at Mt. Etna during July 2008 and 2009. Depicted values correspond to the mean and standard deviation of average retrieved values during each day, binned onto a 5 min plume age grid. A general error in wind speed of 25% is assumed. Model runs shown are taken from von Glasow (2010). Model run A corresponds to the case Etna 85:15, model run B to pure volcanic volatiles and model run C to volcanic plume chemistry without aerosol chemisty, as discussed in von Glasow (2010).

The in this thesis presented BrO/SO_2 ratios are the first data sets which simultaneously capture the evolution of volcanic BrO by BrO/SO_2 ratios in the first 60 min (July 2008) and 100 min (July 2009) after emission. In comparison to previous data sets, the measurements were performed during and after a longer eruptive phase of the volcano. Both data sets and model runs extracted from von Glasow (2010) are depicted in fig. 9.22. It is apparent that both data sets show a different evolution of BrO/SO_2, and that the model runs do not agree with either of them. After an initial strong increase of BrO/SO_2 from 0 to $0.85 \cdot 10^{-4}$ for July 2008 and $0.65 \cdot 10^{-4}$ for July 2009 during the first 5 min, the evolution of ratios

starts to differ. Whereas in July 2008 the ratios further increase, ratios measured in 2009 show only a minor increase till a plume age of approximately 30 min, if not a constant ratio, and afterwards a decrease is indicated for older plume ages.

Original composition at time of emission: These differences in evolution are remarkable, because Mt. Etna was in a different eruptive state during both time periods. Without further measurements of volcanic volatiles, it remains speculative whether these observations reflect changes in emitted plume composition. However, actual studies suggest an increase of emitted bromine to sulphur ratio before eruptive phases due to new magma ascending, and a decrease during and after eruptive phases (Bobrowski and Giuffrida, prep).

Capture of plume chemistry by atmospheric chemistry models: Once the volcanic volatiles are emitted, atmospheric chemistry models are used to describe the further evolution of plume chemistry (see chap. 2). The model runs depicted in fig. 9.22 are an example from (von Glasow, 2010), but comparable in predicted ratio evolution to the ones published by Roberts et al. (2009). Model run A corresponds to "Etna 85:15", meaning that initial volcanic volatiles in the model are based on Mt. Etna specific conditions, and volcanic volatiles are mixed with ambient air in the ratio 85:15 prior to release. Model run B represents the case of no entrainment of ambient air ("pure volcanic volatile") at release and model run C does not consider aerosol chemistry.
The disagreement between measured data and model runs is one of the most important findings of the work presented here. Comparisons between model runs and measured data shows, that none of the described model runs describe the evolution of BrO/SO_2 ratio qualitatively. Dependence of the ratio on plume age can be split into two parts:

1. Strong increase of BrO/SO_2 ratio in the first five minutes after plume release: BrO is not emitted but a product of a photochemically reaction cycle. The initial "BrO-explosion" is believed to be strongly influenced by the amount of volcanic aerosols present, NO_x chemistry, and entrainment of ambient air and thus O_3 and NO_x. Observed evolution of BrO/SO_2 is very in good agreement with results of model run A.

2. Slow increase or even decrease in BrO/SO_2 ratio at older plume ages: The evolution of BrO/SO_2 ratios is qualitatively best approximated by model run

C, which neglects aerosol chemistry. However, aerosols were clearly present in the plume for both measurement campaigns, and model run C fails to reproduce the strong increase in ratio in the first minutes.

Thus the measurements suggest very different model scenarios if the two different stages of evolution are considered apart. Neglecting aerosol chemistry does not agree with observed conditions, and since model run C clearly fails to reproduce the early stage of ongoing reactions, it may only be considered as a lower bound of BrO/SO_2 ratios at older plume ages. Model run A does not qualitatively describe the measurements well, since measured data show a very different evolution after the first 5 min, which indicates that model might not be initialized with parameters allowing direct comparison.
One possible explanation is the uncertainty of BrO + NO_x reactions, which may lead to strong increase of BrO production in the young plume (Oppenheimer et al., 2006). Another possible explanation for the observed evolution may be strong turbulence at the crater rim and in close vicinity of to it, with consequent stronger entrainment of ambient O_3 enhancing the production of BrO. This would implicate also a greater increase in the ratio of BrO to total Br (Br_{tot}) emitted. Calculations from model run A yield a BrO/Br_{tot} ratio of 5% at 5 min plume age increasing to about 10 % at 45 min. For a dilution increased by ×10, BrO/BrO_{tot} has already reached ≈ 30 % at 5 min plume age and stabilizes between 40 % and 45 % from 15 min to 45 min plume age (von Glasow, 2010). This would indicate that the so far believed partitioning of bromine in its different species emitted may be wrong by a factor of up to ×6, with strong implications on all reactions involving bromine species in volcanic plumes, e.g. halogen chemistry involving Chlor and Iodine, chemistry of gaseous elemental and reactive gaseous mercury (Hg^0 and Hg(II)).

9.4.2 BrO/SO_2 ratios at Pacaya

The results of measurements at Pacaya presented in sec. 9.3.2 are the first detection of Bromine monoxide (BrO) at Pacaya volcano and the hitherto first capture of volcanic BrO chemistry at high resolution at very early (<5 min) plume ages. An expected increase of BrO/SO_2 ratio from below the detection limit of $2 \cdot 10^{-5}$ during the first 2 minutes to $1.25 \cdot 10^{-4}$ in the following 3 minutes was observed. The evolution is ploted in fig. 9.23, toghether with model runs by von Glasow (2010). Model runs A, B and C correspond to secanrios “Etna85:15”, “pure

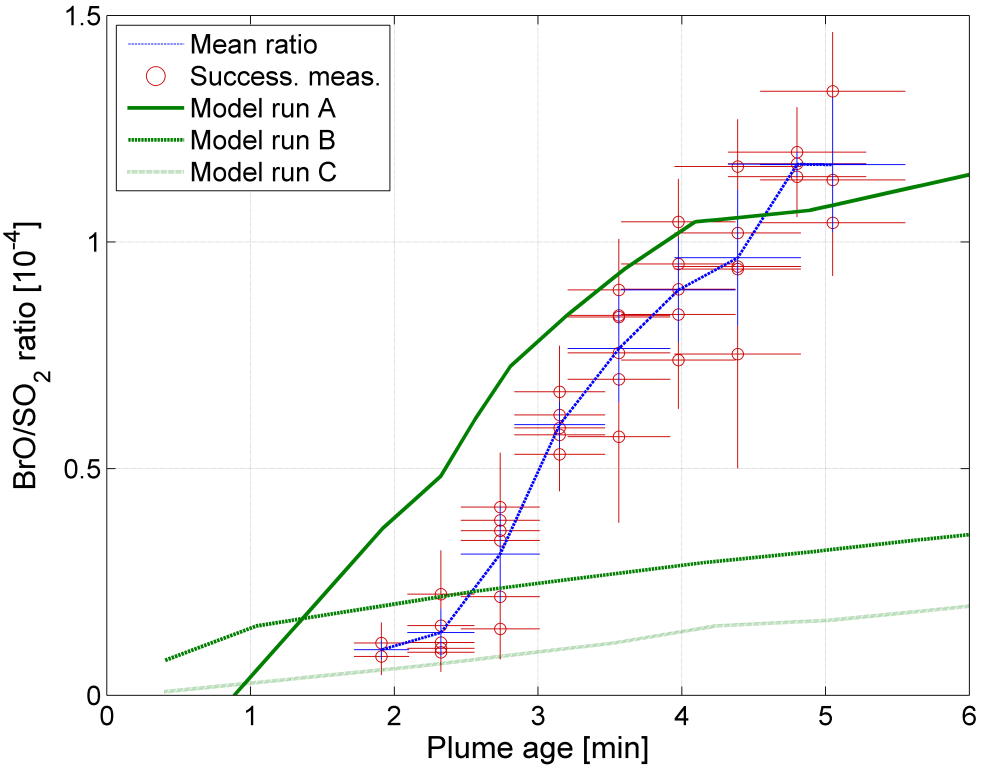

Figure 9.23. Comparison of BrO/SO_2 at early plume ages at Pacaya with model runs by von Glasow (2010). The dashed blue line depicts average BrO/SO_2 ratios at the respective plume age. Model runs A, B and C are drawn in green lines (solid, dashed and light dashed, respectively). For a description of the different model runs see sec. 2.2.

volcanic volatiles" and "without aerosol chemisty" as described in the previous section. The observations at Pacaya are in remarkable good agreement with model run A, even if these calculations were done with initial model settings for Mt Etna, Italy. Model runs B and C are not characterized by the same rapid production of BrO and thus do not capture bromine chemistry at early plume ages for this case. A small offset of about 1 min is observed for the start of the auto-catalytic reaction producing BrO. However, this does not diminish the correlation between measurement and model run, since it can not be assumed that the start of the reaction is matched for model run A and conditions encountered at Pacaya. With the here presented data curve, proof is given that model run A is indeed capturing volcanic Bromine explosions on realistic time scales in the early plume.

9.5 Conclusions

Published model runs on BrO chemistry in volcanic plumes (Bobrowski et al., 2007; von Glasow et al., 2009; Roberts et al., 2009; von Glasow, 2010) have been tuned to fit a relatively sparse data set. In the case of Mt. Etna, published studies so far are Bobrowski et al. (2007); Bobrowski and Platt (2007); Louban et al. (2009), which discuss data sets gathered during August-October 2004, September/October 2003 and August-October 2004, May 2005, respectively. Although these datasets supply valuable insights into volcanic plume chemistry, they do not represent simultaneous observations of volcanic plume chemistry with several instruments at different plume ages. Only in Bobrowski et al. (2007) data of one day is presented, where several instruments measured the volcanic plume simultaneously and at different distances (see also sec. 2). However, only the distance of the instrument to the crater is given, which leads to a mixing of ratios from different plume ages depending on the wind speed and wind direction if the plume is not observed directly over the instrument. Plume ages derived from these data in von Glasow (2010) assume a general wind speed of 7 m/s.

The in this thesis presented BrO/SO_2 ratios measured at Mt. Etna constitute the first simultaneous capture of the evolution of BrO/ratios at plume ages up to 100 min. The presented data set show different evolutions for both measurement campaigns. On the one hand, a small but constant increase is observed for BrO/SO_2 ratios with increasing plume age, measured during July 2008. A maximum of $1.2 \cdot 10^{-4}$ is obtained at a plume age of 60 min, which also the maximum plume age that was measured. On the other hand, measurements during July 2009 showed lesser BrO/SO_2 ratios, which do not significantly increase further and might even be decreasing after an initial increase from 0 to $0.65 \cdot 10^{-4}$ during the first 5 min. Giving the different state of Mt. Etna during campaigns (ongoing eruption and shortly after the cease of activity) this strongly suggests a difference in composition of the volcanic plume during both time frames. Compared to different model runs, the presented ratios proof that current atmospheric chemistry model do not adequately predict bromine chemistry in volcanic plumes. A comparable increase in ratio in the early plume (< 5 min plume age) is only observed in a scenario, which overestimates further development of ratios by a factor of $\times 3$. Model runs yielding a better agreement of BrO/SO_2 ratios compared to measurements from July 2009 at plume ages > 40 min are based are neglect-

ing aerosol chemistry, which does not reflect real measurement conditions observed.

The hitherto first observation of BrO at Pacaya and measurements of BrO/SO_2 ratios of early plume ages ($< 5\,\text{min}$) at high time resolution are presented in this thesis. The rise of BrO/SO_2 ratios from below the detection of $0.2 \cdot 10^{-4}$ in the first two minutes to $1.25 \cdot 10^{-4}$ in the following three minutes is shown. It proofs, model runs well predict the measurements qualitatively at on the time scales observed. The measurements also yield the presence of HCHO in the lower atmospheric layers around Pacaya with only negligible concentrations of NO_2. These findings are valuable additions to the measured BrO/SO_2 ratios, since their role in the chemistry of volcanic plumes is not well understood but may have significant impact.
Inconsistencies of retrieval results of two co-located instruments were encountered, which measured the plume simultaneously and at approximately the same plume ages. These findings highlight the need for further investigation of instrument depending effects, with consequence on previous and future measurement results gathered with lower grade instruments.

10 Early in-flight detection of volcanic plumes

Volcanic gaseous emissions are typically composed of carbon dioxide (CO_2), water vapour, sulphur dioxide (SO_2), and halogen compounds. Depending on the conditions the plumes/clouds can also contain large amounts of ash (i.e. small, solid particles). A series of life threatening encounters of aircraft with ash-loaded volcanic clouds in the 1980s highlighted the risk of volcanic emissions to aviation. The main threat is posed by volcanic ash (Miller and Casadevall, 2000; ICAO, 2007; Prata and Tupper, 2009, and references therein), which may lead to engine failure via flame-outs if allowed to enter high temperature jet engines. Severe incidents were reported from Mt. St. Helens 1980, where a Lockhead C-130 lost two of its four turboprop engines; in the 1982 eruption of Galunggung, Indonesia, two Boing 747 lost power in one case of all four, in the other of three out of four engines at 11 300 m and 9000 m above sea level (a.s.l.), respectively. The crew of both airplanes managed to restart enough engines to make a safe landing at nearby airports, but only after descending several kilometres. A similar encounter occurred in 1989, when a Boing 747 flew into the cloud from nearby Redoubt volcano, Alaska, and lost power of all of its four engines (Casadevall, 1994). Also in this case, the crew managed to restart the engines one or two minutes prior to impact on the ground. Fortunately only economic losses resulted from these encounters and no human lives were lost. The eruption of Mt. Pinatubo 1991 resulted in more than 40 incidents, but none as dramatic as the above-mentioned ones. Nevertheless, damage to aircraft as a result of the Mt. Pinatubo eruption were estimated to exceed US$ 100 million (Miller and Casadevall, 2000).

Even encounters with volcanic clouds of relatively low ash and SO_2 content may have severe consequences to aircraft. Grindle and Burcham (2003) describe an incident in August 2000, where a DC-8-72 research airplane of NASA flew into a volcanic cloud of Hekla volcano, Iceland. The presence of a volcanic plume was only verified afterwards by the scientific in-situ instruments on-board the airplane.

No signs of a volcanic cloud were perceived by the crew. Although no damage was revealed by a first visual inspection of the engines, a later inspection showed that significant damage to the engines had occurred with clogged cooling passages of turbine blades and SO_2 in the engine oil. It was estimated that the remaining lifetime of certain vital parts of the engine was likely reduced to only about 100 h.

The incidents described above resulted from the melting point of volcanic ash (≈1100 K) being below typical operational temperature (1400 K) of jet engines if thrust is above idle. This can lead to clogging and accumulation of molten debris in the hotter part of the engine and its consequent loss of power. Other effects include clogging of cooling mechanisms which greatly reduces the engines' lifetime, and abrasion of engine parts. Next to its effects to the engines, the abrasive properties of volcanic ash can damage the outer hull of aircraft, avionic systems e.g. pitot-static tubes and abrade windscreens to the point of becoming opaque. Besides volcanic ash, certain volcanic gases can also be hazardous to aviation, especially sulphur dioxide SO_2 and sulphuric acid H_2SO_4. Although they do not impair the airworthiness of an aircraft in such drastic ways as volcanic ash, prolonged exposure might reduce the lifetime of aircraft systems and lead to costly repairs and ground time of the aircraft (Bernard and Rose, 1990; ICAO, 2007).

One of the latest volcanic eruptions severely impacting commercial aviation was the April/May 2010 eruption of Eyjafjallajökull in April 2010 with a volcanic cloud being blown over Europe. Most of European airspace was closed for up to several weeks and although no life-threatening encounters occurred, economic losses are estimated to range up to 2.5 € billion for the airline industry alone (Zehner, 2010). This eruption demonstrated the vulnerability of modern societies to volcanic hazards. In the course of the Eyjafjallajökull crisis, the "no-fly-rule", which states that aircraft are not allowed to fly through volcanic clouds of any ash concentration, was replaced by conditional flying zones. The "No Fly Zone" encompasses areas with ash concentration higher than $2 \times 10^{-3}\,\mathrm{g\,m^{-3}}$ and the "Enhanced Procedures Zone", where volcanic ash concentrations are predicted to be between 2×10^{-4} and $2 \times 10^{-3}\,\mathrm{g\,m^{-3}}$. This more flexible approach was meant to keep European air-traffic operational, but also has the risk of reduced life times of aircraft parts. Also, this new approach places new and more demanding necessities for modelling on the volcanic advisory centres (VAACs), because a much more detailed initiation of models, knowledge of source terms, and incorporation of all physical processes are necessary (ADF, 2010).

Commercial carriers rely on the volcanic ash advisory centrers (VAACs) of the

International Airways Volcano Watch (IAVW) for volcanic cloud warnings and predicted locations of these clouds (Romero, 2004; ICAO, 2007). The VAACs use a wide set of observations and measurements, including ground based measurements from observing networks, special air-reports from pilots and observations from satellites (meteorological and non-meteorological). Most active volcanoes are not routinely monitored. Even if they are in remote locations, they can be in close proximity to busy air routes e.g. the Aleutian islands (Kasatochi volcano) and volcanoes in Kamchatka for trans-Pacific air routes. Furthermore, volcanic ash ejected into higher atmospheric layers can be rapidly dispersed over great distances (Prata, 2009), and eruption strength is not directly linked to ejection height (Tupper et al., 2009). Satellite based measurements of ash and SO_2 are thus the most important tool to detect volcanic clouds and eruptions (Prata, 2009; Thomas and Watson, 2010).

Ash detection from satellite platforms can be accurately performed in the infra-red (IR) spectral region. Retrievals are typically based on the "reverse absorption", the different absorption structures of water and ice versus ash in the 10 to 13 μm range, by taking the difference of these absorption structures ("brightness temperature difference (BTD) method", Prata, 1989; Wen and Rose, 1994). In recent years the addition of further channels in the retrievals has improved the detection limit and the ability to identify volcanic ash (e.g. Pavolonis et al., 2006; Pavolonis and Sieglaff, 2010; Clarisse et al., 2010; Thomas and Watson, 2010, and references therein). While pure ash clouds can be distinguished from water/ice clouds, mixed clouds are more difficult to separate. Volcanic dust clouds can also be masked by "ordinary" meteorological clouds, and artefacts associated with dust or very cold cloud tops can cause false detections. These limitations have been discussed extensively and are known to the community (Prata, 1989; Rose et al., 1995; Simpson et al., 2000; Prata et al., 2001). With the introduction of high resolution instruments like Infrared Atmospheric Sounding Interferometer (IASI) and Atmospheric Infrared Sounder (AIRS), false ash detection induced by dust can be reduced significantly (Clarisse et al., 2010).

In the context of volcanic aviation hazards, SO_2 detection is used as a supplementary technique, because volcanic ash clouds are usually associated with SO_2 clouds of approximately equal size and location. SO_2 can be identified by its molecular absorption structures, both in the UV and IR spectral regions, the extent of a SO_2 cloud can serve as an indicator for areas affected by volcanic ash. Typically SO_2-levels in the free troposphere are very low (< 100 ppt above 2 km, Berglen et al.,

2004), therefore there is only a very small background signal. Detection in the IR is mainly based on SO_2 absorptions bands around 7.3 μm (Prata et al., 2003; Prata and Bernardo, 2007), the 8.6 μm (Realmuto et al., 1994), and recently was combined with the 4 μm band (Karagulian et al., 2010). Remote sensing of SO_2 in the ultraviolet (UV) range is more sensitive and this region has been used since 1977 (COSPEC and later TOMS, see for instance Krueger, 1983). Today retrievals of SO_2 are based on Differential Optical Absorption Spectroscopy Technique (DOAS) (e.g. Platt and Stutz, 2008), and satellite-based SO_2 detection has proven very useful in detecting and tracking volcanic plumes in several cases in the past (Khokhar et al., 2005, 2008; Rix et al., 2009; Carn et al., 2009). Although reliable, the major drawback of volcanic SO_2 detection in the UV range is its limitation to daylight and limited coverage/overpass. Also, it can only be a proxy for the greater hazard, volcanic ash, which will fall out and might lead to two different clouds moving in different directions due to wind shear. However, for young clouds (up to three days after emission) SO_2 remains a good tracer for a volcanic cloud with dangerous ash contents (Carn et al., 2009; Guffanti et al., 2010; Schumann et al., 2011; Thomas and Prata, 2011). Even if most of the ash and SO_2 have separated, the SO_2 cloud might still contain fine ash particles (Thomas and Prata, 2011).

Detection of a volcanic eruption that potentially poses a danger to aviation should in the best case lead to a warning to aircraft within minutes. However, if the eruption goes unnoticed because the volcano is in a remote location, the weather conditions are unfavourable for satellite detection, or the satellite overpass misses it, several hours might pass before the thread is recognized and warning can be given. Thus already Prata et al. (1991) proposed an instrument on board aircraft to sense volcanic ash by its IR emission signature. A portable camera applicable for this purpose was presented in Prata and Bernardo (2009). The maximum detection range of such a system is $\approx$100 km (Barton and Prata, 1994).

Although cameras for the detection of SO_2 based on two-wavelength detection in the UV range exist since 2006 (Mori and Burton, 2006; Dalton et al., 2009; Kantzas et al., 2010; Bluth et al., 2007; Kern et al., 2010a), detection limits reported to date are of the order of 10^{17} molec cm^{-2} SO_2 slant column densities (SCDs) (Mori and Burton, 2006; Lübcke, 2010). This is not sufficient to detect expected SO_2 SCDs measured at greater distances to the volcanic cloud, as will be shown in this study. Remote sensing with the DOAS technique is more specific and offers better sensitivity than two-wavelength detection schemes.

In this thesis the feasibility of the DOAS technique will be explored to be a central

component of an early in flight warning system of SO_2 and hence volcanic plumes. Prototype systems were tested, during a flight of a small airplane with forward looking DOAS instruments mounted. The volcanic plume of Popocatépetl was approached several times. Popocatépetl volcano is a suitable candidate for this test, because its summit is at a height of 5426 m (a.s.l.) while the elevation of the surrounding terrain is around 2000 m a.s.l. With the planetary boundary layer extending to an altitude of 2500–3000 m above ground (Doran et al., 1998), the plume disperses usually outside the planetary boundary layer at heights comparable to low flying commercial aircraft. Reported average emissions during April 2010 were of about $20\,\mathrm{kg\,s^{-1}}$ ($1.730\,\mathrm{Gg\,d^{-1}}$) according to the measurements of local monitoring stations from the Network for Observation of Volcanic and Atmospheric Change (NOVAC).

The chapter is structured as follows: the general concept of an early in-flight detection system for SO_2 based on the DOAS technique is presented in Sect. 10.1. Section 10.2 describes the experimental setup used to proof the concept and the performed airborne measurements as well as additional ground based measurements. Also, the retrieval of SO_2 from gathered spectra is given. Radiative transfer studies performed with the conditions at hand are introduced and an analytical description of the expected decrease of SO_2 signal with distance is derived (sec. 10.2.5). Subsequently, the results are discussed in Sect. 10.3. Experimental data is compared with radiative transfer studies to infer the maximum distance for detecting SO_2 in Sect. 10.4. The results of this study are concluded in Sect. 10.5.

10.1 Early in-flight detection of SO_2 as a proxy for volcanic plumes

Airborne DOAS measurements are routinely performed from various research aircraft. Recent examples from CARIBIC (Civil Aircraft for Regular Investigation of the atmosphere Based on an Instrument Container) of observations of volcanic plumes are described in Heue et al. (2011), which measured volcanic clouds originating from Kasatochi (2008), and Eyjafjallajökull (2010). Different trace gases could be identified (BrO, SO_2). These measurements were performed with sideways looking instruments and interest was focused on satellite validation and plume chemistry. Here, we explicitly study the capabilities of a forward looking DOAS instrument as an early warning system for SO_2.

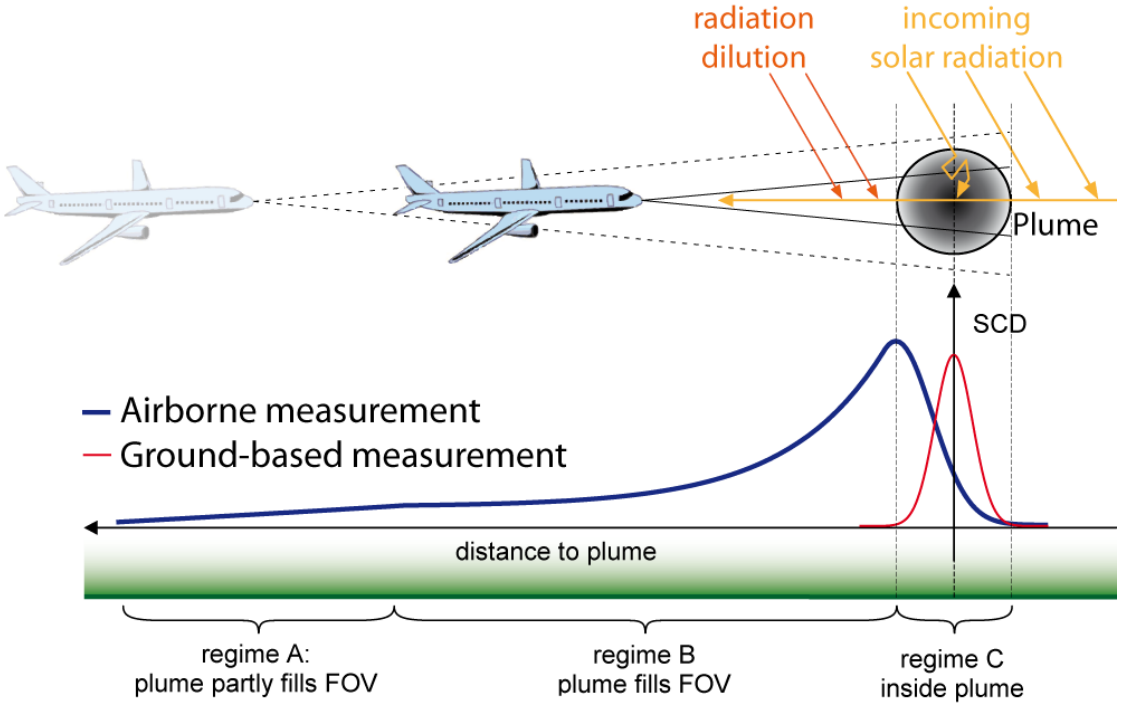

Figure 10.1. Upper part: sketch of observation geometry of a forward looking telescope in an aircraft approaching a volcanic plume. There are three regimes: A – the plume only partly fills the field of view (FOV) of the instrument, B – the plume completely fills the FOV, C – the instrument is inside the plume. Lower part: SO_2 SCD seen by aircraft based (blue line) and ground based instruments (red line). Details see text.

Figure 10.1 illustrates the SO_2 signal to be expected from a forward looking telescope mounted in an airplane. In the upper part, it shows a sketch of the observation geometry for a forward looking telescope in an aircraft approaching a volcanic plume and in the lower part the expected SO_2 slant column densities (SCDs) for an airborne approach traversing through the plume as well for a ground-based, upward looking instrument (e.g. an instrument mounted on a car) traversing beneath the plume. A gaussian distribution of the SO_2 concentration in the plume is assumed. Also indicated are three regimes for airborne approaches:

A – the plume only partly fills the field of view (FOV) of the instrument,

B – the plume completely fills the FOV,

C – the measurements are performed inside the plume.

In regime A there is a strong increase of the SO_2 SCD with decreasing distance to the plume for two reasons, (1) as the instrument approaches the plume continues to fill a larger part of the FOV, (2) less radiation is scattered into the FOV between

the instrument and the plume. The radiation from the FOV not having penetrated the plume does not carry the SO_2 absorption signature, thus, both effects will lead to increase of the SO_2 optical density seen by the instrument at smaller distances to the plume. Once the volcanic plume fills the FOV of the instrument (regime B), increase in SO_2 absorption structure with decreasing distance should follow an exponential increase with a subsequent drop in retrieved SO_2 signal inside the plume.
It is interesting to note that (for an optically thin plume with little multiple scattering inside) the airborne measurements will see the maximum SO_2 SCD when the aircraft (and thus the instrument) reaches the front edge of the plume. Ground-based instruments will see the maximum SO_2 SCD when the instrument is just below the plume centre. As our radiative transfer study (Sect. 10.2.4) and measured data (Sect. 10.2) show in this study, the exact gradient seen by an instrument inside the plume depends on the aerosol load at hand. Also, the maximum SO_2 SCD might be perceived not at the edge but further inwards in the plume for airborne approaches.

In order to take evasive measures and prevent an encounter of the aircraft with a volcanic cloud, the above described approach of an instrument looking along the direct flight vector needs to be extended to resolve the plume spatially. This is easily achieved by additional instruments with viewing directions along a horizontal and vertical offset to the flight vector. In the best case this would result in displaying a two dimensional distribution of SO_2 SCDs in the direction of flight of the aircraft (see Sect. 10.2), allowing to circumvent areas of increased SO_2 concentration and minimizing the chance to encounter volcanic ash by evasive action.

An additional radiative transfer study was conducted to reproduce the measurements, extrapolate found dependencies to greater distances and infer the limit of detectability of the plume.

10.2 Experimental setup

In order to provide experimental proof of the concept for a DOAS-based early warning system, measurements were performed on board a small airplane probing the plume of Popocatépetl volcano, Mexico, on 24 April 2010. As mentioned above, Popocatépetl is especially well suited for studies on the detection of SO_2 from airplanes for the following reasons:

Figure 10.2. A schematic of the different airborne viewing directions. All telescopes were mounted at the airplane close to co-pilots window. The viewing directions (up, down, starboard, port) were looking at angles of 40 mrad with respect to centre and a horizontal plane (up, down) or a vertical plane (starboard, port).

1. Its high altitude of 5426 m a.s.l. and its relatively high SO_2 emission flux.

2. Popocatépetl is one of the volcanoes, which are equipped with ground-based DOAS instrumentation for continuous monitoring of the SO_2 emission flux within the NOVAC network (Galle et al., 2010), thus independent measurements of the SO_2 emission were available, which were – according to the ground-based network – around 1.9 Gg day^{-1} during the time of the measurements. Also, plume height and direction were monitored by two additional ground based stationary scanning instruments and conventional car traverses of the plume were conducted with a zenith sky looking DOAS instrument.

3. These flights provided a largely realistic simulation of an encounter with an arbitrary volcanic plume in the troposphere outside of the planetary boundary layer (PBL) as e.g. encountered during the Eyjafjallajökull eruption over Europe during April and May 2010.

The meteorological conditions were stable with clear visibility at flight altitude for all approaches. An open cloud cover well above the plume was present as well as a slight haze in the boundary layer below.

The airborne measurements were conducted with a Cessna 421, on which three telescopes were installed next to the window of the copilot. One telescope was pointing directly forward at 0 mrad elevation angle, where as the other two were dual beam telescopes similar to the ones described in Johansson et al., 2009. Each dual beam telescope has two viewing directions separated by 80 mrad (4.6°). These telescopes were aligned such that they were pointing 40 mrad (2.3°) towards port and starboard and 40 mrad above and below the central viewing direction, respectively (Fig. 10.2). Each of the tree telescopes was connected to

Spectrograph model	viewing direction [mrad]		SO_2 [10^{16} molec cm^{-2}] detec. limit	σ
QE65000	0	centre	1.6	0.8
S2000	40	up	2.9	1.5
S2000	40	down	2.8	1.4
S2000	40	port	2.6	1.3
S2000	40	starboard	2.9	1.4

Table 10.1. Spectrographs used for airborne measurements, their respective viewing direction in mrad from centre and detection limits ($95\,\% = 2\times\sigma$). σ is the mean error of all measurements with distance greater than 10 km to the plume of approaches III–V for the respective instrument.

a spectrometer (or two in the case of the dual beam telescopes) with which the incident light was spectrally analysed. The fibre from the centre looking telescope was connected to a high grade spectrograph (QE65000, Ocean Optics), light from the sideways looking dual-beam telescopes was analysed with dual spectrograph of type S2000 (Ocean Optics) with (compared to the QE65000 instrument) somewhat lower resolution and higher noise (Table 10.1). The field of view (FOV) for all five viewing directions was 8 mrad (0.46°). In this way, the setup was able not only to detect the volcanic plume but also gather information on its spatial extent. The instrumental setup was very compact with telescopes of size 115 mm × 40 mm (length × diameter) and spectrograph dimensions (length × width × height) of 141.6 mm × 104.9 mm × 40.9 mm (S2000) and 182 mm × 110 mm × 47 mm (QE65000).

10.2.1 Airborne DOAS measurements

In total, six approaches towards and subsequent traverse through the volcanic plume were made between 16:00 h and 17:15 h UTC. They are labelled I till VI in Fig. 10.3. Further information on average altitude a.s.l. and direction of approach [azimuth ° N] are given in Table 10.2. The azimuth and elevation angles were calculated from the GPS data recorded on board the aircraft. Thus both values represent viewing direction based on the difference between two subsequent locations of measurement and can only be approximates for the planes orientations yaw, pitch and actual viewing direction of the telescopes.

The purpose of approaches I and II was to gather information about the plume altitude and to test the instrumental setup before going to greater distances from

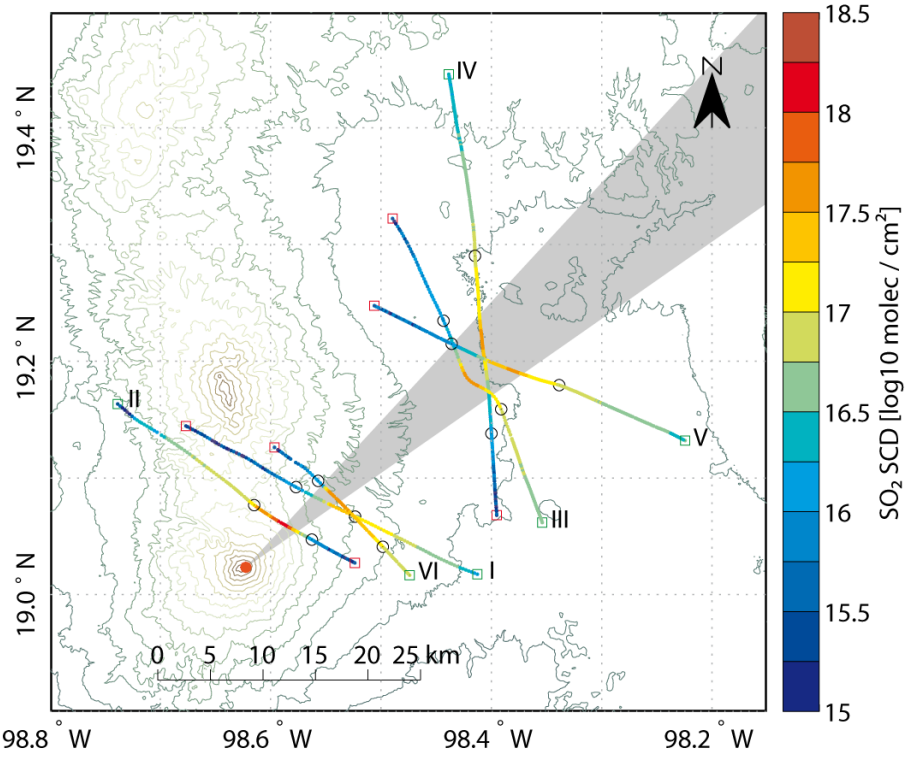

Figure 10.3. Map of all six flown approaches. The start of each approach is marked by a green square, the end by a red square. The roman numbers next to the starting point correspond to the cronological order of the different approaches. Note the logarithmic colour scale of the SO_2 SCDs. Popocatépetl is indicated with an orange dot at the lower left corner and its plume by the grey shaded area.

the plume. Like approach VI, they are not well suited for studying the detectability of SO_2 due to the encounter of strong inhomogeneities in the plume, or since the aircraft flew at the wrong altitude and/or changes in flight course had to be made. The effect of a misaligned approach of the plane can be seen e.g. in approach II, where a change in the plane's approach elevation angle was associated with a sudden increase in the SO_2 column density measured by the central DOAS instrument (Fig. 10.8). While this approach can not be used to study DOAS as an early detection technique of SO_2, it still allows comparison with the car traverse (Sect. 10.3.1). Approaches III, IV and V were conducted starting at larger distance to the plume and will be discussed in detail in the following. Due to air space restrictions the maximum distance to the plume achieved at the start of an approach was only 25 km or less. To draw conclusions about the maximum distance at which SO_2 from the plume might still be detected, the measurements need to be extrapolated using theoretical considerations (Sect. 10.2.5) as well as radiative transfer model studies (Sect. 10.4).

Approach	Time [UTC]	Altitude [m]	Azimuth [° N]
I*	15:58–16:03	5067	297
II^{+}	16:06–16:11	5184	124
III	16:15–16:21	5197	334
IV	16:24–16:31	5186	174
V	16:42–16:49	5207	293
VI*	17:09–17:13	5546	314

Table 10.2. Mean altitude a.s.l. and azimuth direction from north for all plane approaches. Approaches marked by (*) are not used for the study e.g. due to variability in flight direction during approach or insufficient distance to the plume. Approach II ($^{+}$) with stable flight vector inside the plume is only used for comparison between ground based and airborne measurements (Sect. 10.3.1).

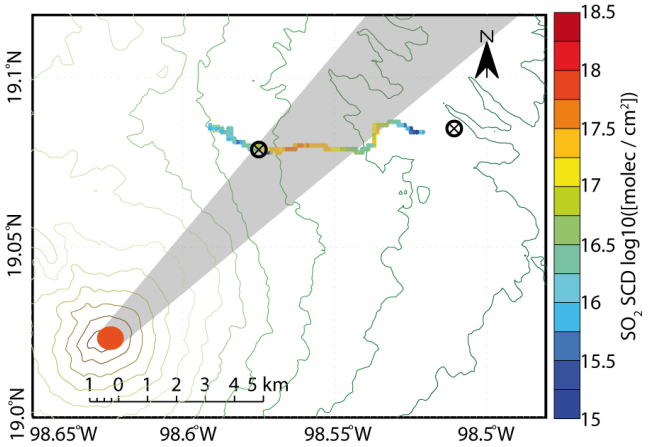

Figure 10.4. Ground based measurements: an example of conducted car traverses is shown with measured SO_2 SCDs on a logarithmic scale. The locations of the stationary scanning instruments are marked by black circles. Popocatépetl as a source is indicated with an orange dot at the lower left corner and its plume by the grey shaded area.

10.2.2 Ground based DOAS measurements

Further measurements were conducted from the ground to provide plume altitude and wind direction. These parameters were communicated to the airplane via radio link. A zenith pointing DOAS instrument was mounted on a car and used to conduct traverse measurements under the plume between 8 and 14 km distance to the crater, yielding location and extent of the plume as well as wind direction (Fig. 10.4). Because of road conditions and construction along the way, traversing the plume generally took about one hour. Also, the plume was not blown perpendicular to the road. Calculation of fluxes and wind direction was performed using the MobileDOAS software package (Zhang and Johansson, 2008). Addition-

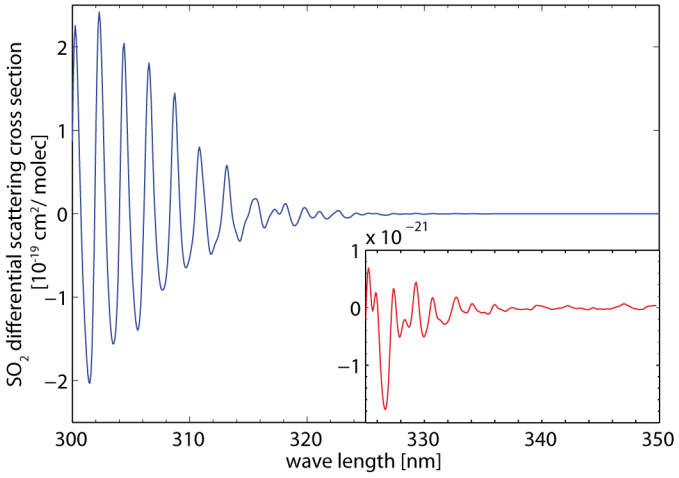

Figure 10.5. A high pass filtered SO_2 cross section at the same optical resolution as the QE65000 spectrograph used with the centre looking telescope. The inserted graph displays the respective part of the SO_2 cross section magnified by a factor of 100.

ally, two stationary DOAS instruments were deployed on both edges of the plume (Fig. 10.4), allowing to approximate wind direction as well as the plume altitude. The instrumental design is analogue to the NOVAC instrument Version I as described in Galle et al. (2010). They scan the volcanic plume along a 60° cone, which is a routinely performed volcanic gas emission measurement technique in the NOVAC network. Calculation of plume height and direction was also performed with the NOVAC software package. The stationary instruments had the advantage of a higher time resolution (≈10 min per scan) than the traverses.

10.2.3 The DOAS retrieval

All gathered spectra were evaluated using the DOASIS software package from the Institute for Environmental Physics, Heidelberg, Germany (Doasis, 2010; Kraus, 2006; Lehmann, 2011). The program applies a combination of a non-linear Levenberg-Marquardt and a standard least-squares fit to determine the optical density of trace gas absorption (Platt and Stutz, 2008). Absorption cross sections of the following species were included in the fit: SO_2 at 273 K (Bogumil et al., 2003) and O_3 at 280 K (Voigt et al., 2001), both chosen for their close vicinity to ambient temperature at the flight height. In addition to SO_2 and O_3, also a Fraunhofer reference spectrum (FRS) and a Ring spectrum (Solomon et al., 1987)

were fitted. The latter was calculated from the FRS with the software DOASIS. Broad band absorptions and Mie scattering were accounted for by using a polynomial of 3rd order and a wavelength-independent offset was included to correct for possible stray light. All spectra collected were evaluated in the wavelength range between 307.4 nm - 317.8 nm. For all instruments and approaches of the airborne measurements, FRSs were constructed from 10 consecutively recorded spectra, measured after the plane had passed the plume but still continued on the same course. Thus the FRS was recorded under as similar as possible illumination conditions as the actual measurements and in close temporal proximity. The FRS was wavelength calibrated by comparison to a high resolution solar spectrum (Kurucz, 2005), which was convoluted with the respective instrumental slit function. The obtained calibrations were transferred to all other spectra of corresponding approach and instrument. The ambient temperature at flight altitude was approximately $-1\,^{\circ}\mathrm{C}$ according to data from the READY NOAA model (READY, 2008) at 500 mbar or 5120 m a.s.l. at the time of the flight on 24 April 2010.

Note that in contrast to previous radiative transfer studies (Mori et al., 2006; Kern et al., 2010b), here the aim is not to retrieve correct SO_2 SCDs but the intention only to study the gradient of the SO_2 signal with distance to the plume. Thus the evaluation of gathered data in this fit range most sensitive to SO_2 is justified. A correction factor of 2 was used to calculate the measurement error from the fit error according to (Platt and Stutz, 2008) based on residual structures and SO_2 absorption band widths. The mean measurement error is determined from all measurements gathered at distances greater than 10 km for approaches III–V of the respective instrument (Table 10.1). In this way, the error reflects uncertainties of measurements at greater distance to the plume.

10.2.4 Radiative transfer modelling

Several model scenarios were set up in the 3-D radiative transfer model McArtim (Deutschmann, 2008; Deutschmann et al., 2011), successor of the model TRACYII (Wagner et al., 2007a), to assess the sensitivity of DOAS measurements of SO_2 to the distance between the instrument and the plume and on the wavelength of the measurement. Figure 10.1 depicts the model setup schematically and effects influencing the measured absorption signal.

Two different types of model runs were conducted with the radiative transfer model. Type A model runs were set up in an attempt to match the conditions observed

during the measurements at Popocatépetl. Afterwards, type B model runs were conducted to examine the differences that might be encountered when flying towards a volcanic cloud of much larger extent, as might be the case after a large-scale volcanic eruption.

For both types of model runs, the ambient atmosphere contained a typical O_3 layer with a maximum concentration of $5 \cdot 10^{12}$ molec cm^{-3} at 22 km altitude and total column of $9 \cdot 10^{18}$ molec cm^{-2} (≈ 330 DU), as this influences the atmospheric radiative transfer in the ultraviolet wavelength region. A 30° solar zenith angle was assumed for the calculations. For all simulations, the instrument was located at the same altitude as the plume centre, and was aimed with a narrow field of view (0.3°) in horizontal direction towards the centre of the plume. Note that both model run types assume a plume which has no concentration gradient from centre to its edges.

Model runs type A: spaciously confined plume with different aerosol contents

In these model runs, the measurement geometry and atmospheric conditions were initialized using the conditions observed during the measurement at Popocatépetl. The volcanic plume was simulated with a centre at 5.5 km altitude, a height of 2 km, a horizontal width of 6.5 km and infinite length. All aerosol particles were characterized as purely scattering with a single scattering albedo (SSA) of 1 and a Heyney-Greenstein asymmetry parameter of 0.8, which is typical for scattering sulphate aerosols.

With these boundary conditions, several model runs were performed with variations of the plume's SO_2 concentration and aerosol extinction coefficient (AEC), given in Table 10.3. For model runs A1 and A2, the SO_2 concentration would result in a measured SCD of $1 \cdot 10^{18}$ molec cm^{-2} if measured from the edge of the plume without occurrence of multiple scattering. For model run A3 the SO_2 concentration was reduced in order to reproduce column densities similar to those observed in the aircraft measurements.

Model runs B: large scale SO_2 clouds

This scenario has been chosen to model the response of the proposed technique to volcanic clouds, as they might occur after large scale volcanic eruptions. Once

Model run	A1	A2	A3
SO_2 [10^{12} molec cm^{-3}]	1.54	1.54	0.77
AEC [km^{-1}]	1	10	40
Visibility [m]	4000	400	100

Table 10.3. SO_2 concentrations, AEC and corresponding visibilities of the plume for different type A model runs. For further details see text.

the volcanic plume has travelled a large distance from the volcano, its horizontal dimensions are typically such that they considerably exceed the mean free photon path length in the atmosphere (several 10 km). In such cases, light entering a UV-spectroscopic instrument will not have passed through the entire volcanic cloud. To test the sensitivity of such instruments to large scale volcanic SO_2 clouds, model runs B were set up using a SO_2 cloud with infinite extent in one horizontal direction at 10 km altitude. A SO_2 concentration of $1 \cdot 10^{12}$ molec cm^{-3} was assumed for the simulation. Aerosol particles are simulated in model run B1 as in model runs A as purely scattering with a SSA of 1, a Heyney-Greenstein asymmetry parameter of 0.8, assuming scattering of sulphate aerosols. The cloud exhibited an AEC of 0.1 km^{-1}. Additionally model run B2 is performed which simulates different ash contents of the cloud. The ash is assumed to have a SSA of 0.8, which can be regarded as a conservative estimation of SSA of ash (Prata and Grant, 2001; Pavolonis et al., 2006; Kudo et al., 2008). The varying ash contents are studied by assuming different AEC of 0.1 km^{-1}, 0.5 km^{-1}, 1 km^{-1} and 4 km^{-1}. The SO_2 concentration is the same as in B1.

The results of this model runs will be discussed in Sect. 10.4 to give an outlook on the base of the conducted measurements.

10.2.5 Analytical approach to the radiation dilution effect

In general, the propagation of radiation in the atmosphere is a complex process. Multiple scattering inside and light dilution outside the plume both affect the measured signal. For a valid assessment of volcanic emissions both effects need to be taken into account. For this study, the gradient of measured SO_2 SCDs with distance between instrument and plume needs to be determined to assess the feasibility of DOAS as an early detection system for SO_2. The true concentrations inside the plume are only of secondary concern, and we focus on radiation dilution.

An analytical solution can be derived to estimate the dependency of measured SCD

to distance to the volcanic plume. The approach is analogous to the simplified determination of visibility and contrast that can be found in text books about radiation transport in the atmosphere (e.g. Platt and Stutz, 2008, p. 110). A similar strategy has been applied for radiative transfer corrections of UV-camera measurements in Bluth et al. (2007).

There, a black object of zero intensity is viewed from distance L with a background intensity I_0 next to the object. Radiation scattered into the field of view of the observer will lead to an increase of the perceived intensity I_R with increasing distance to the object until background intensity I_0 is reached. Certain approximations are made. (1) The probability is negligible that a photon is scattered into the viewing direction of the telescope after having been scattered out of it (Narrow Beam approximation). Consequently, extinction, which is comprised as the sum of Rayleigh and Mie scattering, can be treated like absorption as described by Lambert-Beer's Law. In our case it is the radiation scattered into the viewing direction. (2) The atmosphere is considered homogeneous. With these approximations, the scattered radiation intensity I_R received by the observer when looking at a black object at distance L is given by

$$I_R(\lambda) = I_0(\lambda) \times \left(1 - e^{-\epsilon(\lambda) \times L}\right) \quad (1)$$

where the extinction coefficient $\epsilon(\lambda) = \epsilon_R(\lambda) + \epsilon_M(\lambda)$ is the sum of the Rayleigh and Mie extinction coefficients.

The wavelength dependency of Rayleigh and Mie scattering can be disregarded for a 1st order approximation of the dependency of DOAS retrieval on radiation dilution. Rayleigh scattering is approximately proportional to λ^{-4}, whereas Mie scattering has a wavelength dependency proportional to $\lambda^{-1.3}$. This results in a relative difference of scattered intensity of $\approx 18\,\%$ between 10 nm (wavelength range of DOAS retrievals) in the range of 300 nm and 330 nm. The evaluation of SO_2 is strongly dependent on the stronger differential optical absorption features at smaller wavelengths (see Fig. 10.5). The difference between minima of the differential optical absorption cross sections of SO_2 is (≈ 2 nm). On this scale, the relative difference due to Rayleigh and Mie scattering is only $\approx 3\,\%$. Thus the error introduced by neglecting the wavelength dependency of Rayleigh and Mie scattering will be at the lower end of the interval 3 %–18 %.

Measured SO_2 SCDs (S) are proportional to the amplitude of its differential optical

absorption structures:

$$S \propto \ln\left(\frac{I_0}{I}\right) \tag{2}$$

Taking the intensity of absorption minima as background intensity I_0 and absorption maxima as intensity I, a retrieved SO_2 SCD $S(L')$ will decrease with distance to the source. I_1 and I_2 are denoting the intensity at absorption maxima at L_1 and L_2 distance. Applying Eq. (1), the intensity I_2 can be described in terms of I_1:

$$\begin{aligned} I_2 &= I_0 \times (1 - e^{-\epsilon \cdot L_2}) \\ &= I_1 + (I_0 - I_1)\ (1 - e^{-\epsilon \times \Delta L}) \end{aligned} \tag{3}$$

where ΔL is the difference between L_1 and L_2. Thus $S(L_2)$ can be written as

$$\begin{aligned} \ln\left(\frac{I_0}{I_2}\right) &= \ln\left(\frac{I_0}{I_1 + (I_0 - I_1)\ (1 - e^{-\epsilon \times \Delta L})}\right) \\ &= \ln\left(\frac{I_0}{I_0 + (I_1 - I_0) \times e^{-\epsilon \times \Delta L}}\right) \\ &= -\ln\left(\frac{I_0 + (I_1 - I_0) \times e^{-\epsilon \times \Delta L}}{I_0}\right) \\ &= -\ln\left(1 + \frac{I_1 - I_0}{I_0} \times e^{-\epsilon \times \Delta L}\right) \end{aligned} \tag{4}$$

The logarithm $ln(\xi)$ can be expressed as a Taylor series if $-1 < \xi < 1$ with

$$\ln(\xi + 1) = \sum_{k=1}^{\infty} (-1)^{k-1} \times \frac{\xi^k}{k} \tag{5}$$

If ξ is close to 0, the logarithm can be approximated by using only the first term ($\ln\ (\xi + 1) = \xi$). This means that Eq. (4) can estimated by

$$S(L_1) \propto -\frac{I_1 - I_0}{I_0} \tag{6}$$

$$S(L_2) \propto -\frac{I_1 - I_0}{I_0} \times e^{-\epsilon \times \Delta L} \tag{7}$$

as long as $I_0 \approx I_1$, which is the case for weak absorber with optical densities on the order of a few percent. The relative change of SCD $S(L_1)$ to $S(L_2)$ with distance

ΔL is given by

$$\begin{aligned} \frac{S(L_2)}{S(L_1)} &= \frac{\ln\left(\frac{I_0}{I_2}\right)}{\ln\left(\frac{I_0}{I_1}\right)} \\ &\approx \frac{\frac{I_1-I_0}{I_0} \times e^{-\epsilon\times\Delta L}}{\frac{I_1-I_0}{I_0}} \\ &\approx e^{-\epsilon\times\Delta L} \end{aligned} \tag{8}$$

Thus Eq. (8) can be used to estimate the dependence of DOAS measurements of a confined trace gas on distance between instrument and absorber. ϵ is an extinction coefficient, which depends on retrieval wavelength range and the absorption structure of the trace gas of interest in the respective retrieval wavelength range. E.g. depending on how the dominant absorption bands of the trace gas of interest are distributed within the retrieval wavelength range. Also, it must be stressed that above approximation is only valid for weak absorbers, because all but the the first term of Eq. (A5) are omitted.

10.3 Results

10.3.1 Measurement results from airborne observations

All approaches successfully detected SO_2 from the first measurement of the approaches onwards, but restrictions in airspace prevented measurements at distances further than 25 km from the plume. Figure 10.6 depicts the SO_2 column densities as a function of distance from the plume centre for approaches III through V for the different viewing directions. The mean error σ for a measurement is specified in Table 10.1 (see Sect. 10.2.3). The result of the retrieval for the spectrum gathered at greatest distance to the plume (first spectrum of approach IV) is shown in Fig. 10.7.

Measurement regimes and extent of plume

First, the SO_2 column time series are discussed. At 25 km distance to the plume, the FOV of each telescope corresponds to a circle of 200 m diameter at the plume, their centre being 2 km apart for the horizontal and vertical off-centred viewing

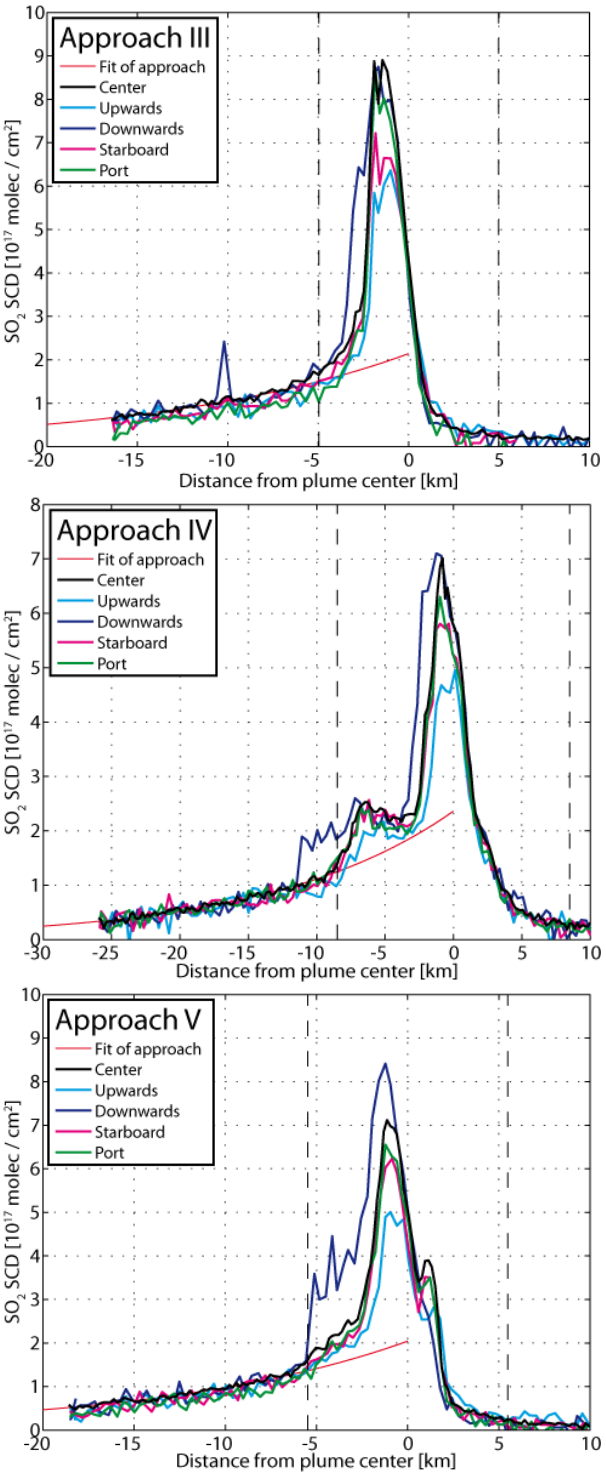

Figure 10.6. Results from approaches III–V. The solid red lines indicate the fit of Eq. (10) to the measurement results in the far field. Dashed vertical lines indicate regime C. Errors of measurements are given in Table 10.1. SO_2 was detected from the first measurements onwards.

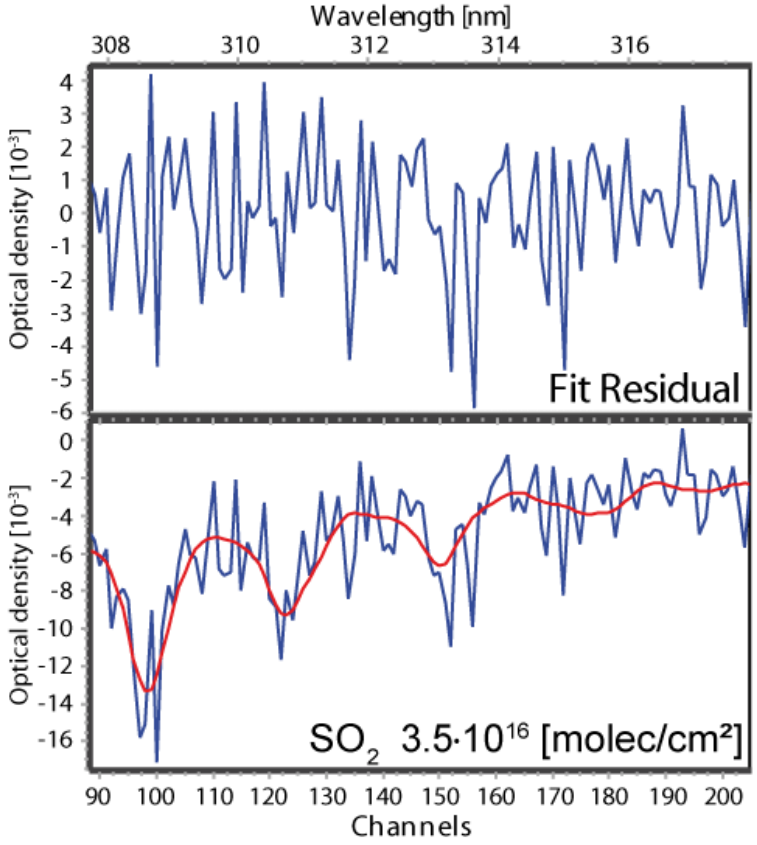

Figure 10.7. Fit result for the spectrum gathered at greatest distance (first spectrum of approach IV), taken at 25 km distance. Shown is the residual above and the fitted SO_2 SCD of $3.5 \cdot 10^{16}$ molec cm^{-2} below.

directions, respectively. Thus it can be assumed that the centre, port and starboard looking telescopes started measuring in regime B (plume fills FOV), and the upwards and downwards looking telescopes started at regime B or in the transition from measurement regime A (plume partly fills FOV) to B. Due to the lower signal to noise ratio of the S2000 spectrograph (up, down, port, starboard telescope), a clear transition point can not be distinguished. In order to discuss the transition between regime B and C, the airborne approaches are best compared to ground based car traverses.

Approach II was performed approximately between 16:06 h–16:10 h UTC and compared with car traverse 2, which was measured from 15:34 h–16:05 h UTC. It can not be used in the study on SO_2 detectability due to changes in flight altitude in the first minute. However, the plane did not change direction during the rest of approach II and while travelling through the plume. Due to its close proximity to the car traverses in space and time, it can be used to compare both measurements. For that purpose, the ground based measurements were interpolated onto

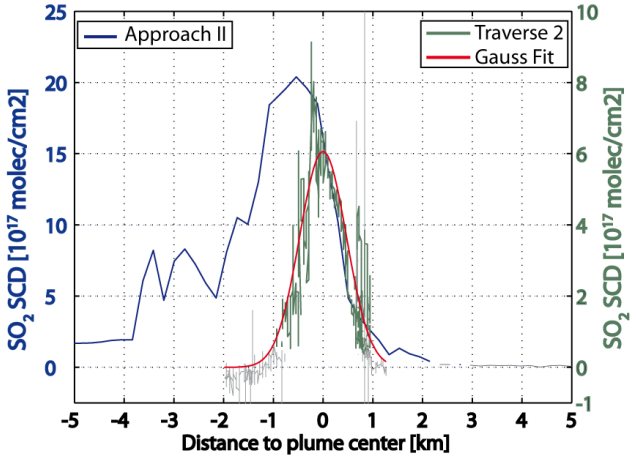

Figure 10.8. Comparison of results from car traverses and airborne measurements, with scale of measured SO_2 SCDs on the right and left ordinate, respectively. Values below 3x measurement error are drawn in grey. Strong variations in the car traverse (e.g. at 1 km from plume centre) are artefacts due to vegetation blocking the view. The gradients shown agree with expected characteristics of transition between regime B to regime C (see Fig. 10.1), although the starting point of the plume of the car traverse does not correlate with the maximum of the values retrieved from the airborne measurement.

the path of the airplane approach assuming a linear expansion from the source to each measurement point. The result is depicted in Fig. 10.8. The plume can be well approximated by a gaussian fitted to the car traverses, which sets the plume center at 0 km at the maximum of the gaussian.

Comparing airborne approach II and car traverse 2, the expected characteristics as argued in Sect. 10.1, Fig. 10.1, are clearly visible. The SO_2 SCD of the airborne measurements is increasing approximately until entering the plume, which horizontal distribution is captured by the car traverses. It is also apparent, that the maximum SO_2 SCD of the airplane approach does occur almost, but not exactly at the edge of the plume but not exactly at the edge of the plume. It is rather measured several hundred meters inside the plume. It is rather measured several hundred meters inside the plume. The model results discussed in Sect. 10.3.3 show that the retrieved SO_2 SCDs might change significantly with the transition from outside to inside the plume, with a shift of the maximum SO_2 SCD to the centre of the plume with increasing AEC. Thus the comparison between car traverse and airborne approach indicates that multiple scattering inside the plume causes the maximum column density to be measured within the plume, not at its front edge.

Airborne approaches III–V crossed the plume further downwind. Thus plume position and size can not be simply extrapolated from the ground based measurements to the location of the airborne measurements. Also, the exact plume position can only be approximated from airborne measurements applying only forward looking DOAS telescopes.

The exponential relationship (Eq. 10) between retrieved SCD and distance to source as derived in Appendix 10.2.5, is only valid in regime B. Also, approximations made might not hold for higher SO_2 SCDs and in close proximity of the plume, in which light scattered into the viewing direction of the telescope might still be affected by absorption structures from the plume's gases. Thus regime C is approximated by fitting function 10 to the signal of the centre looking telescope for the far field of approaches III, IV and V. The start of regime C was set to the start of a steadily increasing difference ($> 2.5 \cdot 10^{16}\,\mathrm{molec\,cm^{-2}}$) between fitted curve and retrieved values. The end of the plume is reached when the SO_2 values are below the detection limit of the instrument. The so determined regime C is marked by the dashed vertical lines in Fig. 10.6.

Spatial separability of the different viewing directions

The airplane was flying at the same altitude as the volcanic plume and approached it from the side. Although SO_2 was detected by all instruments from the first measurement onwards, significant differences between the retrieved SCDs of the telescopes can not be distinguished for measurements at greater distance to the plume. The signal-to-noise ratio of the Ocean Optics S2000 spectrometers used for the measurements with non-centre-looking telescopes was inferior to that of the QE65000 (centre-looking telescope). Thus the precision of the measurements done with the S2000 was not sufficient to detect differences in SO_2 column at large distances from the plume.

Theoretically, SO_2 SCDs measured in starboard, centre and port direction during the approach should not differ greatly for a homogeneous plume along its path of propagation. For the vertical viewing directions (down, centre, up), differences in signal should depend on the distance to the plume and its vertical extent. At some point close to the edge or inside the plume, the gradients of all instruments should coincide until the plume is passed (and afterwards showing no SO_2 signal), because the different telescopes are observing increasingly similar parts of the plume.

While the plane approaches, the upward and downward looking instruments start observing the plume and their gradients should increase and start converging to the gradient of the centre looking instrument, because the different telescopes are observing increasingly similar parts of the plume. Again, at some point at the edge or inside the plume, the gradients of all instruments should coincide until the plume is passed (and afterwards showing no SO_2 signal).

Comparing the horizontally sideways pointing telescopes, similar SO_2 gradients are observed at most times except for approach III, where a change in flight direction while inside the plume lead to a strong increase in the port signal (see also Fig. 10.3).

For the different vertical viewing directions, differences in the results obtained become more pronounced when the measurements are performed in and close to regime C. The telescope looking downwards always detects a significantly higher SO_2 SCD than the upwards looking telescope. Furthermore, it shows a comparable (Approach III and IV) or greater (Approach V) SO_2 SCD than the centre looking telescope. Possible issues are discussed:

1. The plume was traversed above its centre altitude although results from the ground based measurements indicate that the plume's height was slightly above the plane's approach altitude (see Sect. 10.3.2). Changes in plume height due to e.g. Lee-waves cannot be ruled out, but as described above, the differences in optical path lengths inside the plume should become negligible closer to the plume.

2. A severe misalignment of telescopes; this can be ruled out, because even at greatest distances all telescopes observed the plume.

3. Strong small scale inhomogeneities of SO_2 concentrations inside the volcanic plume should be negligible due turbulences between source and measured plume section.

4. Light detected by the downward looking telescope is subject to an increased path length inside the plume; this effect is certainly present but should only be of second order, because the telescopes are observing very similar plume cross sections as discussed above.

5. Errors in calibration and instrumental function for the different spectrograph should lead to additional structures in the residuum of the DOAS fit algorithm. This was not observed. A final conclusion is not possible because

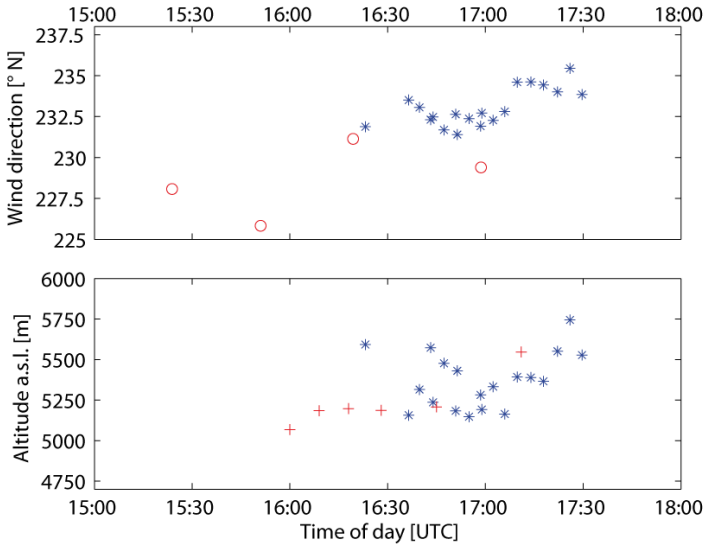

Figure 10.9. Wind direction and altitude of plume centre derived from the ground based measurements, showing the stable meteorological conditions on 24 April 2010. Values derived by the two stationary scanning instruments according to (Galle et al., 2010) are depicted as blue asterisks, red circles show results from the car traverses (upper graph). Also the mean altitude of the airplane is indicated for all approaches by red pluses (bottom graph). Note that the different types of measurements were conducted at different distances to the plume, which could explain the slightly differing values.

additional calibration quartz glass cells filled with SO_2 were not available to perform calibration and comparison of the different viewing directions.

Although early detection capabilities of DOAS for SO_2 could be proven, future studies are necessary with higher grade spectrometers for all viewing directions combined with additional calibration and instrument intercomparison. This includes additional modelling to assess radiative transfer effects for the different viewing directions.

10.3.2 The ground based measurements

The wind direction derived from automobile based measurements (the direction between the volcano's summit and the maximum encountered column densities) are depicted in Fig. 10.9. Both car traverses and the stationary ground-based instruments yield comparable wind directions with an average of 232° N. The small systematic differences between the results of the two methods might be explained by the different cross sections of the plume seen by each measurement technique.

Also, the algorithm for the stationary instruments assumes that both instruments are measuring the same cross section of the plume. Regardless of these small systematic errors, the results clearly show the stability of meteorological conditions during the time of the airborne approaches. The altitude of the centre of the plume was calculated to be between 5250 and 5750 m a.s.l., the spread of plume heights can be explained by varying emission strengths and wind speeds. Stronger winds tend to press the plume slightly downwards in the proximity of the volcano. Given the summit height of 5426 m a.s.l., the retrieved plume heights correspond well to the visual observations of a plume at approximately the same or slightly lower altitude as Popocatépetl's summit.

Comparing the altitude of plume centre derived by the two stationary instruments with the altitude of airplane approaches, the plume's centre is generally measured about 200 m higher than the mean altitude of airplane approaches (5250 m a.s.l.). These measurements confirm that the airplane approaches were performed at the approximate plume height and during stable meteorological conditions.

10.3.3 Results from radiative transfer study

Here, model runs A will be discussed because they allow conclusions over the measurements. The reader is referred to Sect. 10.4 for the results of model run type B as an outlook on bases of the conducted experiment. As exemplary result of the model runs A, model run A2 is shown in Fig. 10.10. Its AEC was chosen, so that the gradients of measurements and model run A2 match qualitatively (see also Fig. 10.6). With an assumed FOV of 5.2 mrad (0.3°), at the maximum distance modelled (100 km) a circle of diameter of ≈520 m is observed at the plume. Thus all modelled approaches correspond to measurements in regime B and C.

In Fig. 10.10, the dependency of the measured SO_2 SCD on distance can be seen. The gradient of the retrieved SO_2 SCD follows the expected line with a clear separation of wavelengths. Longer wavelengths are less affected by Rayleigh scattering than smaller ones and thus less dependent on distance to the cloud. This leads to a difference in relative decrease of about a factor 10 at 100 km distance to the plume. Studying the transition between simulated measurements in regime B and regime C (the plume is indicated as a grey shaded area), some interesting features are immediately visible: intuitively, one would suspect the maximum SO_2 signal just when the plane enters the plume, because light can no longer be scattered into the instrument's field of view without having passed the plume. This is reproduced by

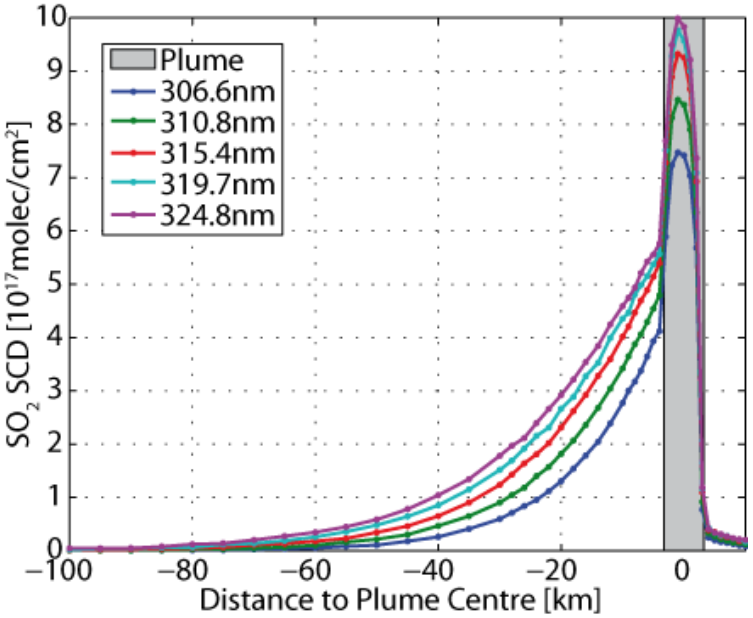

Figure 10.10. The figure shows the results of model run A2. The AEC was set to $10\,\mathrm{km}^{-1}$ corresponding to a visibility of 400 m inside the plume, which is marked as shaded area. The graph depicts simulated SO_2 column density as a function of the distance of the instrument from the plume.

the model run A1 when low AEC is assumed. With increasing AEC in model runs A2 and A3 however, a shift to the centre of the plume becomes apparent of maximum SCDs. Also, a sharp edge can be seen in the SCD distribution at the position where the aircraft enters the plume (+3.25 km). This could be the explanation for the distribution observed in the measurement and the differences shown between car traverse and plane approach II (Fig. 10.8). Measurements taken at the front edge of the plume are not detecting radiation that has penetrated the entire plume, but rather measure light scattered by aerosols in the front portion of the plume. On the other hand, measurements taken inside the plume can be affected by significant enhancement of the light path inside the plume due to multiple scattering. Although the modelled cases are greatly simplified, e.g. a real plume is not evenly distributed over a discrete interval, they show that the maximum SO_2 column is not necessarily detected at the front edge of the plume. Thus, care must be taken when judging which spectra have been taken in and outside of the plume (regime B and C, respectively).

10.4 Comparing measurements to model results: Inferring maximum distance at which SO_2 can be detected

To compare model results and measurements, an exponential function was fit to the different approaches. It is based upon a simplified determination of visibility and contrast that can be found in textbooks about radiation transport in the atmosphere (e.g. Platt and Stutz, 2008, p. 110) and an analogue has been applied for radiative transfer corrections of UV-camera measurements in Bluth et al. (2007).

$$\frac{S(L_2)}{S(L_1)} \approx e^{-\epsilon\times\ (L_2-L_1)} \tag{9}$$

The above function describes the relative change of retrieved SCD $S(L_1)$ and $S(L_2)$ between distance L_1 and L_2 to the plume. For a detailed derivation see Appendix 10.2.5. ϵ is the total extinction coefficient depending on Rayleigh and Mie scattering, retrieval wavelength range and the distribution of absorption structure of the trace gas of interest in the respective retrieval wavelength range. Because the retrieved SCDs all possess a certain error, it is advantageous to use

$$S(L) = \mathrm{A} \times e^{-\epsilon\times L} \tag{10}$$

where A is a hypothetical SCD at zero distance or in our case the plume's centre. Function (10) is only valid for measurements taken in the regime B (see Fig. 10.1). Also, the "narrow beam" approximation must hold, thus light scattered into the viewing directions should not have passed the plume at an earlier point. In order to ensure these boundary conditions, only measurements taken more than 8 km from the assumed plume centre were used to retrieve the parameters of function (10) for the respective approaches.

The results for all fits are depicted in Fig. 10.11. They are extrapolated to 50 km distance to the plume. The individual obtained parameters are also shown in Table 10.4. The mean extinction coefficient ϵ returned by the fit was $7.33{\cdot}10^{-5}\mathrm{m}^{-1}$, and the mean coefficient of determination r^2 was 0.94. Thus with the experimental setup, which was not specially tuned for this kind of measurements, and a detection limit of $1.6{\cdot}10^{16}$ molec cm^{-2} for the centre looking telescope (Table 10.1), the plume of Popocatépetl could have been detected from a distance greater than 35 km.

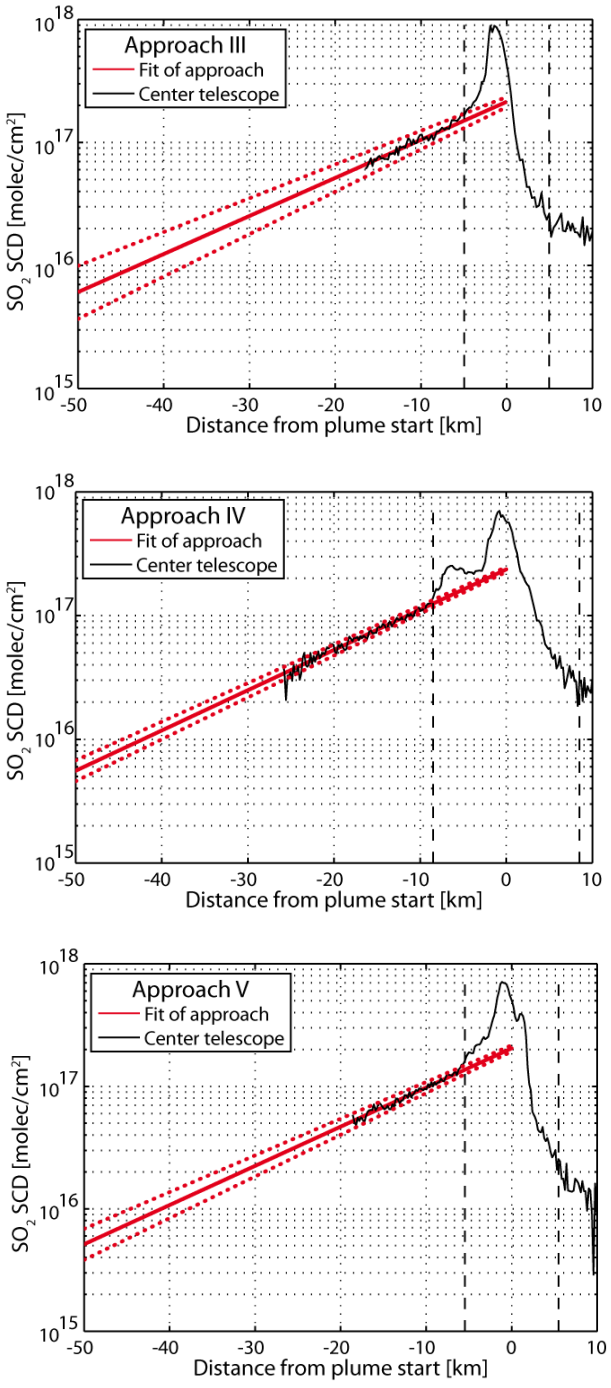

Figure 10.11. Approaches III–V extrapolated to 50 km distance. Fitted function is depicted as red line with 95 % confidence bands as red dots. Measurement regime C is indicated by dashed vertical lines.

Approach		III	IV	V	Mean
ϵ	$[10^{-5}\,\mathrm{m}^{-1}]$	7.13	7.50	7.37	7.33
conf ϵ	$[10^{-6}\,\mathrm{m}^{-1}]$	0.81	0.30	0.47	0.53
A	$[10^{17}\,\mathrm{molec\,cm}^{-2}]$	2.14	2.34	2.04	2.18
conf A	$[10^{17}\,\mathrm{molec\,cm}^{-2}]$	0.20	0.10	0.12	0.14
r^2		0.89	0.97	0.95	0.94

Table 10.4. Results from the fits of function (10) to approaches III–V.

Modell run		A1	A2	A3	Mean
	ϵ	9.08	7.63	7.14	7.95
306.6 nm	conf ϵ	0.166	0.089	0.136	0.130
	r^2	0.9994	0.9998	0.9994	0.9995
	ϵ	7.80	6.65	6.24	6.89
310.8nm	conf ϵ	0.083	0.105	0.144	0.111
	r^2	0.9998	0.9996	0.9991	0.9995

Table 10.5. Results from the fits to the radiative transfer models. ϵ and the $\pm\Delta$ to calculate confidence bands of 95 % (conf ϵ) are given in $[10^{-5}\,\mathrm{m}^{-1}]$.

In order to compare the measurements to the modelled results, function 10 was fitted also to all model runs type A. The fit was performed between 10 and 100 km. The model runs are reproduced well by the analytical approach. All fits achieve a coefficient of determination (r^2) of more than 99.8 %. Table 10.5 summarizes the fitted extinction coefficients ϵ for 306.6 nm and 310.8 nm of model runs A1, A2 and A3. For model run A1 the fitted extinction coefficient is slightly increased in comparison to the other two. The reason is that model run A1 displays stronger absorptions at 10 km distance then the other two model runs. The approximation made in deriving function 10 are only valid for small absorptions and thus for model run A1 an additional systematic error is induced.

The extinction coefficients from the airborne approaches can be compared to the mean extinction coefficients obtained from the model runs. The relative decreases in SCDs calculated from the extinction coefficients of the approaches are encompassed between the mean results obtained for model runs A for 306.6 nm and 310.8 nm. The fitted ϵ of all approaches and their 95 % confidence bands are depicted together with the mean ϵ derived from the model runs A in Fig. 10.12. The differences between model and measurements can be explained by the wavelength interval used in the DOAS evaluation. The first and strongest absorption line in the

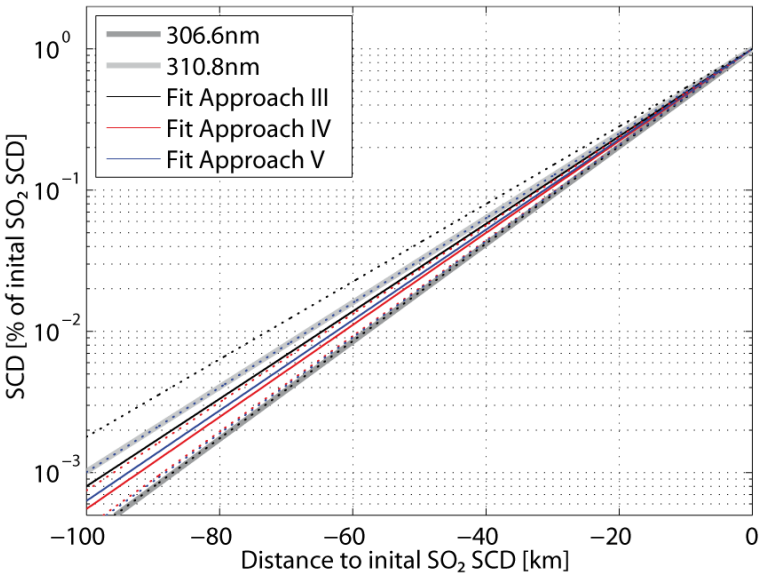

Figure 10.12. Relative changes of SO_2 SCDs for approaches III–V and comparison to the mean extinction coefficients derived by model runs A1–A3. The dashed lines indicate the 95 % confidence interval.

DOAS retrieval interval 307.4–317.8 nm is the absorption maximum at 308.7 nm, influencing the DOAS retrieval heavily. Thus, it is consistent that the value of the extinction coefficient ϵ of the DOAS retrieval lies about halfway between the extinction coefficients of 306.6 nm and 310.8 nm of the modelled scenarios. These results validate the model runs and allow to extent the experimental "proof of concept" measurement with model run B.

Early detection of an extensive volcanic cloud, results model runs B

As an example for the response of the proposed early detection system, an extensive volcanic cloud was simulated in model runs type B. The volcanic cloud was modelled with infinite horizontal extent and was located at 10 km altitude, a typical flight altitude for commercial airplanes. The results of model run B1 are shown in Fig. 10.13. A cloud containing mainly sulfate aerosols is assumed. Note that in contrast to Fig. 10.10, the ordinate is displaying a logarithmic scale to enhance visibility of the gradients at large distances to the volcanic cloud. Again, a clear separation of retrieved SO_2 SCDs at different wavelength intervals with distance can be observed.

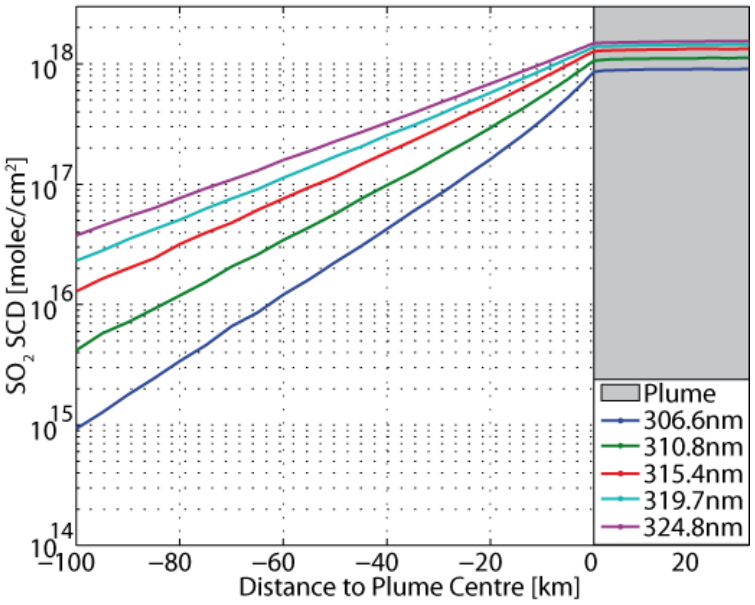

Figure 10.13. Simulated SO_2 SCD from model scenario B1. Here, a volcanic cloud with infinite extent in propagation direction and from the edge onwards was assumed to be at 10 km altitude. An SO_2 concentration of $1 \cdot 10^{12}$ molec cm^{-3} is assumed for the simulation, and the cloud exhibited an aerosol optical depth of 0.1 km^{-1}.

The relative changes in signal strength do not directly correspond to relative changes in detectability because the SO_2 absorption cross-section decreases with wavelength. The detection limit is instead given by the optical density obtained in a measurement, which is the product of the column density and the differential absorption cross-section. For model run B1, the simulated optical density is depicted as a function of wavelength in Fig. 10.14. A typical DOAS instrument which has been tuned to the task might be able to resolve optical densities of about 10^{-3} at a measurement integration time of a few seconds. This limit is reached at 80–90 km distance to the volcanic cloud for the wavelength range 310–315 nm. Thus, given a slightly enhanced setup, there is a realistic option of a feasible early detection of a volcanic SO_2 cloud at these distances.

The results of model run B2 show the system's response to varying ash contents of the volcanic cloud. Ash was simulated by decreasing the single scatter albedo (SSA) of the plume aerosol to 0.8. This is thought to represent a lower limit for the SSA of an ash-rich volcanic cloud (see e.g. Prata and Grant, 2001; Pavolonis et al., 2006; Kudo et al., 2008). The modelled optical densities obtained for 310.8 nm are shown in Fig. 10.15, as the highest sensitivity was obtained at this wavelength for model run B1. For comparison, the result of B1 (Fig. 10.14) for 310.8 nm is depicted as a dashed blue line. Reducing the SSA from 1 to 0.8 at

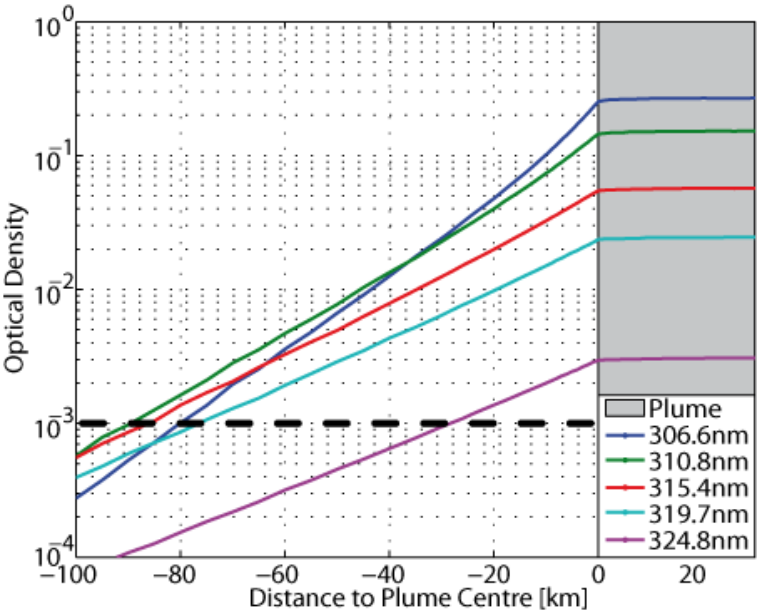

Figure 10.14. Optical densities are shown for model scenario B1 in order to assess detectability of large scale volcanic cloud. Optical densities of more than 10^{-3} are still obtained at distances greater than 80 km from the plume for the wavelength range 310–315 nm, thus indicating the possibility of a significantly earlier detection than is possible at lower altitudes.

an aerosol extinction coefficient (AEC) of 0.1 km^{-1} reduces the sensitivity very slightly, decreasing the detection range from about 90 km to 85 km. However, a further reduction in signal is observed for optically thick plumes, as the light path inside the cloud is reduced. Moderate AECs of <1 km^{-1} lead to a decrease of the maximum distance of detection from >80 km to about 60 km. A very thick cloud with an AEC of 4 km^{-1} would only be detectable from ≈35 km distance. However, such a cloud would be clearly visible in the sky, as the scattering extinction length is only 250 m. While such conditions may be encountered in close proximity to the volcanic source, they are not typical of a large-scale, diluted volcanic cloud that has travelled many tens or hundreds of kilometres in the atmosphere.

10.5 Conclusion

The measurements presented here clearly demonstrate the general applicability of DOAS as an early detection technique for SO_2 in a "proof of concept" campaign. A number of plume approaches were flown, and the measurement results were reproduced with a radiative transfer model. Although the approaches were only started at up to 25 km distance to the plume, the found relationship of signal to dis-

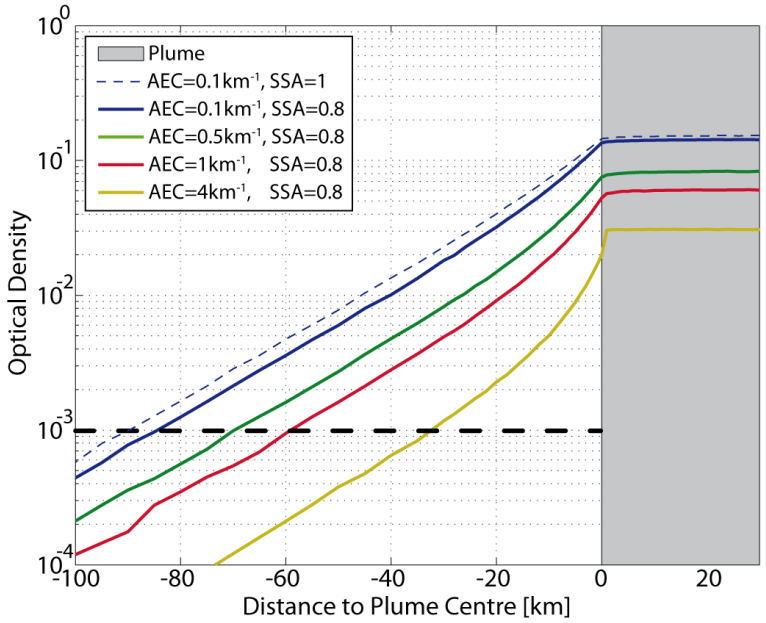

Figure 10.15. Optical densities for model scenario B2: Depicted are Simulated Optical densities at 310.8nm as a function of distance to an extended volcanic cloud (scenario B2) and varying ash content. Volcanic ash is simulated with a SSA = 0.8 and varying AECs. For comparison, the dashed blue line shows the result for a cloud with a purely scattering aerosols at an AEC of 0.1 km^{-1} (see Fig. 10.14). The dashed black line represents the assumed detection limit of 10^{-3} in optical density. Higher ash content reduces the detection limit, but a detection range of $>$ 60 km is still obtained for AEC $<$ 1. Only for extremely thick plumes, such as those encountered in close proximity to the volcanic source, does the detection range drop further.

tance of the measurements could be used to extrapolate the experiment to 100 km distance. Due to the lower air pressure at typical flight altitudes (about 10 km) when compared to the altitude of the Popocatépetl plume, additional radiative transfer studies conclude that a volcanic plume with a SO_2 slant column density of 10^{18} molecules cm^{-2} as viewed from the outside can be detected at distances up to 80 km away for both, a cloud consisting only of purely scattering sulfate aerosols (SSA = 1) and a cloud consisting of ash with a SSA of 0.8. This range provides enough time for pilots to take actions to avoid plume fly-through under typical flight conditions, suggesting that this technique can be used as an effective aid to prevent dangerous aircraft encounters with potentially ash-laden volcanic plumes.

However, certain issues must be addressed. Because the technique is based on radiation in the UV spectral region, it is only applicable during daylight. At twilight the signal to noise ratio will drop due to reduced intensities in the UV, which can partly be compensated by longer exposure times with consequent lower measurement frequency. The technique does not detect the main hazard volcanic

ash. Although certain algorithms have been proposed which should be able to determine aerosol optical densities of the plume from UV measurements (Kern et al., 2010b), these concepts need high computational power and are not feasible for real time evaluation. SO_2 is only a good proxy for ash which is the greater hazard if there is no separation of the ash and SO_2 cloud. Thus the technique is only complementary to ash detection systems in the IR.

One has to keep in mind that this study is only "proof of concept" and does not present a mature system. Further efforts are needed in experiment and modelling to fully explore the capabilities of the technique. This includes the ability to spatially resolve volcanic plumes at greater distances in order to allow avoidance measures to be initiated. Strategies must be developed to supply clear sky reference spectra without SO_2 absorptions. One approach would be to construct a small database with reference spectra constructed from high resolution solar spectra (e.g. Chance and Kurucz, 2010) including dependencies on altitude, solar zenith and azimuth angle. Furthermore, algorithms need to be developed which reduce or eliminate the influence of a SO_2 cloud above or below the aircraft which could influence the perceived signal at all viewing directions. Also investigations of the limitations e.g. in case of high altitude clouds between plume and instrument need to be done. This includes sensitivity to a volcanic cloud with ash particles covered in ice, because this is one of the cases were IR techniques based on the reverse absorption method are not suitable.

Last but not least, great potential lies in the development of DOAS instruments developed to this specific task. Large volcanic clouds are much more easily evaded by flying over or under them than by trying to go around them. Therefore, the vertical direction is arguably more important than the horizontal one. E.g. one could imagine a DOAS instrument applying an imaging spectrometer, which could be positioned so that its spatial axis is in the vertical, its dispersive axis is horizontal (IDOAS, Louban et al., 2009).

Besides the limitations and need for future research mentioned above, DOAS based SO_2 detection is a complementary technique to the detection of ash in the infra-red regime and in combination can greatly mitigate the risk from volcanic clouds to aviation.

11 Summary and Outlook

11.1 Retrieval wavelength mapping

Optical remote sensing via Differential Optical Absorption Spectroscopy (DOAS, Platt and Stutz, 2008) has become a standard technique to measure various trace gases in the atmosphere. Spectroscopic techniques are usually classified into active instruments applying an artificial light source and passive instruments, which use scattered or direct sunlight. Platforms range from ground-based to satellites, studying trace gases in all kinds of different environments (e.g. in the marine boundary layer, volcanic plumes, the in Arctic and Antarctic, from the lower troposphere to the stratospheric). Naturally, due to this wide range of measurement conditions, atmospheric compositions and instruments used, the evaluation of gathered spectra needs to be optimized for each specific case and particular trace gas of interest. This becomes especially important if the trace gas concentration is close to the detection limit of the instrument.

A well chosen evaluation wavelength range is critical to the DOAS technique. It should include strong absorption bands of the trace gas of interest, in order to maximize the sensitivity of the retrieval, while at the same time minimizing absorption structures of other trace gases and thus potential interference. Generally, a broader range increases the information supplied to the retrieval algorithm but also might encompass potentially interfering absorption structures of other gases present. Furthermore, instrumental limitations (e.g. non-linear dispersion) need to be taken into account. Most often, not all of these requirements can be fulfilled simultaneously and a compromise needs to be found depending on the conditions at hand.

In this thesis a novel tool was present to determine the optimal evaluation wavelength range. It is based on mapping retrieved values on the evaluation wavelength space and thus on visualizing structures introduced, e.g., by slightly erroneous absorption cross sections, cross correlations and instrumental features. The

technique is applied at the example of a theoretical study of BrO retrievals for stratospheric BrO measurements and for BrO measurements in volcanic plumes. Next to synthetic spectra, the tool was applied to measured spectra of volcanic plumes. However, due to the general nature of the tool, it is applicable to any DOAS retrieval.

An optimal evaluation fit range for the retrieval of BrO in volcanic plumes could be determined by combining results from synthetic and measured spectra. The wavelength range 330.6 nm – 352.7 nm is advised, since it offers minimal cross correlation of BrO with other absorbers like HCHO, minimal bias of BrO SCDs when comparing FRSs and reasonable agreement with theoretical studies. In addition, measured spectra were studied by retrieval wavelength mapping for the retrieval of SO_2. Together with consideration of radiative transfer effects, an optimal SO_2 retrieval wavelength range of 314.8 nm – 326.8 nm was found. This range offers the best compromise between detectability of SO_2 and least influence by radiative transfer effects. Together with the advised BrO retrieval wavelength range, a best approximation of BrO/SO_2 ratios is achieved if radiative transfer calculation of high computational needs are excluded.

11.2 Evolution of BrO/SO_2 ratios in volcanic plumes

The main species emitted by volcanoes are H_2O, CO_2, SO_2 and H_2S in order of magnitude (Textor et al., 2004). Next to these species, also higher amounts of HCl are emitted together with a minor fraction of other hydrogen halides (HF and HBr). By measuring the composition of volcanic emissions, one can draw conclusions on the influence of volcanic emissions onto the atmosphere at a regional and global scale. They also provide insight into the state of the respective volcano, since the composition of the volcanic emissions depends on magma composition and ongoing processes inside the volcanic system. Volcanic plumes were thought to be relatively chemical inert, until Bobrowski et al. (2003) discovered high abundances of BrO in the volcanic plume of Soufrière Hills Volcano, Montserat. It is believed, that BrO is produced in the volcanic plume in an auto-catalytic reaction cycle similar to the "Bromine-Explosion" known from the Arctic and Antarctic. In short, the volcanic HBr emitted is partly scavenged by aerosol particles. In a photochemical reaction cycle, one BrO molecule leads to the release of Br_2 from aerosol particles, which in turn produce two BrO molecules by destroying two O_3. This auto-catalytic cycle produces a rapid increase in BrO together with a decrease of O_3 concentration.

Since O_3 is not present in the initial emissions, it is entrained into the plume with ambient air. Due to the destruction of O_3 depletion inside the volcanic plume, it may have further effects on the constitution of the atmosphere. Other species involved in the reactions are HO_x, NO_x and ClO_x.
Volcanic emissions are commonly characterized by varying emission strengths on short time scales, and are subject to dispersion and dilution by ambient air. In comparison to BrO, SO_2 is assumed to be relatively inert during common plume ages observed. Thus it is used as a tracer to track bromine chemistry via BrO/SO_2 ratio, where dilution, dispersion and variations in emissions cancel.
For a given BrO/SO_2 and plume age, chemical models are necessary to determine the total amount of bromine emitted by the volcano together with its speciation as well as further impact of the volcanic plume on the atmosphere.

Published model runs on BrO chemistry in volcanic plumes (Bobrowski et al., 2007; von Glasow et al., 2009; Roberts et al., 2009; von Glasow, 2010) have been tuned to fit a relatively sparse data set. In the case of Mt. Etna, published studies so far are Bobrowski et al. (2007); Bobrowski and Platt (2007); Louban et al. (2009), which discuss data sets gathered during August-October 2004, September/October 2003 and August-October 2004, May 2005, respectively. Although these datasets supply valuable insights into volcanic plume chemistry, they do not represent simultaneous observations of volcanic plume chemistry with several instruments at different plume ages. Only in Bobrowski et al. (2007) data of one day is presented, where several instruments measured the volcanic plume simultaneously and at different distances (see also sec. 2). However, only the distance of the instrument to the crater is given, which leads to a mixing of ratios from different plume ages depending on the wind speed and wind direction if the plume is not observed directly over the instrument. Plume ages derived from these data in von Glasow (2010) assume a general wind speed of 7 m/s.

Here, BrO/SO_2 ratios are presented, which were measured at Mt. Etna and constitute the first simultaneous capture of the evolution of BrO/SO_2 ratios at plume ages up to 100 min. The presented data set show different evolutions of ratios for both measurement campaigns. On the one hand, a small but constant increase is observed for BrO/SO_2 ratios with increasing plume age, measured during July 2008. A maximum of $1.2 \cdot 10^{-4}$ is obtained at a plume age of 60 min, which also the maximum measured plume age. On the other hand, measurements during July 2009 showed smaller BrO/SO_2 ratios, which do not significantly increase further and might even be decreasing after an initial increase from 0 to $0.65 \cdot 10^{-4}$ during

the first 5 min. Giving the different state of Mt. Etna during campaigns (ongoing eruption and shortly after the cease of activity) this strongly suggests a difference in composition of the volcanic plume during both time frames. Compared to different model runs by von Glasow (2010), the presented ratios proof that current atmospheric chemistry model do not adequately predict bromine chemistry in volcanic plumes. A comparable increase in ratio in the early plume (< 5 min plume age) is only observed in a scenario, which overestimates further development of ratios by a factor of $\times 3$ at 60 min plume age. Model runs yielding a better agreement of BrO/SO_2 ratios compared to measurements from July 2009 at plume ages > 40 min are based are neglecting aerosol chemistry, which does not reflect real measurement conditions observed.
A source of the differences between measured BrO/SO_2 ratios and chemical model may lie in a falsely assumed dilution factor of the volcanic plume in the model initialisation. For example, further model runs in (von Glasow, 2010) showed that BrO constitutes 30% of the total bromine species present already after 5 min if a $\times 10$ stronger entrainment of ambient air occurs at the crater rim than assumed for the model run, which is believed to represent conditions at Mt. Etna (model run A, 5% BrO/Br_{total} at 5 min plume age).

Next to simultaneous measurements of BrO/SO_2 ratios at older plume ages, also the hitherto first observation of measurements of BrO/SO_2 ratios at early plume ages (< 5 min) and at high time resolution were presented for Pacaya. These measurements are also the first observation of BrO at Pacaya. The rise of BrO/SO_2 ratios from below the detection of $0.2 \cdot 10^{-4}$ in the first two minutes to $1.25 \cdot 10^{-4}$ in the following three minutes is shown. It proofs that model runs well predict the measurements qualitatively on the time scales observed. The measurements also yield the presence of HCHO in the lower atmospheric layers around Pacaya with only negligible concentrations of NO_2. These findings are valuable additions to the measured BrO/SO_2 ratios at Pacaya, since the role of these species is not well understood in the chemistry of volcanic plumes, but may have significant impact.

The here presented BrO/SO_2 ratios are big step forward in unravelling bromine chemistry in volcanic plumes and up to date the most comprehensive data sets capturing the evolution of BrO/SO_2. However, many aspects remain unclear. Further modelling of atmospheric chemistry is necessary, based on these measurements. The amount of other bromine species need to be assessed, e.g. HBr and $BrNO_x$. Next to bromine, also chlorine species and other trace gas are assumed to play an important role, which are not necessarily of volcanic origin. This includes O_3,

NO_x, HO_x and HCHO. Combined, simultaneous measurements of these species at different plume ages would help to better constrain the boundaries for the assumed chemical reactions in volcanic plumes.

11.3 Early in-flight detection of SO_2

Volcanic ash constitutes a risk to aviation, mainly due to its ability to cause jet engines to fail. Other risks include the possibility of abrasion of wind shields and potentially serious damage to avionic systems. These hazards have been widely recognized since the early 1980s, when volcanic ash provoked several incidents of engine failure in commercial aircraft. In addition to volcanic ash, volcanic gases also pose a threat. Prolonged and/or cumulative exposure to sulphur dioxide (SO_2) or sulphuric acid (H_2SO_4) aerosols potentially affects e.g. windows, air frame and may cause permanent damage to engines. SO_2 receives most attention among the gas species commonly found in volcanic plumes because its presence above the lower troposphere is a clear proxy for a volcanic cloud and indicates that fine ash could also be present.

Up to now, remote sensing of SO_2 via Differential Optical Absorption Spectroscopy (DOAS) in the ultraviolet spectral region has been used to measure volcanic clouds from ground based, airborne and satellite platforms. Attention has been given to volcanic emission strength, chemistry inside volcanic clouds and measurement procedures were adapted accordingly. Here we present a set of experimental and model results, highlighting the feasibility of DOAS to be used as an airborne early detection system of SO_2 in two spatial dimensions. In order to prove our new concept, simultaneous airborne and ground-based measurements of the plume of Popocatépetl volcano, Mexico, were conducted in April 2010. The plume extended at an altitude around 5250 m above sea level and was approached and traversed at the same altitude with several forward looking DOAS systems aboard an airplane. These DOAS systems measured SO_2 in the flight direction and at ± 40 mrad (2.3°) angles relative to it in both, horizontal and vertical directions. The approaches started at up to 25 km distance to the plume and SO_2 was measured at all times well above the detection limit. In combination with radiative transfer studies, this study indicates that an extended volcanic cloud with a concentration of 10^{12} molecules cm^{-3} at typical flight levels of 10 km can be detected unambiguously at distances of up to 80 km away. This range provides enough time (approx. 5 min) for pilots to take action to avoid entering a volcanic cloud in the

flight path, suggesting that this technique can be used as an effective aid to prevent dangerous aircraft encounters with potentially ash rich volcanic clouds.

Further efforts are needed in experiment and modelling to fully explore the capabilities of the technique. This includes the ability to spatially resolve volcanic plumes at greater distances in order to allow avoidance measures to be initiated. Strategies must be developed to supply clear sky reference spectra without SO_2 absorptions. Furthermore, algorithms need to be developed which reduce or eliminate the influence of a SO_2 cloud above or below the aircraft which could influence the perceived signal at all viewing directions. Also investigations of the limitations need to be performed. This includes sensitivity to a volcanic cloud with ash particles covered in ice, since this is one of the cases were IR techniques based on the reverse absorption method are not suitable. Great potential lies in the development of DOAS instruments build for this specific task. Large volcanic clouds are much more easily evaded by flying over or under them than by trying to go around them. Therefore, the vertical direction is arguably more important than the horizontal one. E.g. one could imagine a DOAS instrument applying an imaging spectrometer, which could be positioned so that its spatial axis is in the vertical, its dispersive axis is horizontal (IDOAS, Louban et al., 2009).

Bibliography

(2010). *Ash Dispersal Forecast and Civil Aviation Workshop, Consensual Document*, Geneva, Switzerland.

Afe, O., Richter, A., Sierk, B., Wittrock, F., and Burrows, J. (2004). Bro emission from volcanoes: A survey using gome and sciamachy measurements. *Geophys. Res. Lett.*, 31(24).

Aiuppa, A., Bagnato, E., Witt, M. L. I., Mather, T. A., Parello, F., Pyle, D. M., and Martin, R. S. (2007). Real-time simultaneous detection of volcanic hg and SO2 at la fossa crater, vulcano (aeolian islands, sicily). *GeoPhys. Res. Lett.*, 34(21).

Aiuppa, A., Baker, D. R., and Webster, J. D. (2009). Halogens in volcanic systems. *Chem. Geol.*, 263(1-4):1–18.

Aiuppa, A. and Federico, C. (2004). Anomalous magmatic degassing prior to the 5th April 2003 paroxysm on Stromboli. *GeoPhys. Res. Lett.*, 31(14).

Aliwell, S., Roozendael, M. V., Johnston, P., Richter, A., Wagner, T., and Arlander, D. (2002). Analysis for BrO in zenith-sky spectra: An intercomparison exercise for analysis improvement. *J. Geophys. Res.*, 107(D14).

Bani, P., Oppenheimer, C., Tsanev, V. I., Carn, S. A., Cronin, S. J., Crimp, R., Calkins, J. A., Charley, D., Lardy, M., and Roberts, T. R. (2009). Surge in sulphur and halogen degassing from Ambrym volcano, Vanuatu. *B. Volcanol.*, 71(10):1159–1168.

Barrie, L., Bottenheim, J. W., Schnell, R. C., Crutzen, P. J., and Rasmussen, R. A. (1988). Ozone destruction and photochemical reactions at solar sunrise in the lower Arctic atmosphere. *Nature*, 334:138 – 141.

Barrie, L. and Platt, U. (1997). Arctic tropospheric chemistry: An overview,. *Tellus, Ser. B*, 49:450 – 454.

Barton, I. J. and Prata, A. J. (1994). Detection and discrimination of volcanic ash clouds by infrared radiometry – ii: experimental. In Casadevall, T. J., editor, *Volcanic Ash and aviation safety: proceedings of the first International Symposium on Volcanic Ash and Aviation Safety*, volume 1, pages 313–317, Washington, D.C. U.S. Geological Survey bulletin, U.S. Geological Survey bulletin.

Begoin, M., Richter, A., Weber, M., Kaleschke, L., Tian-Kunze, X., Stohl, A., Theys, N., and Burrows, J. P. (2010). Satellite observations of long range transport of a large bro plume in the arctic. *Atmos. Chem Phys.*, 10(14):6515–6526.

Berglen, T. F., Berntsen, T. K., Isaksen, I. S. A., and Sundet, J. K. (2004). A global model of the coupled sulfur/oxidant chemistry in the troposphere: The sulfur cycle. *J. Geophys. Res.*, 109(D19):D19310.

Bernard, A. and Rose, W. I. (1990). The injection of sulfuric acid aerosols in the stratosphere by el chichón volcano and its related hazards to the international air traffic. *Nat. Hazards*, 3:59–67.

Bluth, G. J. S., Shannon, J. M., Watson, I. M., Prata, A. J., and Realmuto, V. J. (2007). Development of an ultra-violet digital camera for volcanic SO2 imaging. *J. Volcanol. Geotherm. Res.*, 161(1-2):47–56.

Bobrowski, N. and Giuffrida, G. (in prep.). Bro/so2 ratios in relation to volcanological observations at mt etna 2006-2009.

Bobrowski, N., Honninger, G., Galle, B., and Platt, U. (2003). Detection of bromine monoxide in a volcanic plume. *NATURE*, 423(6937):273–276.

Bobrowski, N. and Platt, U. (2007). SO_2/BrO ratios studied in five volcanic plumes. *J. Volcanol. Geoth. Res.*, 166:147–160.

Bobrowski, N., von Glasow, R., Aiuppa, A., Inguaggiato, S., Louban, I., Ibrahim, O. W., and Platt, U. (2007). Reactive halogen chemistry in volcanic plumes. *J. Geophys. Res.-Atmos.*, 112(D6).

Bogumil, K., Orphal, J., Homann, T., Voigt, S., Spietz, P., Fleischmann, O., Vogel, A., Hartmann, M., Kromminga, H., Bovensmann, H., Frerick, J., and Burrows, J. (2003). Measurements of molecular absorption spectra with the SCIAMACHY pre-flight model: instrument characterization and reference data for atmospheric remote-sensing in the 230-2380 nm region. *J. Photoh. Photobio. A.*, 157(2-3):167–184.

Boichu, M., Oppenheimer, C., Roberts, T. J., Tsanev, V., and Kyle, P. R. (2011).

On bromine, nitrogen oxides and ozone depletion in the tropospheric plume of Erebus volcano (Antarctica). *Atmospheric Environment*, 45(23):3856 – 3866.

Burrows, J., Richter, A., Dehn, A., Deters, B., Himmelmann, S., and Orphal, J. (1999). Atmospheric remote-sensing reference data from gome - 2. temperature-dependent absorption cross sections of o-3 in the 231-794 nm range. *J. Quant. Spectrosc. Radiat. Transfer*, 61(4):509–517.

Bussemer, M. (1993). Der ring effekt: Ursachen und einfluß auf die spektroskopischen messungen stratosphaerischer spurenstoffe. Master's thesis, IUP, University Heidelberg.

Carn, S. A., Krueger, A. J., Krotkov, N. A., Yang, K., and Evans, K. (2009). Tracking volcanic sulfur dioxide clouds for aviation hazard mitigation. *Nat. Hazards*, 51(2):325–343.

Casadevall, T. (1994). The 1989-1990 eruption of Redoubt volcano, Alaska - Impact on aircraft operations. *Journal of Volcanology and Geothermal Research*, 62(1-4):301–316.

Chance, K. (1998). Analysis of BrO measurements from the Global Ozone Monitoring Experiment. *Geophys. Res. Lett.*, 25(17):3335–3338.

Chance, K. (2002). OMI algorithm theoretical basis document – volume iv. Technical report, Smithsonian Astrophysical Observatory, Cambridge, MA, USA.

Chance, K., Kurosu, T., and Sioris, C. (2005). Undersampling correction for array detector-based satellite spectrometers. *Appl. Opt.*, 44(7):1296–1304.

Chance, K. and Kurucz, R. L. (2010). An improved high-resolution solar reference spectrum for earth's atmosphere measurements in the ultraviolet, visible, and near infrared. *J. Quant. Spectrosc. Radiat. Transfer*, 111(9):1289–1295.

Chance, K. and Spurr, R. (1997). Ring effect studies: Rayleigh scattering, including molecular parameters for rotational Raman scattering, and the Fraunhofer spectrum. *Appl. Opt.*, 36(21):5224–5230.

Clarisse, L., Prata, F., Lacour, J.-L., Hurtmans, D., Clerbaux, C., and Coheur, P.-F. (2010). A correlation method for volcanic ash detection using hyperspectral infrared measurements. *GeoPhys. Res. Lett.*, 37.

Coltelli, M. (2008). Rapporto settimanale sull'attività eruttiva dell'etna (7-13 luglio 2008). Technical report, INGV-Sezione di Catania.

Curci, G., Palmer, P. I., Kurosu, T. P., Chance, K., and Visconti, G. (2010). Estimating european volatile organic compound emissions using satellite observations of formaldehyde from the ozone monitoring instrument. *Atmos. Chem. Phys.*, 10(23):11501–11517.

Dalton, M. P., Watson, I. M., Nadeau, P. A., Werner, C., Morrow, W., and Shannon, J. M. (2009). Assessment of the uv camera sulfur dioxide retrieval for point source plumes. *J. Volcanol. Geotherm. Res.*, 188(4):358 – 366.

de Beek, R., Vountas, M., Rozanov, V., Richter, A., and Burrows, J. (2001). The Ring Effect in the cloudy atmosphere. *GeoPhys. Res. Lett.*, 28(4):721–724.

De Smedt, I., Van Roozendael, M., and Jacobs, T. (2004). Optimization of doas settings for bro fitting from sciamachy nadir spectra – comparison with gome bro retrievals. Technical report, Belg. Inst. for Space Aeron., Brussels, Belgium.

Deutschmann, T. (2008). Atmospheric radiative transfer modelling using monte carlo methods. Master's thesis, University Heidelberg.

Deutschmann, T., Beirle, S., Friess, U., Grzegorski, M., Kern, C., Kritten, L., Platt, U., Prados-Roman, C., Pukite, J., Wagner, T., Werner, B., and Pfeilsticker, K. (2011). The Monte Carlo atmospheric radiative transfer model McArtim: Introduction and validation of Jacobians and 3D features. *J. Quant. Spectrosc. Ra.*, 112(6):1119–1137.

Doasis (2010). Doas intelligent system. Institute of Environmental Physics, University Heidelberg, Germany.

Doran, J., Abbott, S., Archuleta, J., Bian, X., Chow, J., Coulter, R., de Wekker, S., Edgerton, S., Elliott, S., Fernandez, A., Fast, J., Hubbe, J., King, C., Langley, D., Leach, J., Lee, J., Martin, T., Martinez, D., Martinez, J., Mercado, G., Mora, V., Mulhearn, M., Pena, J., Petty, R., Porch, W., Russell, C., Salas, R., Shannon, J., Shaw, W., Sosa, G., Tellier, L., Templeman, B., Watson, J., White, R., Whiteman, C., and Wolfe, D. (1998). The IMADA-AVER boundary layer experiment in the Mexico City area. *B. Am. Meteorol. Soc.*, 79(11):2497–2508.

Edmonds, M., Herd, R. A., Galle, B., and M., O. C. (2003). Automated, high time resolution measurements of SO2 flux at soufrière hills volcano, montserrat. *Bull. Volcanol.*, 65:578 – 586.

Edner, H., Ragnarson, P., Svanberg, S., Wallinder, E., Ferrara, R., Cioni, R., Raco, B., and Taddeucci, G. (1994). Total fluxes of sulfur-dioxide from the

italian volcanos etna, stromboli, and vulcano measured by differential absorption lidar and passive differential optical-absorption spectroscopy. *J. Geophys. Res.-Atmos.*, 99(D9):18827–18838.

Fickel, M. (2008). Measurement of trace gas fuxes from point sources with multi-axis differential optical absorption spectroscopy. Master's thesis, Faculty of Physics and Astronomy, University of Heidelberg.

Fleischmann, O., Hartmann, M., Burrows, J., and Orphal, J. (2004). New ultraviolet absorption cross-sections of BrO at atmospheric temperatures measured by time-windowing fourier transform spectroscopy. *J. Photochem. Photobiol. A*, 168(1-2):117–132.

Frins, E., Bobrowski, N., Platt, U., and Wagner, T. (2006). Topographic multiaxis-differential optical absorption spectroscopy observations of sun-illuminated targets: a technique providing well-defined absorption paths in the boundary layer. *Appl. Opt.*, 45(24):6227–6240.

Galle, B. (2007). Method and device for measuring emissions of gaseous substances to the atmosphere using scattered sunlight spectroscopy.

Galle, B., Delgado, H. Garzon, G., Vogel, L., and Platt, U. (2011). *NOVAC: Network for Observation of Volcanic and Atmospheric Change, Final Report.*

Galle, B., Johansson, M., Rivera, C., Zhang, Y., Kihlman, M., Kern, C., Lehmann, T., Platt, U., Arellano, S., and Hidalgo, S. (2010). Network for observation of volcanic and atmospheric change (novac) - a global network for volcanic gas monitoring: Network layout and instrument description. *J. Geophys. Res.*, 115(D5):D05304.

Galle, B., Oppenheimer, C., Geyer, A., McGonigle, A. J. S., Edmonds, M., and Horrocks, L. (2002). A miniaturised ultraviolet spectrometer for remote sensing of so2 fluxes: a new tool for volcano surveillance. *J. Volcanol. Geotherm. Res.*, 119(1-4):241 – 254.

Gerlach, T. (2004). Volcanic sources of tropospheric ozone-depleting trace gases. *Geochem. Geophys. Geosyst.*, 5.

Giammanco, S. (2009). Rapporto settimanale sul monitoraggio vulcanologico dell'etna (6 - 12 luglio 2009). Technical report, INGV-Sezione di Catania.

Grainger, J. F. and Ring, J. (1962). Anomalous fraunhofer line profiles. *Nature*, 762:193.

Grindle, T. and Burcham, F. (2003). Engine damage to a nasa dc-8-72 airplane from a high-altitude encounter with a diffuse volcanic ash cloud. Technical report, NASA, Dryden Flight Research Center.

Guffanti, M., Schneider, D. J., Wallace, K. L., Hall, T., Bensimon, D. R., and Salinas, L. S. (2010). Aviation response to a widely dispersed volcanic ash and gas cloud from the august 2008 eruption of kasatochi, alaska, usa. *J. Geophys. Res.*, 115:D00L19.

Hebestreit, K., Stutz, J., Rosen, D., Matveiv, V., Peleg, M., Luria, M., and U., P. (1999). Doas measurements of tropospheric bromine oxide in mid-latitudes. *Science*, 283:55 – 57.

Heckel, A., Richter, A., Tarsu, T., Wittrock, F., Hak, C., Pundt, I., Junkermann, W., and Burrows, J. P. (2005). Max-doas measurements of formaldehyde in the po-valley. *Atmos. Chem. Phys.*, 5(4):909–918.

Hegels, E., Crutzen, P., Klupfel, T., Perner, D., and Burrows, J. (1998). Global distribution of atmospheric bromine-monoxide from GOME on earth observing satellite ERS-2. *GeoPhys. Res. Lett.*, 25(16):3127–3130.

Hermans, C., A.C., V., Fally, S., Carleer, M., Colin, R., Coquart, B., Jenouvrier, A., and Mérienne, M.-F. (2003). Absorption cross-section of the collision-induced bands of oxygen from the uv to the nir, proceedings of the nato advanced research workshop, weakly interacting molecular pairs: Unconventional absorbers of radiation in the atmosphere, france, april 24-may 2, 2002. *NATO Science Series IV Earth and Environmental Sciences*, 27:193–202.

Heue, K.-P., Brenninkmeijer, C. A. M., Baker, A. K., Rauthe-Schöch, A., Walter, D., Wagner, T., Hörmann, C., Sihler, H., Dix, B., Frieß, U., Platt, U., Martinsson, B. G., van Velthoven, P. F. J., Zahn, A., and Ebinghaus, R. (2011). So_2 and bro observation in the plume of the eyjafjallajökull volcano 2010: Caribic and gome-2 retrievals. *Atmos. Chem. Phys.*, 11(6):2973–2989.

Hönninger, G., Leser, H., Sebastian, O., and Platt, U. (2004). Ground-based measurements of halogen oxides at the hudson bay by active longpath doas and passive max-doas. *Geophysical Research Letters*, 31(4):L04111.

Huijnen, V., Eskes, H. J., Poupkou, A., Elbern, H., Boersma, K. F., Foret, G., Sofiev, M., Valdebenito, A., Flemming, J., Stein, O., Gross, A., Robertson, L., D'Isidoro, M., Kioutsioukis, I., Friese, E., Amstrup, B., Bergstrom, R., Strunk, A., Vira, J., Zyryanov, D., Maurizi, A., Melas, D., Peuch, V.-H., and Zere-

fos, C. (2010). Comparison of OMI NO2 tropospheric columns with an ensemble of global and European regional air quality models. *Atmos. Chem. Phys.*, 10(7):3273–3296.

ICAO (2007). *Manual on Volcanic Ash, Radioactive Material, and Toxic Chemical Clouds, 2nd Edition*. International Civil Aviation Organization, 2 edition. Doc 9691-AN/954.

INGV (2008). Comunicato del 09 luglio 2008 aggiornamento alle ore 11:00. Technical report, INGV-Sezione di Catania.

Jähne, B. (2005). *Digital Image Processing*. Springer.

Johansson, M., Galle, B., Zhang, Y., Rivera, C., Chen, D., and Wyser, K. (2009). The dual-beam mini-DOAS technique-measurements of volcanic gas emission, plume height and plume speed with a single instrument. *B. Volcanol.*, 71(7):747–751.

Kantzas, E. P., McGonigle, A. J. S., Tamburello, G., Aiuppa, A., and Bryant, R. G. (2010). Protocols for UV camera volcanic SO2 measurements. *J. Volcanol. Geotherm. Res.*, 194(1-3):55–60.

Karagulian, F., Clarisse, L., Clerbaux, C., Prata, A. J., Hurtmans, D., and Coheur, P. F. (2010). Detection of volcanic SO2, ash, and H2SO4 using the Infrared Atmospheric Sounding Interferometer (IASI). *J. Geophys. Res.-Atmos.*, 115.

Kern, C. (2009). *Spectroscopic measurements of volcanic gas emissions in the ultra-violet wavelength region*. PhD thesis, Combined Faculties for the Natural Sciences and for Mathematics, University of Heidelberg.

Kern, C., Deutschmann, T., Vogel, L., Woehrbach, M., Wagner, T., and Platt, U. (2010a). Radiative transfer corrections for accurate spectroscopic measurements of volcanic gas emissions. *B. Volcanol.*, 72(2):233–247.

Kern, C., Kick, F., Luebeck, P., Vogel, L., Woehrbach, M., and Platt, U. (2010b). Theoretical description of functionality, applications, and limitations of SO2 cameras for the remote sensing of volcanic plumes. *Atmos. Meas. Tech.*, 3(3):733–749.

Kern, C., Sihler, H., Vogel, L., Rivera, C., Herrera, M., and Platt, U. (2009). Halogen oxide measurements at Masaya Volcano, Nicaragua using active long path differential optical absorption spectroscopy. *BULLETIN OF VOLCANOLOGY*, 71(6):659–670.

Khokhar, M., Frankenberg, C., Van Roozendael, M., Beirle, S., Kuhl, S., Richter, A., Platt, U., and Wagner, T. (2005). Satellite observations of atmospheric so2 from volcanic eruptions during the time-period of 1996-2002. In Burrows, JP and Eichmann, KU, editor, *Atmospheric remote sensing: earth's surface, troposhere, stratosphere and mesosphere - I*, volume 36 of *Advances in space research*, pages 879–887. ELSEVIER SCIENCE LTD.

Khokhar, M. F., Platt, U., and Wagner, T. (2008). Temporal trends of anthropogenic so_2 emitted by non-ferrous metal smelters in peru and russia estimated from satellite observations. *Atmospheric Chemistry and Physics Discussions*, 8(5):17393–17422.

Kraus, S. G. (2006). *DOASIS, A Framework Design for DOAS*. PhD thesis, University of Mannheim.

Krueger, A. (1983). Sighting of el chichon sulfur dioxide clouds with the nimbus 7 total ozone mapping spectrometer. *Science*, 220:1377–1379.

Kudo, R., Uchiyama, A., Yamazaki, A., Kobayashi, E., and Nishizawa, T. (2008). Retrieval of aerosol single-scattering properties from diffuse and direct irradiances: Numerical studies. *J. Geophys. Res.-Atmos.*, 113(D9):D09204.

Kurucz, R. L. (2005). High resolution irradiance spectrum from 300 to 1000 nm. AFRL Transmission Meeting, Lexington, Mass.

Kurucz, R. L., Furenlid, I., Brault, J., and Testermann, L. (1984). Solar flux atlas from 296 to 1300 nm. Natl. Sol. Obs. Atlas, Sunspot.

La Spina, A., Burton, M., and Salerno, G. G. (2010). Unravelling the processes controlling gas emissions from the central and northeast craters of Mt. Etna. *J. Volcanol. Geotherm. Res.*, 198(3-4):368–376.

Langford, A. O., Schofield, R., Daniel, J. S., Portmann, R. W., Melamed, M. L., Miller, H. L., Dutton, E. G., and Solomon, S. (2007). On the variability of the ring effect in the near ultraviolet: understanding the role of aerosols and multiple scattering. *Atmos. Chem. Phys.*, 7(3):575–586.

Lehmann, T. (2011). *Improving the sensitivity of spectroscopic measurements of atmospheric trace gases by modern signal processing algorithms, in preparation.* PhD thesis, IUP, University Heidelberg.

Leser, H., Honninger, G., and Platt, U. (2003). Max-doas measurements of bro and no2 in the marine boundary layer. *Geophys. Res. Lett.*, 30(10).

Lodato, L. (2009). Rapporto sull'attività eruttiva dell'etna (13 - 21 luglio 2009). Technical report, INGV-Sezione di Catania.

Louban, I., Bobrowski, N., Rouwet, D., Inguaggiato, S., and Platt, U. (2009). Imaging DOAS for volcanological applications. *B. Volcanol.*, 71(7):753–765.

Lübcke, P. (2010). Development of a new so_2 camera for volcanic gas flux measurements. Master's thesis, Insitute of Environmental Science, University Heidelberg.

Martin, R., Mather, T., and Pyle, D. (2006). High-temperature mixtures of magmatic and atmospheric gases. *Geochem. Geophys. Geosyst.*, 7.

McGonigle, A., Oppenheimer, C., Galle, B., Mather, T., and Pyle, D. (2002). Walking traverse and scanning DOAS measurements of volcanic gas emission rates. *GEOPHYSICAL RESEARCH LETTERS*, 29(20).

Meller, R. and Moortgat, G. (2000). Temperature dependence of the absorption cross sections of formaldehyde between 223 and 323 K in the wavelength range 225-375 nm. *J. Geophys. Res.-Atmos.*, 105(D6):7089–7101.

Merten, A., Tschritter, J., and Platt, U. (2011). Design of differential optical absorption spectroscopy long-path telescopes based on fiber optics. *Appl. Opt.*, 50(5):738–754.

Millard, G. A., Mather, T. A., Pyle, D. M., Rose, W. I., and Thornton, B. (2006). Halogen emissions from a small volcanic eruption: Modeling the peak concentrations, dispersion, and volcanically induced ozone loss in the stratosphere. *GeoPhys. Res. Lett.*, 33(19).

Miller, T. and Casadevall, T. (2000). *Encyclopedia of volcanoes*, chapter Volcanic ash hazards to aviation. Academic Press, San Diego, USA.

Moffat, A. J. and Millan, M. M. (1971). The applications of optical correlation techniques to the remote sensing of so2 plumes using sky light. *Atmospheric Environment (1967)*, 5(8):677 – 690.

Mori, T. and Burton, M. (2006). The SO2 camera: A simple, fast and cheap method for ground-based imaging of SO2 in volcanic plumes. *GeoPhys. Res. Lett.*, 33(24).

Mori, T., Mori, T., Kazahaya, K., Ohwada, M., Hirabayashi, J., and Yoshikawa, S.

(2006). Effect of UV scattering on SO2 emission rate measurements. *GeoPhys. Res. Lett.*, 33(17).

Nriagu, J. and Becker, C. (2003). Volcanic emissions of mercury to the atmosphere: global and regional inventories. *Sci. Total Environ.*, 304(1-3):3–12. 6th International Conference on Mercury as a Global Pollutant, MINAMATA, JAPAN, OCT 15-19, 2001.

OceanOptics (2008).

Oppenheimer, C., Pyle, D., and J., B., editors (2003). *Volcanic Degassing.* Geological Society.

Oppenheimer, C., Tsanev, V. I., Braban, C. F., Cox, R. A., Adams, J. W., Aiuppa, A., Bobrowski, N., Delmelle, P., Barclay, J., and McGonigle, A. J. S. (2006). BrO formation in volcanic plumes. *Geochim. Cosmochim. Acta*, 70(12):2935–2941.

Otten, C., Ferlemann, F., Platt, U., Wagner, T., and Pfeilsticker, K. (1998). Groundbased doas uv/visible measurements at kiruna (sweden) during the sesame winters 1993/94 and 1994/95. *J. Atmos. Chem.*, 30(1):141–162.

Pavolonis, M. and Sieglaff, J. (2010). Goes-r advanced baseline imager (abi) algorithm theoretical basis document for volcanic ash (detection and height). Technical report, STAR, NESDIS, NOAA, Camp Springs, Maryland, USA.

Pavolonis, M. J., Feltz, W. F., Heidinger, A. K., and Gallina, G. M. (2006). A daytime complement to the reverse absorption technique for improved automated detection of volcanic ash. *JOURNAL OF ATMOSPHERIC AND OCEANIC TECHNOLOGY*, 23(11):1422–1444.

Pennisi, M. and Le Cloarec, M. (1998). Variations of Cl, F, and S in Mount Etna's plume, Italy, between 1992 and 1995. *J. Geophys. Res.*, 103:5061–5066.

Platt, U., Marquard, L., Wagner, T., and Perner, D. (1997). Corrections for zenith scattered light doas. *Geophysical Research Letters*, 24(14):1759–1762.

Platt, U. and Stutz, J. (2008). *Differential Optical Absorption Spectroscopy: Principles and Application.* Springer.

Prata, A. (1989). INFRARED RADIATIVE-TRANSFER CALCULATIONS FOR VOLCANIC ASH CLOUDS. *GeoPhys. Res. Lett.*, 16(11):1293–1296.

Prata, A., Barton, I., Johnson, R., Kamo, K., and Kingwell, J. (1991). Hazard from volcanic ash. *Nature*, 354(6348):25. Scientific Correspondence.

Prata, A., Rose, W., Self, S., and O'Brien, D. (2003). Global, long-term sulphur dioxide measurements from the tovs data: a new tool for studying explosive volcanism and climate. *Geophys Monogr*, 139:75–92.

Prata, A. J. (2009). Satellite detection of hazardous volcanic clouds and the risk to global air traffic. *Nat. Hazards*, 51(2):303–324.

Prata, A. J. and Bernardo, C. (2007). Retrieval of volcanic SO2 column abundance from atmospheric infrared sounder data. *J. Geophys. Res.-Atmos.*, 112(D20).

Prata, A. J. and Bernardo, C. (2009). Retrieval of volcanic ash particle size, mass and optical depth from a ground-based thermal infrared camera. *J. Volcanol. Geotherm. Res.*, 186(1-2, Sp. Iss. SI):91–107.

Prata, A. J. and Grant, I. F. (2001). Retrieval of microphysical and morphological properties of volcanic ash plumes from satellite data: Application to mt ruapehu, new zealand. *Q. J. Roy. Meteor. Soc.*, 127(576):2153–2179.

Prata, A. J. and Tupper, A. (2009). Aviation hazards from volcanoes: the state of the science. *Nat. Hazards*, 51(2):239–244.

Prata, F., Bluth, G., Rose, B., Schneider, D., and Tupper, A. (2001). Failures in detecting volcanic ash from a satellite-based technique - Comments. *REMOTE SENSING OF ENVIRONMENT*, 78(3):341–346.

Press, W., Flannery, B., Teukolsky, S., and Vettering, W. (1986). *Numerical Recipes in C*. Cambridge University Press, Cambridge.

QDOAS (2011). Belgian Institute for Space Aeronomy, S&T dependable solutions.

READY (2008). Real-time Environmental Applications and Display sYstem, Air Resources Laboratory, NOAA.

Realmuto, V., Abrams, M., Buongiorno, M., and Pieri, D. (1994). The use of multispectral thermal infrared image data to estimate the sulfur-dioxide flux from volcanos - a case-study from mount etna, sicily, july 29, 1986. *J. Geophys. Res.-So Ea*, 99(B1):481–488.

Richter, A., Eisinger, M., Ladstätter-Weißenmayer, A., and Burrows, J. (1999). DOAS Zenith Sky Observations: 2. Seasonal Variation of BrO over Bremen (53° N) 1994-1995. *J. Atmos. Chem.*, 32:83–99.

Richter, A., Wittrock, F., Eisinger, M., and Burrows, J. (1998). Gome observations

of tropospheric bro in northern hemispheric spring and summer 1997. *Geophys. Res. Lett.*, 25(14):2683–2686.

Richter, A., Wittrock, F., Ladstätter-Weißenmayer, A., and Burrows, J. P. (2002). GOME measurements of stratospheric and tropospheric BrO. *Adv. Space Res.*, 29(11):1667–1672.

Rix, M., Valks, P., Hao, N., van Geffen, J., Clerbaux, C., Clarisse, L., Coheur, P.-F., Loyola R, D. G., Erbertseder, T., Zimmer, W., and Emmadi, S. (2009). Satellite Monitoring of Volcanic Sulfur Dioxide Emissions for Early Warning of Volcanic Hazards. *IEEE J. Sel. Topics Appl. Earth Observ.*, 2(3):196–206.

Roberts, T. J., Braban, C. F., Martin, R. S., Oppenheimer, C., Adams, J. W., Cox, R. A., Jones, R. L., and Griffiths, P. T. (2009). Modelling reactive halogen formation and ozone depletion in volcanic plumes. *Chem. Geol.*, 263(1-4, Sp. Iss. SI):151–163.

Robock, A. (2007). Volcanic eruptions and climate (vol 45, 2007). *Rev. Geophys.*, 45(3).

Romero, R., editor (2004). *The International Airways Volcano Watch (IAVW). Proceedings of 2nd International Conference on Volcanic Ash and Aviation Safety*, Virginia,USA.

Roscoe, H. K., Fish, D. J., and Jones, R. L. (1996). Interpolation errors in uv-visible spectroscopy for stratospheric sensing: Implications for sensitivity, spectral resolution, and spectral range. *Appl. Opt.*, 35(3):427–432.

Rose, W., Delene, D., Schnelder, D., Bluth, G., Krueger, A., Sprod, I., Mckee, C., Davies, H., and Ernst, G. (1995). Ice in the 1994 rabaul eruption cloud - implications for volcanic hazard and atmospheric effects. *NATURE*, 375(6531):477–479.

Rose, W. I., Millard, G. A., Mather, T. A., Hunton, D. E., Anderson, B., Oppenheimer, C., Thornton, B. F., Gerlach, T. M., Viggiano, A. A., Kondo, Y., Miller, T. M., and Ballenthin, J. O. (2006). Atmospheric chemistry of a 33-34 hour old volcanic cloud from Hekla Volcano (Iceland): Insights from direct sampling and the application of chemical box modeling. *J. Geophys. Res.-Atmos.*, 111(D20).

Salawitch, R. J., Canty, T., Kurosu, T., Chance, K., and Jacob, D. J. (2010). A new interpretation of total column bro during arctic spring. *Geophys. Res. Lett., in press*, XX:XX.

Sander, S. P., Friedl, R. R., Golden, D. M., Kurylo, M. J., Moortgat, G. K., Keller-

Rudeck, H., Wine, P. H., Ravishankara, A. R., Kolb, C. E., Molina, M. J., Finlaysson-Pitts, B. J., Huie, R. E., and Orkin, R. L. (2011). Chemical kinetics and photochemical data for use in atmospheric studies. Technical Report Evaluation Number 17, JPL Publication, 10-6, Jet Propolsion Laboratory, Pasadena.

Schumann, U., Weinzierl, B., Reitebuch, O., Schlager, H., Minikin, A., Forster, C., Baumann, R., Sailer, T., Graf, K., Mannstein, H., Voigt, C., Rahm, S., Simmet, R., Scheibe, M., Lichtenstern, M., Stock, P., Rüba, H., Schäuble, D., Tafferner, A., Rautenhaus, M., Gerz, T., Ziereis, H., Krautstrunk, M., Mallaun, C., Gayet, J.-F., Lieke, K., Kandler, K., Ebert, M., Weinbruch, S., Stohl, A., Gasteiger, J., Groß, S., Freudenthaler, V., Wiegner, M., Ansmann, A., Tesche, M., Olafsson, H., and Sturm, K. (2011). Airborne observations of the eyjafjalla volcano ash cloud over europe during air space closure in april and may 2010. *Atmos. Chem. Phys.*, 11(5):2245–2279.

Sefnov, N. N. (1959). Spectroscopic, photoelectric and radar investigations of the aurora and the nightglow. *Izd. Akad. Nauk.*

Sihler, H., Platt, U., Beierle, S., Mahrbach, T., Kühl, S., Dörner, S., Verschaeve, J., Pöhler, D., Vogel, L., Sander, R., and Wagner, T. (2011). A new algorithm to retrieve tropospheric column densities of bro during episodes of polar halogen activitation from satellite measurements. *in prep.*

Simpson, J., Hufford, G., Pieri, D., and Berg, J. (2000). Failures in detecting volcanic ash from satellite-based technique. *REMOTE SENSING OF ENVIRONMENT*, 72(2):191–217.

Smithsonian (2011). Smithsonian, global volcanism program.

Solomon, S., Schmeltekopf, A. L., and Sanders, R. W. (1987). On the interpretation of zenith sky absorption-measurements. *J. Geophys. Res.-Atmos.*, 92(D7):8311–8319.

Spilliaert, N., Metrich, N., and Allard, P. (2006). S-G-F degassing pattern of water-rich alkali basalt: Modelling and relationship with eruption styles on Mount Etna volcano. *Earth Planet. Sci. Lett.*, 248(3-4):772 –786.

Stoiber, R. and Jepsen, A. (1973). Sulfur dioxide contribution to the atmosphere by volcanoes. *Science*, 182:577–578.

Stutz, J. and Platt, U. (1996). Numerical analysis and estimation of the statistical

error of differential optical absorption spectroscopy measurements with least-squares methods. *Appl. Opt.*, 35(30):6041–6053.

Textor, C., Graf, H.-F., C., T., and Robock, A. (2004). Emissions from volcanoes. In Granier, C., Artaxo, P., and Reeves, C., editors, *Emissions of Atmospheric Trace Compounds*, pages 269–303. Klewer, Dordrecht, Netherlands.

Theys, N., Roozendael, M. V., Dils, B., Hendrick, F., Hao, N., and Maziere, M. D. (2009). First satellite detection of volcanic bromine monoxide emission after the Kasatochi eruption. *Geophys. Res. Let.*, 36.

Theys, N., Van Roozendael, M., Hendrick, F., Fayt, C., Hermans, C., Baray, J.-L., Goutail, F., Pommereau, J.-P., and De Maziere, M. (2007). Retrieval of stratospheric and tropospheric BrO columns from multi-axis DOAS measurements at Reunion Island (21 degrees S, 56 degrees E). *Atmos. Chem. Phys.*, 7(18):4733–4749.

Thomas, H. E. and Prata, A. J. (2011). Sulphur dioxide as a volcanic ash proxy during the april-may 2010 eruption of eyjafjallajökull volcano, iceland. *Atmos. Chem. Phys.*, 11(14):6871–6880.

Thomas, H. E. and Watson, I. M. (2010). Observations of volcanic emissions from space: current and future perspectives. *Nat. Hazards*, 54(2):323–354.

Tupper, A., Textor, C., Herzog, M., Graf, H.-F., and Richards, M. S. (2009). Tall clouds from small eruptions: the sensitivity of eruption height and fine ash content to tropospheric instability. *Nat. Hazards*, 51(2):375–401.

Valks, P., Loyola, D., Hao, N., and Rix, M. (2009). Algorithm theoretical basis document for GOME-2 total column products of ozone, minor trace gases, and cloud properties. Technical report, Deutsches Zentrum für Luft und Raumfahrt, Oberpfaffenhofen, Germany.

Vance, A., McGonigle, A. J. S., Aiuppa, A., Stith, J. L., Turnbull, K., and von Glasow, R. (2010). Ozone depletion in tropospheric volcanic plumes. *GeoPhys. Res. Lett.*, 37.

Vandaele, A., Hermans, C., and Fally, S. (2009). Fourier transform measurements of SO2 absorption cross sections: Ii. temperature dependence in the 29 000-44 000 cm(-1) (227-345 nm) region. *J. Quant Spectrosc. Radiat. Transfer*, 110(18):2115–2126.

Vandaele, A., Hermans, C., Simon, P., Carleer, M., Colin, R., and Fally, S. (1998).

Measurements of the NO2 absorption cross-section from 42 000 cm(-1) to 10 000 cm(-1) (238-1000 nm) at 220 K and 294 K. *J. Quant Spectrosc. Radiat. Transfer*, 59(3-5):171–184.

Voigt, S., Orphal, J., Bogumil, K., and Burrows, J. (2001). The temperature dependence (203-293 K) of the absorption cross sections of O-3 in the 230-850 nm region measured by Fourier-transform spectroscopy. *J. Photoh. Photobio. A.*, 143(1):1–9.

von Glasow, R. (2010). Atmospheric chemistry in volcanic plumes. *Proc. Natl. Acad. Sci. U. S. A.*, 107(15):6594–6599.

von Glasow, R., Bobrowski, N., and Kern, C. (2009). The effects of volcanic eruptions on atmospheric chemistry. *Chem. Geol.*, 263(1-4, Sp. Iss. SI):131–142.

von Glasow, R. and Crutzen, P. (2007). Tropospheric halogen chemistry. In Keeling, R., Holland, H., and Turekion, K., editors, *Treatise on Geochemistry - Vol. 4 The Atmosphere, Update 1*, volume 4. Oxford: Elsevier/Pergamon.

von Glasow, R., Sander, R., Bott, A., and Crutzen, P. (2002). Modeling halogen chemistry in the marine boundary layer - 1. Cloud-free MBL. *J. Geophys. Res.-Atmos.*, 107(D17).

Vountas, M., Rozanov, V., and Burrows, J. (1998). Ring effect: Impact of rotational Raman scattering on radiative transfer in earth's atmosphere. *J. Quant. Spectrosc. Ra.*, 60(6):943–961.

Wagner, T., Beirle, S., and Deutschmann, T. (2009a). Three-dimensional simulation of the ring effect in observations of scattered sun light using monte carlo radiative transfer models. *Atmospheric Measurement Techniques*, 2(1):113–124.

Wagner, T., Burrows, J. P., Deutschmann, T., Dix, B., von Friedeburg, C., Frieß, U., Hendrick, F., Heue, K.-P., Irie, H., Iwabuchi, H., Kanaya, Y., Keller, J., McLinden, C. A., Oetjen, H., Palazzi, E., Petritoli, A., Platt, U., Postylyakov, O., Pukite, J., Richter, A., van Roozendael, M., Rozanov, A., Rozanov, V., Sinreich, R., Sanghavi, S., and Wittrock, F. (2007a). Comparison of box-air-mass-factors and radiances for multiple-axis differential optical absorption spectroscopy (max-doas) geometries calculated from different uv/visible radiative transfer models. *Atmospheric Chemistry and Physics*, 7(7):1809–1833.

Wagner, T., Chance, K., Frieß, U., Gil, M., Goutail, F., Hönninger, G., Johnston, P., Karlsen-Tørnkvist, K., Kostadinov, I., Leser, H., Petritoli, A., Richter, A.,

Van Roozendael, M., and Platt, U. (2002a). Correction of the ring effect and i0effect for doas observations of scattered sunlight. *ESA Technical Report*.

Wagner, T., Deutschmann, T., and Platt, U. (2009b). Determination of aerosol properties from max-doas observations of the ring effect. *Atmospheric Measurement Techniques*, 2(2):495–512.

Wagner, T., Ibrahim, O., Sinreich, R., Frieß, U., von Glasow, R., and Platt, U. (2007b). Enhanced tropospheric BrO over Antarctic sea ice in mid winter observed by MAX-DOAS on board the research vessel Polarstern. *Atmos. Chem. Phys.*, 7:3129–3142.

Wagner, T. and Platt, U. (1998). Satellite mapping of enhanced BrO concentrations in the troposphere. *Nature*, 395(6701):486–490.

Wagner, T., von Friedeburg, C., Wenig, M., Otten, C., and Platt, U. (2002b). Uv-visible observations of atmospheric o-4 absorptions using direct moonlight and zenith-scattered sunlight for clear-sky and cloudy sky conditions. *J. Geophys. Res.-Atmos.*, 107(D20):4424.

Wahner, A., Ravishankara, A. R., Sander, S. P., and Friedl, R. R. (1988). Absorption cross-section of bro between 312 and 385nm at 298 and 223k. *Chem. Phys. Lett.*, 152(6):507–512.

Wen, S. and Rose, W. (1994). Retrieval of sizes and total masses of particles in volcanic clouds using AVHRR bands 4 and 5. *J Geophys. Res.*, 99:5421–5431.

Wilmouth, D. M., Hanisco, T. F., Donahue, N. M., and Anderson, J. G. (1999). Fourier transform ultraviolet spectroscopy of the a (2)pi(3/2) <- x (ii3/2)-i-2 transition of bro rid a-2329-2008. *J. Phys. Chem. A*, 103(45):8935–8945.

Wöhrbach, M. (2008). Weiterentwicklung und erprobung einer uv-kamera zur bestimmung atmosphärischer spurengasverteilungen. Master's thesis, Fakultät für Physik und Astronomie, Ruprecht-Karls-Universität Heidelberg.

Zehner, C., editor (2010). *Monitoring Volcanic Ash from Space. Proceedings of the ESA-EUMETSAT workshop on the 14 April to 23 May 2010 eruption at the Eyjafjoll volcano, South Iceland*, volume ESA Publikation STM-280, Frascati, Italy. ESA, ESA.

Zhang, Y. and Johansson, M. (2008). Mobiledoas. Optical Remote Sensing Group, Chalmers University of Technology, Sweden.

Figure

List of Tables

Acknowledgements

This work would not have been possible without many people and I have to apologize that this most read part of the thesis received the least attention timewise.

Above all, I need to thank my family. My mother Gretel and father Hans-Martin, and my brothers and sisters Lotti, Wiebke and Knud, as well as my love Laura Alonso. Although I could not spend as much time with you as I wished, you are the greatest bunch and I could not have done this without knowing you were there.

Biggest thanks to Ulrich Platt, for letting me join the his group, constant support and the freedom to expand my horizon also outside the boundaries of thesis' subject. Especially my stay on the icebreaker Amundsen during the Arctic campaign, Winter 2008, changed my life. I also owe much to Bo Galle. Working together with Ulrich Platt and him was an inspiration and I feel honoured to have participated in the NOVAC project. The Etna campaigns would not have been possible without Roland von Glasow, who spend most of his time in July 2009 driving around the volcano. We had a great time also when not driving and many fruitful discussions. And last but not least Thomas Wagner, who was a great help discussing many aspects of this thesis and found the time to referee it.

We are a big group at the Institute of Environmental Physics in Heidelberg, and everyone deserves a big thank you! Nevertheless, I would like to give special thanks to Christoph Kern. Working closely together during the greater part of our doctoral theses, we had some great times in Heidelberg and on the numerous measurement campaigns. Nicole Bobrowski also deserve a big hug. Always with an open ear and helpful, even if she could not be present in Heidelberg all the time.

Visiting volcanoes is always fun, but even more with Matthias Fickel, Christoph "Il Mago" Hörmann, Sebastian Illing, Felix Kick, Lena Kritten, Peter Lübcke, Holger Sihler, Tobias Sommer, Markus Wöhrbach, and Johannes Zielcke. The measurements presented in this work would not have been possible without your help, and it was always a great pleasure to work with you. The same is true for

Johannes Lampel, Thomas Lehmann, Denis Pöhler and Holger Sihler. Here, I need to thank Holger again, since our "colorful pictures" are based on his ingenious idea.

Special thanks also to Hinrich Aue, Marcel Dorf, Lena Kritten, Cristina Prados-Roman, Susanne Reichinnek and Katja Seitz. Biking uphill is good, but downhill even better! Skat, the Orange, and many good conversations, to name just a few.

The backbone of the institute, Inge Clos and Karoline Thomas, not only for handling ugly things like travel cost statements and project audits.

During the thesis I also had the luck to meet and work together with many other people. First of all the Swedish team: Bo Galle, Santiago Arellano, Vladimir Conde, Mattias Johansson, Patrik Norman and Claudia Rivera, I hope to see you guys soon, either in Sweden or somewhere around the world. The same goes for Hugo Delgado and José Manuel Alvarez from Mexico, as well as Fabio Vita and Salvo Inguaggiato (Italy), and Thor Hansteen from Kiel.